Design, manufacturing, experimental evaluation and numerical analysis of novel composite helical springs

By

Ling Chen

PhD of Mechanical Engineering

Thesis

Submitted to Flinders University

for the degree of

Doctor of Philosophy

College of Science and Engineering

17/04/2025

Contents

ABSTRACT IV

DECLARATION VI

LIST OF FIGURES VII

LIST OF TABLES XII

1. INTRODUCTION 1

- **1.1 The importance of CHSs** 1
- **1.2 Development of CHSs** 3
- **1.3 Research aims** 4
- **1.4 Gaps and challenges** 5
- **1.5 Research objectives** 6
- **1.6 Research approaches** 8
- **1.7 Relationship between chapters** 9

2. LITERATURE REVIEW 12

- **2.1 Introduction of literature review** 13
- **2.2 The optimization methods of CHSs** 14
  - **2.2.1 Single-objective optimization of CHSs** 14
  - **2.2.2 Dual-objective optimization of CHSs** 18
  - **2.2.3 Finite element design and optimization of static performance of CHSs** 21
- **2.3 Experimental design and optimization of static performance of CHSs** 22
  - **2.3.1 Progress of manufacturing method of CHSs** 22
  - **2.3.2 Design and optimization of composite material of CHSs** 25
  - **2.3.3 Design and optimization of reinforcement structure of CHSs** 28
  - **2.3.4 Design and optimization of geometric dimension of CHSs** 31
- **2.4 Design and optimization of dynamic performance of CHSs** 32
  - **2.4.1 Design and optimization of fatigue of CHSs** 32
  - **2.4.2 Design and optimization of nature frequencies of CHSs** 34
- **2.5 Summary** 36

3. DESIGN AND MANUFACTURING OF CHSs 37

- **3.1 Structure design of CHSs** 38
- **3.2 Calculation and verification of fiber volume content of CHSs** 40
  - **3.2.1 Calculation of fiber volume content of CHSs** 40
  - **3.2.2 Verification of fiber volume content of CHSs** 41
- **3.3 Preparing of reinforcement of CHSs** 41
  - **3.3.1 Preparing of reinforcement of UCHS** 41
  - **3.3.2 Preparing of reinforcement of MCHS** 42
  - **3.3.3 Preparing of reinforcement of WCHS** 42
  - **3.3.4 Preparing of reinforcement of BCHS** 43
- **3.4 Manufacturing of CHSs** 43
  - **3.4.1 Equipment assembly** 43
  - **3.4.2 Design and customized of mold** 44

3.4.3 Experimental materials and instruments 45
3.4.4 The manufacturing process and precautions of the experiment.46
3.5 Summary 50
4. STUDY ON STATIC PERFORMANCE OF SBCHSs..52
4.1 Test methods...54
4.1.1 Compression test...54
4.1.2 Resilience test 54
4.2 FEM 55
4.2.1 3D meso model of SBCHSs 55
4.2.2 FEM of SBCHSs...56
4.3 Results and analysis of static performance...58
4.3.1 Analysis and verification of simulation results 58
4.3.2 Von Mises stress evolution of SBCHSs under compression ...60
4.3.3 Max. principal stress distribution with helical angles of SBCHSs under compression 63
4.3.4 Advanced analysis of SBCHSs 65
4.4 Summary 67
5. IMPACT PERFORMANCE ANALYSIS OF MBLs-CHS 69
5.1 Impact test..71
5.2 Impact simulation 72
5.2.1 VFM of MBLs...72
5.2.2 FEA modelling of MBLs-CHSs..73
5. 3. Results and discussion 77
5. 3.1 Experimental analysis of impact 77
5. 3.2 Verification of impact model 79
5. 3.3 Equivalent stress evolution of MBLs-CHSs under impact...........80
5.3.4 Kinematics of MBLs-CHSs under impact..84
5.4 Summary 86
6. STIFFNESS DEGRADATION ANALYSIS OF MBLs-CHS UNDER IMPACT 88
6.1 Compression and impact test of MBLs-CHS 90
6.2 Material damage evolution in simulation 90
6.3 Result and discussion 92
6.3.1 Experimental analysis and simulation verification of impact 92
6.3.2 Von Mises stress distribution under impact...................................94
6.3.3 Time domain analysis of impact respond 99
6.3.4 Prediction of stiffness degradation of MBLs-CHS under impact 101
6.4 Summary 103
7. FATIGUE PERFORMANCE OF TBCHSs...104
7.1 Fatigue test and analysis...104
7.1.1 Fatigue test standard...104
7.1.2 Fatigue test 104

7.1.3 Fatigue degradation 105
7.1.4 Analysis of fatigue test results 106
7.2 Fatigue damage analysis 107
7.2.1 Fundamental assumption 107
7.2.2 Setting of boundary condition 108
7.2.3 Failure criterion of fatigue 108
7.2.4 Damage morphology analysis 109
7.3 Summary 110
8. APPLICATION OF TBCHSs 111
8.1 Application vehicle - Jeep TJ2004 111
8.2 Test 112
8.2.1 Test preparation and precautions 113
8.2.2 Strain test method 114
8.3 Result and discussion 118
8.3.1 Damage morphology analysis 118
8.3.2 Strain analysis of TBCHSs during installation 119
8.3.3 Optimization of resin and geometry of TBCHSs 125
8.3.4 Strain analysis of optimal TBCHSs during installation 130
8.4 Summary 133
9. CONCLUSION 134
10. FUTURE WORK AND PROSPECTION 139
10.1 Future work 139
10.1.1 Strain analysis of original metal springs and optimal TBCHSs during driving 139
10.1.2 Stiffness degradation under aging test 142
10.2 Prospections 142
10.2.1 New manufacturing technology of CHSs 142
10.2.2 CHSs mixed with metal 144
10.2.3 Intelligent sensing monitoring system for CHSs 144
PUBLICATIONS AND AWARDS 146
ACKNOWLEDGEMENT 147
REFERENCE 149

ABSTRACT

The past few years have witnessed a potentially increase of composite helical springs (CHSs) deployment. They can not only save fuels and thus expand overall cruising ranges but also reduce greatly carbon dioxide emissions. However, the insufficient of design method and the lack of comprehensive performance evaluation methods limit the application and development of CHSs. To solve this problem, the reinforcement structure of CHSs first is designed by combining the force analysis and textile structure, The initial compression comparison shown that CHSs with braided reinforcement (BCHS) have optimal stiffness among them. Hence the BCHS have been selected for studying further static and dynamic performance by combining experiment and simulation. The static performance has been optimized based on BCHS with single braided layer (SBCHS) with different braided angle of 0°, 15° and 30° (UCHS, SBCHS15° and SBCHS30°) The compression experimental results show that the spring constant of SBCHS15° and SBCHS30° can reach 105.4% and 171.4% higher than that of UCHS respectively. Therefore, the 30° braided angle have been selected to further optimized the dynamic performance based on the braided layer number. Then, the dynamic impact performance has been explored by comparing BCHS with multi-braided layers (MBLs-CHS) including BCHS with single, double and triple braided layers (SBCHS, DBCHS and TBCHS). Experimental results elucidate a sequential improvement in the impact performance of SBCHS, DBCHS, and TBCHS. Due to damage evolution under impact is challenging to detect physically in real time. Time domain analysis is introduced to explore the in real time relationship between impact force and damage. The stiffness degradation under various amplitude intensity of MBLs-CHS have been fitted to predict the global stiffness degradation of MBLs-CHS in real time. Based on above analysis, the TBCHS not only have best static and dynamic impact performance but also have minimum damage than SBCHS and DBCHS. Therefore, TBCHS is used to further explore the fatigue performance. The result shown that the life of TBCHSs under 100% and 90% stress levels is only 2000 and 6500 respectively based on the failure stiffness of 38.7kgf/mm. But when the stress level drops to 70%, the stiffness decreases only 1.3% after 30000 cycles, which shows that the TBCHSs can be used for long time under the stress level of less than 70%. Apart from the optimization of static and dynamic performance, the feasibility of replace metal spring using TBCHS have been further investigated through installing TBCHSs in the vehicle. The experiment result showed that there is no damage to the front TBCHSs. The damage just occurs on the resin component of the posterior region of rear TBCHSs. After resin optimization, the optimal TBCHSs have been successfully installed on the vehicle without damage, illustrating the feasibility of applicating optimal TBCHSs. This research establishes a robust foundation for performance studies and offers valuable guidelines for the engineering application of CHSs.

Keywords: composite helical springs, reinforcement structure, braided angle and layer, static and dynamic performance, numerical analysis

DECLARATION

I certify that this thesis:

1. does not incorporate without acknowledgment any material previously submitted for a degree or diploma in any university

2. and the research within will not be submitted for any other future degree or diploma without the permission of Flinders University; and

3. to the best of my knowledge and belief, does not contain any material previously published or written by another person except where due reference is made in the text.

Signed......................Ling Chen..................

Date..........................17/04/2025................

LIST OF FIGURES

Fig. 1.1 Use environment of CHSs. 1

Fig. 1.2 Relationship diagram among chapters 11

Fig. 2.1 Compressive deformation process of CHSs (a) Original state; (b) Compressive state; (c) Failure state; (d) Fully compressive state (T.-W. Liu et al., 2021). 17

Fig. 2.2 Comparison of Pareto fronts for different populations sizes. (a) MOEA/D; (b) MLSGA-NSGAII; (c) NSGA-II; (d) MTS; (e) MLSGA-MOEA/D; (f) MLSGA and (g) SPEA-II (J.-B. Bai et al., 2021). 20

Fig. 2.3 (a) Von Mises stresses of CMHS45%, CMHS50%, CMHS55%, CMHS4 and CMHS6; (b) Von Mises stress distribution of cross section of CMHS45%, CMHS50%, CMHS55%, CMHS4 and CMHS6(Wu, Chen, et al., 2020). 22

Fig. 2.4 Schematic diagram of the forming process of CHSs (a) hot press molding (C.-H. Chiu et al., 2007; Sardou et al., 2005); (b) RTM (B.-L. Choi & B.-H. Choi, 2015); (c) integrated forming (Wu, Chen, et al., 2020). 23

Fig. 2.5 Manufacture of CHSs by the lost mold method. (a) The resin impregnated fiber in a flatbed mold to form prepreg; (b), (c) the uncured prepreg was taken out from the mold; (d) the uncured prepreg was placed and cured in the plaster sacrificial mold; (e) the plaster (sacrificial core) was broken; and (f) CHSs were obtained(Kim et al., 2021). 25

Fig. 2.6 (a) SEM diagram of spring wire rod (Kim et al., 2021); (b) Crack at the opening end of CHSs (C.-H. Chiu et al., 2007); (c) Inner rim delamination of CHSs (C.-H. Chiu et al., 2007); (d) Breaking of inner rim fiber of CHSs (C.-H. Chiu et al., 2007); (e) The inner rim of the CHS breaks and contacts with its neighboring coil (C.-H. Chiu et al., 2007). 28

Fig. 2.7 Reinforcement structures of CHSs, (a) braided structure (Luger et al., 2018); (b) ply structure (Ke et al., 2020a); (c) twisted structure (Wu, Chen, et al., 2020); (d) skin-core structure (Jiang et al., 2021) and (e) hybrid structure (C.-H. Chiu et al., 2007). 29

Fig. 3.1 (a) Force analysis of cross section of CHSs (b)dimensions of CHSs. 39

Fig. 3.2 The diagram of UCHS, MCHS, WCHS and BCHS. 40

Fig. 3.3 The diagram schematic of preparing multistrand reinforcement. 42

Fig. 3.4 The diagram schematic of preparing wrapped reinforcement 43

Fig. 3.5 Preparation process of braided reinforcement. 43

Fig. 3.6 The assembled equipment of manufacturing CHSs. 44

Fig. 3.7 The diagram schematic of designed winding mold of CHSs 45

Fig. 3.8 Manufacturing of CHSs by injection-winding method. 49

Fig. 3.9 The diagram of UCHS, SBCHS15°. SBCHS30°, DBCHS and TBCHS. 50

Fig. 3.10 The diagram of shape of CHSs 50

Fig. 4.1 Compression test of SBCHSs 54
Fig. 4.2 Resilience test of SBCHSs 55
Fig. 4.3 The process of building SBCHS model. (a) Braided projection curve, (b) helical braiding surface, (c) rotating sweep surface, (d) braided fiber bundle center line, (e) the center lines of 24 braided fiber bundles, (f) braided reinforcement, (g) reinforcement core, and (h) resin model of SBCHS. 56
Fig. 4.4 Finite element modeling of SBCHSs. (a) The discrete local coordinate system, (b) meshing and (c) boundary condition. 58
Fig. 4.5 (a) Validation of simulation model and (b) spring constant of SBCHS by simulation. 59
Fig. 4.6 (a) Load-displacement curves of UCHS55%, SBCHS15° and SBCHS30° and (b) spring constants of UCHS55%, SBCHS15° and SBCHS30° through experiment and by simulation. 60
Fig. 4.7 (a) Mises stresses distribution of UCHS55%, SBCHS15° and SBCHS30° under compression, (b) mises stresses distribution of reinforcement core of SBCHS15° and SBCHS30° under compression, (c) mises stresses distribution of braided reinforcement of SBCHS15° and SBCHS30° under compression, and (d) mises stresses distribution of resin of SBCHS15° and SBCHS30° under compression. 62
Fig. 4.8 (a) Four reference curves of the spring wire outer layer of UCHS55% and (b) helical angle-mises stress curves of spring wire periphery of UCHS55%, SBCHS15° and SBCHS30° within 0~360° under compression. 63
Fig. 4.9 Max. principal stress distribution under compression within 0~360° of (a) right braided reinforcement, (b) left braided reinforcement, (c) two fiber bundles of right braided reinforcements corresponding to the F_{in} and F_{ex} at 180° section and (d) two fiber bundles of left braided reinforcements corresponding to the F_{in} and F_{ex} at a 180° section. 65
Fig. 4.10 Helical angle-max. principal stress curves under compression of (a) UCHS55%, (b) SBCHS15° and (c) SBCHS30°. 65
Fig. 4.11 (a) The height change of UCHS55%, SBCHS15°, SBCHS30° and steel with time during loading experiment, and (b) the heighe change of UCHS55%, SBCHS15°, SBCHS30° and steel with time during unloading experiment. 67

Fig. 5.1 Impact test of MBLs-CHS 72
Fig. 5.2 (a) solid models of MBLs in SBCHS, DBCHS and TBCHS, (b) transformation from solid model to VFM and (c) a VFM of MBLs. 73
Fig. 5.3 Finite element shrinkage modeling of MBLs. (a) The discrete local coordinate system of reinforcement core, (b) The discrete local coordinate system of braided reinforcement, (c) boundary condition, and (d) shrinkage progress of MBLs. 75
Fig. 5.4 The cross-section of MBLs at (a) 0.1s, (b) 0.2 s, (c) 0.3 s, (d) 0.4 s, (e) 0.5 s shrinkage time and (f) optical microscopy image. 76

Fig. 5.5 Finite element modelling of MBLs-CHS. (a) The discrete local coordinate system, (b) meshing and (c) impact boundary condition. 77
Fig. 5.6 (a) Deflection-impact force curves, (b) time-energy curves and (c) D_{max}, F_{max}, E_a and E_r of SBCHS, DBCHS and TBCHS under 5 J, 10 J, 20 J, 40 J and 60 J. 79
Fig. 5.7 (a) The cross-section of MBLs of DBCHS after shrinking based on different VF quantities of 30, 60, and 120 per yarn (b) the deflection-impact force curves of DBCHS after impact simulation based on different mesh sizes of 0.4, 0.2 and 0.1 mm with 30, 60 and 120 VFs per yarn and (c) the mesh size-time curves of DBCHS with 30, 60 and 120 VFs per yarn for impact simulations. 80
Fig. 5.8 (a) Deformation process of DBCHS recorded by high-speed camera during impact experiment and (b) deformation process of DBCHS during impact simulation. 81
Fig. 5.9 (a) Von Mises stress of braided reinforcement of SBCHS, DBCHS and TBCHS during impact 83
Fig. 5.10 (a) Schematic diagram of coils in MBLs-CHS, (b) time-displacement response curves and (c) time-velocity response curves of each coil in SBCHS, DBCHS and TBCHS..85
Fig. 5.11 The mitigation rate η of SBCHS, DBCHS and TBCHS under impact. 86

Fig. 6.1 (a) Time-energy curves and (b) time-impact force curves of SBCHS, DBCHS and TBCHS under different impact energy and (c) the damage morphology of SBCHS, DBCHS and TBCHS under 60 J impaction. 94
Fig. 6.2 Von Mises stress distribution of (a) braided reinforcement and (b) reinforcement core and (c) damage evolution of SBCHS, DBCHS and TBCHS under 5 J, 10 J, 20 J, 40 J and 60 J impact simulation. 98
Fig. 6.3 (a) maximum mises stress curves of resin, (b) maximum mises stress curves of braided reinforcement and (c) maximum mises stress curves of reinforcement core of SBCHS, DBCHS and TBCHS under 5 J, 10 J, 20 J, 40 J and 60 J impact simulation. 98
Fig. 6.4 Element removal fraction of SBCHS, DBCHS and TBCHS under 5 J, 10 J, 20 J, 40 J and 60 J impact simulation. 99
Fig. 6.5 Time domain signal of SBCHS, DBCHS and TBCHS under 5 J, 10 J, 20 J, 40 J and 60 J impaction. 100
Fig. 6.6 (a) Amplitude intensity and (b) stiffness degradation of SBCHS, DBCHS and TBCHS under 5 J, 10 J, 20 J, 40 J and 6 0 J impaction, and (c) the prediction of stiffness degradation of SBCHS, DBCHS and TBCHS based on amplitude intensity. 102

Fig. 7.1 Fatigue test of TBCHSs 105
Fig. 7.2 The load-displacement curves at 25%, 50%, 75% and 100% of the total cycle of TBCHSs...106

Fig. 7.3 (a) The plastic strain energy of TBCHSs under stress level of 100%, 90% and 70%, (b) the spring stiffness of TBCHSs under stress level of 100%, 90% and 70%, (c) the displacement of TBCHSs under stress level of 100%, 90% and 70%, ...107
Fig. 7.4 Setting of two analysis steps of TBCHSs during fatigue simulation 109
Fig. 7.5 The damage evolution of TBCHS under 100% stress level........................110

Fig. 8.1 (a) The distinguishing of anterior and posterior region of TBCHSs, (b) paste method of front TBCHS for testing strain data in different directions, (b) paste method of rear TBCHS for testing strain data in different directions, (d) installment of TBCHSs and (e) strain test during the vehicle had been fallen slowly until totally contact ground 116
Fig. 8.2 Tension and bending test of resin..........117
Fig. 8.3 (a) damage morphology of front TBCHSs and (b) damage morphology of rear TBCHSs..........119
Fig. 8. 4 (a) The strain of axial, radial and tangential directions of inner and outer diameter region of anterior and posterior region of front TBCHSs in middle coil and (b) the strain of axial and tangential directions of inner diameter region of anterior region of front TBCHSs in different coils..........122
Fig. 8.5 (a) The strain of axial, radial and tangential directions of inner and outer diameter region of anterior and posterior region of rear TBCHSs in middle coil and (b) the strain of axial and tangential directions of outer diameter region of posterior region of rear TBCHSs in different coils..........125
Fig. 8.6 (a) the tensile strain-stress curves of GCC135/GCC137, (b) the tensile strain-stress curves of R118/H103, (c) the tensile strain-stress curves of TDE86/70 acid anhydride/24 imidazole accelerator and (d) the optimal tensile strain-stress curves of GCC135/GCC137, R118/H103, TDE86/70 acid anhydride/24 imidazole accelerator 127
Fig. 8.7 (a) the flexural strain-stress curves of GCC135/GCC137, (b) the flexural strain-stress curves of R118/H103, (c) the flexural strain-stress curves of TDE86/70 acid anhydride/24 imidazole accelerator and (d) the optimal flexural strain-stress curves of GCC135/GCC137, R118/H103, TDE86/70 acid anhydride/24 imidazole accelerator..........129
Fig. 8.8 The installation experiment of optimal front and rear TBCHSs..................131
Fig. 8.9 (a) The strain of axial, radial and tangential directions of inner and outer diameter region of anterior and posterior region of optimal front TBCHSs in middle coil, (b) the strain of axial and tangential directions of inner diameter region of anterior region of optimal front TBCHSs in different coils, (c) The strain of axial, radial and tangential directions of inner and outer diameter region of anterior and posterior region of optimal rear TBCHSs in middle coil and (d) the strain of axial and tangential directions of outer diameter region of posterior region of optimal rear TBCHSs in different coils. 132

Fig. 10.1 (a) the strain of front metal spring during process of acceleration, constant speed of 20 km/h and deceleration, (b) the strain of front metal spring during process of acceleration, constant speed of 40 km/h and deceleration, (c) the strain of front metal spring during process of acceleration, constant speed of 60 km/h and deceleration, (d) the strain of rear metal spring during process of acceleration, constant speed of 20 km/h and deceleration, (e) the strain of rear metal spring during process of acceleration, constant speed of 40 km/h and deceleration and (f) the strain of rear metal spring during process of acceleration, constant speed of 60 km/h and deceleration. 140
Fig. 10.2 (a) the strain of front metal spring during process of turning, (b) the strain of front metal spring during process of uphill, (c) the strain of front metal spring during process of downhill, (d) the strain of rear metal spring during process of turning, (e) the strain of rear metal spring during process of uphill and (f) the strain of rear metal spring during process of downhill. 141
Fig. 10.3 (a) Shows the schematics of the UV-assisted coextrusion deposition of 3D continuous carbon fiber multifunctional composites; (b) a printed free standing CHSs; (c) a hollow cylinder structure CHSs and (d) a free-standing tapered CHSs (Yuan et al., 2021). 144

LIST OF TABLES

Table 2.1 : Various stiffness formulae for single-objective optimization, depending on the spring type and loading characteristics 14
Table 2.2: Advantages and disadvantages of five manufacturing methods of CHSs including filament winding (Ekanthappa et al., 2017; Hamed et al., 2020; Shende et al., 2016; Suresh et al., 2014), hot press molding (C.-H. Chiu et al., 2007; Nagao et al., 1998), RTM (B.-L. Choi & B.-H. Choi, 2015), integrated forming (Arularasan & Sabapathy, 2014; Luger et al., 2018) and lost mold method (Chen et al., 2014; Sardou et al., 2005)....................23
Table 2.3 ：The performances of CHSs made of different materials are compared. (Carbon, Glass, Kevlar, Calotropis gigantea and Steel are referred to as c, g, k, cg and s respectively) 26
Table 2.4 : Material, spring diameter and structure parameter of five types of CHSs. (Glass fiber, Carbon fiber, Kevlar fiber, Ultra-high molecular weight polyethylene fiber and Rubber core are referred to as g, c, k, um, r respectively)....................29
Table 2.5: Studied geometry parameters and correspond to materials and reinforcement structures of CHSs. (Active number of turns, Spring diameter, Wire diameter, Screw pitch, Inner wire diameter are referred to as n, D, d, p, d_i respectively) 31

Table 3.1: Experimental materials....................45
Table 3.2: Experimental instruments 46

Table 4.1: Material properties of carbon fiber and resin (Chakladar et al., 2014; Miyagawa et al., 2006; Miyagawa et al., 2005; Sommer et al., 2022; Xie & Koslowski, 2017; Zhang et al., 2013)....................57
Table 4.2: The comparison of specific spring stiffness of UCHS55%, SBCHS15°, SBCHS30° and steel springs....................67

Table 6.1: Amplitude intensity of SBCHS, DBCHS and TBCHS under different E_i.100
Table 6.2: The stiffness (N/mm) of SBCHS, DBCHS and TBCHS before and after impact under different E_i....................102

Table 8.1：the tensile fracture strain, tensile strength, tensile modulus and toughness of three types of resin under different curing temperatures. 127
Table 8.2：the flexural fracture strain, flexural strength, flexural modulus and flexural toughness of three types of resin under different curing temperatures. 129

1. INTRODUCTION

1.1 The importance of CHSs

As a mechanical part widely used in various fields, helical spring plays a very important role in production practice, as shown in Fig. 1.1. It deforms due to the elastic and structural characteristics of materials under the action of external load. Firstly, the mechanical energy or kinetic energy is transformed into potential (deformation) energy, and the deformation is restored immediately after unloading and then transformed into mechanical energy or kinetic energy. The helical spring is used to cushion the impact caused by fluctuation, which can effectively slow down the vibration and ensure smooth operation. At present, the demand for coil springs in the automotive field is the largest. Relevant data shows that 70% of coil springs are used in the automotive industry (Houlu & Chunan, 2008). Traditional metal materials have excellent plastic toughness and ductility. The forming method of metal spring can coil the metal bar into spiral ladder shape through cold coil spring or hot coil spring process, and then improve the surface quality of metal spring by shot blasting, painting and other processes, so as to improve the fatigue performance of spring (Yong et al., 2009). The indicators of metal materials, such as carbon content and cleanliness of spring steel, will greatly affect the performance of spring products (De-xiang & Zhong-da, 2003). At present, the development of the properties of spring steel has reached a bottleneck period that is difficult to break through (Dexiang & Zhongda, 2004), although many researchers continue to explore different preparation methods such as low-temperature nitriding and other technologies to improve the fatigue resistance and other properties of spring steel.

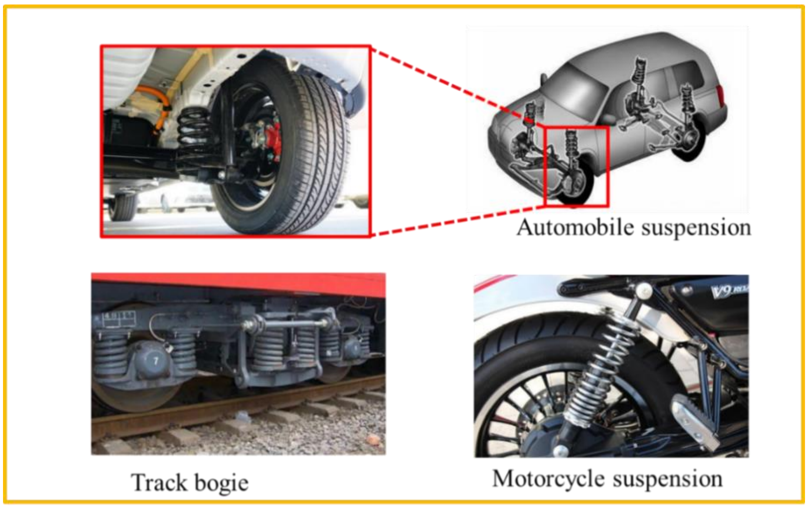

Fig. 1.1 Use environment of CHSs.

In recent years, the whole transportation field has been developing in the direction of lightweight and reducing carbon emissions. Composite materials have been widely used in automobile parts, such as automobile side guard, bumper, wind guide cover, etc, and even composite vehicles have appeared (Kun et al., 2011). This kind of vehicle not only has a high safety factor, but also their self-weight has been greatly reduced. The use of composite spiral springs is of special significance to reduce the weight of bicycles, cars, even aircraft and satellites. Reducing the weight of the bicycle is not only easy to carry but also can reduce the exercise energy consumption of cycling. Reducing the weight of automobiles and aircraft can not only reduce the consumption of raw materials and reduce costs, but also significantly reduce energy consumption, reduce harmful gas emissions, and improve the overall mobility and carrying capacity. The research shows that when the vehicle mass is reduced by 50 kg, the driving distance per liter of fuel can be increased by 1 km; If the mass is reduced by 10%, the fuel economy can be improved by about 5.5%.

Compared with the traditional metal coil spring, the most obvious advantage of using composite material coil spring is the weight reduction effect. Due to the great designability and low density of composite materials, the weight reduction of alternative products with the same performance is generally more than 50%. By selecting different materials and optimizing the design, the weight reduction ratio can even reach more than 70%, which is also a very rare weight reduction advantage in the optimization process of other components. Compared with steel coil spring, composite helical spring not only reduces weight, but also has the following advantages:

(1) "Fracture lag" improves reliability to a certain extent. When the composite coil spring is overloaded, it will not break instantaneously but will be delaminated or broken gradually along the inner fiber direction. Although the spring stiffness is greatly reduced in this process, it still has a certain strength, which can be found and remedied in time.

(2) Corrosion resistance, low and high temperature resistance. It can cope with the extreme environment that steel materials cannot be competent.

(3) Electrical and heat insulation and electromagnetic wave transmission, so it can be used in some special occasions, such as radar stations, geomagnetic observation stations, medical nuclear magnetic resonance equipment structure, etc.

(4) The life cycle cost is reasonable. Compared with high-grade steel springs, composite spiral spring has the advantages of low manufacturing cost, light weight and less energy consumption, which further reduces the total lift cycle cost.

(5) The material has large damping, and the noise generated under various working conditions is small, which reduces pollution to the environment and improves the human-machine environment.

(6) Under the same load capacity, composite spiral spring has great designability.

In view of the above reasons, it can be explained that the controllable and designable composite helical spring has a very broad application prospect.

1.2 Development of CHSs

So far, a great deal of research has been conducted (Xiong et al., 2017) to develop CHSs for fulfilling specific requirements (Jancirani & Assarudeen, 2015). Sarh *et al.* evaluated the stiffness response, material degradation and other basic performance of carbon fiber reinforced plastic (CFRP) composite helical springs. The performance of these coils is compared to alternative composite leaf spring and elliptical spring designs based on mechanical testing. They found the performance of the composite helical spring is much better than alternative composite leaf spring and elliptical spring designs (Sarh & Kad, 2010). Ekanthappa *et al.* investigated the prime parameters of composite helical spring like stiffness, maximum compression, failure load and physical dimensions. All the tests were carried out by the following ASTM standards. They found that the weight of composite helical spring is 40% less than steel helical spring, and the stiffness of composite helical spring is greater compared to steel helical spring with the same dimension. Therefore, composite helical springs can be efficiently used for light vehicles. Ekanthappa *et al.* also investigated the basic performance of composite helical spring. Their study results indicate that there is considerable weight saving of composite helical spring and it is possible to increase the stiffness of the spring by reducing the number of coils and increasing the area of the spring. The filament winding technique is used to fabricate the continuous fiber reinforced composite helical spring. The weight of the composite spring obtained is 42.63% less than the conventional metal spring. Stiffness of the composite spring is 43.76% less compared to conventional metal spring. Even though stiffness of the composite helical spring is less when compared to conventional metal spring, the spring is designed with less number of coils to increase the stiffness without sacrifice the strength or load carrying capacity of the spring (Ekanthappa et al., 2013). Ma *et al.* also investigated several features of composite helical springs including light weight, dynamic response, flexibility of design and fatigue resistance through testing. Depending the steel counterpart considered, composite helical springs offer weight saving of about 75%, fatigue life improvement, no rust, no creep, and no notch sensitivity at a cost close to that of a steel spring (Djomseu et al., 2008). Sui *et al.* tested and analyzed the bending resilience, bending restoration rate and tensile property of composite helical spring. The experimental results indicate that bending mechanical performance of CHSs is directly associated with the inside diameter of the spring, and the diameter, twist and number of fiber bundles.

In addition to using experimental methods to study and analyze springs, some scholars also predict and reveal stress characteristics of CHSs by simulation methods. Yang *et al.* (Wooster, 1964) and Azzam *et al.* (Yang et al., 2013; Zhan et al., 2018) simulated the stiffness of helical spring and found that the prediction result deviated within 6% from that of the mathematical formulation and experimental measurement, which demonstrated the feasibility and accuracy of the simulation. Apart from the stiffness prediction, the FEM based simulation can provide information of displacement, strain and stress fields which cannot be accessed directly through experimental tests. Five finite element models (FEM) of CHSs with different configurations were established by Wu *et al* (Wu, Chen, et al., 2020) by controlling the reinforcement twist and fiber volume content (V_f): three twistless CHSs with V_f of 45%, 50%, and 55% (CMHS45%, CMHS50%, and CMHS55%), and two twisted CHSs with different twist coefficients of 4 and 6r/10 cm but the same V_f of 55% (CMHS4 and CMHS6). By applying FEA, the effects of reinforcement structure and V_f on the stress distribution of CHSs were analyzed and discussed. The stress distribution corresponding to each CHS at different compressions is analyzed. The stress of the CHSs increases with the increase of fiber content and twist; the stress of the CHSs in each loop is the same; and the stress concentration region in the structure of the twistless CHSs is in the internal radial zone. This analysis method based on FEA deeply reveals the force law of CHSs, which lays a foundation for optimization of CHSs (Jiang et al., 2021; Kaoua et al., 2011).

1.3 Research aims

The reinforcement structure of CHSs can be determined by combining the analysis of the spring force and the characteristic of textile structure, and the performance of CHSs can be accurately controlled by changing the structural parameters.

The static (such as compression and resilience) and dynamic (such as impact and fatigue) performance of CHSs can be explored and improved according to the use scenario of CHSs in traffic by combination of experiment and macro and micro scale simulation.

CHSs can meet the needs of the automotive industry and become a qualified automotive suspension helical spring. They can replace the traditional metal helical springs to be widely used in the automotive field for achieving energy saving and carbon dioxide emission reduction. The application of CHSs can reduce travel costs and increase the mileage of private cars from a personal perspective, reduce material and production costs from enterprises perspective and reduce environmental pollution and power consumption to save natural energy from a social perspective.

1.4 Gaps and challenges

Many researchers put forward its practicability in reducing the weight of vehicles by considering the manufacturing, performance, and cost-effectiveness of CHSs. The preparation and study process of CHSs is complex and tedious, and the factors that need to be controlled and considered are very diverse. Using composite material instead of traditional metal material will bring new challenges to the optimization and manufacture of CHSs.

1. At present, although some achievements have been made in the study of using CHSs instead of traditional steel spring, and the development of CHSs has been promoted to a higher level, there are still have some challenges (C.-H. Chiu et al., 2007; Sardou et al., 2005) due to the structural characteristics of helical. Compared with the traditional metal spring, the reinforcement fiber in CHSs is anisotropic, which causes the preparation process of CHSs complex, so the wide application of composite in the preparation of helical spring is limited. Although some current preparation methods can produce composite springs with high fiber contents, there are many defects such as dry spots and defects (Al-Qureshi, 2001), requiring complex processing equipment, with high scrap rate and high manufacturing cost (J. Ekanthappa et al., 2016; Zhang & Zhang, 2006). To break through the bottleneck of CHSs preparation, it is important to further expand and improve the utilization rate of CHSs, and to find a processing technology that can produce CHSs mass. It is necessary to improve the current technology combined with the preparation characteristics of CHSs.
2. The mechanical performance of CHSs under the different use conditions needs to be evaluated. Therefore, to maximum the contribution of CHSs, the suitability between CHSs performance and use environment should be considered. This will involve how to adjust the mechanical performance of CHSs. As for traditional metal spring, the mechanical performance can be controlled by changing the geometry size. However, the geometry size of spring can be limited by installation environment. So that it is difficult to adjust the range of mechanical performance to meet extreme application scenarios. Similarly, CHSs also meet the challenge, but it can try to be solved by changing the reinforcement structure. In addition, some scholars have studied the damage modes of CHSs. The results show that the possible failure modes of CHSs are primarily resin cracking, interfacial debonding,

and fiber breakage. The resin cracking and interfacial debonding mostly occur before fiber breakage, which prevented the contribution of the fibers in CHSs. Therefore, in addition to the selection of a proper reinforcement structure CHSs, the mechanical performance of resin is crucial for optimizing the overall performance of CHSs. However, there is currently a lack of research on the effect of resin on performance of CHSs. Therefore, the balance between resin performance and performance of CHSs needs further exploration and optimization.

3. It is worth mentioning that the research of CHSs mainly focuses on static performance and not much research focuses on dynamic performance, especially impact and fatigue. However the spring is mainly used in dynamic environment, it is necessary to conduct a systematic study on the dynamic performance of the spring according to its use scenario. Moreover, many studies evaluate the feasibility and application progress of using CHSs to replace the metal spring based on performance evaluation. Because the application evaluation in the field is complex and need cost lots of human resources, funds and time. There are not many researchers to install the CHSs on the vehicle to evaluate in field the feasibility by professional analysis method. So that the progress of CHSs is only at the experimental stage, which limits the application of CHSs. To solve the problem, the installation in field of CHSs should be implemented and relevant evaluation should be provided to adjust whether the CHSs can been applicated to replace the metal spring.
4. Many scholars have also analyzed springs through simulation methods. To increase the convergence of the simulation optimization process and improve the calculation speed, some researchers not only simplify the working environment of the CHSs but also ignore the internal reinforcement structure of the CHSs and directly establish the isotropic 3D helical structure model. These models can only see the overall stress state of CHSs, and it is difficult to analyze the reinforced structure. Therefore, it is also a challenge to establish meso and micro models with fine structure to accurately express the stress state of CHSs.

1.5 Research objectives

Based on the abovementioned research and application gaps, this thesis tries to solve some of the challenges, as shown below.

1. To solve the limitations of manufacturing CHSs. According to the structure characteristics of CHSs, a set of integrated preparation methods based on VARI process is designed and established that is injection-winding technology. This method has the advantages of simple preparation process, easy operation and low

cost. It can manufacture CHSs without product defects and high yield. This method not only gives full play to the advantages of high fiber content and good product properties but also overcomes the limitations of the pultrusion process in terms of product form, providing new manufacturing technology for the development of CHSs.

2. Several types of reinforcement structure have been proposed for adjusting accurately the performance of CHSs. The influence of different structure parameters on the spring performance can be analyzed through experiment data to find out the adjusted law of performance of CHSs without changing the geometry size significantly.
3. To comprehensively research the performance of CHSs. In addition to the compression and resilience static performance, impact and fatigue dynamic performance of CHSs was tested and analyzed including the damage evaluation of CHSs under dynamic, which will lay a reliable theoretical basis for the development and popularization of CHSs.
4. Based on the primary helical formula of the spring and combined with 3D modeling software, the macro, meso and micro model of each CHS is established. According to the structural characteristics of each CHS, the establishment of meso and micro models of CHSs can not only make the overall simulation results more accurate, but also accurately reveal the real stress state of each small part of each spring component, to find out the stress law. In addition, the numerical method can be used to predict the trend of parameters affecting the performance of CHSs.
5. To determine whether the CHSs can successfully replace steel spring. The installation experiment has been done on JEEP TJ 2004 in Kraft Motorsports Pty Ltd., in Perth, Australia. The research will further ensure the feasibility of application of CHSs. The installation evaluation is implemented for application of CHSs. Because in general there always exists the gap between theory experiment and real application. Just using theory research in the laboratory is difficult to adjust the possibility of application of CHSs in real field.
6. To solve the problem of poor resin performance in composite helical spring, this project selects three types of resin to test and comparing their performance by the data analysis of tensile and bend performance.

The goal of this project is to enable the composite helical spring to meet the needs of the automotive industry and become a qualified automotive suspension helical spring, which is widely used in the automotive field to achieve energy saving and carbon dioxide emission reduction.

1.6 Research approaches

The research approaches corresponding to the research objectives are following.

1. In this project, the forming problem of CHSs is studied. An injection-winding technology is developed to prepare CHSs with smooth surface and no internal gap, to solve the forming problem of spring and greatly improve the performance of springs. The project comprehensively considered the process method for preparing CHSs, including connecting devices, injection containers, resin recovery devices and equipment that could provide positive and negative pressure. At the same time, the structure of the winding mold was also considered, which should not only be easy to demold, but also save the cost. The injection mold used in the experiment is the PVC pipe. If the air tightness is good, start resin injection. If the air tightness is poor, repair the air tightness first, and then carry out the experiment. The process adopted in this project has the advantages of simple preparation process, good resin wettability, smooth surface and no internal defects.
2. Combined with the force analysis and textile structure, the internal reinforcement of CHSs has been designed including unidirectional, multistrand, wrapped and braided structure. The performance of CHSs can be controlled by changing the relative parameters of reinforcement structure, such as fiber volume content of unidirectional reinforcement, the number of strand and degree of twisting of multistrand reinforcement, the wrapped degree of wrapped reinforcement and the braided angle and layer number of braided reinforcement. The optimal structure first selected through the primary comparison of spring stiffness. Then the performance will be accurately adjusted based on the parameters of optimal structure reinforcement.
3. The performance evaluation of CHSs has been carried out by combining experiments and simulation. First the braided structure CHSs has been selected to further research the impact of braided angle on performance of CHSs based on static performance. The optimal braided angle will be selected. Then the braided layers will be researched to further explore the optimization degrees of CHSs based on different braided layers based on dynamic impact performance. It is worth mentioning that a types of stiffness degradation predict method under impact have been proposed based on time domain information. Finally, the CHSs with optimized braided angle and braided layer have been selected and used to explore fatigue performance.
4. Based on the primary helical formula of the spring and combined with 3D modeling software, the macro, meso and micro models of CHSs are established

to reveal the internal mechanism of CHSs under different boundary conditions. The compression process of CHSs with single braided layer is simulated based on meso model firstly, the more applicable calculation methods of material engineering constants are first compared and determined to ensure the accuracy of the calculation results. After proving the accuracy of the model, the mechanical properties are analyzed step by step through the stress distribution, cross-section stress and angle stress curve. In addition, due to the meso model of CHSs with multiple braided layers cannot simulate the real structure of CHSs with multiple braided layers, a types of virtual fiber model have been introduced to further optimize the accuracy of the impact model.

5. The front and rear suspension CHSs will be installed on JEEP TJ 2004 after the vehicle has been suspended and the strain information will be collected through the strain sticking on CHSs during the vehicle fall. Meanwhile, the damage situation will be detected by recording video. If there is no damage and the strain information of CHSs has little change during driving, we can determine the CHSs can be successfully applicated on the vehicle. Otherwise, the weakness will be found to guide the optimization of CHSs.
6. The damage parts and model will be ensured after the installation experiment. The damage morphology shown that there is no damage happening in the front CHSs until the vehicle is totally on the ground. In addition, the damage morphology of rear CHSs is obvious that the damage of rear CHSs gradually occurs just on resin part with the descend of vehicle. There are two damage models that are crack and debonding of resin. We can find the optimization of resin is the key point to fulfilling the successful application. Therefore, the GCC135, R118 and TDE86 resin have been selected to compare the tensile and bend performance under different curing temperatures. After that, the new optimal CHSs has been manufactured and installed on the JEEP TJ2004 again. The result showed that there is no damage happening no matter what front and rear CHSs. Moreover, the strain of CHSs is like that of steel spring. The results mean that CHSs can successfully replace the steel spring.

1.7 Relationship between chapters

All chapters in the research have close correlation to make the research logical.

(1) The introduction chapter 1 describes the background, aims and research objectives and approaches of CHSs, which provided the guide direction for the whole research.

(2) Chapter 2 reviews lots of references about CHSs, indicating detailly the current research situation of CHSs. So that we can understand the research gap to avoid

repeat research and capture the important research direction. After that we can clearly get the key points of the research. It can be found that the performance of CHSs is not enough, and the evaluation method of performance is not comprehensive, which limits the application and development. To solve the problems, the performance and evaluation methods have been improved in following chapters. (3) Chapter 3 designs the CHSs with textile structure based on the force analysis for exploring the reinforcement structure that can significantly improve spring performance and invest injection-winding methods to manufacture the CHSs. The initial stiffness compression of four types CHSs (UCHS, MCHS, WCHS and BCHS) shows that the optimal CHSs is BCHS. Therefore, the BCHS have selected for further static performance, dynamic performance and application research. (4) Chapter 4 first explores static performance by using SBCHS with 0°, 15°, and 30° braided angles. The result showed that the static performance of UCHS, SBCHS15° and SBCHS30° increased sequentially, indicating 30° braided angle is better. (5) After that, SBCHS, DBCHS and TBCHS have been manufactured based on 30° braided angle to further explore the impact of braided layers on dynamic impact performance in chapter 5. The results show that the impact performance of SBCHS, DBCHS and TBCHS improve in turn, which means that TBCHS have better performance. (6) In addition, there exist stiffness degradation during impact of SBCHS, DBCHS and TBCHS, a real time predicting method of stiffness degradation has been proposed based on time domain analysis in chapter 6. TBCHS have less stiff degradation than the other two under the same impact conditions, highlighting the advantages of TBCHS. (7) It is well known that fatigue performance is important in terms of parts. Hence, the dynamic fatigue performance of TBCHS has been studied in chapter 7. When the stress level drops to 70%, the stiffness decreases only 1.3% after 30000 cycles, which shows that the TBCHSs can be used for long time under the stress level of less than 70%. (8) Based on the above chapters, the feasibility of potential application of TBCHS has been proved according to experimental and numerical analysis of static and dynamic performance. However, the feasibility of the application of TBCHS is unknown. So, the application evaluation of TBCHS in field have been detected and analyzed by combining morphology and strain information in chapter 8. Finally, the optimal TBCHS can be successfully installed on the vehicle after resin optimization. (9) Chapter 9 summary structure design, manufacturing, static and dynamic performance evaluation and application in field, which prove the feasibility of application of CHSs to replace traditional metal spring. (10) The future work and prospections of CHSs have been listed in chapter 10, which can guide future research direction. The internal links among those chapters are shown in Fig. 1.2. This research laid the foundation for the large-scale applications and development of CHSs.

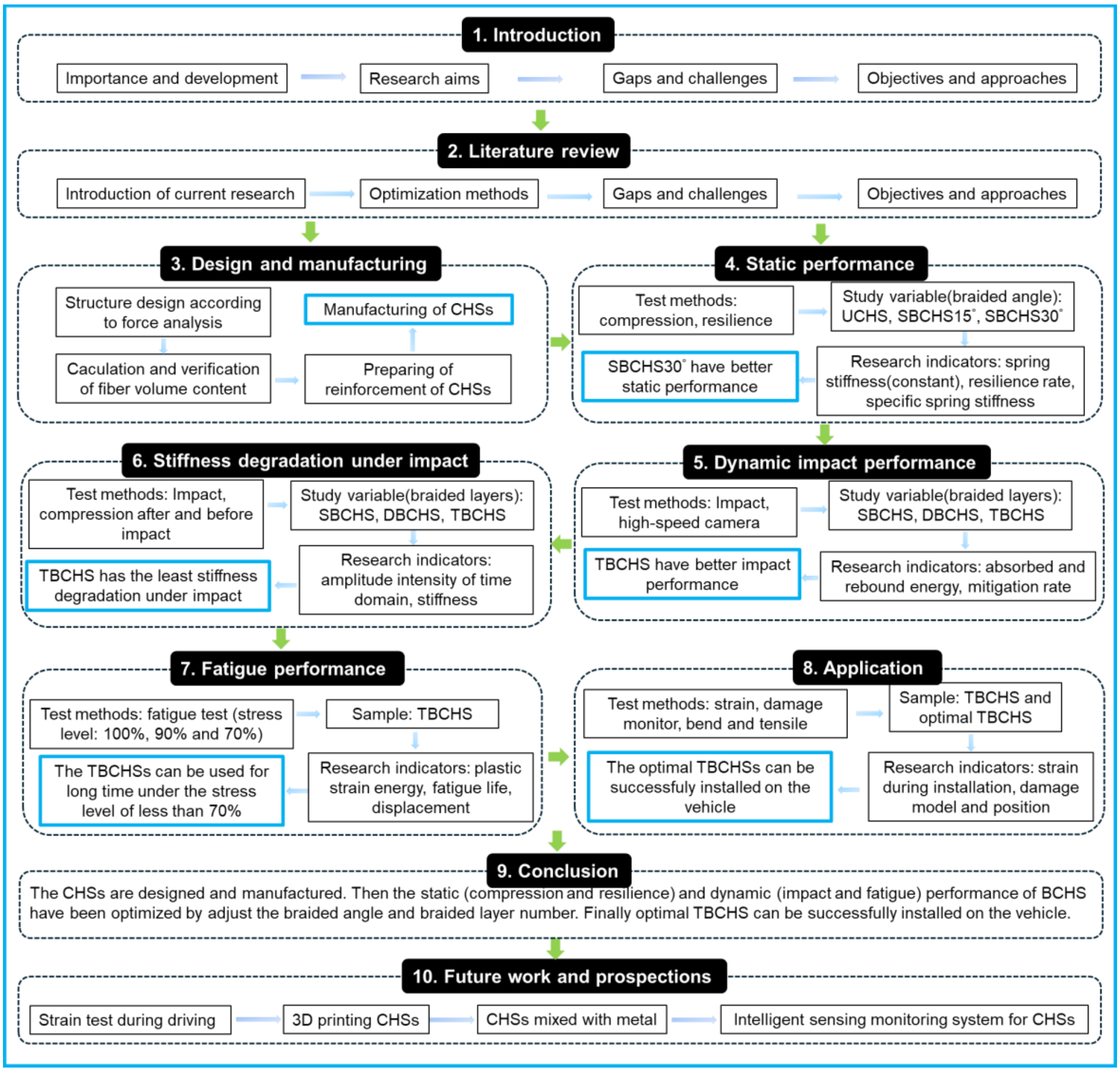

Fig. 1.2 Relationship diagram among chapters

2. LITERATURE REVIEW

This chapter comes from the publication of “Ling Chen, Wenjin Xing, Liwei Wu, Joel Chong, Tongda Lei, Qian Jiang, Youhong Tang. Understanding multiple parameters affecting static and dynamic performances of composite helical springs. Journal of Materials Research and Technology, 2022;20:532–50” with format modifications.

Composite helical springs (CHSs) are mainly used in transportation and aerospace fields, such as automobile suspension, railway bogie and aircraft engine systems. It has become a trend to replace the traditional metal helical springs with CHSs with the advantage of energy conservation during service and emission reduction during manufacturing. The advantages of CHSs such as low weight, high specific strength, high specific modulus, corrosion resistance, fatigue resistance and high strain energy storage capacity mean that it has great development potential. The static and dynamic performances of CHSs together determine whether they can be used on a large scale in the engineering field. The static performance of the CHS determines their service-load range and the dynamic performance determines the service life and safety performance of CHSs under dynamic load environmental conditions. Therefore, it is an important task to optimize the static and dynamic performance of CHSs. To provide a reliable reference for the development of CHSs, this review analyzes the important factors affecting the static and dynamic performance optimization of CHSs from the perspectives of theory, finite element method (FEM), and experiment.

2.1 Introduction of literature review

As a kind of engineering machinery parts with the capability of storing and releasing elastic energy (T.-W. Liu et al., 2021), springs are to store energy when deflected and to return equivalent amount of energy when released (Ekanthappa et al., 2013). This process enables the mutual transformation of internal energy and kinetic energy, which is quite useful in damping and buffering (Ashok et al., 2021). In recent years, the industrial sectors such as transportation and aerospace have been evolving towards efficient energy conservation and emission reduction (Jadhav et al., 2015; Kumar & Vijayarangan, 2007). The metal helical springs of high density and poor corrosion resistance are hard to meet the challenging demands from industries. Therefore, light composite materials are becoming more popular, which are gradually replacing metals in the development of springs. They are able to not only save fuels and expand overall cruising ranges (Ghassemieh, 2011), but also reduce greatly carbon dioxide emissions. In addition to excellent weight reduction effects (Shinde et al., 2018), composite materials have the advantages of high specific modulus, specific strength (Kara, 2017; Londhe, 2013), and fatigue resistance (Shokrieh & Rezaei, 2003; C. Stephen et al., 2019). These attributes make composite material a promising material for manufacturing the springs (Charles & Srikanth, 2014; B.-L. Choi & B.-H. Choi, 2015; Kumar & Vijayarangan, 2007). In terms of practical applications, composite helical springs (CHSs) are likely applied in the suspension system of tricycles (Pawar & Desale, 2018), mountain bikes (J. K. Frank, 2020), motorcycles (Bhatia & Bergaley, 2014), automobiles and trains, and the engine system of aircrafts (Na & Chunyang, 2019; Subramanian & Senthilvelan, 2010). They can also be used as a deployable aerospace antenna to transmit signals (Cheng et al., 2015; Sproewitz et al., 2011). Moreover, they support long-term operation of devices or equipment in harsh marine environments, due to non-conductivity and corrosion resistance (Sarh & Kad, 2010).

So far, a great deal of research has been conducted (Xiong et al., 2017) to develop CHSs for fulfilling specific requirements (Jancirani & Assarudeen, 2015). It is necessary to summarize the present attempts and findings associated with CHSs. To this end, this review will assess existing literature, placing an emphasize on analysis of influencing factors both the static and dynamic performance of CHSs. This study summarizes the influencing factors of optimizing the static performance of CHSs from the theoretical perspective of single-objective optimization and double-objective optimization. This discusses the internal mechanism of CHSs optimization through finite element method, and summarizes the optimization laws of preparation method, material, reinforcement structure and spring geometry on the static performance based on experiments. What's more, the influencing factors and optimization laws of CHSs dynamic performance, fatigue and resonance, are summarized.

2.2 The optimization methods of CHSs

2.2.1 Single-objective optimization of CHSs

To ensure the prediction accuracy of static performance in the optimization of CHSs, single-objective optimization methods choose the spring stiffness as the performance index (objective function). Spring stiffness is estimated generally based on a formula initially proposed for metal springs according to spring type and loading characteristics. Common stiffness formulas used for single-objective optimization are summarized in Table 2.1.

Table 2.1 : Various stiffness formulae for single-objective optimization, depending on the spring type and loading characteristics

Reference	Spring type	Force characteristics	Stiffness
Choi *et al.* (B.-L. Choi & B.-H. Choi, 2015)	Metal	T	$k=\frac{P}{\delta}=\frac{Gd^4}{8nD^3}$

Lekhnitskii *et al.* (Wooster, 1964)	CHSs with solid ply structure	T	$\hat{k}=\frac{P}{\delta}=\frac{\hat{G}d^4}{8nD^3}$
Yang *et al.* (Yongbao et al., 2013)		M, T, F, V	$k=\frac{1}{2\pi J_{22}(\frac{D}{2})^3N}=\frac{4}{\pi J_{22}ND^3}$
Jin *et al.* (Jin et al., 2013)	Metal	T	$k=\frac{P}{\delta}=\frac{G(\mathrm{d}_0^4\text{-}\mathrm{d}_\mathrm{i}^4)}{8nD^3}$
Xiong *et al.* (Xiong et al., 2017)	CHSs with hollow ply structure	T	$\kappa=\frac{P}{\lambda}=\frac{\left(d_o^4-d_i^4\right)\left(E_fV_f+E_mV_m+E_m\frac{1+V_f}{V_m}\right)}{32n\left(1+\mu_{12}\right)D^3}$
Liu *et al.* (T.-W. Liu et al., 2021)		M, T, F, V	$K_i=\frac{\cos\alpha_i\left(d_1^4-d_0^4\right)}{8N_iD_i^3}\left[\frac{\cos^2\alpha_i}{G_{xy}}+\frac{2\sin^2\alpha_i}{E_x}+\frac{\left(d_1^2+d_0^2\right)\sin^2\alpha_i}{2E_xD_i^2}+\frac{\left(d_1^2+d_0^2\right)\cos^2\alpha_i}{G_{xy}D_i^2}\right]^{-1}$

Note: The meaning of the letters in Table 2.1 can be found in the nomenclature or the corresponding literature.

To illustrate the optimization principle of single-objective optimization methods based on stiffness, the case will be described in detail that deals with CHSs with a hollow ply structure and simultaneously subjected to four forces: bending moment M, torque T, tension force F and shear force V (T.-W. Liu et al., 2021). In fact, geometric parameters of CHSs change continuously in the compression process, as shown in Fig. 2.1. It is assumed that the spring can be compressed to the maximum compressive limit (i.e., spring reaches its solid length). This process can be divided into n steps; in each step, a small compressive load increment ΔP is applied to the helical spring, leading to its continuous geometrical change. The effect induced by geometrical change needs to be considered. So, the geometric parameters are calculated in each step until the maximum compressive displacement of the helical spring is reached. During the whole compression process, the Tsai - Hill criterion widely used for failure prediction of composite materials can be employed to determine whether failure occurs in the spring. If failure occurs, the current ith step is recorded and labeled by mth. The height variation (i.e., compressive displacement increment) of the helical spring in the ith step can be derived as (T.-W. Liu et al., 2021)

$$\Delta h_i = \frac{8N_i \Delta P D_i^3}{\cos\alpha_i \left(d_1^4 - d_0^4\right)} \left[\frac{\cos^2\alpha_i}{G_{xy}} + \frac{2\sin^2\alpha_i}{E_x} + \frac{\left(d_1^2 + d_0^2\right)\sin^2\alpha_i}{2E_x D_i^2} + \frac{\left(d_1^2 + d_0^2\right)\cos^2\alpha_i}{G_{xy} D_i^2} \right] \tag{2.1}$$

Therefore, the helical spring stiffness in the ith step can be expressed as

$$K_i = \frac{\cos\alpha_i \left(d_1^4 - d_0^4\right)}{8N_i D_i^3} \left[\frac{\cos^2\alpha_i}{G_{xy}} + \frac{2\sin^2\alpha_i}{E_x} + \frac{\left(d_1^2 + d_0^2\right)\sin^2\alpha_i}{2E_x D_i^2} + \frac{\left(d_1^2 + d_0^2\right)\cos^2\alpha_i}{G_{xy} D_i^2} \right]^{-1} \tag{2.2}$$

where the laminate material properties E_x and G_{xy} are the elastic modulus in the tangential direction of helix center-line and in-plane shear modulus in the x–y direction respectively; i refers to the ith step (i=1, 2, 3,…m or i=1, 2, 3…n). N_i, D_i, and α_i denote the number of active turns, mean coil diameter and helical angle of the helical spring respectively; d_1 and d_0 are the outer and inner diameters of the spring wire respectively. According to Eq. (1), total height variation (i.e., accumulated compressive displacement) and total compressive load in the kth step can be obtained by summing up Δh_i and ΔP, as follows:

$$\delta_k = \sum_{i=1}^{k} \Delta h_i \tag{2.3}$$

$$P_k = k\Delta P \tag{2.4}$$

After fitting the data points [δ_k, P_k] (k=1, 2, 3,…m or k=1, 2, 3,…n), the compressive load - displacement curve of the helical spring can be obtained up to the maximum compressive displacement δ_{max} or compressive failure load P_m. Using the linear least squares method to linearly fit these data points, the compressive stiffness of the helical spring can be derived as

$$K = \begin{cases} \dfrac{\sum_{k=1}^{m}\left(\delta_k - \bar{\delta}\right)\left(P_k - \bar{P}\right)}{\sum_{k=1}^{m}\left(\delta_k - \bar{\delta}\right)^2} & (\text{Failure}) \\[2ex] \dfrac{\sum_{k=1}^{\mathrm{n}}\left(\delta_k - \bar{\delta}\right)\left(P_k - \bar{P}\right)}{\sum_{k=1}^{\mathrm{n}}\left(\delta_k - \bar{\delta}\right)^2} & (\text{Reaching } \delta_{\max}) \end{cases} \tag{2.5}$$

where, δ and P are the average compressive displacement and average compressive load in the direction of helix axis, respectively.

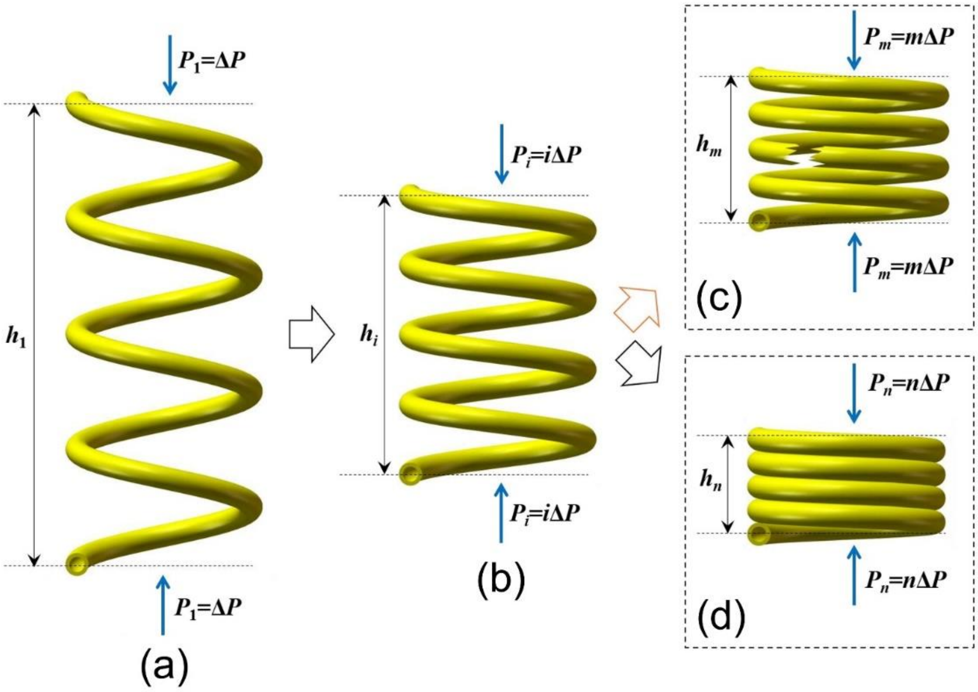

Fig. 2.1 Compressive deformation process of CHSs (a) Original state; (b) Compressive state; (c) Failure state; (d) Fully compressive state (*T.-W. Liu et al., 2021*).

For CHSs that are made from composite laminates, the stiffness formula needs to be theoretically established according to the force characteristics and spring structure as previously described. The static strength is mostly subjected to an optimization constraint, so the Tsai - Hill criterion is generally employed that stress component interactions (Gobbi & Mastinu, 2001; Jin et al., 2013; Jones, 2018). This optimization constraint prevents the spring material from failure by identifying maximum allowable stress states. The critical static strength of CHSs during the compression process is then checked against the Tsai–Hill criterion as following below.

$$\frac{\sigma_1^2}{X^2}-\frac{\sigma_1\sigma_2}{X^2}+\frac{\sigma_2^2}{Y^2}+\frac{\tau_{12}^2}{S^2}\le 1 \tag{2.6}$$

where σ_1, σ_2 and τ_{12} are Cauchy stress components; X, Y and S are the longitudinal, transverse, and in - plane shear tensile (or compressive) strengths of the selected composite material. These strength parameters are usually determined through experimental tests.

Maximizing the lightweight feature of springs is a general design aim for CHSs. The mass of CHSs may become the sole optimization index other than the spring stiffness discussed above in the single-objective optimization. Yokota *et al.* (Yokota et al., 1997) proposed an optimal mass design problem of CHSs for a constrained allowable shearing stress, number of active coils and coil's mean diameter as a nonlinear integer programming (NIP) problem and solved it directly by keeping the nonlinear constraint by using an improved genetic algorithm (GA). Zhan *et al.* (Bowen et al., 2018) determined 16 groups of sample points through the Latin method experimental design and established the response surface model. Based on the response surface model, the structure of CHSs with the best lightweight effect is obtained by using genetic algorithm, which can further reduce the spring mass, to achieve the lightweight goal of CHSs.

In a single-objective optimization of CHSs involving a single optimization index, different parameters (e.g., stiffness, mass, and stability) can be considered the sole index. After determining the design parameters (variables) to tune related to the geometry or material properties, the single-objective optimization algorithm is executed to find optimum solutions under various constraints (e.g., Tsai–Hill criterion, maximum outer diameter, and maximum deflection). In this way, the optimization procedure finds suitable design parameters and helps to achieve the optimal static performance of CHSs. Factors such as the force characteristics and the structure of CHSs may affect the mathematical expression for the optimization index. It is important to note that these factors must be taken into consideration to meet the requirements in practical applications. In addition, it is necessary to refer to specific technical specifications and manufacturing techniques associated with CHSs in the optimization process.

2.2.2 Dual-objective optimization of CHSs

Dual-objective optimization is a kind of method that can be used to obtain simultaneously minimum mass and maximum stiffness of CHSs. At present, there are some methods and technologies that can meet the requirements of dual-objective optimization of CHSs. Azzam *et al.* (Azzam, 2010) obtained the optimum value of the parameters (the number of active coils, coil diameter, wire diameters, spring index, and helix angle) for springs made from glass-epoxy, Kevlar-epoxy, and carbon epoxy composite materials by the Kuhn-Tucker technique. To expand the selectivity of optimized parameters about CHSs. Gobbi *et al.* (Gobbi & Mastinu, 2001) obtained the optimal value range of several design variables (the mean coil diameter spring, the inner diameter wire, the laminate thickness, the pitch, the number of active coils, the initial braiding angle, the number of plies) by an evolutionary algorithm. The optimization of CHSs by the evolutionary algorithm requires thousands of iterative cycles to screen the optimal value according to the set theoretical constraints, which will be very time consuming. To improve work efficiency and optimization accuracy, some scholars are committed to improving the dual-objective optimization method. Zhan *et al.* (Bowen et al., 2018) proposed an evolutionary algorithm based on a response surface model that can sharply reduce the number of iterations and greatly reduce the computational time compared with the ordinary evolutionary algorithm. Ratle *et al.* (Ratle et al., 2004) used a dual kriging interpolation to modify evolutionary algorithms and proved its rationality to improve the accuracy of a dual-objective optimization of CHSs. To select the best evolutionary algorithm, Bai *et al.* (J.-B. Bai et al., 2021) compared seven state - of - the - art evolutionary algorithms (NSGA - II, SPEA - II, MOEA/D, MTS, MLSGA, MLSGA - NSGAII, MLSGA - MOEA/D) to optimize two conflicting objectives, maximizing the compressive stiffness while minimizing the weight. The runs generating the best Pareto front from 30 simulations are illustrated in Fig. 2.2 for the highest and lowest population sizes for each of the seven algorithms. It is shown in Fig. 2.2 that MOEA/D finds the continuous Pareto front with the best spread of results, covering a similar range, which means MOEA/D is the best solver on searching the designs of the maximum compressive stiffness and the minimum weight.

The factors that affect the optimization results in the dual-objective optimization are the same as those in the single-objective optimization, namely the performance parameters of the composite material made of CHSs, the structural parameters of the reinforcement structure of CHSs and the dimension parameters of CHSs. To obtain accurate optimization results and improve optimization efficiency, optimization methods need to be compared or modified in a dual-objective optimization, the comparison of evolutionary algorithms shows that MOEA/D is most suitable for the optimization of CHSs, and other methods can be modified according to the actual situation to reduce the error. In fact, dynamic performance such as fatigue, resonance, damping and creep of CHSs should also be paid enough attention in the application process. Future theoretical design and optimization should focus on extending this work to three or more objectives which are important in comprehensive experimental assessments of CHSs.

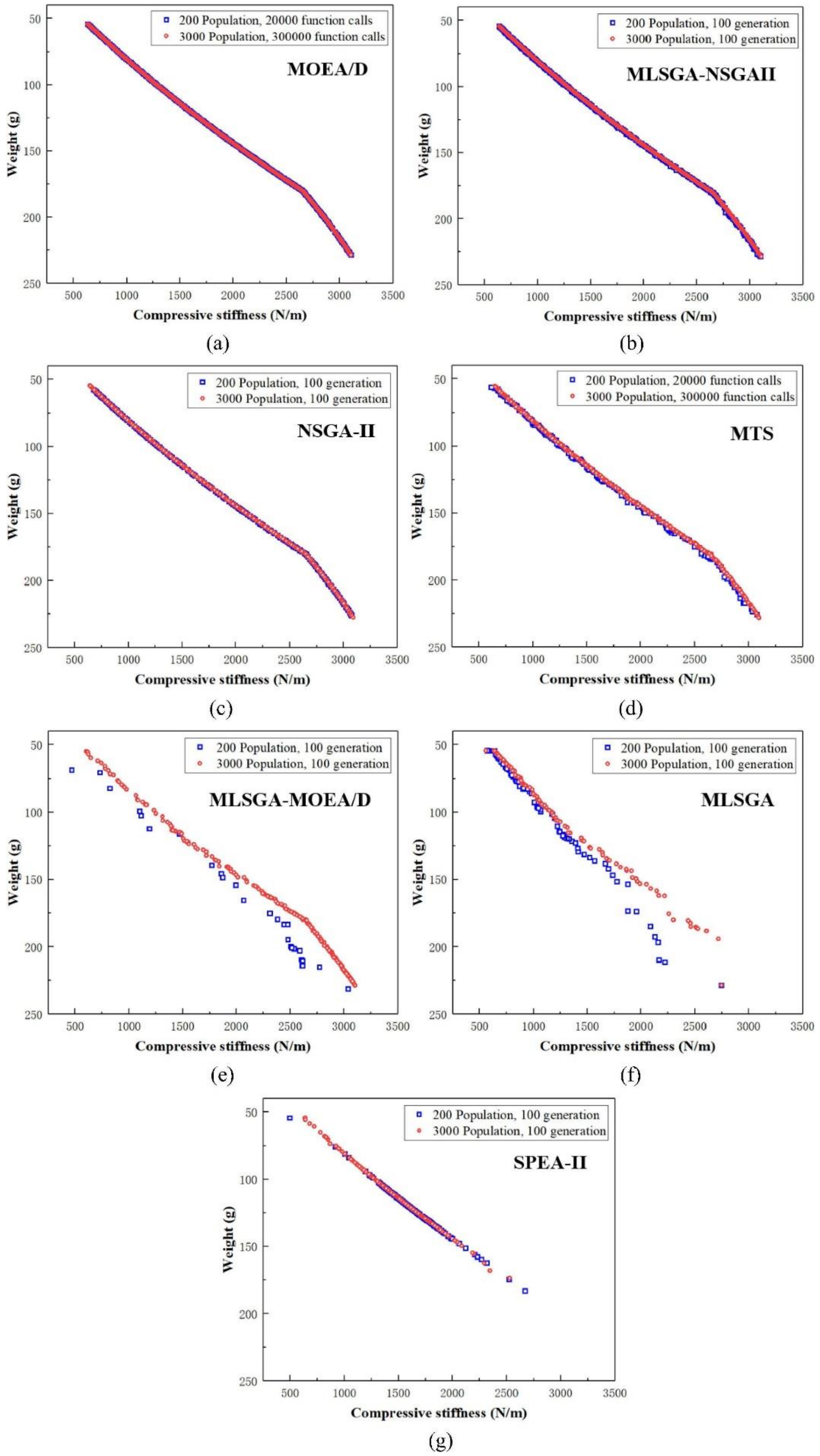

Fig. 2.2 Comparison of Pareto fronts for different populations sizes. (a) MOEA/D; (b) MLSGA-NSGAII; (c) NSGA-II; (d) MTS; (e) MLSGA-MOEA/D; (f) MLSGA and (g) SPEA-II (*J.-B. Bai et al., 2021*).

2.2.3 Finite element design and optimization of static performance of CHSs

Numerical optimization based on the finite element method (FEM) is often used to assist in the design complex types of CHSs that are difficult to optimize by mathematical optimization discussed above. Since CHSs with fiber reinforcement has the characteristics of anisotropy, anisotropic material constitutive models of CHSs are essential. At present, according to the structure of CHSs, the optimized setting method of material anisotropy of CHSs can be integrated into 3D model (Wu, Chen, et al., 2020), material attribute (Hamed et al., 2020; Jiang et al., 2021) or mesh module (Jilun, 2017) individually. Displacement (B.-L. Choi & B.-H. Choi, 2015) or pressure (Sequeira et al., 2016) controlled loading can be prescribed boundary conditions in the simulation. Yang *et al.* (Wooster, 1964) and Azzam *et al.* (Bowen et al., 2018; Yongbao et al., 2013) simulated the stiffness of helical spring and found that the prediction result deviated within 6% from that of the mathematical formulation and experimental measurement, which demonstrated the feasibility and accuracy of the simulation. Apart from the stiffness prediction, the FEM based simulation can provide information of displacement, strain and stress fields which cannot be accessed directly through experimental tests. Such details are always helpful during the optimization process of CHSs. In the recent work by Wu *et al.* (Wu, Chen, et al., 2020), five finite element models of CHSs with different configurations were established by controlling the reinforcement twist and fiber volume content (V_f): three twistless CHSs with V_f of 45%, 50%, and 55% (CMHS45%, CMHS50%, and CMHS55%), and two twisted CHSs with different twist coefficients of 4 and 6r/10 cm but the same V_f of 55% (CMHS4 and CMHS6). By applying FEA, the effects of reinforcement structure and V_f on the stress profile of CHSs were analyzed and discussed. The stress distribution corresponding to each CHS at different compressions is displayed in Fig. 4. Clearly, the stress of the CHSs increases with the increase of fiber content and twist, and the stress of the CHSs in each loop is the same, as shown in Fig. 2.3(a). The stress concentration region in the structure of the twistless CHSs is in the internal radial zone, and center of spring wire has the lowest stress levels, while the stress distribution of the twisted CHSs is uniform, as shown in Fig. 2.3(b). This optimization analysis method based on FEA deeply reveals the force law of CHSs, which lays a foundation for optimization of CHSs (Jiang et al., 2021; Kaoua et al., 2011).

Beyond static stress analysis, the FEM based simulation can be used to inform possible mechanical failure of CHSs during compression. For example, Zhao *et al.* (Wu, Zhao, et al., 2020) established a virtual fiber model, incorporated material failure criteria, and analyzed the slip mechanism between fibers together with the failure processes in the fibers and resin of CHSs at its mesoscale.

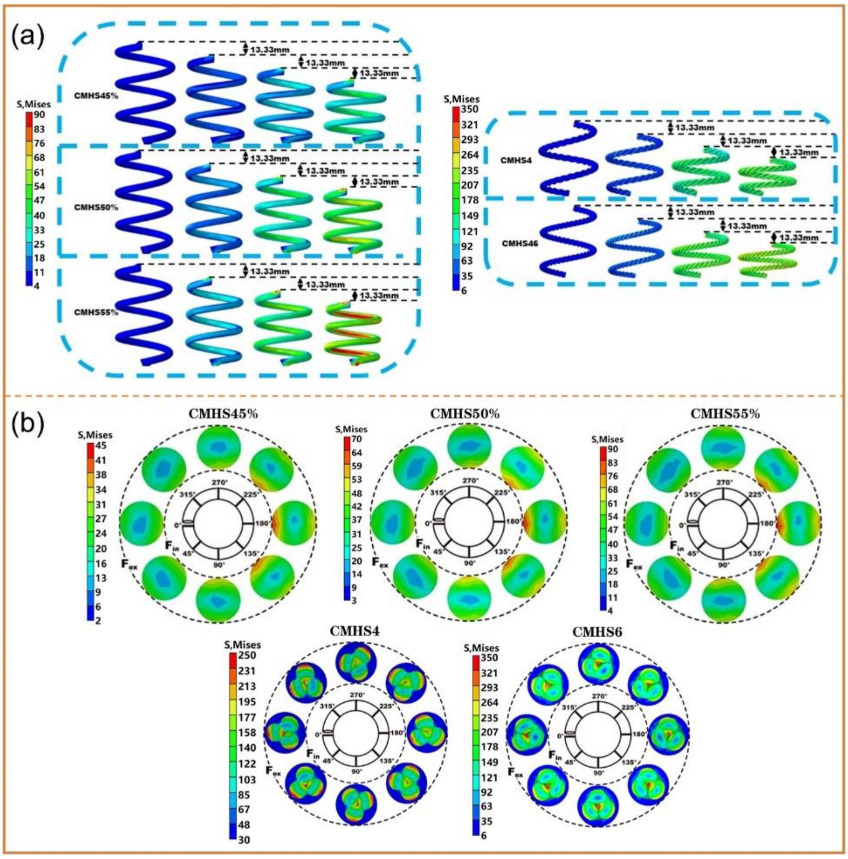

Fig. 2.3 (a) Von Mises stresses of CMHS45%, CMHS50%, CMHS55%, CMHS4 and CMHS6; (b) Von Mises stress distribution of cross section of CMHS45%, CMHS50%, CMHS55%, CMHS4 and CMHS6 (*Wu, Chen, et al., 2020*).

2.3 Experimental design and optimization of static performance of CHSs

2.3.1 Progress of manufacturing method of CHSs

Like many other man-made materials, the manufacturing method of CHSs has a prominent impact on their overall performance and thus should be taken into account in the beginning steps of design and optimization. Despite performance advantages over conventional metal springs, the special helical topology of CHSs demands more complicated manufacturing processes. Just like the performance optimization of CHSs, their manufacturing method is also a subject of extensive research. Inadequate manufacturing methods compromise the appearance and performance of final CHS products. A series of manufacturing methods are compared in detail, with a summary in Fig. 2.4 and Table 2.2. The further explanation of some technical terms referenced in Table 2.2 is given below:

1. Reinforcement structure limitation: Shrink tapes with low adhesion energy cannot be used to hold the helical shape of reinforcement structure which has high elasticity, such as rubber rod.
2. Difficult demolding: Due to the mold with helical groove and unsplit structure, it is difficult to change the shape of cured CHSs wound on mandrel, the demolding process is time and labor consuming.
3. Spring appearance defects: Insufficient resin infiltration causes that the prepared CHSs have many internal pores and irregular surface, seriously affecting the mechanical performance of CHSs.
4. Spring geometric profile limitation: CHSs can only be demolded along the helical groove of the mold by rotating, indicating that the prepared CHSs should have a uniform geometry avoiding flush end, variable pitch, and variable diameter.
5. High-cost: Cumbersome procedures easily incur excessive costs. Significant no cost will be consumed for many design trails.
6. Resin short shot: The low pressure of equipment during resin injection tends to lead to a short resin flow path.

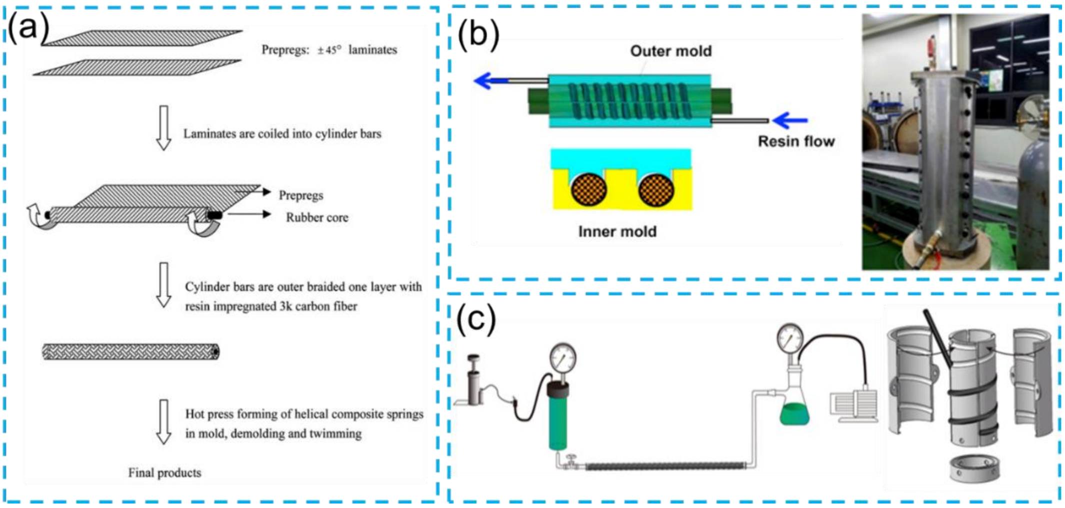

Fig. 2.4 Schematic diagram of the forming process of CHSs (a) hot press molding (*C.-H. Chiu et al., 2007*; *Sardou et al., 2005*); (b) RTM (*B.-L. Choi & B.-H. Choi, 2015*); (c) integrated forming (*Wu, Chen, et al., 2020*).

Table 2.2**:** Advantages and disadvantages of five manufacturing methods of CHSs including filament winding (*Ekanthappa et al., 2017*; *Hamed et al., 2020*; *Shende et al., 2016*; *Suresh et al., 2014*), hot press molding (*C.-H. Chiu et al., 2007*; *Nagao et al., 1998*), RTM (*B.-L. Choi & B.-H. Choi, 2015*), integrated forming (*Arularasan & Sabapathy, 2014*; *Luger et al., 2018*) and lost mold method (*Chen et al., 2014*; *Sardou et al., 2005*)

Method	Advantage	Disadvantages

Filament winding	/	Reinforcement structure limitation difficult demolding Spring appearance defects Spring geometric profile limitation High cost
Hot press forming	Reinforcement structure without limitation Low-cost	Difficult demolding Spring appearance defects Spring geometric profile limitation
Resin transfer molding	Reinforcement structure without limitation High spring quality	Difficult demolding Spring geometric profile limitation High cost Resin short shot
Integrated forming	Reinforcement structure without limitation Easy demolding High spring quality Low-cost	Spring geometric profile limitation Resin short shot
Lost mold method	Reinforcement structure without limitation Easy demolding High spring quality Spring geometric profile without limitation	High cost

The manufacturing methods of CHSs are constantly in progress to remove the inherent limitations in conventional manufacturing methods. The lost mold method basically addresses the problems encountered in the fabrication of CHSs. Fig. 6 shows the whole manufacturing process of CHSs by the lost mold method. A fabricated fiber reinforcement structure is impregnated with resin after eliminating bubble in a flatbed mold at 60 ℃, as shown in Fig. 2.5(a). The uncured prepreg is then taken out from the mold and placed in a plaster sacrificial mold (Fig. 2.5(b)-5(d)). The prepreg is cured at 120 ℃ for 1 h and sequentially at 180 ℃ for 2 h. After complete cure, a CHS is successfully fabricated by breaking the plaster (the sacrificial core), as shown in Fig. 2.5(e) and 2.5(f). The bubble elimination process of resin prevents the appearance defects of CHSs. Although the lost mold process is cumbersome and costly, this method enables fabricating arbitrary shapes of CHSs and repeatedly use the plaster sacrificial mold. It solves the problems of spring appearance defects, reinforcement structure limitation, geometric size limitation and demolding difficulties.

Development of the manufacturing process constitutes the basis for the successful commercialization of CHSs. However, many challenges are present in practice, which justifies the significance of pursuing more effective and sustainable manufacturing methods suitable for mass production.

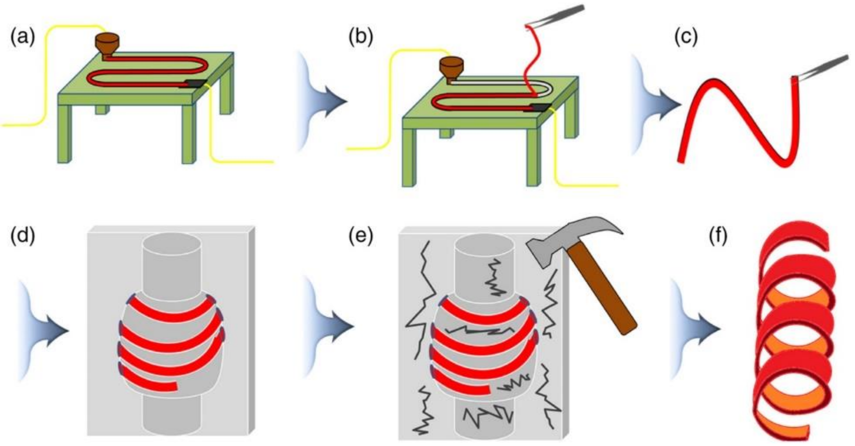

Fig. 2.5 Manufacture of CHSs by the lost mold method. (a) The resin impregnated fiber in a flatbed mold to form prepreg; (b), (c) the uncured prepreg was taken out from the mold; (d) the uncured prepreg was placed and cured in the plaster sacrificial mold; (e) the plaster (sacrificial core) was broken; and (f) CHSs were obtained(*Kim et al., 2021*).

2.3.2 Design and optimization of composite material of CHSs

On the one hand, the density of composite materials determines the mass of CHSs. On the other hand, mechanical properties of composite materials such as Young's modulus, shear modulus, Poisson's ratio, strength, and toughness have a crucial impact on the overall structural performance of CHSs. For this reason, composite materials are required to be designed to achieve ideal properties combination for use in CHSs.

Researchers compared the static performance of the CHSs that contain various types of reinforcement material, namely carbon, glass, Kevlar, Calotropis gigantea fiber, as shown in Table 2.3. The static performance of CHSs depends upon the material in terms of mechanical properties. Compared with steel springs, CHSs show apparent weight-reducing effects. The weight-reducing effect decreases in the carbon, Kevlar and glass fiber CHSs in sequence. Besides, the stiffness of CHSs sequentially decreases for steel spring, carbon, Kevlar, glass and Calotropis gigantea fiber CHSs. To illustrate the influence of spring material on the static performance of springs, certain studies are briefly described as follows. The weight and displacement were compared among the springs by Bakhshesh *et al.* (Bakhshesh & Bakhshesh, 2012) in Table 3. The weights of the carbon, Kevlar, and glass fiber CHSs were 83.55%, 82.52%, 74.25% less than that of steel spring, while the displacement among CHSs in a descending order is the spring made of glass, Kevlar, carbon and steel at the same fiber angle which can reflect the stiffness of the CHSs in an increasing order of glass, Kevlar, carbon and steel. Although the carbon fiber CHS has a lower stiffness but higher cost than that of the steel spring with the same size, the former stiffness can be optimized by designing the proper geometric parameters and reinforcement structure, and the high cost can be compensated by saving fuel due to weight reduction (J Ekanthappa et al., 2016; Manjunatha & Budan, 2012; Shende et al., 2016). The weight-reducing effect of Calotropis gigantea fiber CHS was around 75% by the Renugadevi *et al.* (Renugadevi et al., 2019) investigation. However, the Calotropis gigantea fiber reinforced spring showed a relatively low stiffness value of 1 N/mm when compared to that of a glass fiber CHS. In fact, the most basic work of optimization of CHSs is to ensure that static mechanical properties and weight meet the specific requirements of CHS products. Calotropis Gigantea has the unique advantage of environmental friendliness over other petroleum-derived materials (Boonniteewanich et al., 2014), However, its prominent drawbacks including low modulus and high moisture absorption, impeding its engineering usages as the material of CHSs. Carbon fiber stands out for CHSs from the comparison analysis. Beyond systems with a single type of fiber, the hybrid fiber CHSs were introduced for further optimization by Manjunatha *et al.* (Manjunatha & Budan, 2012), as shown in Table 3. The spring stiffness of the carbon fiber CHS was found to be 24% higher than that of a glass fiber CHS and 10% higher than that of a hybrid glass/carbon fiber CHS. The weight of the carbon fiber spring was 15% and 11% less than that of the glass and hybrid glass/carbon fiber CHS respectively. Interestingly, the static performance of CHSs with carbon fibers exceeds that of glass fiber CHSs and the stiffness reaches the highest when the carbon fiber volume ratio reaches 100%. This is because carbon fibers have a higher elastic modulus but lower density when compared to that of glass fibers (Chiu et al., 2009).

Table 2.3 ：The performances of CHSs made of different materials are compared. (Carbon, Glass, Kevlar, Calotropis gigantea and Steel are referred to as c, g, k, cg and s respectively)

Reference	Materials	Stiffness	Weight-reducing effect
Bhatia (Bhatia & Bergaley, 2014; C. Stephen et al., 2019) and Stephen *et al.* (Bhatia & Bergaley, 2014; C. Stephen et al., 2019)	c, g, s	s＞c＞g	c＞g＞s
Zebdi *et al.* (Zebdi et al., 2009)	c, g, k, s	c＝k＝g＝s	c＞k＞g＞s
Bakhshesh *et al.* (Bakhshesh & Bakhshesh, 2012)	c, g, k, s	s＞c＞k＞g	c＞k＞g＞s
Renugadevi *et al.* (Renugadevi et al., 2019)	cg, g	g＞cg	cg＞g
Manjunatha *et al.* (Manjunatha & Budan, 2012)	c, g, c/ g	c＞c/g＞g	c＞c/g＞g

Spring strength is the ability of the spring to resist excessive deformation and fracture under the action of external force. Spring fails and no longer works if the external load exceeds its critical strength. Although the corrosion resistance of CHSs prevents the formation of corrosion pits that readily trigger distributed cracks (Krishnamoorthy & Karthik, 2015; Pastorcic et al., 2019), there are other possible failure mechanisms during static compression. Kim *et al.* (Kim et al., 2021) explored the potential failure mechanism in a CHS using a straight round bar under torsion, having the same composite structure as the composite spring. In Fig. 2.6 (a), fracture paths identified in SEM images appeared along the interfaces between the fibers and polymer matrix, known as the interfacial failure mechanism (Gao et al., 1988). The interfacial failure was caused by weak interfacial performance (Chen et al., 1992; Chen et al., 2006). Sun *et al.* (Yanbiao, 2020) also studied the failure mechanism of CHSs using SEM observations to view internal crack profiles. The resin enriched regions are relatively more susceptible to cracking. Chiu *et al.* (C.-H. Chiu et al., 2007) divided the failure process of CHSs into four stages revealed by a typical load–deflection curve. The crack occurs with a crisp sound and grows very fast owing to stress concentration at the opening end, belonging to the pure resin area, as depicted in Fig. 2.6(b). Before reaching the failure load, due to the interactive jam occurring in prepregs, the spring begins to crack at the matrix between fiber bundles from the defect of resin in the inner rim of the spring coil, as shown in Fig. 2.6 (c). This is because the maximum shear stress occurs in the inner side of spring coils when a helical spring is under compression and it is further proved by Frank *et al.* (J. K. Frank, 2020) and Krishnamoorthy *et al.* (Krishnamoorthy & Karthik, 2015) based on experiment. As the crack in the matrix between fiber bundles in the inner rim of the spring coils develops to a certain extent, the fibers will delaminate from the inner layer along the acting direction of shear stress, as shown in Fig. 2.6(d). When one section of the spring coils is broken, the failure of this portion can be restrained via contacting the portion with its neighboring section of the spring coils, as shown in Fig. 2.6(e), and the load is then transferred to and carried by other coils not destroyed.

The possible failure modes of CHSs are primarily resin cracking, interfacial debonding, and fiber breakage. The resin cracking and interfacial debonding mostly occur before fiber breakage, which prevented the contribution of the fibers in CHSs. In addition to the selection of a proper fiber reinforcement material for CHSs, the mechanical performance of resin is crucial for optimizing the overall static performance of CHSs (Chiu et al., 2009; Tao, 2016). Specifically, the maximum deflection displacement before failure decreases with increasing resin stiffness (Chiu et al., 2009). However, there is currently a lack of research on the effect of resin on static performance of CHSs. Therefore, the balance between resin performance and static performance of CHSs needs further exploration and optimization.

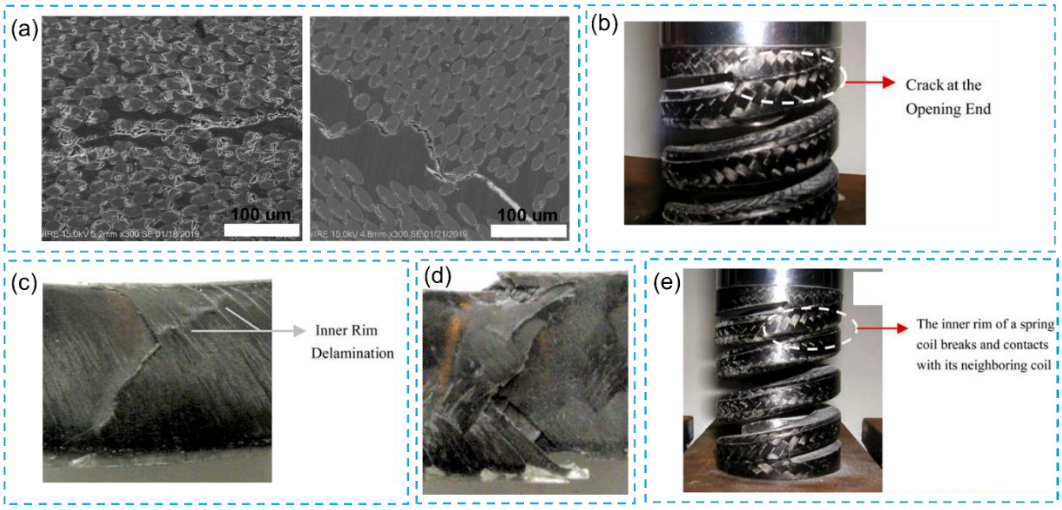

Fig. 2.6 (a) SEM diagram of spring wire rod (*Kim et al., 2021*); (b) Crack at the opening end of CHSs (*C.-H. Chiu et al., 2007*); (c) Inner rim delamination of CHSs (*C.-H. Chiu et al., 2007*); (d) Breaking of inner rim fiber of CHSs (*C.-H. Chiu et al., 2007*); (e) The inner rim of the CHS breaks and contacts with its neighboring coil (*C.-H. Chiu et al., 2007*).

2.3.3 Design and optimization of reinforcement structure of CHSs

In an analogy to any fiber reinforced composite materials, the dominant role of resin is holding together reinforcements in any form and transferring stresses between them. The reinforcements, however, are the major load bearing component in CHSs. Therefore, it is essential to study the effect of the reinforcement structure on the static performance of CHSs. To optimize the reinforcement, the structure and its parameters must be considered. Besides unidirectional structure, there are five other common candidates: braided structure, ply structure, twisted structure, skin-core structure, and hybrid structure (Fig. 2.7). Material, spring diameter and structure parameter of five types of CHSs are shown in Table 2.4. Due to inconsistent design parameters and/or materials in the past works, therefore it is almost impossible to identify which reinforcement structure is the best choice according to literature. In the following, the relationship between the reinforcement structural parameters and the static performance of CHSs is discussed for a specific reinforcement structure.

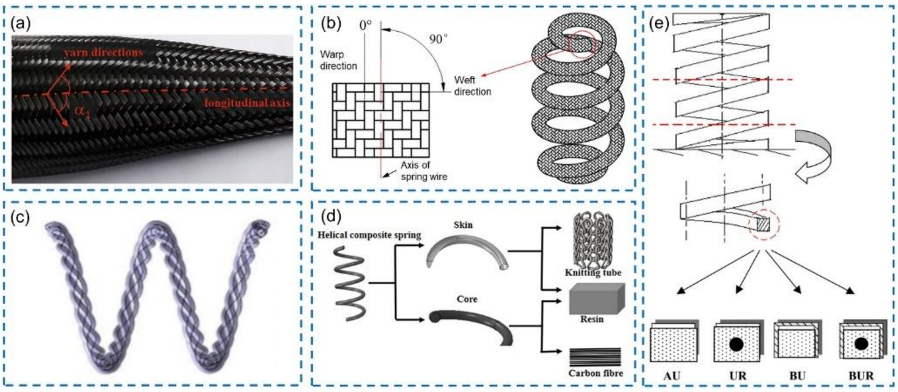

Fig. 2.7 Reinforcement structures of CHSs, (a) braided structure (*Luger et al., 2018*); (b) ply structure (*Ke et al., 2020*); (c) twisted structure (*Wu, Chen, et al., 2020*); (d) skin-core structure (*Jiang et al., 2021*) and (e) hybrid structure (*C.-H. Chiu et al., 2007*).

Table 2.4 **:** Material, spring diameter and structure parameter of five types of CHSs. (Glass fiber, Carbon fiber, Kevlar fiber, Ultra-high molecular weight polyethylene fiber and Rubber core are referred to as g, c, k, um, r respectively)

Reference	Reinforcement structure	Material	Spring diameter(mm)	Structure parameter
Zebdi *et al.* (Luger et al., 2018)	Braided structure	g	100	Braided angle
Zhong *et al.* (Ke et al., 2020)	Ply structure	c	/	Ply angle

Wu *et al.* (Wu, Chen, et al., 2020)	Twisted structure	c	63	Twist amount
Jiang *et al.* (Jiang et al., 2021)	Skin-core structure	c, k, uh	65	Skin material type
Chiu *et al.* (C.-H. Chiu et al., 2007)	Hybrid structure	c, r	40	Rubber core diameter, The Number of braided outer layer

For CHSs with a braided structure (Luger et al., 2018) and ply structure (Ke et al., 2020), the stiffness first increases and then decreases with the increase of braided angle and ply angle respectively. The stiffness is symmetrical from 0 to 90° with respect to a braiding angle of 45° corresponding to the maximum stiffness value. Wu *et al.* (Wu, Chen, et al., 2020) fabricated five types of CHSs by controlling the reinforcement twist amount 4~6r/10cm and the fiber volume content (V_f). According to the results, the load-bearing capacity of CHSs increases with increasing V_f and the load-bearing capacity of CHSs with twisted structures increases with increasing twist amount. The V_f has a greater impact on the static performance for any type of CHS. Therefore, the V_f in CHSs should be a design parameter that needs elaborate consideration. Ying *et al.* (Ying, 2014) proposed the calculation method of V_f in CHSs. In addition, some researchers (Chawla, 2012; C.-H. Chiu et al., 2007; Hwan et al., 2010; Kim et al., 2021) tested and verified V_f of CHSs according to ASTM D3171 to avoid errors caused by manufacturing of CHSs affecting the results. Based on accurate V_f, Jiang *et al.* (Jiang et al., 2021) fabricated four kinds of CHSs with a “skin-core” structure. The compression test results for the four kinds of CHSs demonstrated that the stiffness of CHSs can be improved to varying degrees by using different skin materials at same V_f. The static performance of CHSs with skin made of Kevlar is better than that corresponding to skin of ultra-high molecular weight polyethylene. Chiu *et al.* (C.-H. Chiu et al., 2007) fabricated four different laminated types of CHSs with hybrid structures including unidirectional laminates (AU), rubber core unidirectional laminates (UR), unidirectional laminates with a braided outer layer (BU), and rubber core unidirectional laminates with a braided outer layer (BUR). According to the experimental results, CHSs with BUR show the best static performance. On this basis, Hwan *et al.* (Hwan et al., 2010) fabricated nine kinds of CHSs of BUR with the rubber core diameter being 3 mm, 4 mm or 5 mm and with the number of braided outer layer being 1, 2 or 3 (labelled as R3B1, R3B2, R3B3, R4B1, R4B2, R4B3, R5B1, R5B2, R5B3; R and B stand for rubber core and braided outer layer, respectively). The experimental results show that the stiffness of CHSs with BUR decrease with increase of rubber core diameter for a fixed number of braided outer layers and with increase of the number of braided outer layer for a constant rubber diameter. Therefore, the CHS with a single braided outer layer and rubber core diameter of 3 mm (R3B1) has the highest static properties.

2.3.4 Design and optimization of geometric dimension of CHSs

For optimizing the static performance, other than material and reinforcement structure, geometric parameters of CHSs can be optimized, which include the wire diameter d, the screw pitch p that is equivalent to the helical angle α, the spring diameter D, active number of turns n of CHSs with a solid structure, and the inner wire diameter d_i of CHSs with a hollow structure. Studied geometric parameters and corresponding materials and reinforcement structures of CHSs were summarized in Table 2.5. The important work on optimizing geometry dimension of CHSs is exploring the relationship between the static performance of CHSs and geometry parameters. In general, the stiffness of CHSs increases with the decrease of the active number of turns(Ekanthappa et al., 2013) and spring diameter (T.-W. Liu et al., 2021), and the increase of spring wire diameter (Oh & Choi, 2013; Oh & Choi, 2014) and screw pitch (Yanbiao, 2020). CHSs with hollow structure can reduce the spring weight to the greatest extent without sacrificing the static performance of CHSs by changing the inner diameter of the spring wire within a certain range (Xiong et al., 2015).

Table 2.5: Studied geometry parameters and correspond to materials and reinforcement structures of CHSs. (Active number of turns, Spring diameter, Wire diameter, Screw pitch, Inner wire diameter are referred to as n, D, d, p, d_i respectively)

Reference	Geometry parameter	Material	Reinforcement structure
Ekanthappa *et al* (Ekanthappa et al., 2013).	n	Glass fiber	Unidirectional structure
Liu *et al.* (T.-W. Liu et al., 2021)	D	/	Braided structure

Sung *et al.* (Oh & Choi, 2013; Oh & Choi, 2014)	d	Carbon fiber	Ply structure
Sun *et al.* (Yanbiao, 2020)	p	Basalt fiber	Unidirectional structure
Xiong *et al.* (Xiong et al., 2015)	d_i	Carbon fiber	Ply structure

There is a case to show the influence of geometry parameters of CHSs on static performance. Oh *et al.* (Oh & Choi, 2013; Oh & Choi, 2014) investigated the variations in the wire diameters for three representative ply angles of CHSs. According to the result, the static spring stiffness increases with the increase of the wire diameter of CHSs at the same ply angle. Moreover, for a ply angle of 15°, the wire diameter of CHSs should be 21.80 mm, which has the same static spring stiffness as that of a steel spring; For a ply angle of 30°, the required wire diameter falls to 19.19 mm. For a 45° ply angle, the wire diameter should be approximately 17.17 mm, which can illustrate that reinforcement structure parameter has an impact on the optimization degree of geometry parameters on the static performance of CHSs but cannot change its influence trend.

In addition to the above geometry parameters, the influence of the special parameter of CHSs with square section, and section length width ratio on the static performance of CHSs needs to be further explored, because CHSs with square section have potential to be used in the engineering field due to its advantages of high energy storage and space saving.

2.4 Design and optimization of dynamic performance of CHSs

Fatigue and resonance are the dynamic properties of CHSs, which will affect the service life and safety of CHSs during work. Therefore, they need to be further explored.

2.4.1 Design and optimization of fatigue of CHSs

CHSs are often subjected to repeated impact loading in actual working conditions (e.g., a running vehicle over uneven surfaces). Thus, CHSs are susceptible to fatigue failure. Considering structural integrity and safety, fatigue performance of CHSs is a subject of significant importance. It should be ensured that CHSs can reach the basic number of fatigue cycles before optimizing the fatigue performance of CHSs. Sardou *et al.* (Sardou et al., 2005) found that CHSs can accumulate 300,000 cycles at the full jounce load without a fatigue failure at room temperature. Jang *et al.* (Charles & Srikanth, 2014) performed a 300,000 times fatigue test at a speed of 1.2 Hz by applying the maximum compressive load for four CHSs. The fatigue test results showed that fatigue failure of CHSs does not occur, and deformation height of CHSs was 4~7 mm occurrence after test. However, after a long time in the static state for 1 day, CHSs returns to the initial state, which means that the resilience of CHSs is closely related to fatigue performance. Sui *et al.* (Sui et al., 2001) and Chen *et al.* (Ling, 2020) investigated the resilience of CHSs that included three twistless CHSs with different V_f, two twisted CHSs with different twist and seven braided CHSs with different braid angles. The result show that the resilience of CHSs can be optimized gradually with the decrease of V_f and twist of the twisted CHSs. Resilience decreases with the increase of spring stiffness for CHSs with any structure without fatigue failure. Hwan *et al.* (Hwan et al., 2010) made a comparative study on the fatigue properties of three CHSs with the number of braided outer layers of one, two and three respectively to explore the optimized method of the fatigue performance of CHSs. According to their results, the sharp decline of load of three-layer braided CHSs in the fatigue test indicates that serious fatigue failure has occurred, while the fatigue performance of one and two-layer braided CHSs is better, and the reduction of failure load is less than 5%, which meets the requirements of commercial standards. Sun *et al.* (Yanbiao, 2020) optimized the fatigue performance of CHSs by adding nanosilica particles into CHSs, and fabricated, tested and analyzed the fatigue of CHSs with nanosilica of 2%, 4% and 6% respectively. The results show that CHSs with nanosilica content of 4% has the maximum cyclic life before the reduction of bearing capacity, which is 43.5% higher than that of CHSs without nanosilica, due tostress transfer from the matrix to silica particles, which reduces the bearing pressure of the matrix. When the content of nanosilica increases to 6%, the nanoparticles will agglomerate locally, thereby the fatigue performance cannot be further improved.

Due to the high economic and time cost of the fatigue test of CHSs, currently only a few researchers have conducted research on the fatigue performance of CHSs. However, it can still be found that the resilience performance of CHSs is opposite to the spring stiffness without fatigue failure, which means that the number of fatigue cycles increases with the decrease of spring stiffness. The fatigue performance of CHSs can be optimized by changing the number of braided outer layers of the reinforcement structure of CHSs and adding nanoparticles, such as nanosilica. In addition, the defects on the surface of CHSs will greatly reduce fatigue life. Therefore, in addition to ensuring the product quality of CHSs in the preparation process, it is also necessary to implement correct protective measures in use.

2.4.2 Design and optimization of nature frequencies of CHSs

CHSs are the shock-absorbing parts under dynamic load. To prevent resonance and optimize the stability of CHSs, it is also an important task to study the natural frequency of CHSs. The researchers studied the natural frequency of CHSs from both the calculation methods and influencing factors of the cylindrical and non-cylindrical CHSs. Ayadi *et al.* (Ayadi & Taïeb, 2017) presented a method for calculating the natural frequencies of a cylindrical CHSs. The mathematical formulation presented describes the linear dynamic behavior of CHSs. The governing mathematical model of such a behavior is formed by a system of four partial differential equations of first order of hyperbolic type. Yu *et al.* (A. Yu & Y. Hao, 2013) investigated a free vibration problem of non-cylindrical CHSs. The effect of the warping deformation of a wire cross-section on natural frequencies is first considered in the formulation. The differential equations of motion for CHSs, which are 14 first-order partial differential equations with variable coefficients, are derived using a naturally curved and twisted anisotropic beam theory. The natural frequencies of CHSs are found from an improved Riccati transfer matrix by iteration. Kacar *et al.* and Yildirim *et al.* (Kacar & Yildirim, 2011, 2016) presented the use of the stiffness matrix method based on the first-order shear deformation theory to predict the fundamental natural frequencies of cylindrical and noncylindrical CHSs subjected to initial static axial force and moment. This theoretical study about such springs with large pitch angles was performed for the first time in literature. Derived formulas consider the effects of all the stress resultants such as axial and shearing forces, bending, and torsional moments and are valid for any symmetric cross-sections such as solid/hollow circles, square, and rectangle. Free vibration frequencies were predicted for a given CHS with a large pitch angle in an accurate manner.

In addition to the above-mentioned optimization on natural frequency calculation, many researchers have also studied the factors of natural frequency to guide the optimization of CHSs. The natural frequencies of the cylindrical CHSs were measured experimentally by using an MTS testing machine to study the effect of dimensional parameters. Experimental results revealed that the natural frequency of the cylindrical CHSs can be lowered by increasing the helical diameter, in turn increasing the D/d ratio, and also by increasing the number of turns (Sancaktar & Gowrishankar, 2009). In addition, Ildirim *et al.* (VEBİL Yildirim, 2001) investigated the effects of the helix pitch angle and the number of turns on the natural frequencies of cylindrical CHSs made of carbon-epoxy1 (AS4/3501-6) and carbon-epoxy2 (T300/N5208). The natural frequencies decrease with increasing helix pitch angle and the number of turns for all types of materials. Although two materials have similar free vibration characteristics, the carbon-epoxy2 (T300/N5208) displays the highest frequencies. Hao *et al.* (Ying & Aimin, 2012) not only studied the influence of various design parameters on the natural frequency of CHSs, but also considered the influence of the warping deformation of the spring wire cross section on the natural frequency and vibration mode of CHSs for the first time. The results show that for CHSs, the error of ignoring the warpage is about 40%, and the error is about 2% after considering the warpage, indicating that the warping deformation has a significant impact on its vibration characteristics and it is an important factor that must be considered; Among the helix angle, the number of effective turns and the spring diameter, the helix angle have the least effect on the natural frequency. Considering the warpage, the natural frequency of CHSs increases with the increase of the cross-sectional area (A.-M. Yu & Y. Hao, 2013). The shape of the cross-section has little effect on the frequency of CHSs given that CHSs has same cross-sectional area. The influence trend of each parameter of non-cylindrical CHSs on natural frequency is the same as that of cylindrical CHSs, that is, it decreases with the increase of n, D_{max}/d, and α. Since variable diameter of non-cylindrical CHSs, the influence of R_{min}/R_{max} on natural frequency cannot be ignored. The results of Çalım *et al.* (Çalım, 2009) show that R_{min}/R_{max} increases, both vibration period and displacement amplitude increase as well, natural frequencies decrease. Common non-cylindrical CHSs include Conical, Barrel, and Hyperboloidal. Hao *et al.* (Ying & Aimin, 2013) and Yildirim *et al.* (Vebil Yildirim, 2001) compared the natural frequencies of the three non-cylindrical CHSs. The results show that the hyperbolic conical springs have the highest frequency, followed by conical springs, and barrel springs have the lowest frequency. In addition to the above material and geometric factors of CHSs, the reinforcement structure also has a great influence on the natural frequency of CHSs. The influence of different ply sequences on the natural frequencies of symmetrical laminated non-cylindrical CHSs is investigated for three laminated configurations (A. Yu & Y. Hao, 2013). The first configuration uses a [0/90/90/0] lay-up (the 0° direction is parallel to the helix axis), the second configuration uses a [90/0/0/90] lay-up, and the third configuration uses a [0/0/0/0] lay-up. These CHSs with different stacking sequences have the same geometrical properties. According to the results the third configuration gives the highest frequencies and the natural frequencies for the first configuration are greater than those of the second configuration for all three types of CHSs. This is to be expected because the third configuration has the largest axial and bending rigidities compared with other types of configurations and because the maximum warping displacements will occur at every point on the edge of the wire cross-section of CHSs. Therefore, the configuration with 0° ply angles at the top side and bottom side of the laminate can effectively resist the larger warping deformations. From the above analysis, the relationship between the parameters of CHSs and the natural frequency can derive. The natural frequency of CHSs is not only related to the structure of the reinforcement, the type of material and the geometric size of CHSs but also to warpage.

2.5 Summary

This chapter reviewed lots of references about CHSs, indicating detailly the current research situation of CHSs. So that we can understand the research gap to avoid repeat research and capture the important research direction.

There is no unified optimization method that can be applied to CHSs with any structure in the theoretical optimization of CHSs. FE design can not only obtain the stiffness value of CHSs, but also intuitively show the stress state that can reflect the static performance of CHSs, which cannot be obtained directly through experimental tests, to guide the optimization of CHSs. FE can not only verify the rationality of theoretical optimization but also become the foundation for researchers to analyze factors affecting performance of CHSs from the perspective of experiment to optimize spring performance. Therefore, FE has been selected to assist the optimization of CHSs in this research. The performance parameters of the material used for manufacturing CHSs, the structural parameters of the reinforcement structure of CHSs and the dimension parameters of CHSs jointly affect the design and optimization of CHSs. According to the review, carbon fiber material can provide more excellent performance for CHSs. Therefore, in our research, carbon fiber has been selected. To ensure application efficiency, the dimension parameters have been selected based on suspension environment of private car. Additionally, the review indicates that the performance of CHSs is not enough, and the evaluation method of performance is not comprehensive, which limits application and development of CHSs. To solve these problems, our study should determine the main load-bearing part. Based on this, several reinforcements should be designed to compare and select the optimal reinforcement. Then, based on the structure and forming characteristics, a manufacturing method should be invented and used. Static performance of CHSs should be improved and dynamic performance should be researched comprehensively to ensure the feasibility of application of CHSs. Therefore, the following chapter will be based current research gaps and aims, including invention of manufacturing method, promotion of static performance and supplement of dynamic performance.

3. DESIGN AND MANUFACTURING OF CHSs

This chapter comes from the publication of “Ling Chen, Liwei Wu, Hongjun Fu, Youhong Tang. Design and performance evaluation of polymer matrix composite helical springs. Polymers, 2022, 14(18): 3900” with format modifications.

3.1 Structure design of CHSs

The geometric parameters and basic mechanics of CHSs in their deformation should be recalled before designing and optimizing CHSs in a rational manner. The helical spring is mainly subjected to four forces, the bending moment M, torque T, tension force F and shear force V, as shown in Fig. 3.1(a). When the helix angle is small, the bending moment M and the tension force F can be ignored (Xiong et al., 2015). When the spring winding ratio (spring index) is larger than 10, the shear force V contributes little to the stiffness of the spring, which can also be ignored. It is sufficient to consider only the torque T of the spring wire (Yongbao et al., 2013).Therefore a helical spring can be regarded as a circular beam that is fixed at one end and subject to a twisting moment at the other. Then, the twisting angle φ is given by the equation

$$\varphi = \frac{TL}{GI_{\mathrm{p}}} \qquad (3.1)$$

where G is the shear modulus, I_P is the polar moment of inertia of the area and T is the twisting moment.

Consider a helical spring under a compressive axial load P. Spring has an average radius R, spring wire diameter d, and number of turns n, as shown in Fig. 3.1(b). Then, the variables in Equation (3.1) can be expressed as follows:

$$T = PR,\quad L = 2\pi R\mathrm{n},\quad I_{\mathrm{p}} = \frac{\pi \mathrm{d}^4}{32} \qquad (3.2)$$

By substituting Equation (3.1) into Equation (3.2), the twisting angle of the helical spring φ can be expressed by the following equation:

$$\varphi = \frac{64\mathrm{n}R^2}{G\mathrm{d}^4}P \qquad (3.3)$$

The deflection δ is the product of the spring radius and twisting angle-that is,δ=Rφ. Then, the deflection of the helical spring under compressive axial load can be derived as follows:

$$\delta = \frac{8\mathrm{n}\mathrm{D}^3}{G\mathrm{d}^4} \qquad (3.4)$$

In the above equation, D is the average diameter of the helical spring which is defined as $D = \frac{\left(D_{\mathrm{in}} + D_{\mathrm{outer}}\right)}{2}$, where D_{in} and D_{outer} are the average inner and outer diameters of the helical spring, respectively. Therefore, the spring constant of the helical spring can be expressed by the following equation:

$$\mathrm{k} = \frac{P}{\delta} = \frac{G\mathrm{d}^4}{8\mathrm{n}D^3} \qquad (3.5)$$

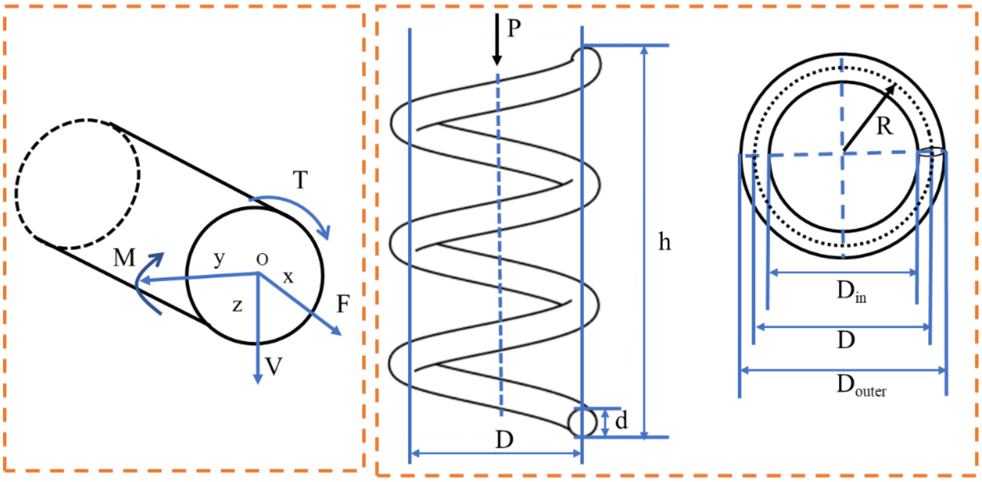

(a) (b)

Fig. 3.1 (a) Force analysis of cross section of CHSs (b)dimensions of CHSs.

As shown in Equation (3.5), the spring constant of a helical spring is proportional to the shear modulus and fourth power of the wire diameter. Furthermore, it is inversely proportional to the number of turns and third of average diameter. Understanding the theoretical relationship between the spring performance and its related parameters can speed up the design process and consequently facilitate forthcoming experimental studies by precluding unnecessary experimental tests to save labor time and cost. For composite materials with orthotropic properties, the constant of CHS can be changed by changing the reinforcement structure that can change the shear modulus (Gobbi & Mastinu, 2001). Spring force analysis explains that when the spring is forced, the spring wire section is mainly subject to torque, which means that increasing the performance of the outer surface of the spring wire is the most effective way for increasing CHS performance. Therefore, combined with textile structure, several CHSs that can change the outer structure are designed， including unidirectional, multistrand, wrapped and braided (Abbreviated as UCHS, MCHS, WCHS and BCHS respectively), as shown in Fig. 3.2.

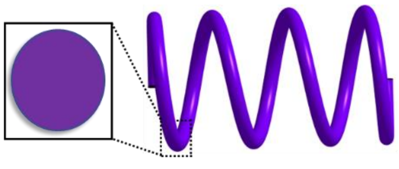

UCHS **(5.4kgf/mm)**

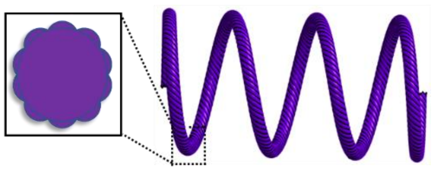

WCHS **(10.5kgf/mm)**

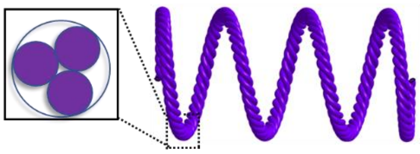

MCHS **(7.1kgf/mm)**

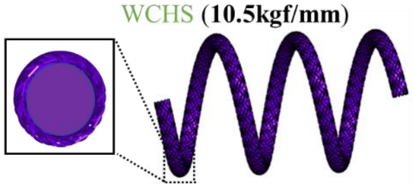

BCHS **(16.8kgf/mm)**

Fig. 3.2 The diagram of UCHS, MCHS, WCHS and BCHS.

3.2 Calculation and verification of fiber volume content of CHSs

3.2.1 Calculation of fiber volume content of CHSs

The calculation of fiber volume content is based on theoretical calculations. In fact, various parameters cannot reach an idealized state, and the calculation process needs to optimize or simplify some complex situations. Therefore, the calculation formulas and methods for various fiber volume contents based on cylindrical molds presented in this article are intended as a theoretical reference.

The following three idealized assumptions are made for the calculation of the volume content of unidirectional fibers:

1. The cross-section of the mold is uniform and consistent in the length direction.
2. The number of carbon fibers in any cross-section is equal.
3. The fibers have no nonparallel structures such as entanglement, twisting, knotting, etc.

The cross-sectional area of PVC mold：

$$S_m = \pi r^2 = \frac{\pi d^2}{4} \qquad (3.6)$$

The cross-sectional area of single fiber bundle：

$$S_f = \frac{10^{-3}T}{\rho} \qquad (3.7)$$

The ratio of cross-sectional area based on the above two formulas can be derived as：

$$P_f = \frac{nS_f}{S_m} = \frac{{}^{nT}\!/_{\rho} \times 10^{-3}}{{}^{\pi d^2}\!/_{4}} = \frac{4nT}{\rho \pi d^2} \times 10^{-3} \qquad (3.8)$$

Because the PVC mold cavity is cylindrical, fiber volume content is the ratio of cross-sectional area：

$$V_{\mathrm{f}} = \frac{V_f^{'}}{V_f^{'} + V_m} = \frac{V_f}{V} = \frac{nS_f \times \mathrm{h}}{S_{\mathrm{m}} \times \mathrm{h}} = P_{\mathrm{f}} \qquad (3.9)$$

In the above formula, S_m: the cross-sectional area of PVC mold（mm^2）; S_f: the cross-sectional area of single fiber bundle (mm^2); d: the inner diameter of the PVC mold (mm) ; T: single fiber bundle line density (tex); ρ: Carbon fiber density (g/cm^3); P_f: The ratio of all fiber to PVC mold cross-sectional area (%); V_f: Fiber volume content (%); $V_f^{'}$: Volume of fibers per unit length (mm^3); V_m: Volume of resin matrix per unit length (mm^3); *h*: Any height of cylindrical composite material (mm); *n*: The number of untwisted fiber bundles.

3.2.2 Verification of fiber volume content of CHSs

The fiber volume content (V_f) of the samples is evaluated according to ASTM D3171. Each sample with approximate 5 gram was first put into a 30 ml nitric acid solution (concentration> 90%) at a constant temperature of 75 ± 1℃ (in an oven) for 5 h. The specimen was taken out then washed with acetone and distilled water, separately. Then, it has been put back to the oven at 100 ℃ for 0.5 h. Finally, it has been taken out. The W_f and V_f can be calculated separately as follows (C. Chiu et al., 2007):

$$W_{\mathrm{f}} = \frac{W_1}{W_2} \times 100\% \tag{3.10}$$

$$V_{\mathrm{f}} = \frac{W_{\mathrm{f}} / \rho_{\mathrm{f}}}{W_{\mathrm{f}} / \rho_{\mathrm{f}} + W_{\mathrm{r}} / \rho_{\mathrm{r}}} \times 100\% \tag{3.11}$$

where W_f is the fiber weight fraction (%), W_1 is the weight of fiber (g), W_2 is the weight of specimen (g), Wr, the resin weight fraction (%) ρ_f is the density of fiber (g/cm^3) and ρ_r is the density of resin (g/cm^3).

3.3 Preparing of reinforcement of CHSs

3.3.1 Preparing of reinforcement of UCHS

The type of carbon fiber bundle used in this experiment is 12K. And the total number of required carbon fiber bundles is calculated based on the fiber volume content (rounded to the nearest integer). Then arrange all fiber bundles in parallel, fix one end tightly and apply tension to the other end, and slowly and evenly fill it into the PVC mold. When filling, try to keep each fiber bundle stretched under force and avoid entanglement and twisting between fiber bundles. In theory, the total carbon fiber should be evenly distributed in cross-section, but the gaps between single fibers within the fiber bundle are much smaller than the gaps between bundles. Moreover, the fiber bundles are irregularly flat without twisting, resulting in uneven distribution of gaps between the fiber bundles. When the fiber volume content is lower, the unevenness of the fiber bundle distribution becomes more apparent, which can easily cause uneven resin rich areas in the later process and reduce the performance of the final product. However, the fiber volume content should not be too high, because the higher the fiber content, the greater the chance of entanglement and twisting between fiber bundles during the process of filling the mold, and even the possibility of knots, which greatly affects the injection resin process. It is recommended to control the fiber content between 40% and 60% based on extensive experimental attempts.

3.3.2 Preparing of reinforcement of MCHS

The carbon fiber used in the experiment is a ribbon shaped fiber bundle. To process the carbon fiber bundle into a multistrand structure, two steps are required. As shown in Fig. 3.3, first twist an appropriate number of fiber bundles into a single strand yarn; Then, the single strand yarn is twisted in reverse to form a multistrand yarn.

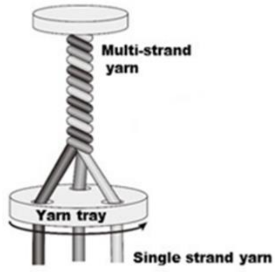

Fig. 3.3 The diagram schematic of preparing multistrand reinforcement.

3.3.3 Preparing of reinforcement of WCHS

The preparation method of the wrapping reinforcement is not much different from the multistrand reinforcement in terms of technology, except that the wrapping reinforcement requires a fiber bundle with a large total density as the inner core yarn, and then the outer periphery of the inner core yarn is just covered by the outer covering yarn at a certain angle. It is a schematic diagram of the simple preparation of the wrapping reinforcement, as shown in Fig. 3.4. There is no cross-layering between the outer covering yarns under ideal conditions. The number of strands of the outer covering yarn is related to the total density of the inner core yarn, the density of the outer covering yarn, and the wrapping angle.

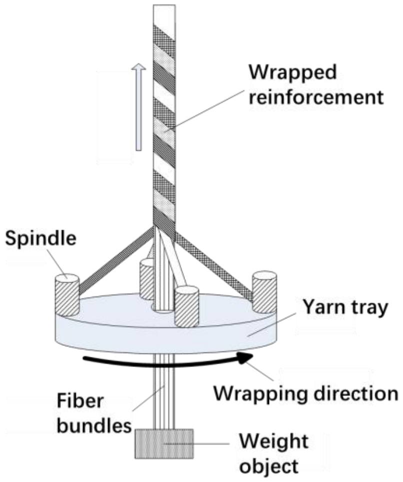

Fig. 3.4 The diagram schematic of preparing wrapped reinforcement

3.3.4 Preparing of reinforcement of BCHS

In this work, braided reinforcement structures are prepared. The braiding methods of braided reinforcement with different braided angles and braided layers are the same. The difference between them is to change braided angle by adjust the braided speed and change braided layer by add braided outer layers. Each braided layer is composed of 24 bundles of fibers. The yarn carrier carries two groups of fiber bundles to move on the chassis of the knitting machine. Each group of fiber bundles is composed of 12 bundles of fibers. One group moves clockwise, and the other group moves counterclockwise, so that the fiber bundles are intertwined above the braid plane, to prepare braided reinforcement shown in Fig. 3.5.

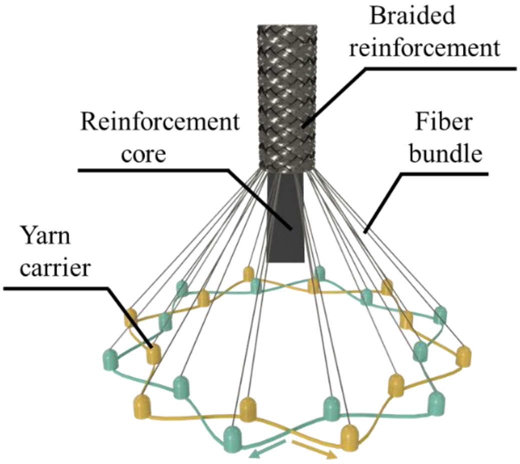

Fig. 3.5 Preparation process of braided reinforcement.

3.4 Manufacturing of CHSs

3.4.1 Equipment assembly

A set of simple equipment for manufacturing CHSs has been built, as shown on Fig. 3.6, which is not only easy operation but also low cost. The manufacturing method is called the injection-winding method. The injection molding process equipment for producing the CHSs includes pressure pump 17, pressure gauge 18, resin injector 19, inlet valve 20, preform 13, buffer bottle 21, vacuum gauge 22, vacuum pump 23, injection tube 24, and outlet valve 25. The pressure gauge 18, valve 20, and vacuum gauge 22 are respectively placed on the resin injector 19, injection tube 24, and buffer bottle 21. The resin injector 19 is connected to the preform 13 through the injection tube 24, and the preform 13 is connected to the buffer bottle 21 through the discharge tube 25.

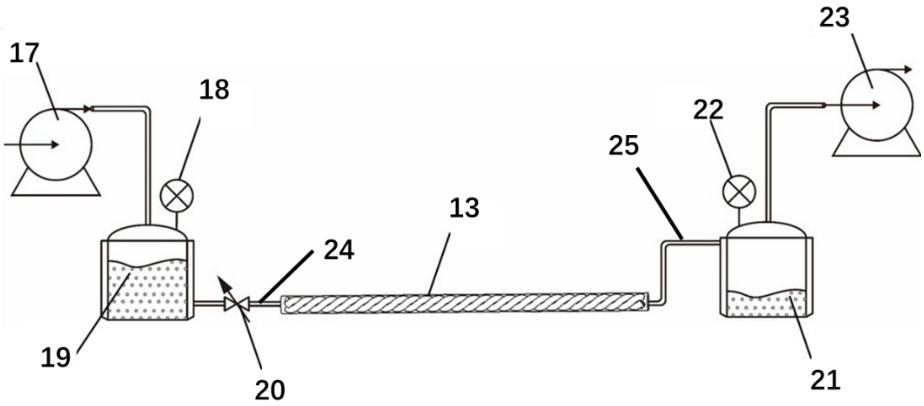

Fig. 3.6 The assembled equipment of manufacturing CHSs.

3.4.2 Design and customized mold

In this experiment, the preparation of the CHSs requires two types of molds, one is an injection mold to control the resin flow and the diameter of the spring wire of CHSs, and the other is a winding mold to fix the size of the CHSs. In this study, the injection mold uses PVC pipes because PVC pipes are soft and easy to operate, which can realize the free regulation of the shape and structure of the CHSs. And it is incompatible with the resin material in this experiment, which makes the demolding process easier. For winding molds, the metal winding molds used in the preparation of CHSs before were bulky and difficult to disassemble. Later, the wax winding mold appeared. This mold is based on the low melting point of the core wax to wind the CHSs on the mold and solidify it and then put it into a high temperature environment to melt the wax core mold to obtain the final CHSs product. However, this mold is a disposable mold and is not suitable for mass production of CHSs. To solve the winding problem in CHSs preparation, this study carefully designed the winding mold of CHSs. This winding mold needs to be designed and prepared based on the required shape of CHSs. First, all the parameters of the mold are calculated according to the geometry of CHSs, and the CATIA modeling software is used to establish the model of the winding mold as shown in Fig. 3.7. The winding mold 5 comprises core mold, outer mold fitted around the core mold, mold base and locking mechanism. The core mold is cylindrical and consists of four segmented core molds 26, each having a fixed circular hole 27 and helical grooves 28 on the outer side. The outer mold consists of the first segmented outer mold 29 and the second segmented outer mold 30. The inner side of the outer mold has helical grooves 31, and the combination of the helical grooves 31 on the inner side of the outer mold and the helical grooves 28 on the outer side of the core mold forms a complete circular groove. The mold base is circular and has circular groove 32 and fixed circular holes 33. The circular groove 32 on the mold base matches the cylindrical core mold. The locking mechanism includes the outer mold locking mechanism 34 and the base locking mechanism 35. The outer mold locking mechanism 34 is semi-circular and located on the outer mold, while the base locking mechanism 35 is located on the core mold and the mold base. The fixed circular holes 33 on the mold base match the fixed circular holes 27 on the core mold. The prepared winding mold is easy to disassemble, which laid a technological foundation for the development of CHSs.

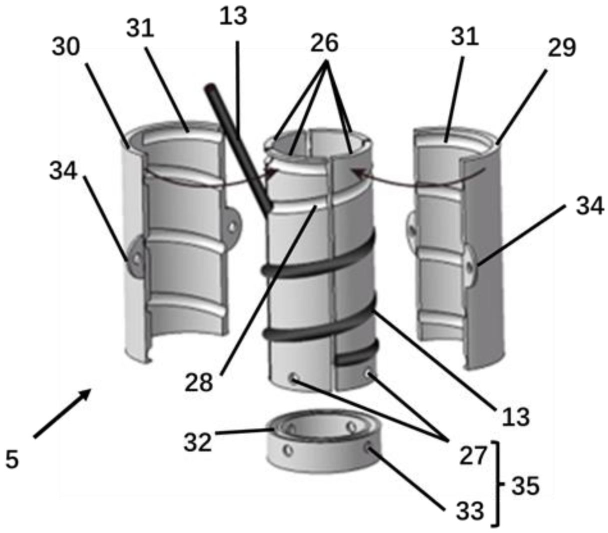

Fig. 3.7 The diagram schematic of designed winding mold of CHSs

3.4.3 Experimental materials and instruments

The experimental materials experimental instruments in the project are shown in Table 6 and Table 7.

The properties and characteristics of resin materials are as follows:

Performance characteristics: This product is cured at room temperature, low viscosity fully transparent epoxy resin and blue transparent epoxy curing agent with low viscosity, excellent strength, excellent toughness, long operation time, excellent fluidity, oil resistance, water resistance, aging resistance, environmentally friendly.

Scope of application: It is applicable to mold casting and can make complex geometric models and long runner products during casting.

Applicable time: the use time is 1-2 hours at 25 ℃, the reaction curing time is 3-4 hours, and the surface drying time is 48 hours.

Table 3.1: Experimental materials

Material	Specification	Producing area

Resin	GCC-135	Suzhou of Jiangsu province, China
Curing agent	GCC-137	Suzhou of Jiangsu province, China
Carbon fiber	T700SC-12K-50C	TOKOY JAPAN
PVC pipe	8mm×10mm	Wuhan, Hubei province, China

Table 3.2: Experimental instruments

Instruments	Specification	Producing area
Vacuum pump	2XZ	Shanghai, China
Vacuum drying oven	DZF-6020	Shanghai, China
Pressure gage	Y-60BF	Shanghai, China
Vacuum meter	Y-N100	Nantong City, Jiangsu Province, China
Tube connector	PU-10	Nantong City, Jiangsu Province, China

3.4.4 The manufacturing process and precautions of the experiment

3.2.4.1 The precautions before manufacturing CHSs

(1) Determine the parameters of CHSs

Since the performance of the CHSs is greatly affected by its external dimensions (such as the inner diameter, outer diameter, helix angle, etc.), it is important to determine the size of the CHSs. The spring size in this experiment matches that of the small sedan car and the large off-road vehicle.

(2) Determine and calculate the fiber volume content

The fiber volume content in the reinforcement structure has a great influence on the mechanical properties of the CHSs. Therefore, it is particularly important to determine the fiber volume content and accurately obtain the CHSs with a certain volume content. It is necessary to comprehensively determine the fiber volume content based on the preparation conditions of the existing equipment and the mechanical properties of the CHSs in general engineering and then calculate the required number of fiber bundles at a certain volume content.

(3) Prepare fiber reinforcement structure

This research includes four types of reinforcement structures, namely unidirectional, multi-strand, wrapped and braided reinforcement. The specific preparation methods are given in 3.1.

(4) Check the airtightness of the injection-winding molding process equipment

Since this equipment was designed and assembled by us, there are multiple connection parts in the equipment that are connected by pneumatic joints, which are prone to airtightness problems. Since this equipment mainly relies on air pressure to infuse resin, the air tightness of the equipment cannot be ignored. The places where poor air tightness may occur in the experiment are mainly the connections between the air inlet pipe-resin injector, the injection pipe-mold, and the outlet pipe-filter bottle. During the experiment, it is sufficient to check the air tightness of these connectors.

(5) Preparation of glue solution

Mix epoxy resin GCC-135 and curing agent GCC-137 in a volume ratio of 3:1, stir evenly with a glass rod, and then place the beaker containing the glue solution in a vacuum drying oven at 30℃~50℃ for 10~20 minutes. The purpose of vacuuming is to remove bubbles in the solution to prevent bubbles from entering the sample, resulting in excessive porosity inside the sample and reduced product performance. Heating can reduce the concentration of the glue solution and make it more fluid, thereby avoiding short shots.

(6). Vacuum degassing of resin

After the resin is stirred, place the beaker in a buffer bottle and connect a vacuum pump to vacuum degassing. This will reduce the number of bubbles generated during the stirring or pouring of the resin. If there are too many bubbles in the resin, it will affect the injection process and reduce the uniformity of injection. And when the resin infiltrates the fiber, some bubbles will adhere to the fiber and not move forward with the resin, which will increase the void ratio of the final product and reduce its performance.

(7). Inspection of the mold

This study uses a PVC pipe with a certain elasticity as an injection mold and a winding mold composed of multiple parts. Before preparation, it should be ensured that the injection mold is not damaged or excessively deformed. And ensure that the winding mold parts are complete.

(8). Fiber filling process

This experiment uses a method in which one end of the fiber reinforcement is fixed, and the PVC injection mold slowly moves from the fixed end to the free end to gradually wrap the fiber reinforcement into the PVC mold. This filling method currently has certain limitations. When the fiber volume content in the mold is too high, the filling process will be difficult and may destroy the structural state of the fiber reinforcement.

3.2.4.2 The manufacturing process of CHSs

The whole manufacturing process of CHSs is shown in Fig. 3.8, which mainly includes three steps. The manufacturing details of CHSs is below.

(1) Resin injection

After the whole experimental device is connected and the airtightness check is completed, the solution is poured into the resin syringe. The first step is to close the outlet valve, use the pressure pump to pre-add a little pressure, fill the injection tube with part of the resin, discharge the gas in the injection tube, and then close the pressure pump. The second step is to close the air inlet valve, turn on the vacuum pump, and discharge the air in the mold. During this period, a small amount of resin will enter the mold due to the vacuum pressure, but it will not affect the entire resin injection process. The third step is to further check the airtightness of the device. If there is no problem, turn on the pressure pump to increase the injection pressure to the specified value, and observe the flow of the resin in the mold. And the pressure gauge and vacuum meter are 0.3 MPa and 0.09 MPa respectively, so that the resin enters the preform at a constant speed and slowly to form preform without glue blocking or short shot. The fourth step is to wait for the resin in the PVC injection mold to flow out of the outlet valve and observe whether there are many bubbles in the outflowing resin. These bubbles are the air attached to the tiny gaps between the fibers in the fiber reinforcement body. This air cannot be completely removed by vacuum pressure, but the resin flow and infiltration injected by positive pressure can bring out this part of the air. Therefore, while the resin flows out of the injection mold, the resin injection should be allowed to continue for a period until the number of bubbles is very small. The fifth step is to turn off the pressure pump and vacuum pump, seal both ends of the PVC injection mold, and then release the air inlet valve and outlet valve to carefully remove the injection mold.

(2) Remove device and seal injection mold

After removing the PVC injection mold after injecting the resin, the suction bottle and the resin syringe should be disassembled first, and carefully cleaned with alcohol and acetone, especially the interface parts. After cleaning, wipe it with a paper towel or rag and dry it for the next cycle. Then fix one end of the PVC injection mold upward, hang a weight of a specified weight on the other end, and hang the mold vertically for 15~20mins. This will allow the PVC mold to shrink evenly in the radial direction, generate uniform radial pressure, discharge excess resin in the fiber reinforcement, make the resin distribution more uniform, and increase the fiber content of the final product. Finally, the injection mold that has been suspended for a period is wound on the winding mold according to the pre-set spring structure parameters and fixed.

(3) Curing, demolding and post-treatment

After the resin is injected and the injection mold is suspended and wound, the winding mold is left upright at room temperature for 48 hours to completely cure the resin. After curing is completed, the PVC mold is removed from the winding mold by disassembling the multi-parts winding mold, and then the PVC mold is peeled off from the sample with a blade to complete the entire demolding process. After demolding is completed, the sample can be cut into standard specimens, and post-processing such as cutting at the beginning and end of the CHSs and finally wait for testing.

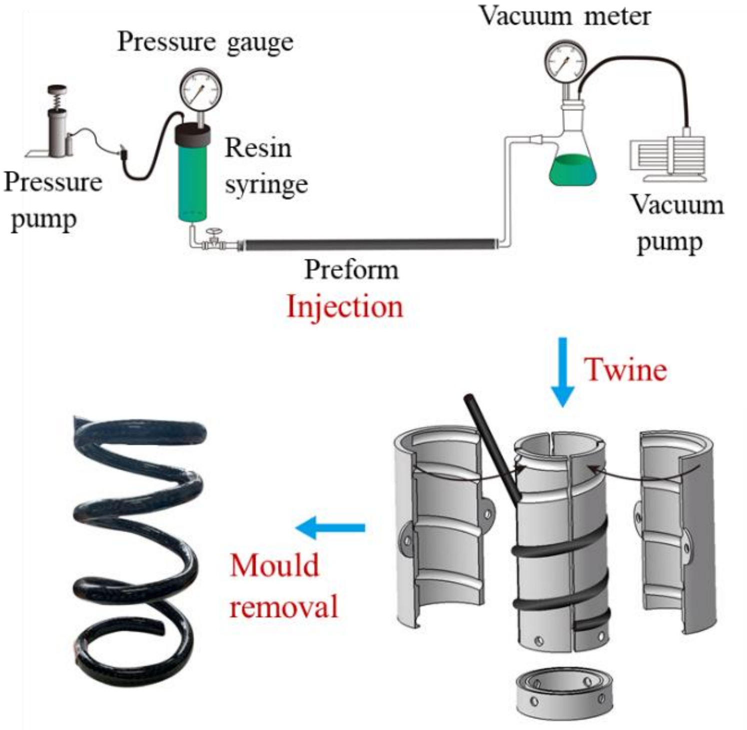

Fig. 3.8 Manufacturing of CHSs by injection-winding method.

3.2.4.3 Types and relevant parameters of CHSs

The types of CHSs manufactured in the research are as follows. CHSs with unidirectional, multistrand, wrapped and braided (Abbreviated as UCHS, MCHS, WCHS and BCHS respectively) is used to adjust which type of reinforcement has the best performance. And their stiffness is 5.4, 7.1, 10.5, 16.8 respectively after initial test analysis. The result shows that BCHS have largest stiffness. Finally, BCHS is selected for further study in the project. And five types of BCHSs are designed based on the braiding angle and the number of braiding layers, as shown in Fig. 3.9. Single-braided layer BCHSs (SBCHS) with braiding angles of 0,15 and 30 are respectively referred to as UCHS, SBCHS15° and SBCHS30° is used to research the impact of braided angle based on static performance research. And BCHSs with multi-braided layers (MBLs-CHS) of 1, 2 and 3 (abbreviated as SBCHS, DBCHS and TBCHS) are used to compare the impact of different braided layers based on impact performance analysis. The geometrical specifications for CHSs include L = 200 mm, D = 74 mm, P = 57 mm, and d = 14 mm, as depicted in Fig 3.10.

Fig. 3.9 The diagram of UCHS, SBCHS15°, SBCHS30°, DBCHS and TBCHS.

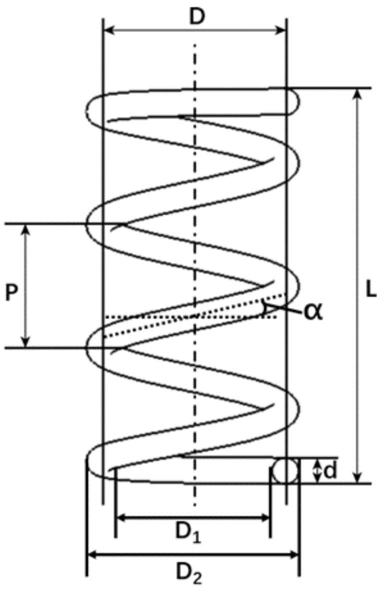

Fig. 3.10 The diagram of shape of CHSs

3.5 Summary

This chapter mainly describes the design and manufacturing of CHSs. Firstly, the force situation of CHSs is analyzed when it works. The stiffness formula has been derived based on the force analysis. The formula shows that the spring stiffness of helical spring is proportional to the shear modulus and fourth power of the wire diameter. Furthermore, it is inversely proportional to the number of turns and third of average diameter.

Moreover, spring force analysis explains that when the spring is forced, the spring wire section is mainly subject to torque, which mean that increasing the performance of the outer surface of the spring wire is the most effective way for increasing CHS performance. Therefore, combined with textile structure, several CHSs that can change the outer structure are designed, including UCHS, MCHS, WCHS and BCHS.

To clear how many fiber bundles should be used in preparing reinforcements, the formula about the relationship between number of fiber bundles and fiber volume content is derived. Then the number of needed fiber bundles can be calculated based on fiber volume content. In addition, due to the fiber volume content is the important factor to impact the performance of CHSs. Therefore, the accuracy of fiber volume content should be ensured. To solve the problem, the proving method of fiber volume content has been used to ensuring the accuracy based on feedback method. And the reinforcement preparation is the first step to manufacturing CHSs, therefore the preparing method of the four types of reinforcement have been explained firstly. The key point of preparing for UCHS reinforcement is trying to keep each fiber bundle stretched under force and avoid entanglement and twisting between fiber bundles. When the reinforcement of MCHS is preparing, the two parameters that are the number of strands and the degree of twisting should be controlled. The reinforcement of WCHS consists of inner core fiber and outer wrapped fibers. When the reinforcement of WCHS is preparing, the number of two components and the degree of wrapping should be considered. And The reinforcement of BCHS also include inner core fiber and outer braided fiber, the braided angle and braided layer are the important parameters. After that the four types of CHSs can be manufactured by the injection-winding method. It is worth mentioning that the equipment is assembled by us, which is portable and low cost. During manufacturing CHSs, two types of molds are needed, that are injection mold and winding mold respectively. The injection mold uses PVC pipes because PVC pipes are soft and easy to operate, which can realize the free regulation of the shape and structure of the CHSs. And the winding mold is carefully designed for assembling simply and permanent use. Finally, UCHS, MCHS, WCHS and BCHS are manufactured to adjust which type of reinforcement has the best performance. UCHS, SBCHS15 ° and SBCHS30 ° is manufactured to research the impact of braided angle on the performance of BCHS. And DBCHS and TBCHS are manufactured to compare the impact of different braided layers on the performance of BCHS.

4. STUDY ON STATIC PERFORMANCE OF SBCHSs

This chapter comes from the publication of “Ling Chen, Joel Chong, Qian Jiang, Liwei Wu, Youhong Tang. Understanding the static performance of composite helical springs with braided nested structures. Composites Part A: Applied Science and Manufacturing, 2023: 107822” with format modifications.

As a widely used mechanical component in industrial fields, helical spring plays a crucial role in production practice (Chen, Xing, et al., 2022). In recent years, the industrial field has shifted toward lightweight and reducing carbon emissions (Bhudolia et al., 2022; S. Liu et al., 2021; T. Liu et al., 2021). The reduction of helical spring weight offers substantial benefits, including significant energy consumption savings, reduced CO_2 emissions, and enhanced overall mobility and load-bearing capacity (Ghassemieh, 2011). Therefore, research on lightweight composite helical springs (CHSs) holds significant importance (J. Bai et al., 2021). The role of resin in CHSs is mainly bonding and force transmission, and its main bearing structure is internal reinforcement structures (Ramaswamy et al., 2023; Wu et al., 2019). Therefore, some research studied the effects of reinforcement structure and relevant parameters on performance of CHSs. Previously, Jiang *et al.* (Jang & Jang, 2014), Choi *et al.* (B. Choi & B. Choi, 2015) and Zhong *et al.* (Zhong, 2017) fabricated CHSs with a ply structure to explore the relationship between ply angle and spring stiffness. The results showed that the stiffness of CHSs with ply structures changed sinusoidally with the ply angle and was symmetrical about 45°. Zhan *et al.* (Zhan et al., 2018) combined the design of orthogonal experiment with the finite element method to establish the response surface model of stiffness and strength of CHSs with ± 45° ply sequence to its geometric parameters. The errors were less than 6% by comparing the finite element values with the theoretical and experimental values, which explained the feasibility and accuracy of the finite element method. Wu *et al.* (Wu, Chen, et al., 2020) manufactured five types of CHSs with twisted structures by controlling different reinforcement twists and fiber volume fraction (V_f). The compression testing shown that the load-carrying capacity of the CHS increases with the increase of fibers content and twist in the CHS. The variation of spring constant with twist angle under different V_f was predicted by the finite element method. Besides, Jiang *et al.(*Jiang et al., 2021*)* fabricated CHSs with "skin-core" structures, the skin structure was a weft knitting tube made of aramid and ultra-high molecular weight polyethylene fibers, and the core structure was unidirectional carbon fibers. The compression test results of CHSs shown that the spring constant of CHSs can be effectively improved by using a knitting tube. Meanwhile the internal mechanism of spring performance improvement was revealed by establishing and analyzing a finite element model corresponding structure.

Based on above research, it is evident that the reinforcement structure of CHSs has significant influence on static performance and the finite element method is an excellent way to understand CHSs' behaviors and internal mechanisms. However, it is widely recognized that V_f of the reinforcement structure has substantial impact on performance of CHSs, but it is difficult to manufacture CHSs with a large V_f. The aforementioned reinforcement structure can't significantly improve spring constant without substantial increasing V_f and manufacturing difficulty (Chen, Xing, et al., 2022). To overcome the problems, this study introduces SBCHSs with braided angle of 0°, 15° and 30° (abbreviated as UCHS, SBCHS15°and SBCHS30°) that is formed by a 2D braided tube nested on unidirectional fibers, enabling a significant improvement in the spring constant with only a slight increase in V_f. Importantly, this enhancement can be achieved without altering the CHS manufacturing process or facilities. Subsequently, simulation is conducted to elucidate the mechanism of reinforcement structure influencing spring constant. Finally, the advantages of SBCHS are highlighted by comparing resilience and specific spring stiffness with those of steel spring.

4.1 Test methods

4.1.1 Compression test

The mechanical properties of UCHS, SBCHS15°, SBCHSS30° were tested by a computer servo control material testing machine (Instron 5969, USA) according to ASTM A125-2001 at the speed of 1 mm/min, as shown in Fig. 4.1 To ensure accuracy of data, five specimens were tested for each type of SBCHSs. The test system automatically recorded the data of an applied force and the corresponding compression at each sampling interval, providing immediate load-displacement curves for each spring during testing.

Fig. 4.1 Compression test of SBCHSs

4.1.2 Resilience test

The resilience test was conducted by pressing SBCHSs until mutual contact between the coil levels was achieved, as shown in Fig. 4.2, and then keeping the compression load for a period of 24 h, 48 h, 72 h, and 96 h, respectively. The spring's height after each loading period was recorded; then, the spring height after unloading for 24 h, 48 h, 72 h, and 96 h was measured and recorded. Five samples were tested for each SBCHS.

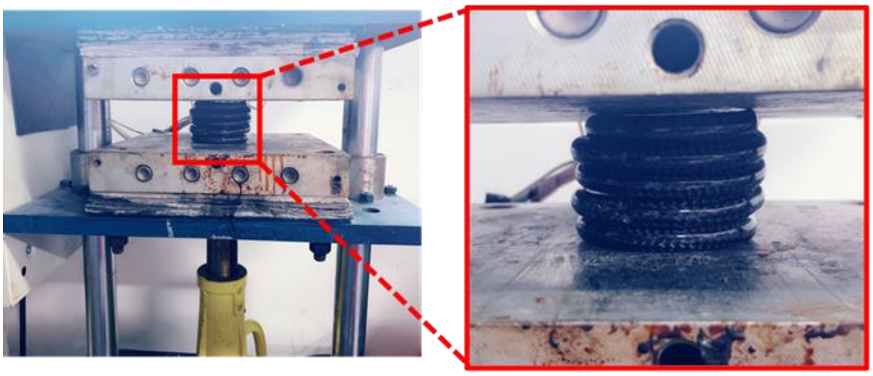

Fig. 4.2 Resilience test of SBCHSs

4.2 FEM

4.2.1 3D meso model of SBCHSs

The initial step involves constructing a precise 3D geometric model of SBCHS to effectively represent its structure for subsequent simulations of the structural characteristics. The trajectory of the helical braiding surface (Fig. 4.3(b)) formed by the motion of the braided projection curve (Fig. 4.3 (a)) expressed by Equation (4.1) along the center helical line expressed by Equation (4.2).

$$\begin{Bmatrix} x = (\mathrm{R}_1 + \mathrm{A}\sin(\mathrm{N}t))\cos(t) \\ y = (\mathrm{R}_1 + \mathrm{A}\sin(\mathrm{N}t))\sin(t) \end{Bmatrix} \tag{4.1}$$

where R_1 is the radius of the center circle, A is the amplitude, and N is the number of curls in a circle.

$$\left(x, y, z\right) = 0_2\left(R\cos\theta, R\sin\theta, \frac{p_0\theta}{2\pi}\right) \tag{4.2}$$

where, p_0 is the pitch of a spring along the Z axis and θ is the polar coordinate angle of the center helical curve around the center axis of a spring.

The spatial helical motion and the circumferential motion in a braided plane motion can be combined into a combined motion, and the trajectory of the combined motion is always located on the rotating sweep surface (Fig. 4.3 (c)) formed by rotation of the red line along the center helical line. Because the spatial shape of fiber bundle in the braided reinforcement should meet the requirements of helical braiding and rotating sweep surface characteristics at the same time (Ning & Yu, 2016), the braided fiber bundle center line should be the intersection of two curved surfaces, as shown in Fig.

4.3 (d). According to the above method, the center lines of all braided fiber bundles are obtained, shown in Fig. 4.3 (e). The structural model of braided reinforcement is established based on the center lines of all braided fiber bundles, as shown in Fig. 4.3 (f). The braided reinforcement of SBCHS has two directions along the helical direction. One direction extending to the left along the helical direction is defined as the left braided reinforcement, and the other direction extending to the right along the helical direction is defined as the right braided reinforcement. Fig. 4.3 (g) shows the reinforcement core model of SBCHS, and the resin model is formed by removing the braided reinforcement and reinforcement core from the macro geomety model of UCHS, as shown in Fig. 4.3 (h).

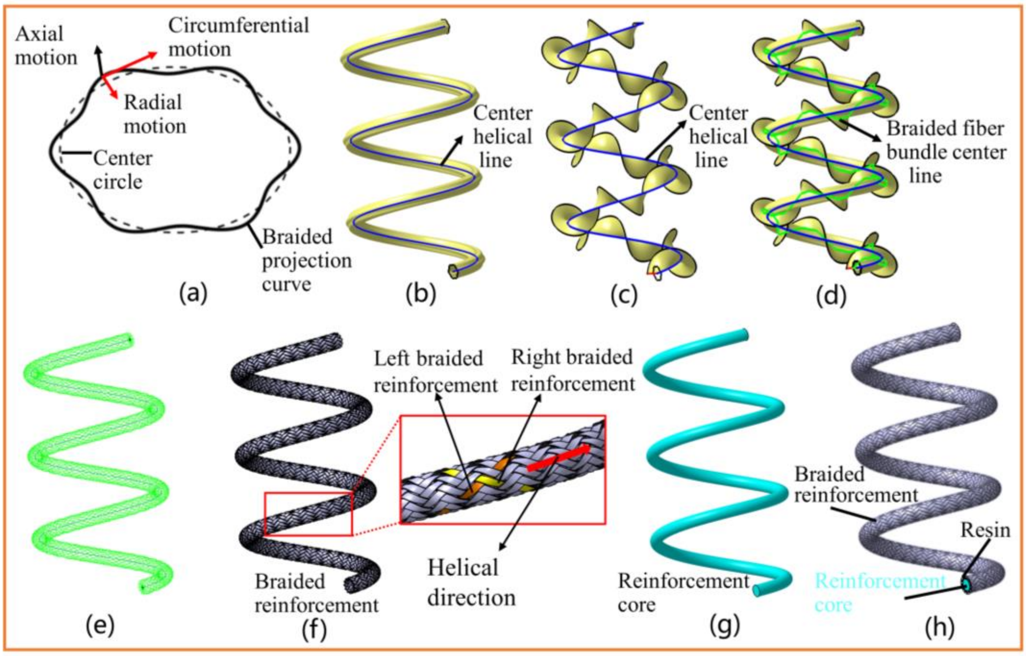

Fig. 4.3 The process of building SBCHS model. (a) Braided projection curve, (b) helical braiding surface, (c) rotating sweep surface, (d) braided fiber bundle center line, (e) the center lines of 24 braided fiber bundles, (f) braided reinforcement, (g) reinforcement core, and (h) resin model of SBCHS.

4.2.2 FEM of SBCHSs

The 3D model of SBCHS was imported into ABAQUS for the prediction of spring constant. Discrete local coordinate system, as depicted in Fig. 4.4 (a), was established, with '1' representing the axial direction of the fiber, and '2' and '3' representing the transverse directions. Because reinforcement core of SBCHS was a homogenization model, the material properties of it were calculated by the mixing method (the calculation formula is Equation (4.3) ~ (4.8)) based on material properties of carbon fiber and resin shown in Table 4.1. The material properties of braided reinforcement and resin of SBCHS were directly endowed with carbon fiber and resin properties.

Elastic modulus:

$$E_{l11} = E_{f11} \times V_f + E_m \times V_m \tag{4.3}$$

$$E_{l22} = E_{33} = \frac{E_m}{(1-\sqrt{V_f}(1-\frac{E_m}{E_{f22}}))} \tag{4.4}$$

Shear modulus:

$$G_{l12} = G_{13} = \frac{G_m}{(1-\sqrt{V_f}(1-\frac{G_m}{G_{f12}}))} \tag{4.5}$$

$$G_{l23} = \frac{G_m}{(1-\sqrt{V_f}(1-\frac{G_m}{G_{f23}}))} \tag{4.6}$$

Poisson's ratio:

$$v_{l12} = v_{13} = v_{f12} \times V_f + v_m \times V_m \tag{4.7}$$

$$v_{l23} = \frac{E_{22}}{2G_{23}} - 1 \tag{4.8}$$

The subscripts l, f and m represent reinforcement core, carbon fibers and resins respectively.

Table 4.1: Material properties of carbon fiber and resin (*Chakladar et al., 2014*; *Miyagawa et al., 2006*; *Miyagawa et al., 2005*; *Sommer et al., 2022*; *Xie & Koslowski, 2017*; *Zhang et al., 2013*)

Properties	Carbon fiber			Resin
Elastic modulus (GPa)	E_{11}=230	E_{22}=10	E_{33}=10,	E=3.05
				,
Poisson's ratio	v_{12}=0.256	v_{13}=0.256	v_{23}=0.30	v=0.41,
Shear modulus (GPa)	G_{12}=27.3	G_{13}=27.3	G_{23}=3.85	
Density (kg/m^3)	1800			
Diameter (mm)	0.007			

The display dynamic analysis step was selected and geometric nonlinearity option had been switched on to account for large deformation. The C3D8R grid was used for the braided reinforcement and reinforcement core , and the C3D10M grid was used for the resin, as shown in Fig. 4.4 (b). In addition, to improve the simulation result, mesh size has been optimized by comparing model accuracy with different mesh sizes. The boundary condition was that one end of the CHS was fixed and the other end was applied with the axial displacement, as shown in Fig. 4.4 (c).

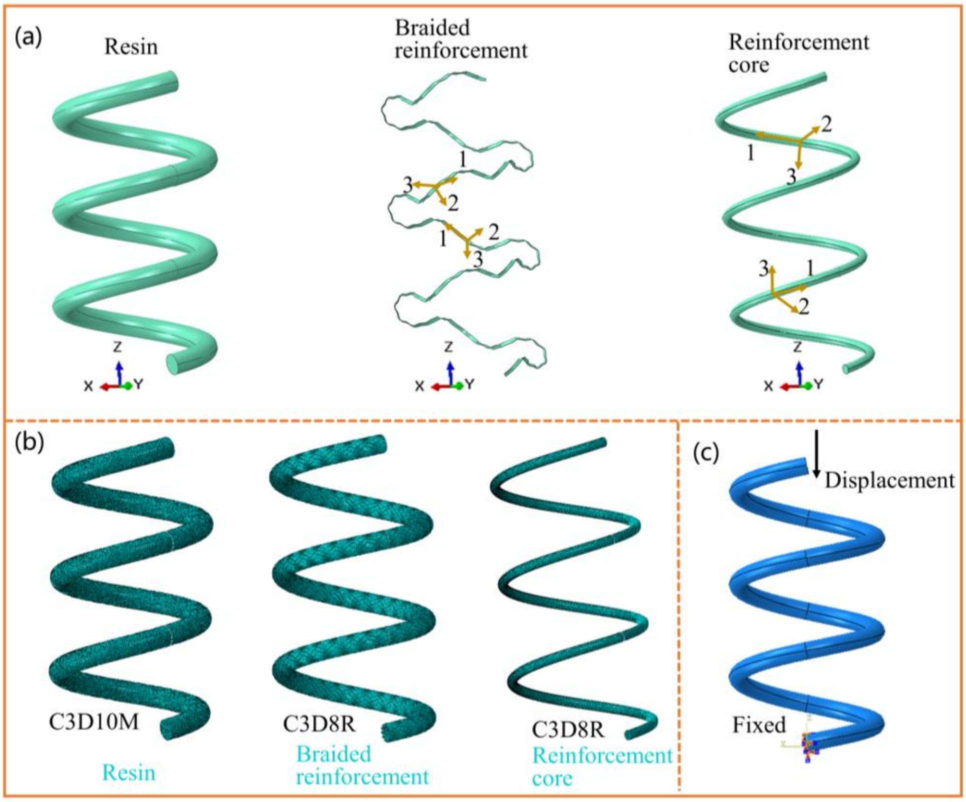

Fig. 4.4 Finite element modeling of SBCHSs. (a) The discrete local coordinate system, (b) meshing and (c) boundary condition.

4.3 Results and analysis of static performance

4.3.1 Analysis and verification of simulation results

The optimized mesh size results, as depicted in Fig. 4.5 (a), indicated that the spring constant tends to stabilize as the mesh size decreasing. Interestingly, the spring constant remains constant between mesh sizes of 0.5 and 0.2. Consequently, a mesh size of 0.5 is selected to strike a balance between maintaining simulation accuracy and reducing computational time. Then, the compression simulation of UCHS and SBCHS with V_f of 55.00%~56.77% (braided angle of 0°~30°) is carried out. The spring constant is extracted after the simulation, as shown in Fig. 4.5 (b). When V_f changes from 55% to 56.8%, the spring constant of UCHS only can be adjusted from 6.7 kgf/mm to 7.0 kgf/mm while the spring constant of SBCHS can be adjusted from 6.7 kgf/mm to 18.3 kgf/mm, which exhibited a larger spring constant control range of SBCHS than that of UCHS, indicating SBCHS can greatly improve the spring constant with a small increment of V_f.

The experimental compression results are analyzed to prove the accuracy of simulation . The experimental load-displacement curves and spring constants of UCHS55%, SBCHS15°, SBCHS30° are compared with the simulation results, as shown in Fig. 6. It can be seen from Fig. 4.6(a) that the simulated load-displacement curves are in a good agreement with the experimental results. The maximum difference of spring constant between simulation and experiment is 4.0%, which verifies the accuracy of the model, as shown in Fig. 4.6(b). The spring constants of UCHS55%, SBCHS15°, SBCHS30° are 6.5 kgf/mm, 13.3 kgf/mm and 17.6 kgf/mm respectively. The spring constant of SBCHS15° and SBCHS30° is 105.4% and 171.4% higher than that of UCHS55%, coresponding V_f only increases 0.9% and 1.8%, respectively. Compared with SBCHS15°, SBCHS30° has a higher spring constant, which is because V_f and braided angle in SBCHS30° are large. A large braided angle indicates that there are more braided intersections in the same length, which means that the friction force is increased by making the fibers closely embrace each other. The above results show that SBCHS has obvious advantage in improving spring performance than that of UCHS, and the internal mechanism needs to be further analyzed in combination with the simulation results.

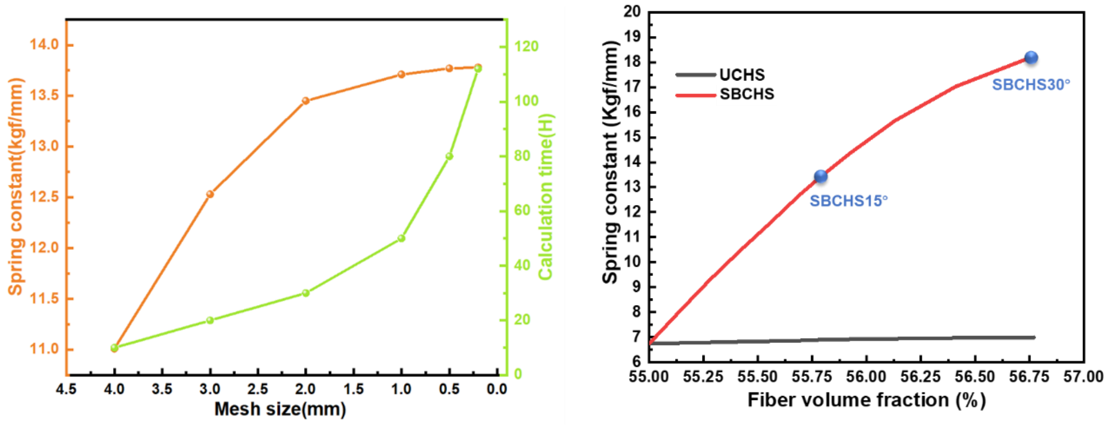

(a) (b)

Fig. 4.5 (a) Validation of simulation model and (b) spring constant of SBCHS by simulation.

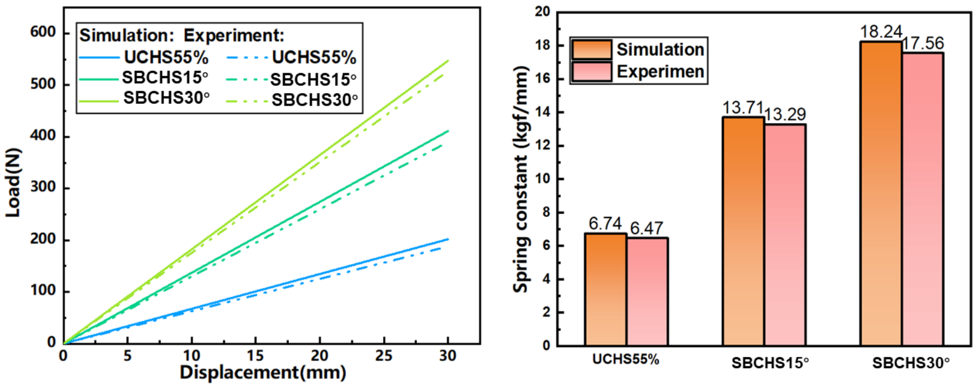

(a) (b)

Fig. 4.6 (a) Load-displacement curves of UCHS55%, SBCHS15° and SBCHS30° and (b) spring constants of UCHS55%, SBCHS15° and SBCHS30° through experiment and by simulation.

4.3.2 Von Mises stress evolution of SBCHSs under compression

The simulation results of UCHS55%, SBCHS15°, SBCHS30° are analyzed to unveil the internal mechanisms behind SBCHS's significant enhancement in spring performance and to establish the relationship between the braided angle and spring constant. Since the stress state of each coil of a CHS is the same (B. Choi & B. Choi, 2015), it suffices to extract stress data from just one coil of UCHS55%, SBCHS15°, and SBCHS30°for analysis. To understand the stress evolution and structure effect during compression, the mises stress distribution of UCHS55% at three displacement points of 10 mm, 20 mm and 30 mm were extracted, as shown in Fig. 4.7(a). Besides, to clearly analyze the bearing mechanism of SBCHS, the stress distribution diagrams of reinforcement core, braided reinforcement and resin of SBCHS are extracted respectively, as shown in Fig. 4.7(b)-4.7(d). The stress values increase with the increase of compression displacement and concentrate gradually on the internal radial zone from both ends to the middle among all parts. The mises stress level of the reinforcement core of SBCHS15°and SBCHS30° are similar with that of UCHS55%. This is because all of them are unidirectional fiber reinforcement structures. The mises stress of the reinforcement core of SBCHS30° is larger than that of SBCHS15°, this is because the force of braided reinforcement of SBCHS30° squeezed on reinforcement core is larger than that of SBCHS15°. The mises stress of the braided reinforcement of SBCHS is much greater than that of the resin and reinforcement core, which shows that the braided reinforcement in SBCHS is the main bearing structure. This is the reason why SBCHS can significantly increase the spring performance by a slightly increase of V_f. The stress concentration of resin in SBCHS30° is more serious than that of SBCHS15° by comparing the mark of intersections of braided reinforcement as illustrated in Fig. 4.7(d), which shows the contribution of resin in SBCHS30° is larger than that of SBCHS15° during compression. The mises stress of resin is far less than those of reinforcement core and braided reinforcement in SBCHS, indicating that the main role of resin in CHS is not bearing force.

It can be seen from the above analysis that the outer layer of the spring wire is the main bearing area of a CHS, so the stress state of the outer layer of a spring wire in UCHS55%, SBCHS15° and SBCHS30° should be further analyzed. Because UCHS has no peripheral reinforcement structure, the stress within 0~360° of the spring wire outer layer of UCHS55% is extracted according to the four corresponding outer layer positions (internal radial (F_{in}), external radial (F_{ex}), left side (F_l) and right side (F_r)), as shown in Fig. 4.8(a). The spring wire outer layers of SBCHS15° and SBCHS30° are braided reinforcement and the stress difference between the left and right braided reinforcements is large, so the mises stress within 0~360° of left and right braided reinforcements should be extracted and compared separately. The mises stress within 0~360° of UCHS55%, SBCHS15° and SBCHS30° (Fig. 4.8(b)) shows a trend of increasing firstly and then decreasing symmetrically at 180°. The mises stress in a spring wire periphery of UCHS55% sequentially decreases for F_{in}, $F_l \approx F_r$, F_{ex} within 0~360°. The maximum mises stress of UCHS55% is concentrated in the F_{in} region corresponding to 180°. By contrast, the mises stress of a spring wire peripheral of SBCHS15° and SBCHS30° at 180° is 2.43 and 3.14 times higher than that of UCHS55% respectively, which indicates that the mises stress increases with the increase of braided angle. Moreover, the fluctuation amplitude of the braided reinforcement of SBCHS30° is less than that of SBCHS15° within 0~360 °, indicating that the degree of force uniformity increases with the increase of braided angle, which is also the reason for the better performance of SBCHS30°.

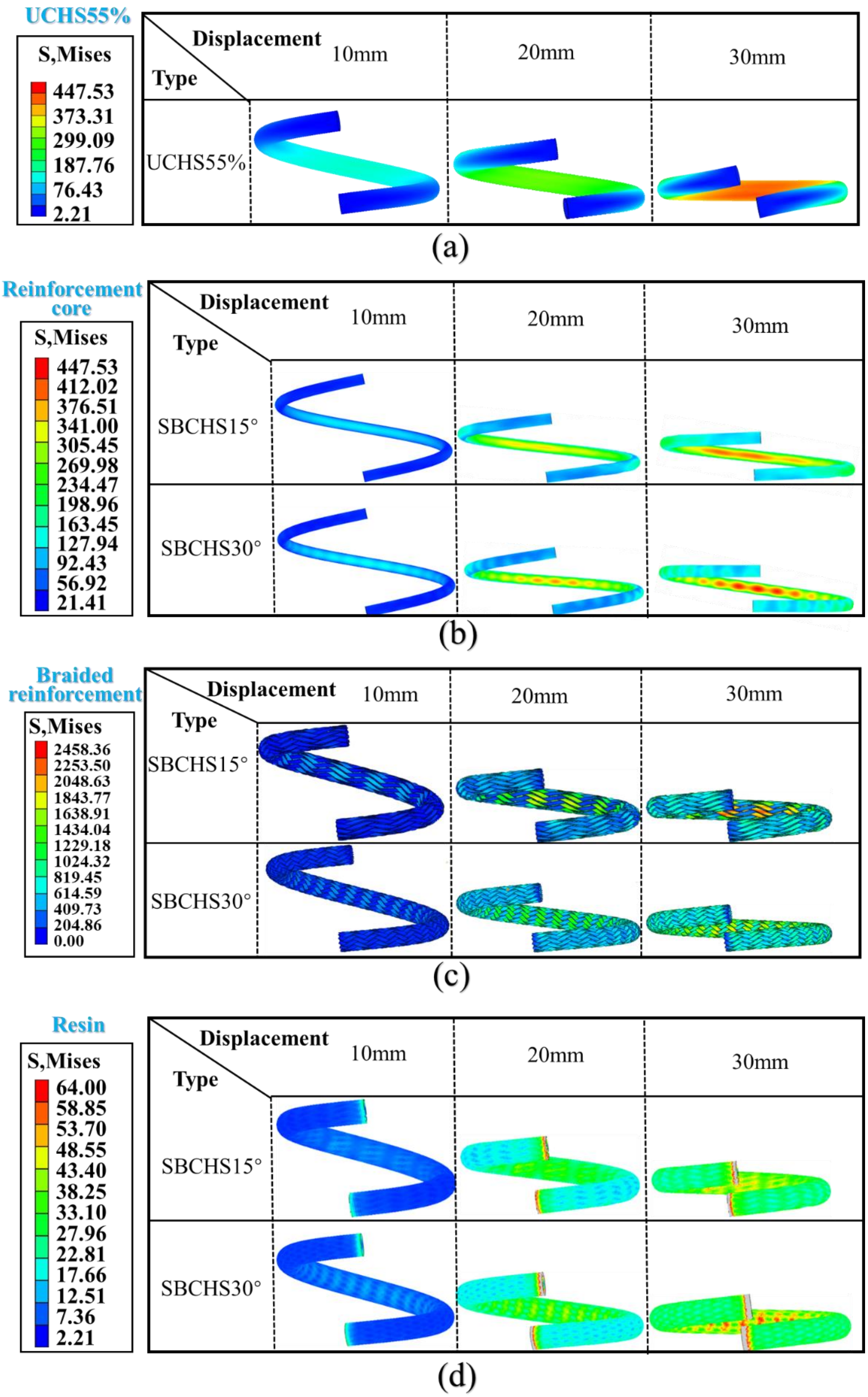

(a)

(b)

(c)

(d)

Fig. 4.7 (a) Mises stresses distribution of UCHS55%, SBCHS15° and SBCHS30° under compression, (b) mises stresses distribution of reinforcement core of SBCHS15° and SBCHS30° under compression, (c) mises stresses distribution of braided reinforcement of SBCHS15° and SBCHS30° under compression, and (d) mises stresses distribution of resin of SBCHS15° and SBCHS30° under compression.

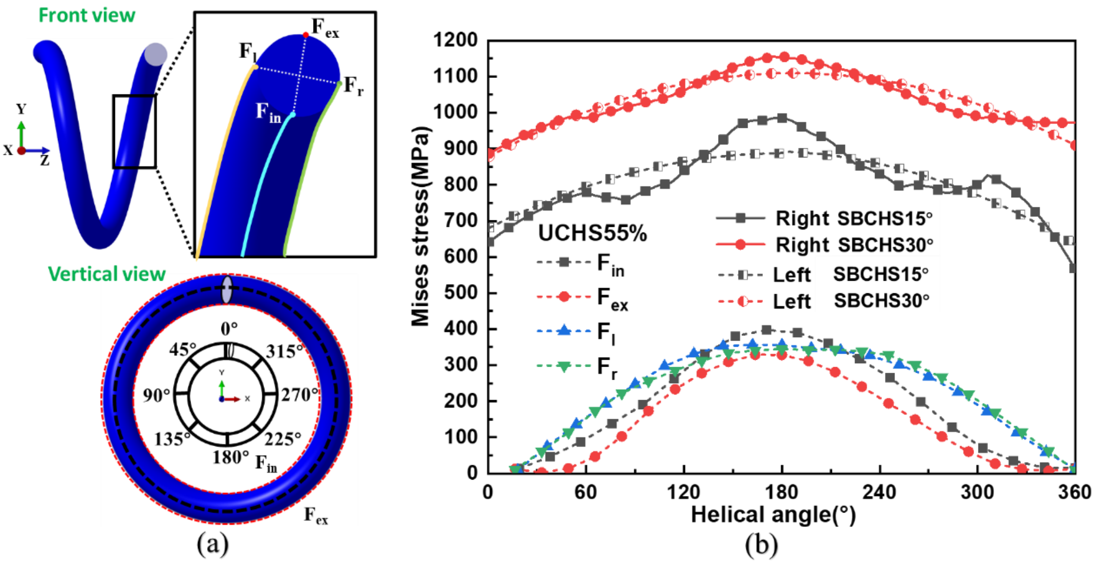

(a) (b)

Fig. 4.8 (a) Four reference curves of the spring wire outer layer of UCHS55% and (b) helical angle-mises stress curves of spring wire periphery of UCHS55%, SBCHS15° and SBCHS30° within 0~360° under compression.

4.3.3 Max. principal stress distribution with helical angles of SBCHSs under compression

To identify the initiation of damage, further analysis of the max. principal stress is conducted. The distribution of max. principal stress is shown on Fig. 9. It can be seen from Fig. 4.9(a) and 4.9(b) that the right braided reinforcement of SBCHS is subjected to pressure, while the left braided reinforcement is under tension during compression. This observation reveals the underlying cause of the stress fluctuation difference of right braided reinforcement and left braided reinforcement. In addition, the right and left braided reinforcements have 12 fiber bundles, it is cumbersome to describe max. principal stress distribution of all 12 fiber bundles. So, two fiber bundles of right and left braided reinforcements are extracted respectively, max. principal stress and direction of two fiber bundles are shown in Fig. 4.9(c) and 4.9(d). The two fiber bundles corresponding to the F_{in} and F_{ex} at a 180° section are called right (in) and right (ex) in the right braided reinforcement and left (in) and left (ex) in the left braided reinforcement. The pressure of right (in) and right (ex) in the right braiding reinforcement gradually decreases from the internal radial zone to the external radial zone, and gradually increases from the external radial zone to the internal radial zone, while the tension of left (in) and left (ex) in the left braiding reinforcement gradually increases from the internal radial zone to the external radial zone, and gradually decreases from the external radial zone to the internal radial zone. In terms of carbon fiber, tension has a huger impact on damage than pressure. Therefore, initial damage will first occur in the external radial zone of left braided reinforcement.

To further reveal the max. principal stress distribution law, the helical angle-max. principal stress curves of left(in), left(ex), right(in) and right(ex) in SBCHS15° and SBCHS30° within 0 ~ 360° are shown in Fig. 4.10. To compare structure characteristics, the max. principal of spring wire periphery of UCHS55% is extracted as shown in Fig. 4.10(a). The results show that ave. of UCHS55%, SBCHS15° and SBCHS30° are 0, indicating that the pressure and tension are balanced. Moreover, there are two aspects to illustrate the reason why the spring performance of SBCHS can significantly increase. On the one hand, max. principal stress range of UCHS55%, SBCHS15° and SBCHS30° are -224.3 MPa~216.7 MPa, -1974.7 MPa ~1412.4 MPa, and -1705.9 MPa ~1411.8 MPa within 0~360° respectively. The positive and negative extreme values of max. principal stress of UCHS55% are only 15.4% and 13.2% of SBCHS30° respectively. On the other hand, both Fl and Fr of UCHS55% fluctuate in positive and negative values range, indicating that the single fiber bundle at the corresponding position is subjected to both pressure and tension within 0-360° simultaneously, reducing the contribution rate of some fiber bundles. In contrast, the single fiber bundle in SBCHS is only subjected to pressure or tension, which makes its performance relatively stable. The fluctuation range of right(in) and right(ex) in SBCHS15° and SBCHS30° is larger than that of left(in) and left(ex), which accurately verifies that the stress of the left braided reinforcement is more uniform than that of the right braided reinforcement within 0~360°. Besides, the results show that the angle-max. principal stress curve of each fiber bundle in the braided reinforcement is a fluctuating cyclic curve. It can be seen from Fig. 4.10(b) and 4.10(c) that the difference between adjacent peak values of right braided reinforcements in SBCHS15° and SBCHS30° is fixed 166.7° and 77.6° respectively, and the difference between adjacent peak values of right (in) and right (ex) in SBCHS15° and SBCHS30° is half of 166.7° and 77.6°, that is ,83.3° and 38.8° respectively. Therefore, it can be deduced that the peak values of max. principal stress of 12 fiber bundles in the right braided reinforcement are distributed evenly, and the phase difference of any two adjacent fiber bundles in right braided reinforcements of SBCHS15° and SBCHS30° is 13.9° and 6.5° respectively. By contrast, the peak values of max. principal stresses of 12 fiber bundles in the left braided reinforcement shown in Fig. 4.10(b) and 4.10(c) are also distributed evenly, but the phase difference of any two adjacent fiber bundles in SBCHS15° and

SBCHS30° is 14.6° and 8.24° respectively, which is larger than that of the right braided reinforcement, reflecting the steady bearing capacity of the left braided reinforcement.

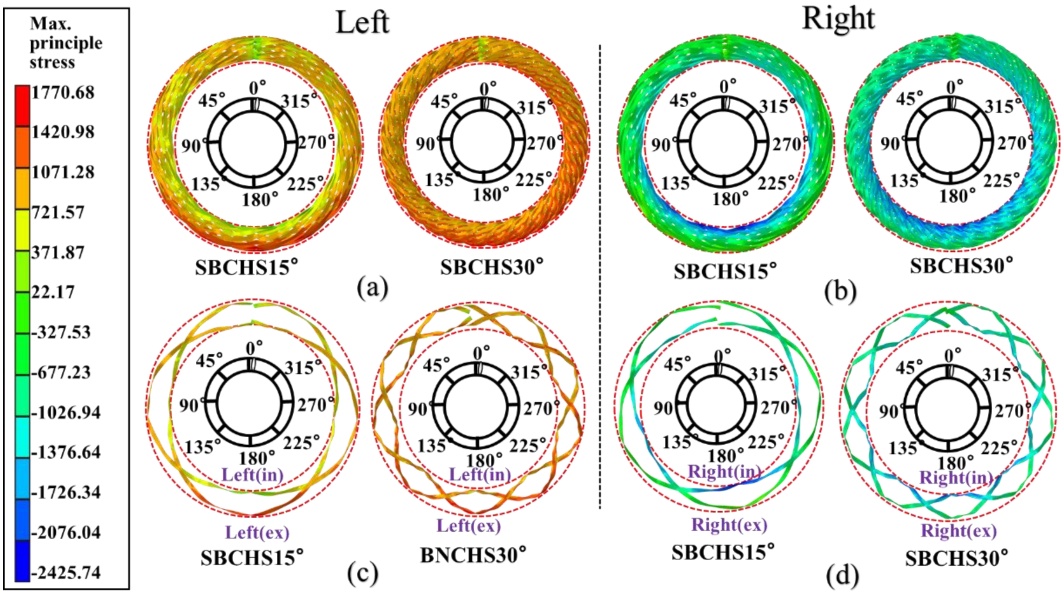

Fig. 4.9 Max. principal stress distribution under compression within 0~360° of (a) right braided reinforcement, (b) left braided reinforcement, (c) two fiber bundles of right braided reinforcements corresponding to the F_{in} and F_{ex} at 180° section and (d) two fiber bundles of left braided reinforcements corresponding to the F_{in} and F_{ex} at a 180° section.

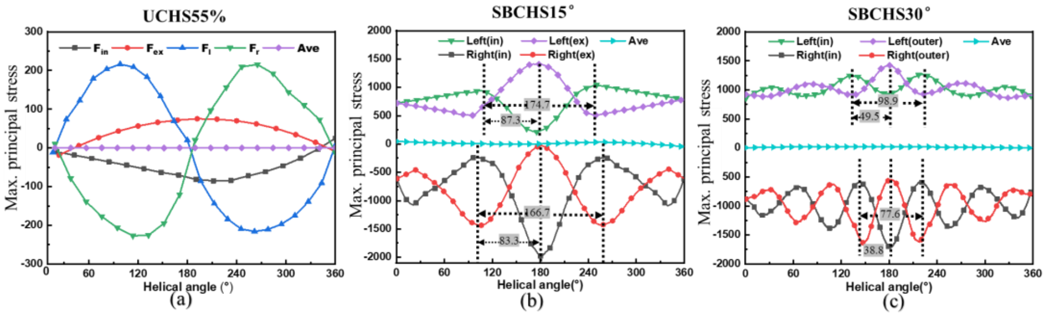

Fig. 4.10 Helical angle-max. principal stress curves under compression of (a) UCHS55%, (b) SBCHS15° and (c) SBCHS30°.

4.3.4 Advanced analysis of SBCHSs

Helical springs are often subjected to prolonged compression during work, making resilience a crucial performance factor. Steel springs with the same dimension as SBCHSs had been customized to compare the resilience of SBCHSs. The heights of both SBCHSs and steel springs were recorded at 0 h, 24 h, 48 h, 72 h and 96 h under a full loading and unloading experiment, as illustrated in Fig. 4.11. The changing trend of the heights of the four springs is similar, that is, the spring heights reduce with loading time as illustrated in Fig. 4.11(a). It is obviously shown that the deformation of steel springs is smallest among four springs. The deformation of UCHS55%, SBCHS15° and SBCHS30° increases in turn during loading. This is because the force capacity of SBCHS increases with increasing braid angle of reinforcement, so that the force acting on UCHS55%, SBCHS15° and SBCHS30° increases in turn, which causes the damage degree of resin in UCHS55%, SBCHS15° and SBCHS30° sequentially increases. The heights of SBCHSs increase gradually and that of steel spring keeps constant during unloading as shown in Fig. 4.11(b), indicating permanent creep happens in the steel spring. The resilience (the ratio of the final height after unloading for 96 h to the initial height of the springs) of UCHS55%, SBCHS15°, SBCHS30° and steel spring are 99.7%, 98.7%, 98.2% and 96.1% respectively, which proves SBCHSs have a better resilience than that of steel spring. It is worth mentioning that the resilience speed (the ratio of the height difference to the corresponding test time difference) of SBCHSs in the first 24 h is largest, this is mainly because SBCHSs have large energy storage, which made them more likely to return to their original state immediately after unloading.

Most of the research about optimization of helical springs is mainly focusing on spring constant and mass. Therefore, it’s meaningful to propose the specific spring stiffness that is spring constantly divided by mass. The comparison of specific spring stiffness of SBCHSs and steel springs in this study and previous research is shown in Table 4.2. The results show that the specific spring stiffness of SBCHSs increases with an increasing braid angle. In addition, it is worth mentioning that the specific spring stiffness of SBCHS30° is higher than that of CHSs reported in reference [24], also higher than that of the steel spring in this study and in reference [25-26]. The result means that SBCHSs can have a lighter mass than steel spring with the same spring constant, indicating SBCHSs have more advantages than steel springs in reducing carbon emissions industry field.

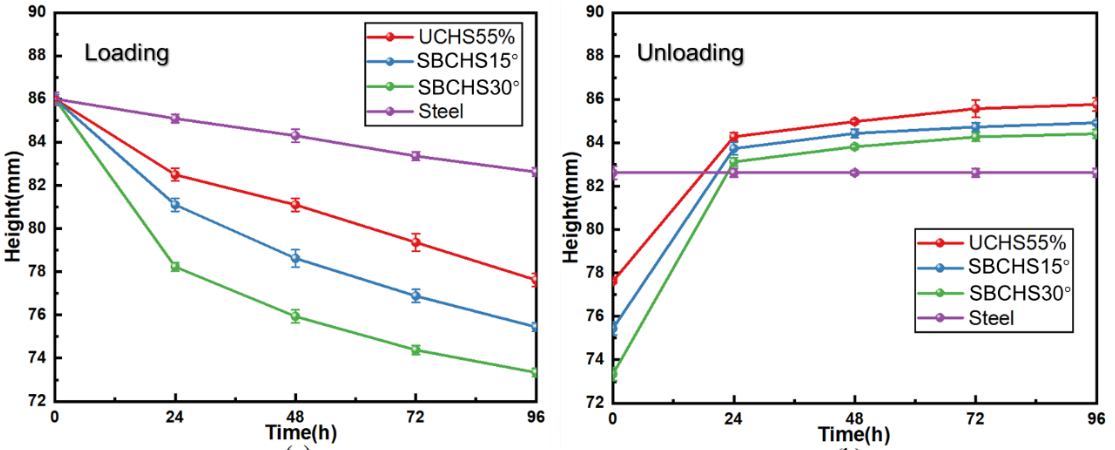

(a) (b)

Fig. 4.11 (a) The height change of UCHS55%, SBCHS15°, SBCHS30° and steel with time during loading experiment, and (b) the heighe change of UCHS55%, SBCHS15°, SBCHS30° and steel with time during unloading experiment.

Table 4.2: The comparison of specific spring stiffness of UCHS55%, SBCHS15°, SBCHS30° and steel springs

Samples	Material	Spring constant (N/mm)	Mass (Kg)	Specific spring stiffness
UCHS55%	Carbon-epoxy	6.47	0.289	22.39
SBCHS15°	Carbon-epoxy	13.29	0.302	44.01
SBCHS30°	Carbon-epoxy	17.56	0.309	56.83
CHSs(Manjunatha & Budan, 2012)	Carbon-epoxy	6.36	0.20	31.80
Steel	Steel	77.63	2.71	28.64
Steel (Clifton Stephen et al., 2019)	Steel	12.56	1.39	9.04
Steel(Zebdi et al., 2009)	Steel	126	8.525	14.78

4.4 Summary

A type of SBCHS which can greatly improve the spring constant is proposed according to the force analysis of helical spring. The advantages of SBCHS are elucidated through a combination of experimental and simulation methods. It is observed that the spring constant of SBCHS increases with an increase in the braid angle. Furthermore, FEM analysis reveals the internal mechanism responsible for this improvement. The mises stress of the braided reinforcement of SBCHS significantly surpasses that of the resin and reinforcement core, underscoring the crucial load-bearing role of the peripheral braided reinforcement in SBCHS. The fluctuation amplitude of the braided reinforcement of SBCHS30° is less than that of SBCHS15° across 0~360°, indicating improved force uniformity with a higher braid angle. Max. principal stress of left and right braided reinforcements is further analyzed to detect the initial damage. The results show that initial damage will first occur in the external radial zone of left braided reinforcement. The fluctuation range and cycle of max. Principal stress of left and right braided reinforcements illustrate that the right braided reinforcement of SBCHS is subjected to pressure, while the left braided reinforcement is under tension during compression. Moreover, stress distribution in the left braided reinforcement appears to be more uniform than that of the right braided reinforcement across the 0-360°. The resilience of SBCHSs is excellent than that of steel spring which permanent creep will happened during long time loading. Furthermore, SBCHSs can achieve a lighter mass than steel spring with the same spring constant, indicating its advantage in reducing carbon emissions in the industrial field.

5. IMPACT PERFORMANCE ANALYSIS OF MBLs-CHS

This chapter comes from a submitted manuscript of “Chen L, Xing W, Chong J, et al. Analysing Impact Characteristics of Composite Helical Springs with Multi-braided Layers Based on Virtual Fiber Model[J]. Composites Communications, 2025: 102255.”.

In engineering practice, the impact problem refers to the transient changes in force, displacement, velocity and acceleration of a system when it is subjected to transient excitation. The dynamic response process of impact is very complex. It has the characteristics of short duration, fast energy release, transfer and conversion rate, non-periodicity and transient motion of the system under impact. Due to the propagation of stress waves, short-term response, elastic-plastic deformation of local areas and local damage during the collision process, it has special dynamic characteristics. Although the vibration of the system impact response is very short, the corresponding deformation speed of the impacted end of the spring is very large, and the deformation and stress distribution are very uneven. When the deformation speed of the spring is higher than the allowable transmission speed of stress in the spring wire, stress concentration occurs, and the maximum stress caused by it can easily damage the spring wire. Therefore, for these springs subjected to impact loads, in addition to impact tests to verify the performance of the springs in bearing impact loads, stress and deformation should also be performed.

Currently, lots of research focus on the improvement of static performance of CHSs(Chen, Chong, et al., 2024; Chen et al., 2021; Chen, Wu, et al., 2022; Chen, Xing, et al., 2022). Dynamic performance study of CHSs is seriously insufficient, especially for impact. In practice, working environment with impact occur more frequently, neglecting impact performance could lead to serious consequences. In addition, Finite element analysis (FEA) is one of the most popular methods to reveal the dynamic response. However, the existing FEM about helical spring impact is all about steel helical spring that is easy to construct 3D model (Clauberg et al., 2012; Clauberg & Huber, 2013; Huber et al., 2010; Kim & David, 1990; Lee, 2004). In term of MBLs-CHS, the reinforcement structure that composed of fibre yarns could be complex extremely. Notably, during the preparation of reinforcement structure, certain fiber may migrate into the spaces of neighbouring layers, resulting in a nesting phenomenon (Chen & Chou, 2000; Lomov et al., 2003; Sevenois et al., 2016). Although the micro-computed-tomography (micro-CT) is a powerful tool for characterizing the reinforcement structure such as slippage, distortion and shift of positions of fibre yarns (Garcea et al., 2018; Schell et al., 2006), to construct the 3D model according to the micro-CT images is significantly time-consuming and low- efficiency. Therefore, it is necessary to establish the precise 3D model of reinforcement structure to accurately understand the characteristics of CHSs during operation. As a matter of fact, fibre structures in the yarns have a significant effect on the calculation results, such as stress and strain fields. The traditional mesoscale FEA was insufficient to accurately simulate the complex deformation of the reinforcement structure(Pourdeyhimi et al., 2019), especially for the deformation at the yarn contact cross-sections(N Isart et al., 2015; Natina Isart et al., 2015). Wang *et al.* (Wang & Sun, 2001; Zhou et al., 2004) proposed the digital-element method to simulate textile processes and reproduce the geometry structures of the preforms in the quasi-fibre scale. In this model, the yarns are modelled as an assembly of virtual fibres and each virtual fibre is represented by a pin connected digital element chain. The deformations and contact interactions of the yarns were simulated. Following the Wang's approach, Durville *et al.* and Mahadik *et al.* investigated the mechanical behaviours of two-dimensional and three-dimensional reinforcement structure using the concept of virtual fibre models (VFM) (Durville et al., 2018; Mahadik & Hallett, 2010). The concept of VFM was increasingly being used to model the forming process and deformation of different prefabricated parts and their composites (Liu et al., 2019; Xie et al., 2018). Drach *et al.* (Drach et al., 2014) developed a procedure to construct meso-scale FEA of textile composites using the point cloud data extracted from the VFM. The yarn shapes derived by this method are consistent with the actual fibre preforms.

Based on preceding description, it is evident that there is a notable research gap in the study of impact dynamics of CHSs. Based on the static performance analysis, the optimal braided angle has been determined, that is 30°. Therefore, the braided angle of all MBLs-CHS in impact research is 30°. Furthermore, MBLs-CHS are selected as the research object in the dynamic impact performance analysis, including (SBCHS, DBCHS and TBCHS). The fiber content of SBCHS, DBCHS and TBCHS is 56.77%, 57.26% and 58.19%, respectively, which was measured and calculated according to ASTM D3171. The weight of SBCHS, DBCHS and TBCHS is 0.309Kg, 0.337Kg and 0.361Kg, respectively, they are 57.32%, 53.45% and 50.13% less than the customized 0.724Kg metal spring of the same size. The impact performance is researched by combining experiments and simulation. To improve simulation accuracy, this study introduces the virtual fibre model (VFM) that is efficient in simulating the deformation of flexible yarn cross-sections to ensure the structure reliability of multi-braided layers (MBLs). The accuracy of the simulation is validated through comparison with experimental results, and VFM adeptly captures the interaction among fibres, along with the non-linear features of MBLs-CHS under impact. Subsequently, the impact stress and motion responses of MBLs-CHS based on simulation result are analysed to compare the impact performance of MBLs-CHS.

5.1 Impact test

The impact test is shown on Fig. 5.1. Impact fixture is first designed and customized according to spring geometric size of spring before impact test, because previous fixture can't meet the spring structure. Designed impact fixtures include impact plate and fixture. The radius of the impact plate is 100 mm, thickness is 8mm, the mass is 8 kg that is matching with DIT302E Instrumented drop hammer impact tester. The length of fixture is 300 mm, and the width is 125 mm. Sample area and fixture hole are designed in fixture to fix the bottom of the spring by using wire. The impact performance of the four types of springs is tested according to ASTM D7136 standard (Daelemans et al., 2018). And the impact energy, impact height and impact speed can be converted to each other based on the known mass of the impact head according to the kinetic energy formula. Five different impact energy levels (i.e., 5, 10, 20, 40, and 60 J) were selected for each configuration of MBLs-CHS. In addition, the deformation process of each MBLs-CHS under impact was monitored with a high-speed camera standing in front of the MBLs-CHS.

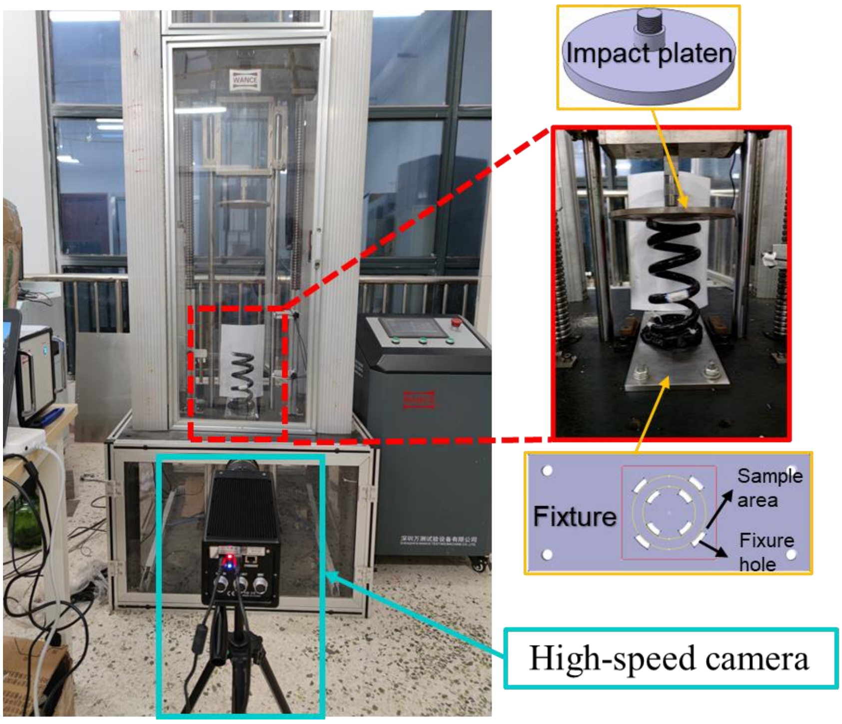

Fig. 5.1 Impact test of MBLs-CHS

5.2 Impact simulation

5.2.1 VFM of MBLs

The solid model of MBLs with precise 3D geometry was first constructed to effectively represent its structure that consist of unidirectional reinforcement core and surrounding braided reinforcement, as shown in Fig.5.2 (a). Although solid model can represent accurately the 3D geometry and braided rules of MBLs. The stiffness characteristic of solid model is not consistent with the flexible characteristic of MBLs made of fibre yarns, which illustrates the extremely complex fibre interaction in MBLs caused by the shifting and nesting between the layers during braiding. It can be seen from the cross section of solid MBLs model of SBCHS, DBCHS and TBCHS that there are extensive gaps among fibre yarns and between adjacent braided layers, highlighting the presence of defects in the solid model. VFM is introduced as an effective solution to address the limitations of the direct numerical solid model. In this specific approach, a virtual yarn is created by assembling a few virtual fibres (VFs). To predict correctly mechanical behaviour of the yarn, it is critical to ensure that the total cross-sectional area of the virtual yarn matches that of the physical yarn. Moreover, for sufficient accuracy, the quantity of VF per yarn cannot be too small. However, it should not be set too large as the corresponding computational cost and simulation time would significantly increase but with minor improvements in accuracy (El Said et al., 2014). According to this trade-off, it is preferred to use a relatively small number of VFs per yarn by increasing their diameter (Green et al., 2014). In the construction of MBLs, three different VF quantities (i.e., 30, 60, and 120 per yarn) are compared to determine an optimal value. Fig. 5.2 (b) displays the three corresponding regular layout profiles of VFs, maintaining the yarn cross-sectional areas the same. MBLs are obtained by replacing the yarn using an assembled virtual fibre structure, as depicted in Fig. 5.2 (c). In this work, chain of structural beam elements that have both tensile and bending stiffness are adopted to mesh VFs. The beam element length also determines the smoothness of VFM and the accuracy of simulation results. Reducing the beam element length improves modelling accuracy but also escalates computational costs. Therefore, a trade-off between modelling precision and computational efficiency needs to be considered based on the chosen beam element length. In this study, VFM of MBLs are generated using three different beam element lengths: 0.1 mm, 0.2 mm, and 0.4 mm.

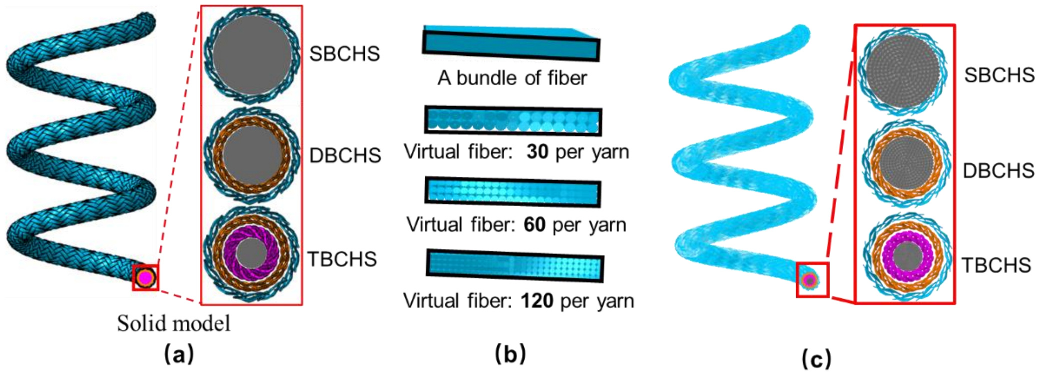

Fig. 5.2 (a) solid models of MBLs in SBCHS, DBCHS and TBCHS, (b) transformation from solid model to VFM and (c) a VFM of MBLs.

5.2.2 FEA modelling of MBLs-CHSs

Impact simulation is conducted in two sequential steps, first involving the shrinkage of MBLs, and second the impact on MBLs-CHS. The former aims to ensure the reliability of the VFM of MBLs, while the latter simulates the dynamic response of the MBLs-CHS under impact.

5.2.2.1 Shrinkage modelling of MBLs

During the manufacturing of MBLs, yarn cross-sections tend to undergo large deformations, leading to the shift from the loose arrangement state to a more crowded one. However, the straightforward application of VFM to MBLs fails to capture this actual geometric change, resulting in an inaccurate representation of the reinforcement structure. To mitigate the issue, a large quantity of discrete compression platens is introduced to prescribe pressure onto the MBLs. As a result, yarns are tensioned in the axial direction, of which fibres will realign and spread out. The shrinkage procedure is illustrated as follows using DBCHS as an example. Since MBLs consist of two reinforcements: unidirectional reinforcement core and surrounding braided reinforcement, two separate sets of discrete local coordinate systems are defined for them (Fig. 5.3 (a) and (b)). In each coordinate system, '1' denotes the axial direction of the fibre, and '2' and '3' represent the transverse directions. Material properties of all parts are listed in Table 4.1. The material properties of braided reinforcement and reinforcement core in DBCHS were assigned carbon fibre properties. Compression platens are set as rigid bodies neglecting their deformations. An explicit dynamic analysis with a duration of 0.5 s is employed to simulate the shrinkage process of MBLs with the geometric nonlinearity option activated in ABAQUS to support large displacements. Contact between VFs is defined using the built-in general contact algorithm, and a friction coefficient of $\mu = 0.3$ (Xie et al., 2018) is specified for the relative sliding of contacting fibre surfaces. To simplify the model, the reinforcement core is completely fixed to be free of motions (Fig. 5.3 (c)). Subsequently, 120 compression platens, surrounding the outermost surface of MBLs, are enforced to move simultaneously toward the reinforcement core, as depicted in Fig. 5.3 (d).

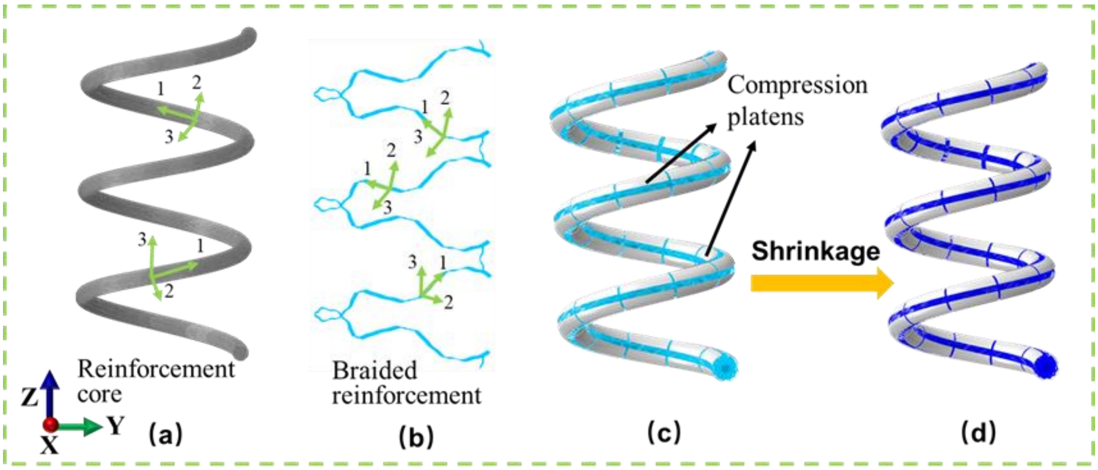

Fig. 5.3 Finite element shrinkage modeling of MBLs. (a) The discrete local coordinate system of reinforcement core, (b) The discrete local coordinate system of braided reinforcement, (c) boundary condition, and (d) shrinkage progress of MBLs.

After the shrinkage step, a more realistic microstructure with improved yarn cross-sectional shape is reconstructed for MBLs. As shown in Fig. 5.4, the apparent cross-section diameter of the MBLs under lateral compression is decreased gradually from 18 mm to 14 mm (Fig. 5.4 (a) - 6(d)) and finally reaches a steady value (Fig. 5.4 (e)). Furthermore, it is observed that the final cross-sectional shape (marked by red dashed lines in Fig. 5.4 (e)) of the virtual yarn fairly agrees with the physical yarn observed using optical microscopy (Fig. 5.4 (f))(Xun et al., 2022), which justifies the importance of introducing the shrinkage step to reproduce the real complex structure of MBLs before the impact modelling is performed.

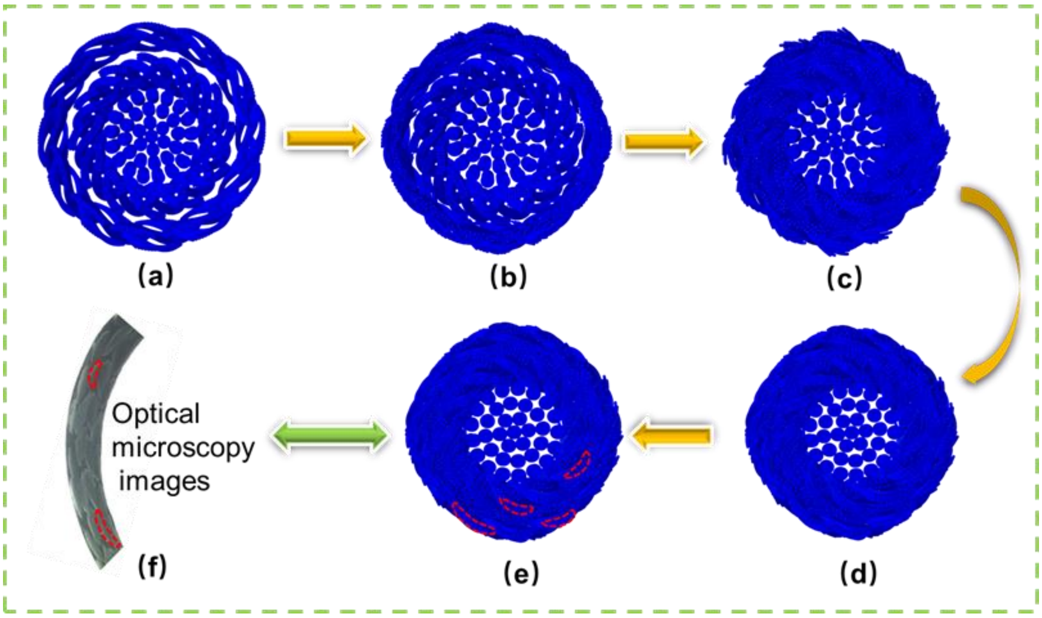

Fig. 5.4 The cross-section of MBLs at (a) 0.1s, (b) 0.2 s, (c) 0.3 s, (d) 0.4 s, (e) 0.5 s shrinkage time and (f) optical microscopy image.

5.2.2.2 Impact modelling of MBLs-CHS

The impact modelling of MBLs-CHS combines the numerical techniques of the VFM and embedded elements (EEs). VFs are ‘embedded’ in the host matrix. The matrix in this approach occupies full volume of the model, including the volume “under” the reinforcement, which created volume redundancy. In the models, the VFs and matrix are simultaneously situated in the MBLs, leading to the volume redundancy of MBLs and increase the global stiffness of the model. To rectify volume redundancy, a stiffness correction for the VFs is implemented by subtracting the matrix stiffness from the fibre stiffness(Tabatabaei & Lomov, 2015). In the model, the constructed 3D model of MBLs-CHS was then imported into ABAQUS for the impact simulation. The impactor was established to impact the MBLs-CHS. The weight of impactor in simulation is same with in experiment that is 8 Kg. Distributed Cartesian local coordinate system, as depicted in Fig. 5.5 (a), was established, with '*1*' representing the axial direction of the fibre, and '*2*' and '*3*' representing the transverse directions. The braided yarns and core yarn that form braided reinforcement and reinforcement core were considered unidirectional fibre/resin composites, due to the fact of resin wetting between individual filaments. The space filling factor of yarns was set to 75% (Wu et al., 2023). The yarn was modelled as elastic-plastic material with transverse isotropy. The elastic engineering constants of yarns can be obtained by bridging matrix and yarn compliance matrix (Li et al., 2009) based on the properties of the component materials that are shown in Table 4.1. The explicit dynamic analysis step was selected, and geometric nonlinearity option was activated to account for large deformation effects. The element types for MBLs, resin and impactor were C3D8R, C3D10M and R3D4, respectively, as shown in Fig. 5.5 (b). The bottom end of the MBLs-CHS was completely fixed and the impactor was initially placed at the top centre of the MBLs-CHS with no gap relative to its highest point (Fig. 5.5 (c)). A mass of 8.0 kg and finite initial velocity were assigned to a reference point coupled to the impactor to impact the MBLs-CHS. In addition, to ensure the simulation accuracy, a mesh sensitivity study was conducted at first by comparing models discretised with different element sizes. Finally, the average element sizes of MBLs, resin and impactor were specified as 0.5, 1 and 1 mm, respectively.

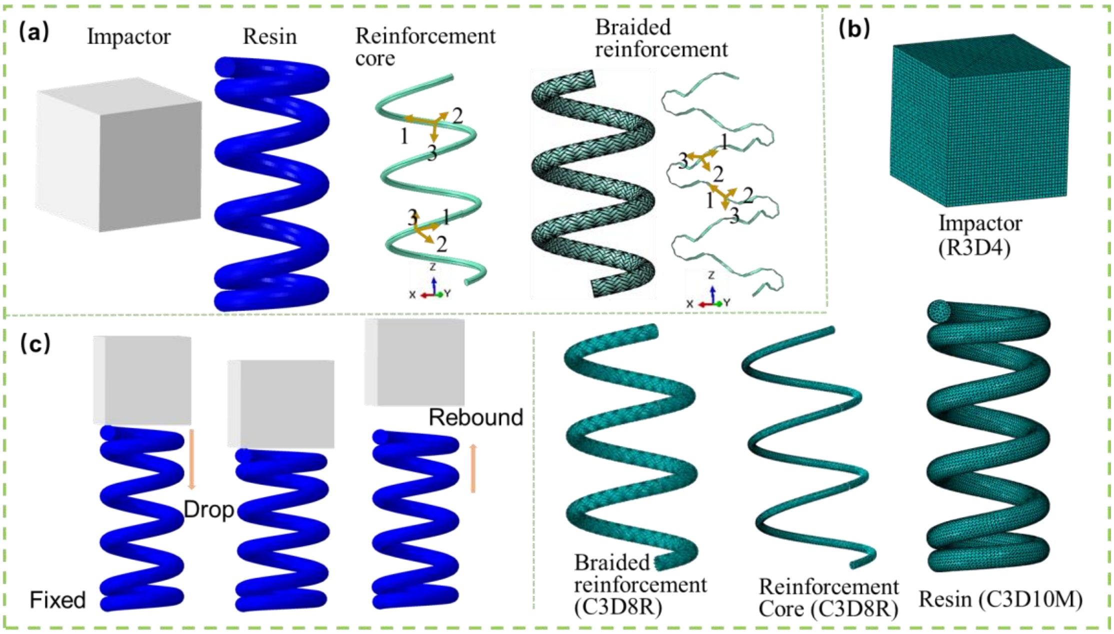

Fig. 5.5 Finite element modelling of MBLs-CHS. (a) The discrete local coordinate system, (b) meshing and (c) impact boundary condition.

5. 3. Results and discussion

5. 3.1 Experimental analysis of impact

To help with the interpretation of experimental results, certain variables of interest D_{max}, F_{max}, E_a, E_r, and E_i need to be defined, as marked in Fig. 5.6 (a) and (b). D_{max} and F_{max} represent the maximum deflection reached during impact, and the maximum impact force. The latter three energy variables E_a, E_r, and E_i represent absorbed, rebound, and impact energy, respectively. The results are shown in Fig. 5.6, in terms of deflection- impact force, time-energy curves, and values of interested variables of SBCHS, DBCHS, and TBCHS subjected to varying levels of E_i. In Fig. 5.6 (a), it is evident that the (dynamic) stiffness of the MBLs-CHS increases with the number of braided layers, as the average slope of the rising curve shows an increasing trend at all impact energy levels. This increased resistance to deformation can also be suggested by comparing D_{max} which decreases as adding more braided layers (Fig. 5.6 (c)). Moreover, the F_{max} of TBCHS improves by 51.3% to 78.3% compared to that of SBCHS when E_i varies from 5 to 60 J, respectively. Fig. 5.6 (b) illustrates that the energy first increases and then declines with increasing impact time, indicating that the E_i is initially absorbed and subsequently released by MBLs-CHS over time. The rate of absorption and release of E_i increases sequentially for SBCHS, DBCHS, and TBCHS. The energy of TBCHS consistently reaches the limit of E_i first and then rapidly releases. The final E_a and the time of E_a decrease sequentially for SBCHS, DBCHS, and TBCHS under the same E_i. The sum of E_a and E_r is equal to E_i, which means that E_r will increase with decreasing E_a at the same E_i. The final E_r increases sequentially for SBCHS, DBCHS, and TBCHS at the same E_i. Fig. 5.6 (c) clearly shows that E_r of TBCHS can improve by 2.6%, 17.5%, 21.1%, 25.3% and 34.1% than SBCHS under 5, 10, 20, 40 and 60 J, respectively, which represents TBCHS can obtain more outstanding E_r than SBCHS with increasing E_i. In terms of rebound component, especially for helical spring, larger E_r represents more outstanding performance under impact. Therefore, TBCHS have the best impact performance among MBLs-CHS.

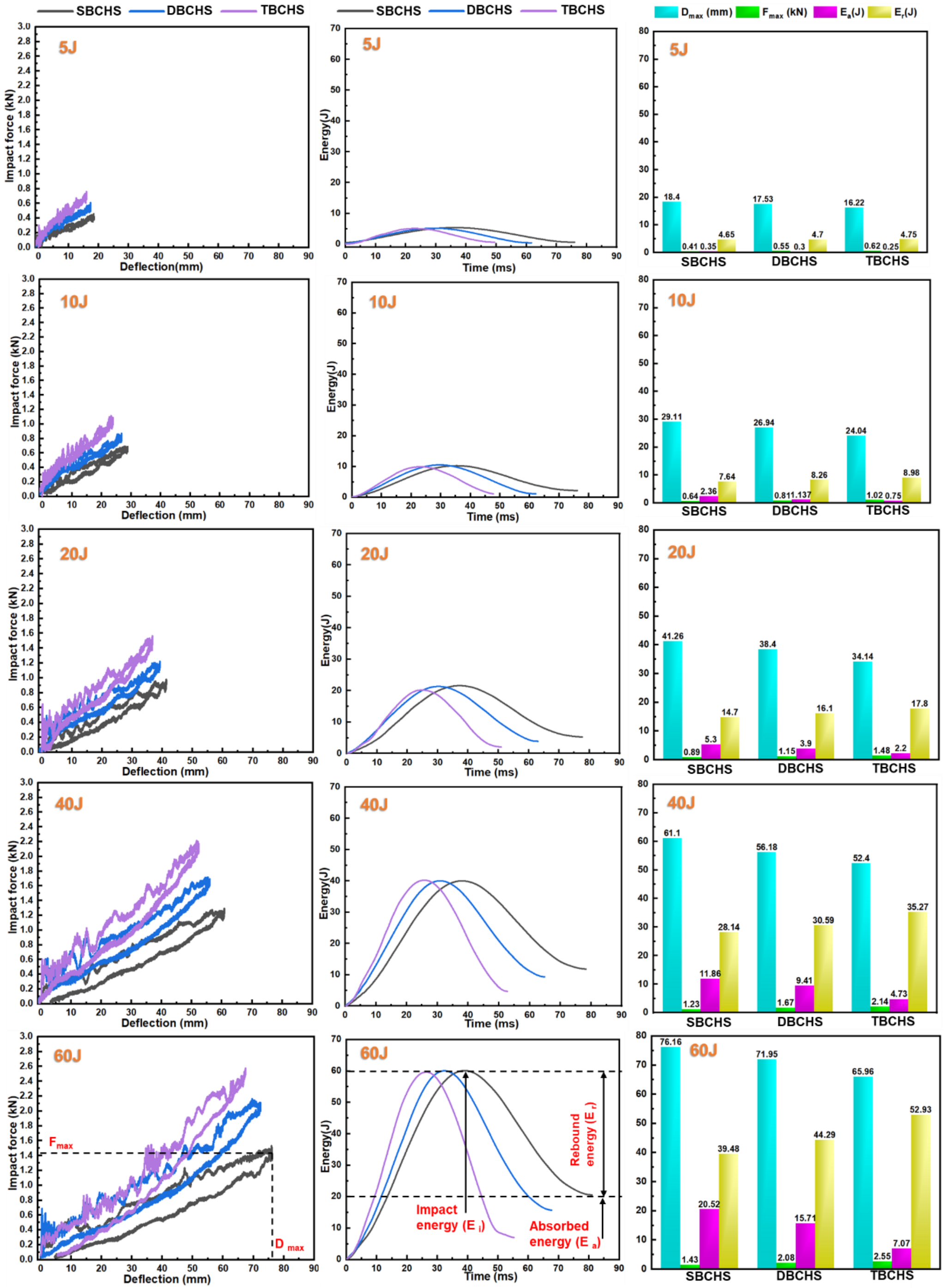

(a) (b) (c)

Fig. 5.6 (a) Deflection-impact force curves, (b) time-energy curves and (c) D_{max}, F_{max}, E_a and E_r of SBCHS, DBCHS and TBCHS under 5 J, 10 J, 20 J, 40 J and 60 J.

5. 3.2 Verification of impact model

The impact of VF quantity and mesh size as two critical governing parameters on the numerical results is examined specifically focusing on the DBCHS under 60 J impact. In Fig. 5.7 (a), the cross-sections of MBLs in DBCHS after shrinkage are presented for the VFM with 30, 60 and 120 VFs per yarn. Fig. 5.7 (b) indicate that the impact force response of DBCHS is affected by both the VF quantity and mesh size. The results show that the accuracy of the impact simulation can also be adjusted by changing the mesh size and VF quantity. While larger VF quantities and smaller mesh sizes can enhance the slope of the displacement-load curve, they also increase computational load and simulation time. Thus, finding the optimal compromise between simulation time and accuracy is crucial. The mesh size-time curves of DBCHS under impact simulation based on different numbers of VFs (30, 60, and 120 per yarn) are plotted in Fig. 5.7 (c). It is evident that simulation time significantly decreases with increasing mesh size at the same VF quantity but increases with increasing VF quantity at the same mesh size. The simulation run time of DBCHS with 120 VFs per yarn is shown to increase significantly compared to those for 30 and 60 VFs per yarn. Three circles marked in Fig. 5.7 (c) represent the run times corresponding to the maximum agreement with experimental measurements based on the results in Fig. 5.7 (b). The model with the 60 VFs per yarn and mesh size of 0.2 mm, costs 18.8% and 50.4% less time amounts, compared to those for other two combinations. It appears to perform the best in terms of the balance of run time and accuracy. Therefore, the VF quantity per yarn 60, and approximate mesh size 0.2 mm will be adopted in all the subsequent impact simulations.

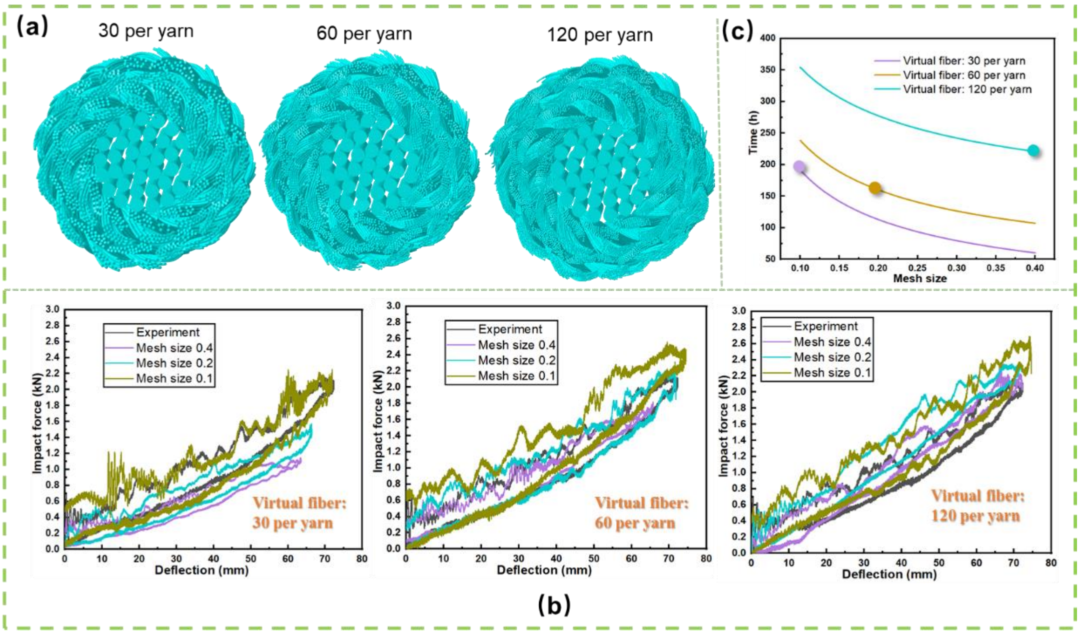

Fig. 5.7 (a) The cross-section of MBLs of DBCHS after shrinking based on different VF quantities of 30, 60, and 120 per yarn (b) the deflection-impact force curves of DBCHS after impact simulation based on different mesh sizes of 0.4, 0.2 and 0.1 mm with 30, 60 and 120 VFs per yarn and (c) the mesh size-time curves of DBCHS with 30, 60 and 120 VFs per yarn for impact simulations.

5. 3.3 Equivalent stress evolution of MBLs-CHSs under impact

The previous experimental section has revealed that the discrepancy in the dynamic response among SBCHS, DBCHS and TBCHS is the largest when the E_i is 60 J. To clearly understand the effect of the braided reinforcement, the impact simulation is performed for SBCHS, DBCHS and TBCHS subjected to the E_i of 60 J. Five discrete impact contact moments in the deformation, corresponding to t = 0, 8.5, 16.9, 25.5 and 33.9 ms, are selected to compare simulated current deformed configurations (Fig. 5.8 b) with camera captured images (Fig. 5.8 a) for DBCHS. It is noticed that the deformed spring shapes appear similar at each time moment during the impact. Obviously, the deformation of the DBCHS is geometrically non-linear. And coils of DBCHS are deformation evenly without coils of contact which can prohibit the plastic failure caused by contact.

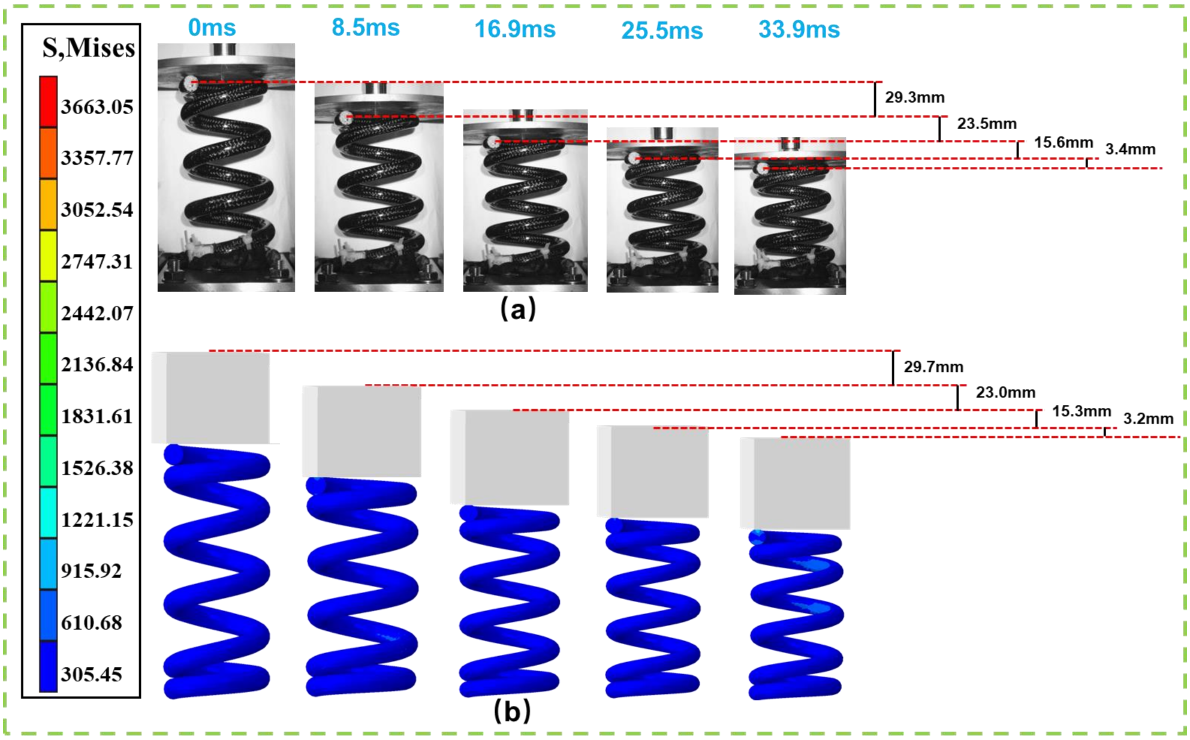

Fig. 5.8 (a) Deformation process of DBCHS recorded by high-speed camera during impact experiment and (b) deformation process of DBCHS during impact simulation.

To study the dynamic effect during impact, the equivalent stress distribution in terms of von Mises stress is examined. SBCHS, DBCHS and TBCHS have 1, 2, and 3 braided layers respectively that are abbreviated as braid 1, braid 2 and braid 3 form outer to inner of spring wire. By comparing results in Fig. 5.9 (a) and (b), the braided layer is more stressed than the resin and reinforcement core, which reveals the importance of braided layer. Von Mises stress of the braided layer of SBCHS, DBCHS and TBCHS based on VFM (Fig. 5.9 (a)) reveals that there exists stress wave during impact. The stress wave shows cycle characteristic, which transit from up to down and then resilience from down to up. Moreover, not only the Von Mises stress of braid 1 of SBCHS, DBCHS and TBCHS but also that of braid 2 of DBCHS and TBCHS is just slightly increase sequentially, indicating the force-bearing contribution of the corresponding braided layer in SBCHS, DBCHS and TBCHS are similar. The impact response difference is mainly caused by the added braided layer. The Von Mises stress of braided layers of DBCHS and TBCHS just declines slightly from outer to inner of spring wire, which illustrated that the force transmission among braided reinforcement layers is excellent. This is because there are lots of braided nodes in braided reinforcement that can lead to strong friction among braided reinforcement layers to outstanding transmission of force. In addition, as seen in Fig. 5.9, the times used for completing one obvious stress wave cycle in the braided layers of SBCHS, DBCHS and TBCHS decline in turn, estimated as 8.2, 6.3 and 4.0 ms respectively, that is caused by their stiffness difference.

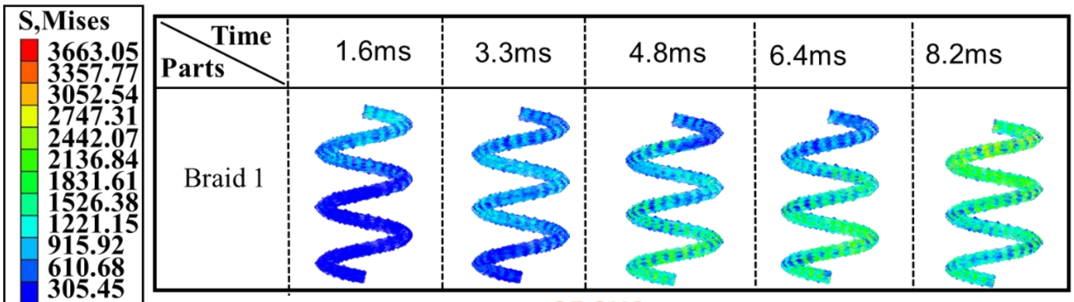

SBCHS

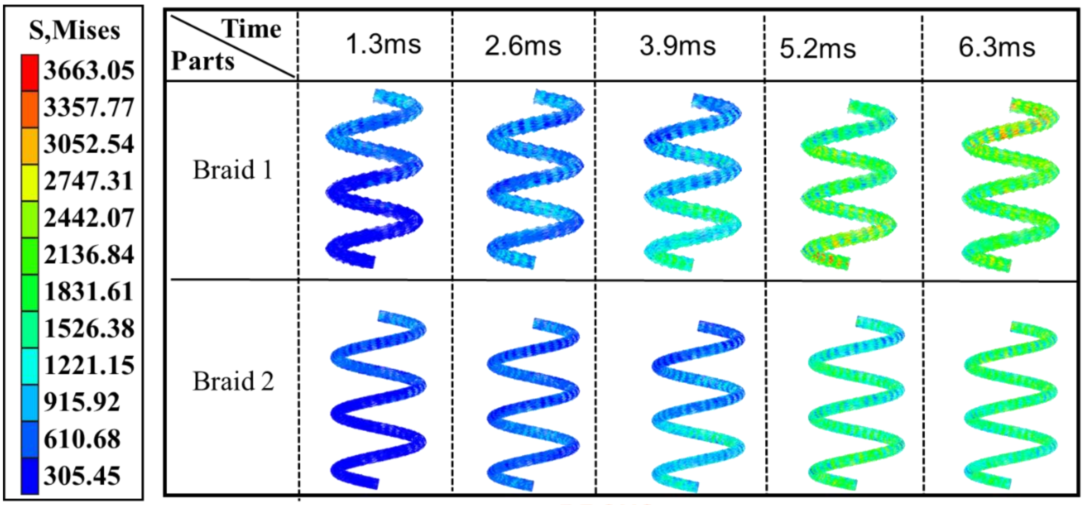

DBCHS

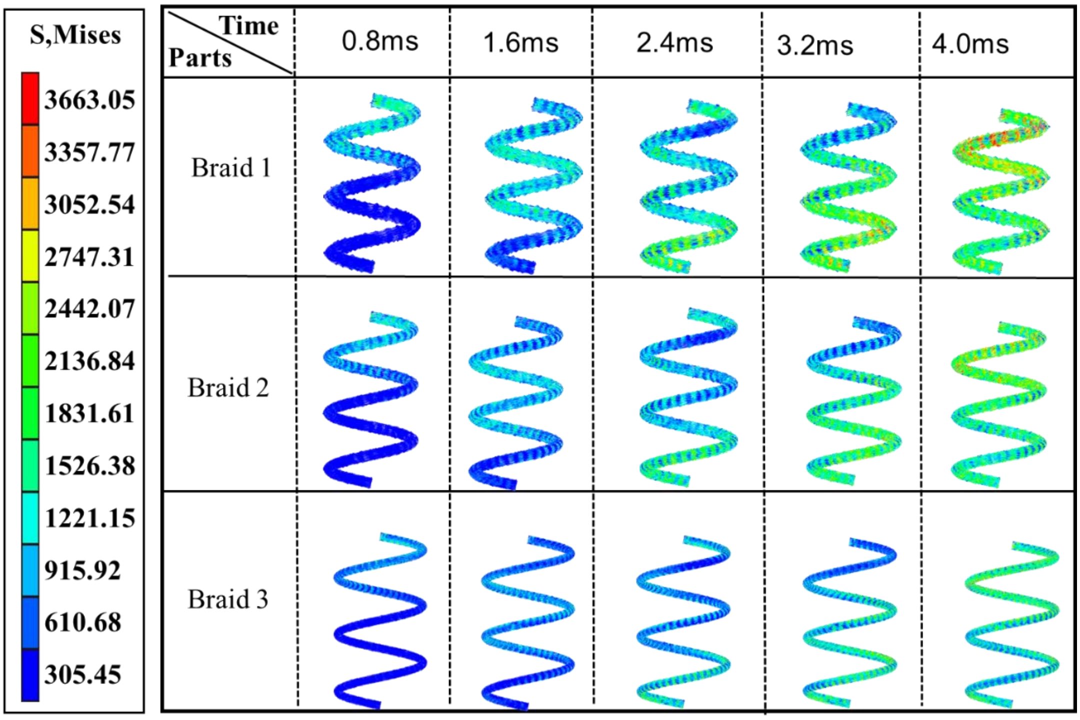

TBCHS

(a)

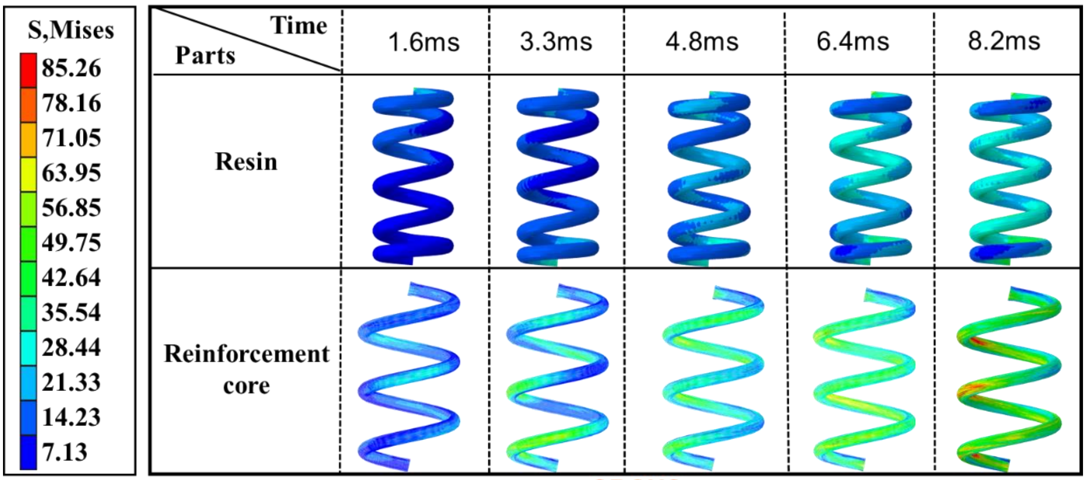

SBCHS

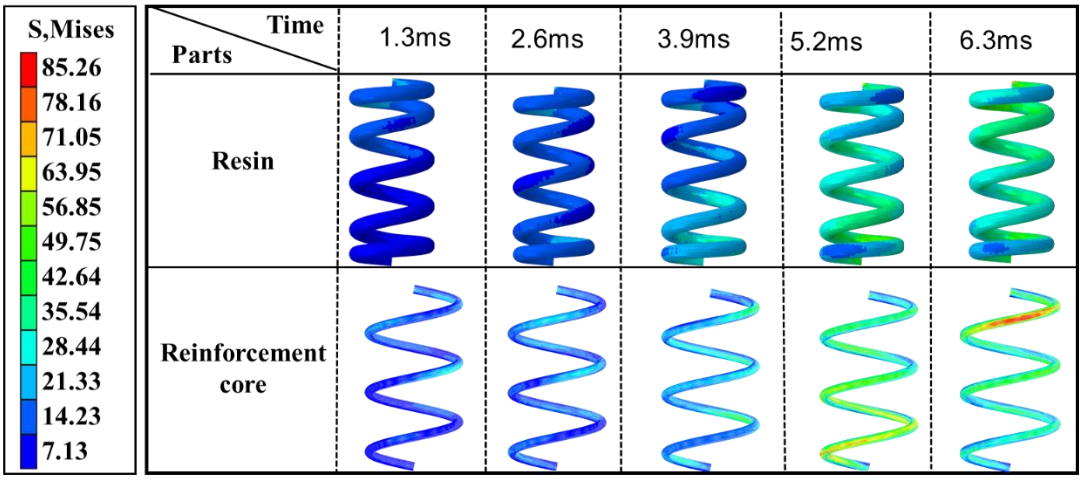

DBCHS

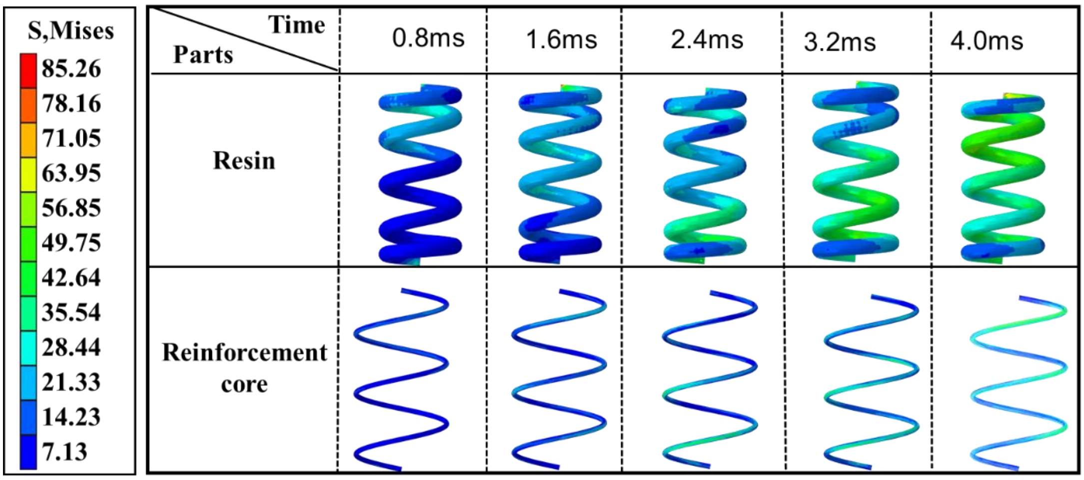

TBCHS

(b)

Fig. 5.9 (a) Von Mises stress of braided reinforcement of SBCHS, DBCHS and TBCHS during impact

5.3.4 Kinematics of MBLs-CHSs under impact

Apart from stress waves, the motion state of each coil in MBLs-CHS is an important parameter for evaluating impact performance. To thoroughly analyse the kinematics of each coil in a MBLs-CHS, the coils have been defined, as illustrated in Fig. 5.10 (a). There are five coils in a MBLs-CHS denoted as Coil 1-5 from bottom to top. Time-displacement response curves for each coil in SBCHS, DBCHS and TBCHS are extracted from simulation results. Moreover, such curves for coil 5 in SBCHS, DBCHS, and TBCHS are collected from impact experiments, as shown in Fig. 5.10 (b). The time- velocity response curves are derived by differentiating displacement with respect to time, as depicted in Fig. 5.10 (c). The numerical time- displacement and time-velocity response curves for coil 5 in SBCHS, DBCHS, and TBCHS are in good agreement with experimental results, validating the impact model. It is evident that the displacement and velocity of each coil display non-linear characteristics due to the significant influence of inertia on deformation of MBLs-CHS during impact. The displacement of each coil in MBLs-CHS increases during the fall of the impactor, whereas it decreases during the rebound. D_{max} of the same coil in SBCHS, DBCHS, and TBCHS declines in sequence at the same E_i, demonstrating that the structural stiffness of SBCHS, DBCHS, and TBCHS increases with the number of braided layers. The velocity of coils gradually declines during the fall, then gradually increases during the rebound, due to continued energy conversion. When impact reaches D_{max}, all kinetic energy converts to elastic energy stored in the MBLs-CHS. Subsequently, the elastic energy converts back to kinetic energy, causing the velocity of all coils to gradually rise during the rebound. The velocity of each coil in MBLs-CHS consistently decreases from Coil 5 to 1 and then increases from Coil 1 to 5, as Coil 1 is the furthest from the impactor. Furthermore, the average rates of change of the velocity of each coil differ in the three MBLs-CHSs, which is associated with the varying number of braided layers.

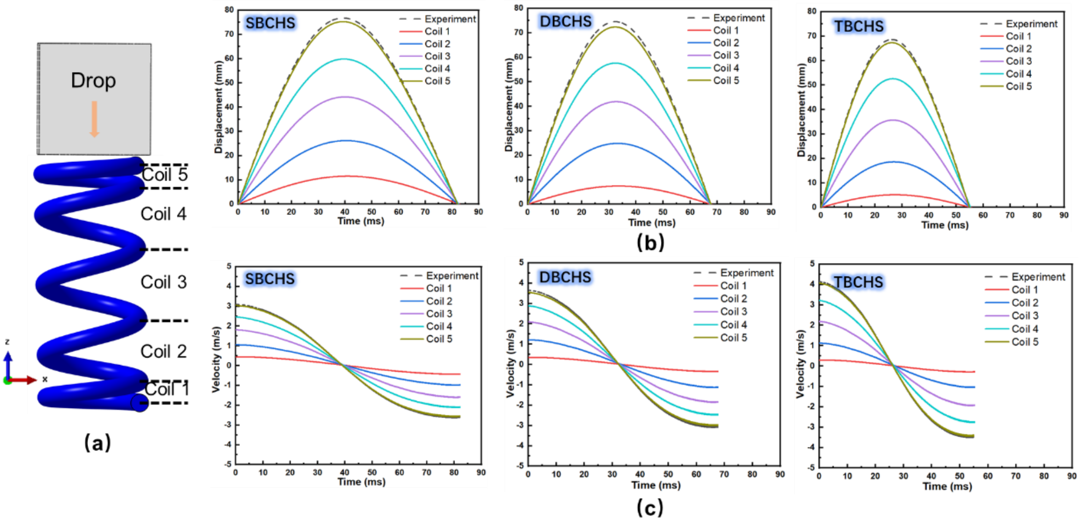

Fig. 5.10 (a) Schematic diagram of coils in MBLs-CHS, (b) time-displacement response curves and (c) time-velocity response curves of each coil in SBCHS, DBCHS and TBCHS.

Impact mitigation refers to the capability of transferring and attenuating E_i. The study of impact mitigation has been a key topic in various industries (Xu et al., 2011; Yuan et al., 2017). Most existing research on impact protection primarily focuses on energy absorption through large, irrecoverable deformations. However, concerning MBLs-CHS, the need to address repeated dynamic loading becomes crucial. Therefore, there is a pressing demand for an exceptional mechanical mitigation system with maximum energy recovery efficiency. The mitigation rate (η), defined as the ratio between maximum output velocity and maximum input velocity, serves as an indicator to evaluate impact mitigation performance (Hu et al., 2019). The η values for SBCHS, DBCHS and TBCHS can be calculated based on Fig. 5.10 (c) and are plotted in Fig. 5.11. The results demonstrate a sequential reduction in η for SBCHS, DBCHS, and TBCHS, with values of 0.146, 0.098, and 0.069, respectively. A smaller η indicates a more excellent impact mitigation capability(Hu et al., 2019). Therefore, the impact mitigation ability of TBCHS improves by 111.6% and 42.0% compared to SBCHS and DBCHS, respectively, highlighting that TBCHS can rapidly restore a stable state after a transient impact.

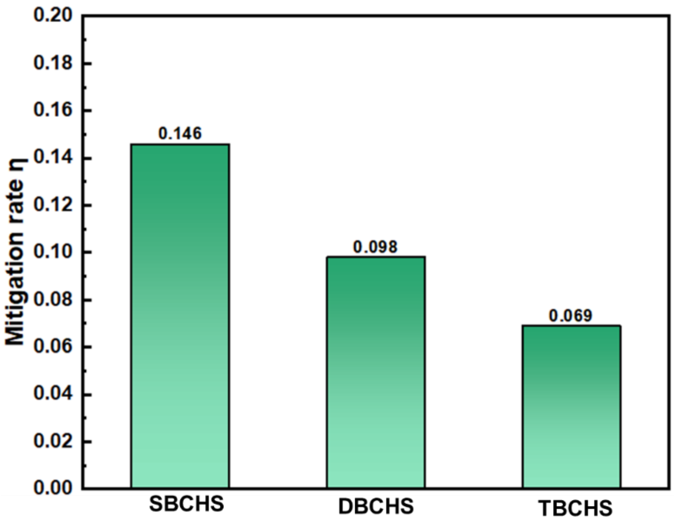

Fig. 5.11 The mitigation rate η of SBCHS, DBCHS and TBCHS under impact.

5.4 Summary

The impact performance of MBLs-CHS is investigated by integrating the VFM, which can eliminate shortages of the corresponding solid model, enabling precise simulation of the impact of MBLs-CHS. The accuracy of VFM is verified by comparing the cross-section of physical yarns and impact test results. Subsequently, the impact performance of MBLs-CHS is elucidated through a combination of experimental and simulation methods. It is observed that the impact performance, including resistance to deformation, F_{max}, and E_r, improves sequentially for SBCHS, DBCHS, and TBCHS. The resistance to deformation, F_{max}, and E_r of TBCHS are enhanced by up to 5.1%, 78.3%, and 34.1%, respectively, compared to SBCHS. Furthermore, the internal mechanism significantly enhancing the impact performance of TBCHS is revealed using VFM. The stress in braid 1 of SBCHS, DBCHS, and TBCHS, as well as braid 2 of DBCHS and TBCHS, increases only slightly in sequence, indicating that the impact response difference in MBLs-CHS is mainly caused by the additional braided reinforcement layer. Moreover, VFM can further precisely reveal stress and motion response of MBLs-CHS during impact. There exists stress wave with cycle characteristic, transitioning from upward to downward motion and then resiliently returning from downward to upward motion. Displacement and velocity of each coil display non-linear characteristics due to the significant influence of inertia on deformation of MBLs-CHS during impact. Finally, the impact mitigation ability is evaluated based on velocity response. The results demonstrate that the impact mitigation ability of TBCHS improves by 111.6% and 42.0% compared to SBCHS and

DBCHS, respectively, illustrating that TBCHS can rapidly restore stable state after instantaneous impact.

6. STIFFNESS DEGRADATION ANALYSIS OF MBLs-CHS UNDER IMPACT

This chapter comes from the publication of “Ling Chen, Wenjin Xing, Joel Chong, Qian Jiang, Yiwei Ouyang, Liwei Wu, Youhong Tang. Understanding stiffness degradation of composite helical springs with multi-braided layers under impact. Composites Part A: Applied Science and Manufacturing, 2024:108327” with format modifications.

Helical springs play a vital role in various vibration systems, such as vibrating screens in mining machinery industries (Dong et al., 2013; Makinde et al., 2015), suspension system of tricycles (Pawar & Desale, 2018), mountain bikes (J. Frank, 2020), motorcycles (Bhatia & Bergaley, 2014), automobiles and trains (Chen, Xing, et al., 2022; B. Choi & B. Choi, 2015). Due to high load bearing working conditions and long-term cyclic loads, stiffness degradation of the spring occurs during service, compromising spring structural performance. Therefore, it is essential to develop stiffness degradation monitoring techniques (David West et al., 2017; Goyal & Pabla, 2016), which can not only inform timely warning at the initial stage of failure, but also provide informative details regarding spring remaining service life prior to reaching the stage of repair and even replacement. Researchers have explored various methods concerning the detection of spring stiffness degradation. Krot *et al.* (Krot & Zimroz, 2019) proposed an approach for monitoring the stiffness degradation of the spring system in vibrating screens based on the trajectories on the phase space plots, which are affected by nonlinear characteristics of the dynamic system. Their results illustrated that linear model response on a phase space plot is considered as a healthy condition of springs. Peng *et al.* (Peng et al., 2016) developed a diagnostic method for identifying the stiffness of helical damping springs with a free response. The asymmetric dynamic model of the vibrating screen with helical damping spring was established, and the vibration differential equation was derived to explain stiffness degradation. Rodriguez *et al.* (Rodriguez et al., 2016) developed a two-dimensional, three-degree-of-freedom nonlinear model considering angular motion and damping, which allowed for the prediction of the behaviour of helical springs in vibrating screen when there was reduction in spring stiffness, and they used this model to determine a limit on spring stiffness degradation before the separation efficiency was affected. The above method based on multiple spring system is complex. Moreover, using traditional non-destructive testing methods of diagnostics (ultra-sound, magnetic etc.) is difficult to implement for stiffness degradation due to complicated helical geometry, configuration of CHSs (Krot & Zimroz, 2019). Therefore, although the optimised CHSs show great potentials to replace the metal spring, there is still a gap of understanding and monitoring stiffness degradation, which significantly limits their development and applications. To overcome the problems, this study proposes a time domain detection method of stiffness degradation for single CHS in suspension and verifies it through finite element simulation. Finally, the formulas have been fitted to predict stiffness degradation in real time of MBLs-CHS under impact. Understanding stiffness degradation and developing suitable damage detection method for composite helical springs (CHSs) are important for their application and further development.

6.1 Compression and impact test of MBLs-CHS

Impact samples and tests method in this chapter is same with section 5.1 of chapter 5. The compression before and after impact of SBCHS, DBCHS and TBCHS was tested. The test method is same with section 4.1.1 of chapter 4.

6.2 Material damage evolution in simulation

The simulation process is same with chapter 5. The only different is that the impact simulation in this chapter add the plastic parameters.

Since the material behaviour of all the components was assumed elastoplastic, the damage initiation of yarns and resin was defined based on ductile and shear damage criteria (Pan et al., 2016; Zhou et al., 2015). For the ductile damage criterion, the equivalent plastic strain is a function of the stress triaxiality:

$$\bar{\varepsilon}_{\mathrm{D}}^{\mathrm{pl}}\left(\eta,\bar{\varepsilon}^{\mathrm{pl}}\right)=\frac{\varepsilon_{\mathrm{D}}^{+}\sinh\left[\mathrm{k}_0\left(\eta^{-}-\eta\right)\right]+\varepsilon_{\mathrm{D}}^{-}\sinh\left[\mathrm{k}_0\left(\eta-\eta^{+}\right)\right]}{\sinh\left[\mathrm{k}_0\left(\eta^{-}-\eta^{+}\right)\right]} \tag{6.1}$$

where $\varepsilon_{\mathrm{D}}^{+}$ and $\varepsilon_{\mathrm{D}}^{-}$ are the equivalent plastic strain at the ductile damage initiation for uniaxial tensile and compressive deformation, respectively. $\eta^{+}=\eta^{-}=1/3$ is the stress triaxiality in uniaxial tensile and compressive deformation state. k_0 is a material parameter. The damage initiation criterion is met when the following condition is fulfilled.

$$\omega_{\mathrm{D}}=\int\frac{\mathrm{d}\bar{\varepsilon}^{\mathrm{pl}}}{\bar{\varepsilon}_{\mathrm{D}}^{\mathrm{pl}}\left(\eta,\bar{\varepsilon}^{\mathrm{pl}}\right)}=1 \tag{6.2}$$

where ω_{D} is a state variable that increases monotonically with plastic deformation accumulation. At each step increment during the analysis, the increase in ω_{D} is computed:

$$\omega_{\mathrm{D}}=\int\frac{\mathrm{d}\bar{\varepsilon}^{\mathrm{pl}}}{\bar{\varepsilon}_{\mathrm{D}}^{\mathrm{pl}}\left(\eta,\bar{\varepsilon}^{\mathrm{pl}}\right)}\geq 0 \tag{6.3}$$

For shear damage criterion, the equivalent plastic strain is a function of the shear stress ratio:

$$\bar{\varepsilon}_{\mathrm{s}}^{\mathrm{pl}}\left(\tau_{\mathrm{s}},\bar{\varepsilon}^{\mathrm{pl}}\right)=\frac{\varepsilon_{\mathrm{s}}^{+}\sinh\left[f_{\mathrm{s}}\left(\tau_{\mathrm{s}}-\tau_{\mathrm{s}}^{-}\right)\right]+\varepsilon_{\mathrm{s}}^{-}\sinh\left[f_{\mathrm{s}}\left(\tau_{\mathrm{s}}^{+}-\eta_{\mathrm{s}}\right)\right]}{\sinh\left[f_{\mathrm{s}}\left(\tau_{\mathrm{s}}^{+}-\tau_{\mathrm{s}}^{-}\right)\right]} \tag{6.4}$$

where $\tau_{\mathrm{s}}=\left(1-k_{\mathrm{s}}\eta\right)/\phi$, $\phi=\tau_{\max}/\sigma_{\mathrm{eq}}$, $\varepsilon_{\mathrm{s}}^{+}$ and $\varepsilon_{\mathrm{s}}^{-}$ correspond to the equivalent plastic strain at shear damage initiation for uniaxial tensile and compressive deformation, respectively. τ_{s}^{+} and τ_{s}^{-} correspond to the values of τ_{s} when $\eta=\eta^{-}$ and $\eta=\eta^{+}$, respectively. f_{s} is a material parameter.

The damage initiates when the following condition is satisfied:

$$\omega_{\mathrm{s}}=\int\frac{\mathrm{d}\bar{\varepsilon}^{\mathrm{pl}}}{\bar{\varepsilon}_{\mathrm{s}}^{\mathrm{pl}}\left(\tau_{\mathrm{s}},\dot{\bar{\varepsilon}}^{\mathrm{pl}}\right)}=1 \tag{6.5}$$

where ω_{s} is a state variable that increases monotonically with plastic deformation. At each increment during the analysis, the increase in ω_{s} is computed as follows:

$$\omega_{\mathrm{s}}=\int\frac{\mathrm{d}\bar{\varepsilon}^{\mathrm{pl}}}{\bar{\varepsilon}_{\mathrm{s}}^{\mathrm{pl}}\left(\tau_{\mathrm{s}},\dot{\bar{\varepsilon}}^{\mathrm{pl}}\right)}\geq 0 \tag{6.6}$$

After damage is initiated, the degradation of the material stiffness complies with the specified damage evolution response. For ductile and shear failure, the energy dissipation for a degrading element during the damage evolution is progressive until effective fracture energy is reached implying the element completely fails and is then eliminated from the computation (Li et al., 2017). The reduction of stiffness is characterized with a scalar damage variable *d*. At any given pseudo-time during the analysis, the stress follows the isotropic damage mechanics:

$$\sigma=(1-d)\bar{\sigma} \tag{6.7}$$

where $\bar{\sigma}$ is the effective stress tensor corresponding to the undamaged material, and *d* is the damage variable, ranging from 0 to 1. As *d* rises to 1, the element loses the stress bearing ability and becomes inactive from the mesh. The increase of damage variable follows the formula (Li et al., 2017):

$$d_{\mathrm{i}}=\frac{L\bar{\varepsilon}^{\mathrm{pl}}}{\bar{u}_{\mathrm{f}}^{\mathrm{pl}}}=\frac{\bar{u}^{\mathrm{pl}}}{\bar{u}_{\mathrm{f}}^{\mathrm{pl}}} \tag{6.8}$$

$$\bar{u}_{\mathrm{f}}^{\mathrm{pl}}=\frac{2G_{\mathrm{f}}}{\sigma_{\mathrm{y0}}} \tag{6.9}$$

where *L* is the length of the element, $\bar{u}_{\mathrm{f}}^{\mathrm{pl}}$ is the effective plastic deformation, G_{f} is the effective fracture energy of per unit area, σ_{y0} is the yield stress value at initial damage. When $d=1$, namely $\bar{u}^{\mathrm{pl}}=\bar{u}_{\mathrm{f}}^{\mathrm{pl}}$. G_{f} is linked to the plastic deformation, following the relation.

$$G_\mathrm{f} = \int_{\bar{\varepsilon}_0^\mathrm{pl}}^{\bar{\varepsilon}_\mathrm{f}^\mathrm{pl}} L\sigma_\mathrm{y} \mathrm{d}\bar{\varepsilon}^\mathrm{pl} = \int_{\bar{\varepsilon}_0^\mathrm{pl}}^{\bar{\varepsilon}_\mathrm{f}^\mathrm{pl}} \sigma_\mathrm{y} \mathrm{d}\bar{u}^\mathrm{pl} \tag{6.10}$$

where $\bar{\varepsilon}_0^\mathrm{pl}$ and σ_y is equivalent plastic strain and yield stress at the onset of damage.

6.3 Result and discussion

6.3.1 Experimental analysis and simulation verification of impact

The impact characteristics of SBCHS, DBCHS and TBCHS under five levels of impact energy are shown in Fig. 6.1. To interpret experimental results, E_a, E_r, and E_i denoting absorbed, rebound, and impact energy have been defined, respectively, as marked in Fig. 6.1 (a). Time-energy profiles of SBCHS, DBCHS, and TBCHS under varying levels of E_i (Fig. 6.1 (a)) illustrate that the energy increases, peaks and then declines with increasing impact time, indicating that E_i is initially absorbed and subsequently released by MBLs-CHS over time. The kinetic energy of the impactor begins to transfer to the MBLs-CHS once the contact is established. When E_i reaches its maximum value, the velocity of the impactor vanishes. After that, E_r of the MBLs-CHS drives the impactor to rebound. Part of the kinetic energy is transformed into E_r of the MBLs-CHS, and the remaining part is E_a. With the increase of impact energy, the MBLs-CHS absorbs more energy. From the comparison, it is obvious that the E_a values of SBCHS, DBCHS and TBCHS decline in sequence at the same E_i. The E_a of TBCHS decline by 56.52%, 60.12%, 67.22%, 72.35% and 79.93% than that of SBCHS under five levels of E_i, respectively. In terms of helical springs, smaller E_a represents more outstanding performance under impact. Therefore, the TBCHS composition has the best impact performance among all tested ones.

To further analyse how the E_a is dissipated by MBLs-CHS, the time-impact force profiles are collected and shown in Fig. 6.1 (b). Time-impact forces of springs with various compositions under all E_i present consistent strong oscillation and the greater impact force leads to more serious oscillation, which is attributed to the vibration of MBLs-CHS under different E_i during impact. There is no massive drop in time-impact force curves, indicative of less critical damage events such as distributed resin cracking and fibre or yarn debonding (Kazemi et al., 2021). Moreover, the curves show that the increase rate of the impact force first slows down gradually and decrease rate of the impact force then raises rapidly with increasing time, which means that the impactor is about to impact and rebound. Clearly, the maximum impact force increases with rising E_i, which means a higher damage evolution likelihood. Also, the maximum impact force of SBCHS, DBCHS, and TBCHS is enhanced in turn under the same E_i, indicating the impact performance of TBCHS is the most excellent among them.

It is known that high stress levels cause matrix cracking. To illustrate the structural composition effect on damage, the damage patterns of SBCHS, DBCHS and TBCHS under 60 J are shown in Fig. 6.1 (c). The results obviously indicate that altering the number of braided layers does not affect the severe damage location, as it always occurs at the inner side surface of impact end of MBLs-CHS. Moreover, the apparent damage amounts of SBCHS, DBCHS and TBCHS decline sequentially, highlighting the positive effect of increasing braided layers. However, the complex helical structure of MBLs-CHS makes it difficult to quantify damage by adopting common NDT. To quantify the damage severity and reveal the damage mechanism, the impact cases of SBCHS, DBCHS, and TBCHS under five types of E_i have been simulated. It can be observed form Fig. 6.1 (b) that the simulation curves show less oscillations as expected, and the trend of time-impact force from each simulation is matched well with that of experiment. Overall, the present FE model is proven reliable to analyse the damage evolution of MBLs-CHS under impact.

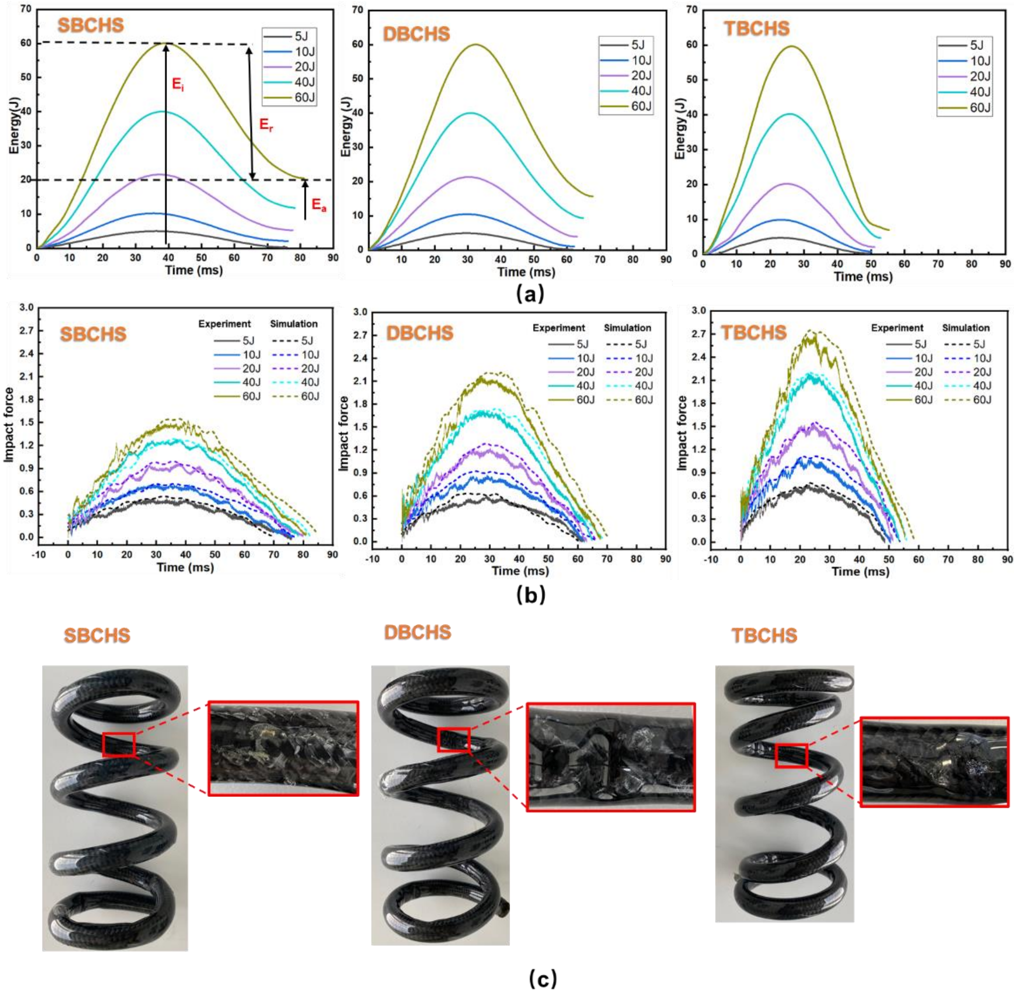

Fig. 6.1 (a) Time-energy curves and (b) time-impact force curves of SBCHS, DBCHS and TBCHS under different impact energy and (c) the damage morphology of SBCHS, DBCHS and TBCHS under 60 J impaction.

6.3.2 Von Mises stress distribution under impact

High-fidelity simulation results can identify damage locations and damage severity. The von Mises equivalent stress in MBLs-CHS can help to indicate the most critical regions where damage is about to take place during the spring impact. For the sake of analysis, the equivalent stress distributions of braided reinforcement, reinforcement core and resin at maximum impact displacement are extracted separately, as shown in Fig 6.2. It can be seen form Fig. 6.2 (a)- 6.2 (c) that the equivalent stress of all three components concentrates on inner side surface, and thus the damage likely occurs there. The only resin damage in MBLs-CHS during impact is certified again. This is because the maximum equivalent stresses in braided reinforcement and reinforcement core are 3795.32 MPa and 325.79 MPa, being below the tensile strength of corresponding material, indicating damage would not happen in these two components. However, the maximum equivalent stress in resin is 65.72 MPa that is beyond the tensile strength of resin, indicating damage onset. To facilitate comparison among structural compositions, the maximum equivalent stress in each component of SBCHS, DBCHS and TBCHS is extracted, as shown in Fig. 6.3. It is obvious that the maximum equivalent stress levels of braided reinforcement, reinforcement core and resin in each type MBLs-CHS increase gradually with raising E_i, which can interpret the damage amount increases with increasing E_i. The maximum equivalent stresses in the resins of SBCHS, DBCHS and TBCHS under the same E_i decrease in turn, which means the damage decreases in turn. On the other hand, the equivalent stress of braided reinforcement far exceeds reinforcement core and resin, indicating braided reinforcement has a huge contribution to the impact performance of MBLs-CHS. When MBLs-CHS is subjected to impact loading, braided reinforcement should be the main load-carrying structure. More braided layers represent higher carrying capability. Meanwhile, the maximum equivalent stress levels of reinforcement core and resin of SBCHS, DBCHS and TBCHS under the same E_i decrease in turn, illustrating more braided layers can greatly reduce the stress in the other two components, which appears to interpret why the damage of resin becomes less with increasing braided layers. On the other hand, the deformation declines sequentially for SBCHS, DBCHS and TBCHS under the same Ei, the change law can be observed clearly form Fig. 6.2, indicating the strain reduces in turn. Therefore, the damage severity of resin declines sequentially for SBCHS, DBCHS and TBCHS.

In addition, due to failed element will be remove during impact simulation, the element removal rate of resin can explain the damage severity to some extent. The element removal rate of SBCHS, DBCHS and TBCHS under different E_i has been shown in Fig. 6.4. The result elucidates that the change speed of element removal rate of SBCHS, DBCHS and TBCHS decline with increasing E_i. The element removal rate of resin of SBCHS, DBCHS and TBCHS decline sequentially at same E_i. TBCHS decline by 36.5%, 38.6%, 42.5%, 48.3% and 51.3% under five types of E_i than SBCHS respectively.

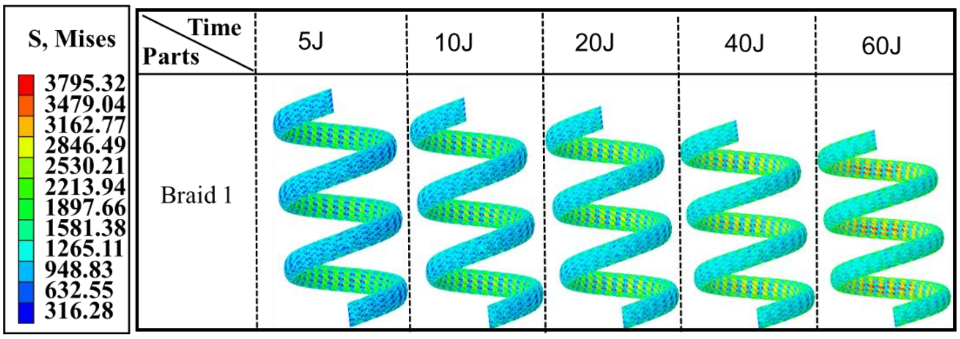

SBCHS

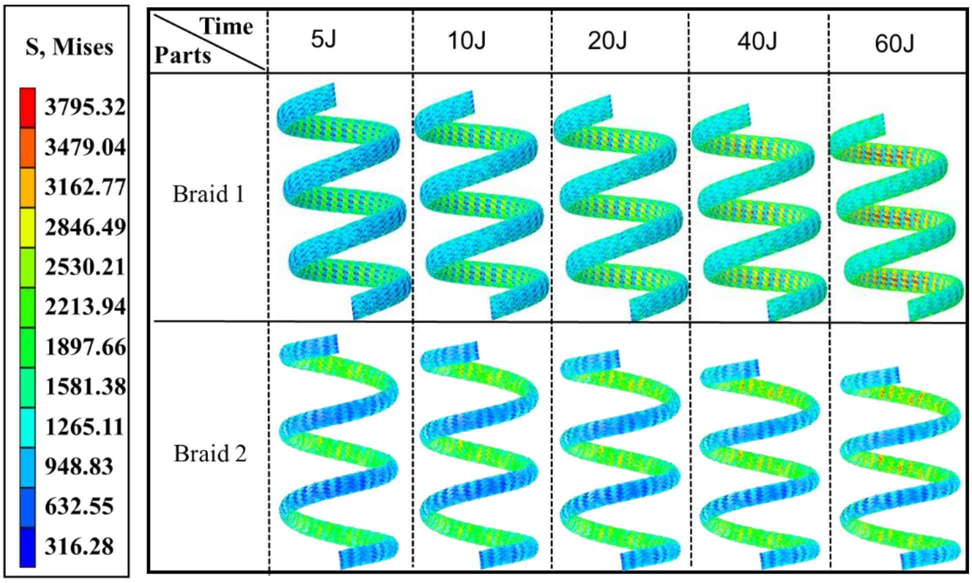

DBCHS

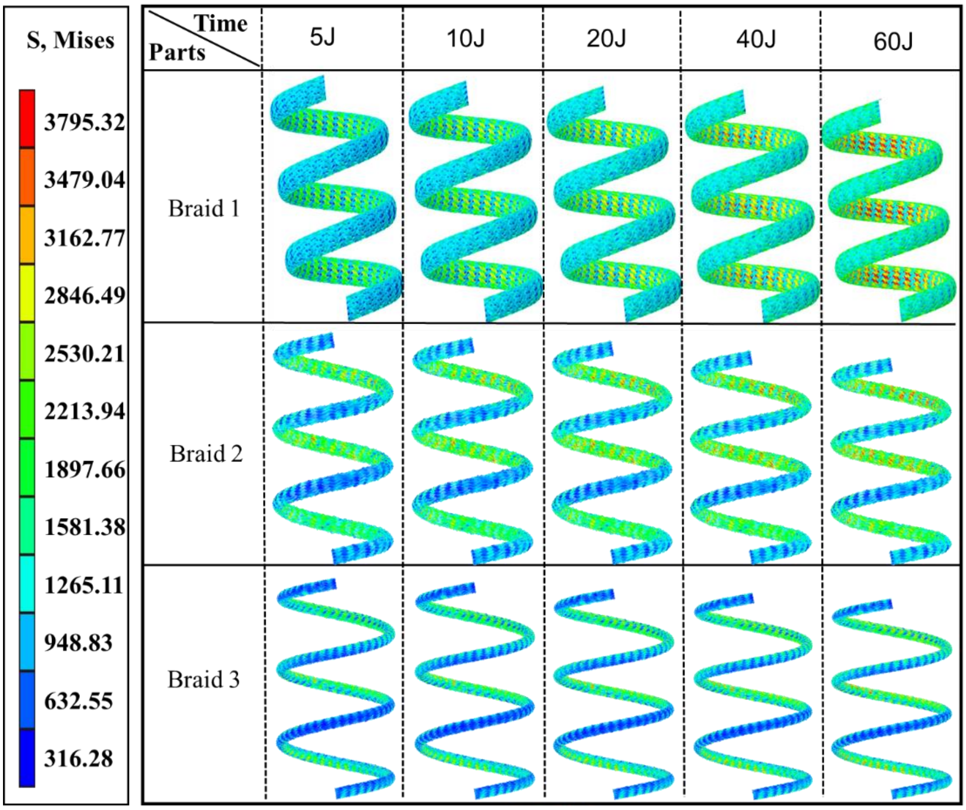

TBCHS

(a)

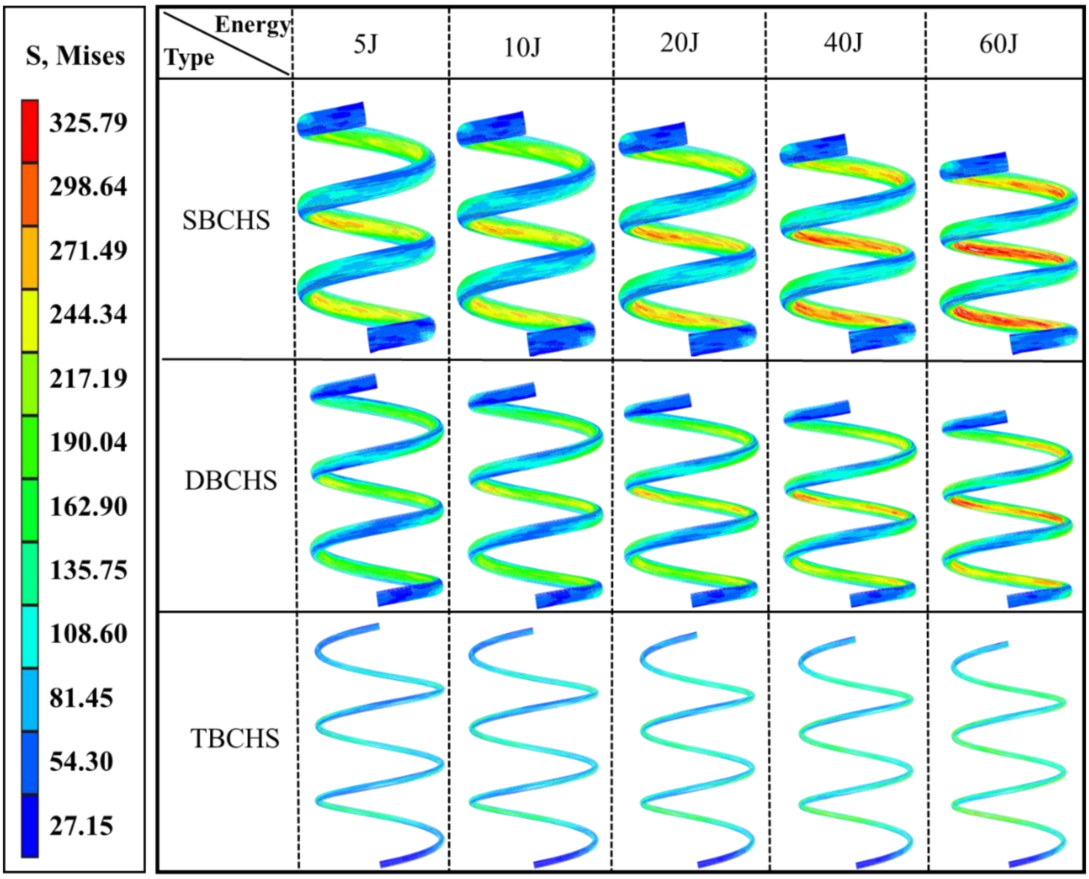
S, Mises
325.79
298.64
271.49
244.34
217.19
190.04
162.90
135.75
108.60
81.45
54.30
27.15
Energy
Type
5J
10J
20J
40J
60J
SBCHS
DBCHS
TBCHS

(b)

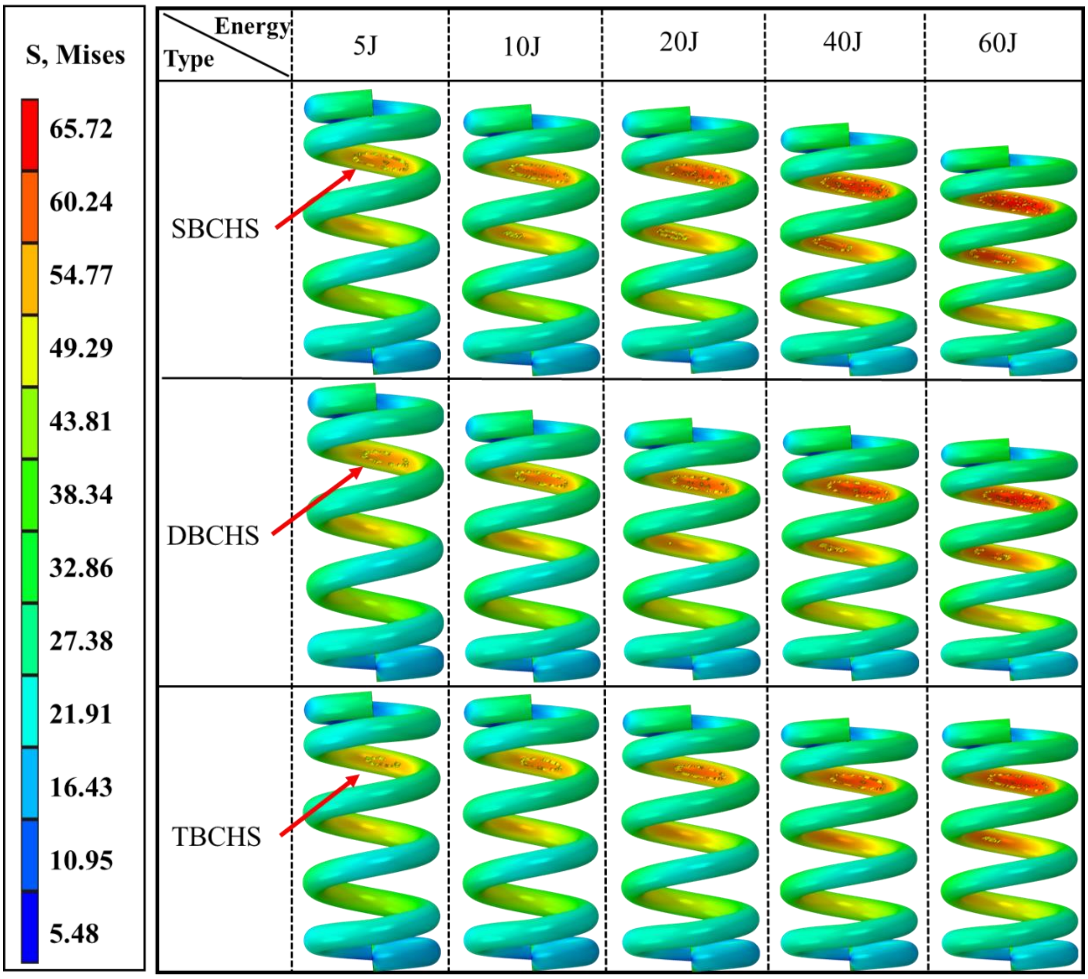

(c)

Fig. 6.2 Von Mises stress distribution of (a) braided reinforcement and (b) reinforcement core and (c) damage evolution of SBCHS, DBCHS and TBCHS under 5 J, 10 J, 20 J, 40 J and 60 J impact simulation.

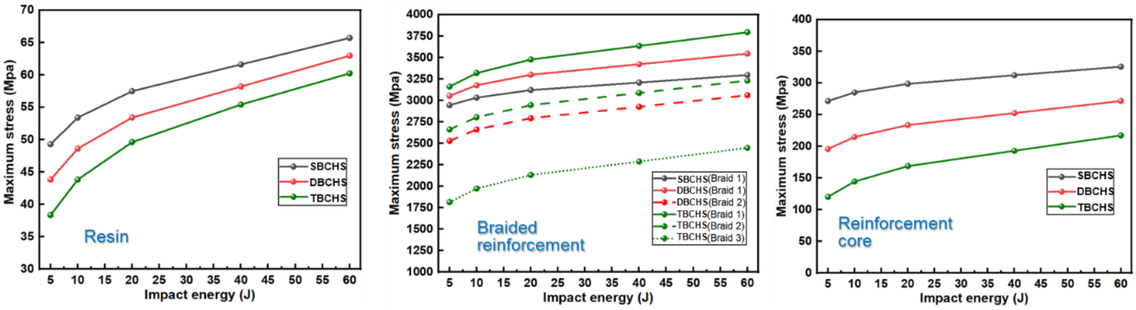

(a) (b) (c)

Fig. 6.3 (a) maximum mises stress curves of resin, (b) maximum mises stress curves of braided reinforcement and (c) maximum mises stress curves of reinforcement core of SBCHS, DBCHS and TBCHS under 5 J, 10 J, 20 J, 40 J and 60 J impact simulation.

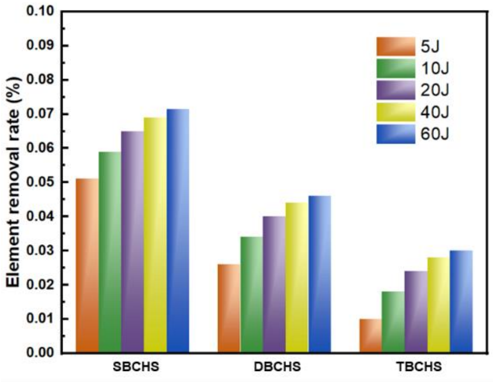

Fig. 6.4 Element removal fraction of SBCHS, DBCHS and TBCHS under 5 J, 10 J, 20 J, 40 J and 60 J impact simulation.

6.3.3 Time domain analysis of impact respond

Although simulation results can predict damage severity and locations, damage evolution is challenging to detect physically in real time. In this work, time domain analysis is introduced to explore the relationship between impact force and damage. The Fourier transform filter is adopted to transform a time-impact force signal to a time domain signal, as shown in Fig. 6.5. Due to the change of local stiffness of sample during impact, the amplitude is expected to change with increasing time. The amplitude of each type of MBLs-CHS increases with rising E_i indicating the damage severity increase gradually. The initial amplitude of SBCHS, DBCHS and TBCHS increases in turn, because initial amplitude is positive relevant with the stiffness, the stiffness of SBCHS, DBCHS and TBCHS increases sequentially. Although the initial amplitude of TBCHS is largest, its evolution amplitude is smallest among them. Overall, it is difficult to obtain the specific damage severity of each MBLs-CHS under different E_i by simply comparing the amplitudes. Therefore, the amplitude intensity is used to express the damage severity. The formula (6.11) is derived to calculate the amplitude intensity during whole impact time.

$$X = \frac{\sum_{i=1}^{n} |A_i|}{2} \tag{6.11}$$

where A_i is the *i*-th amplitude value, i=1, …, n, and *X* is the amplitude intensity.

Finally, the amplitude intensities of SBCHS, DBCHS and TBCHS under different E_i are calculated and summarised in Table 6.1. The amplitude intensity increases with increasing E_i in each MBLs-CHS and decreases sequentially for SBCHS, DBCHS and TBCHS at the same E_i, which means the damage severity follows the same trend. The characterised damage trend using time domain analysis is consistent with simulation results, verifying the feasibility of the damage evaluation method of time domain.

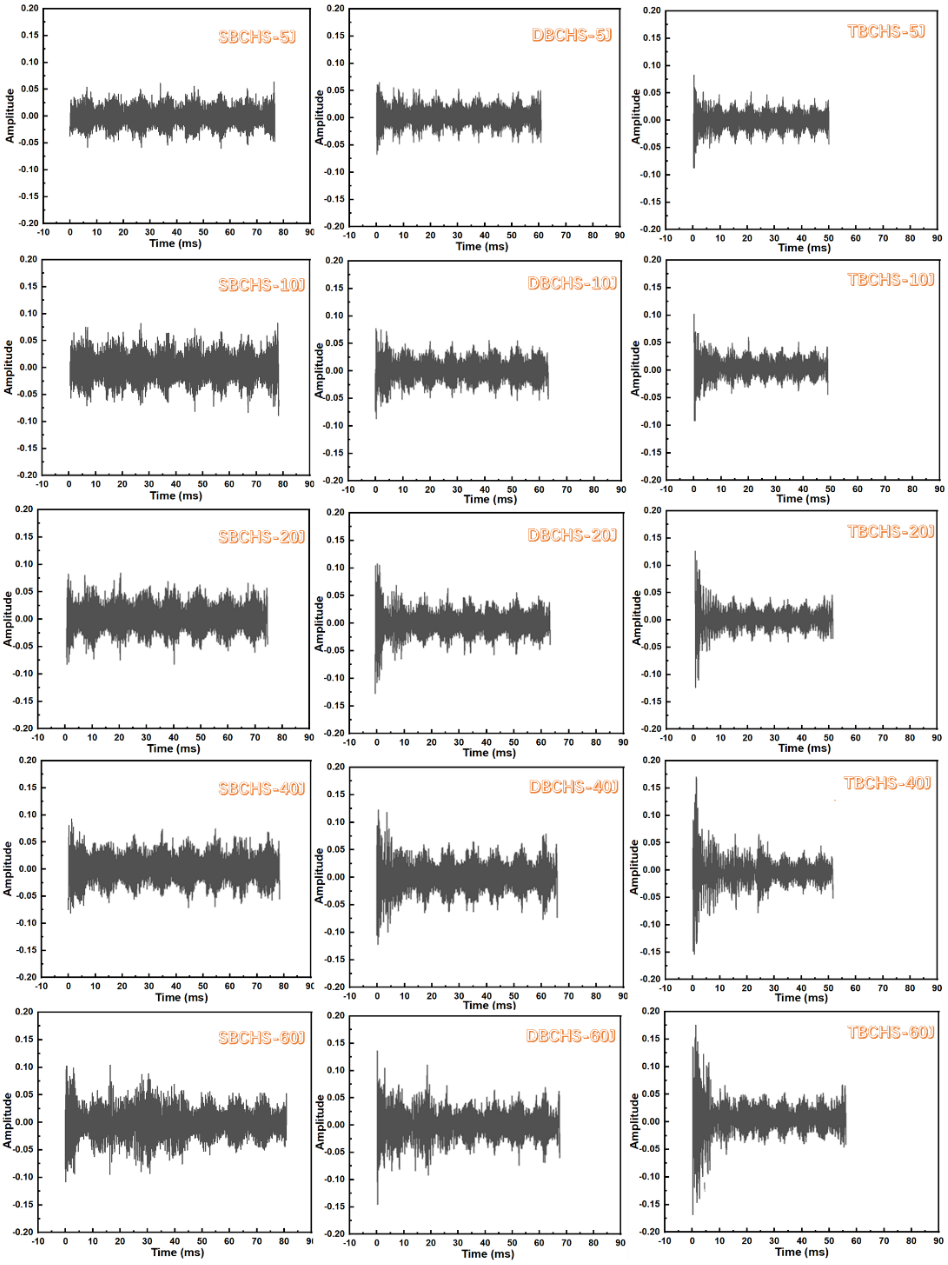

Fig. 6.5 Time domain signal of SBCHS, DBCHS and TBCHS under 5 J, 10 J, 20 J, 40 J and 60 J impaction.

Table 6.1: Amplitude intensity of SBCHS, DBCHS and TBCHS under different E_i

Type	5 J	10 J	20 J	40 J	60 J
SBCHS	474.52	510.76	575.67	675.15	734.19
DBCHS	405.14	443.85	510.55	601.11	634.55
TBCHS	338.91	377.92	443.41	524.30	538.39

6.3.4 Prediction of stiffness degradation of MBLs-CHS under impact

To ensure the safety under impact, the prediction of potential stiffness degradation of MBLs-CHS under impact is necessary. The experiment data and fitted curves of SBCHS, DBCHS and TBCHS that represent the relationship of E_i and amplitude intensity are plotted in Fig. 6.6 (a). The result clearly elucidates that amplitude intensity increases and decreases with E_i and the number of braided layers, respectively. To accurately quantify the stiffness degradation, the compression stiffness of SBCHS, DBCHS and TBCHS under different E_i before and after impact is measured, as depicted in Table 6.2. Subsequently, the experiment data and fitted curves of SBCHS, DBCHS and TBCHS that represent the relationship between E_i and stiffness degradation is plotted in Fig. 6.6 (b). The stiffness degradation increases and decreases with increasing E_i and braided layers, respectively. It is worth mentioning that the relationship (Fig. 6.6 (c)) between stiffness degradation and amplitude intensity can be derived according to Fig. 6.6 (a) and 6.6 (b), which is a normalisation process that can correspond amplitude intensity to the on-time stiffness degradation. The fitting function in Fig. 6.6 (Equations 6.12~6.14) of stiffness degradation Y and amplitude intensity X of SBCHS, BCHS and TBCHS can be used to predict the stiffness degradation of MBLs-CHS during impact. It is obvious that all of the fitting formulas are univariate quadratic equations. The stiffness degradation firstly grows gradually with increasing amplitude intensity, but the growth rate declines gradually with increasing amplitude intensity. This is because the growth rate of stiffness degradation of MBLs-CHS is mainly affected by damage severity. Fig. 6.4 mentioned that the growth rate of damage severity decreases with E_i. The applicable range of amplitude intensity of SBCHS, DBCHS and TBCHS are 0~4100, 0~2075 and 0~1125, respectively. In addition, the difference of stiffness degradation of SBCHS, DBCHS and TBCHS is small at the initial stage and then increases gradually with increasing amplitude intensity. This illustrates that the advantage of reinforcement of SBCHS, DBCHS and TBCHS is not obvious at the initial stage and then the advantage increases with increasing amplitude intensity, indicating that stiffness degradation is expected to be eliminated by increasing the number of braided reinforcements.

$$\text{SBCHS:}\quad Y=-1E^{-6}X^2+0.0082X+0.0035 \qquad R^2=0.9992 \tag{6.12}$$

$$\text{DBCHS:}\quad Y=-2E^{-6}X^2+0.0083X+0.0009 \qquad R^2=0.9998 \tag{6.13}$$

$$\text{TBCHS:}\quad Y=-4E^{-6}X^2+0.009X+0.0008 \qquad R^2=0.9999 \tag{6.14}$$

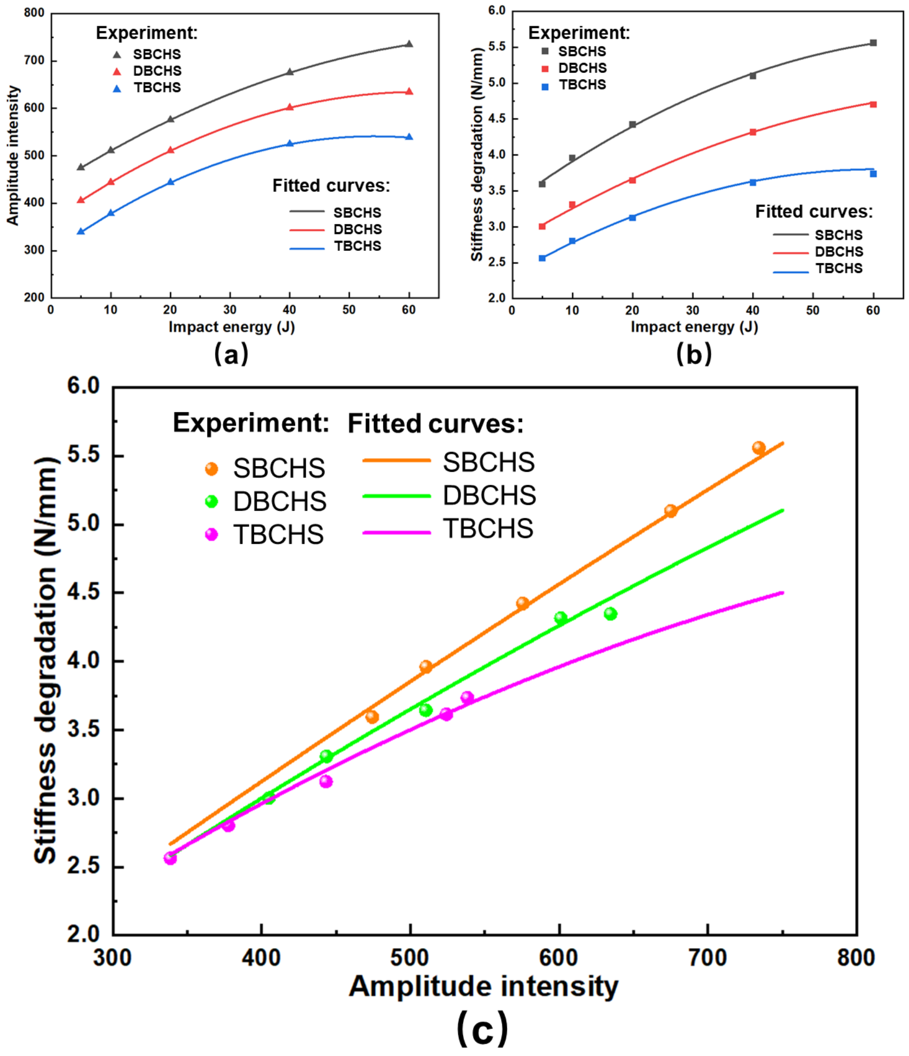

Fig. 6.6 (a) Amplitude intensity and (b) stiffness degradation of SBCHS, DBCHS and TBCHS under 5 J, 10 J, 20 J, 40 J and 6 0 J impaction, and (c) the prediction of stiffness degradation of SBCHS, DBCHS and TBCHS based on amplitude intensity.

Table 6.2: The stiffness (N/mm) of SBCHS, DBCHS and TBCHS before and after impact under different E_i

Type	Status	5 J	10 J	20 J	40 J	60 J
SBCHS	Before impact	17.56	16.97	17.23	17.96	17.33
	After impact	13.97	13.01	12.81	12.87	11.78
DBCHS	Before impact	31.75	31.49	30.80	30.52	31.47
	After impact	28.75	28.18	27.16	26.21	27.12
TBCHS	Before impact	44.57	44.82	45.87	44.60	45.26
	After impact	42.01	42.02	42.75	40.99	41.53

6.4 Summary

Damage model, location and severity of SBCHS, DBCHS and TBCHS under different *Ei* have been studied by combining experiment and simulation methods in this research. Experiment results demonstrate that *Ei* cannot dissipate by rebound rapidly, resulting in energy been absorbed by MBLs-CHS to cause damage. The damage is minor and mainly happened in resin component. Furthermore, the simulation results elucidate that damage happens at the inner side of top end of MBLs-CHS. The max mises stress of braided reinforcement, reinforcement core and resin in each type MBLs-CHS increase gradually with raising *Ei*, which proves the damage increase with increasing *Ei*. When SBCHS, DBCHS and TBCHS is subjected to the same *Ei*, the maximum mises stress of braided reinforcement increases sequentially for SBCHS, DBCHS and TBCHS while that of reinforcement core and resin of SBCHS, DBCHS and TBCHS decrease in turn, illustrating more braided layers can greatly reduce the stress on the other two parts. Therefore, damage decline sequentially for SBCHS, DBCHS, and TBCHS. The damage severity has been expressed using element removal rate, the damage severity of TBCHS declines by 36.5%, 38.6%, 42.5%, 48.3% and 51.3% under 5 J, 10 J, 20 J, 40 J and 60 J than those of SBCHS respectively. Additionally, the time domain is introduced to monitor the damage in real time by transferring the vibration information of impact force. The damage trend of MBLs-CHS under different *Ei* has been indicated through calculating amplitude intensity of time domain. Meanwhile, compression stiffness of SBCHS, DBCHS and TBCHS under different E_i before and after impact have tested to determine the actual value of stiffness degradation. Finally, the fitting formulas about stiffness degradation and amplitude intensity of SBCHS, BCHS and TBCHS under different *Ei* are established to predict the stiffness degradation in real time.

7. FATIGUE PERFORMANCE OF TBCHSs

The CHSs will bear cyclic load during use, therefore the fatigue life and failure process of the spring under cyclic load need to be focused on. Fatigue is an important performance to reflect the service life of CHSs, so it needs to be studied in detail. TBCHS has the best performance according to the above performance analysis, therefore TBCHS is selected for fatigue performance research. The test and analysis of spring fatigue performance based on three stress levels of 100%, 90%, and 70%, the fatigue performance of TBCHS at three stress levels is obtained. And the spring fatigue model is established by finite element method, then the evolution mechanism of spring fatigue damage is analyzed.

7.1 Fatigue test and analysis

7.1.1 Fatigue test standard

At present, the fatigue performance test standards for CHSs are not perfect. For example, the American Society for Testing and Materials (ASTM), the British Society for Standardization (BSI), the Japanese Specification Society (JIS) and the Chinese National Standard (GB) have only established some preliminary test standards for fiber reinforced composite materials, and there are no performance test standards for CHSs. Therefore, this study refers to the Chinese metal spring testing standard GB/T 16947-2009 "Helical spring fatigue testing standard" for fatigue test.

7.1.2 Fatigue test

The fatigue test is carried out by EUM-25k20 fatigue machine according to GB/T 16947-2009, as shown in Fig. 7.1. The sine curve loading mode that is regular alternating load is selected to avoid the creep phenomenon during the test. The loading process under a complete normal cycle is called a loading cycle, as shown in Fig. 7.1 (a), with the loading frequency f=1/T, σ_{max} and σ_{min} is the maximum and minimum stress value under one loading cycle. The cyclic characteristic R is the ratio of the minimum stress to the maximum stress. In this study, the sine wave curve with loading frequency of 0.1 Hz is used for the experiment, and the stress ratio R is 0.1. The fatigue test (Fig. 7.1 (b)) was carried out at three stress levels of 100%, 90% and 70%.

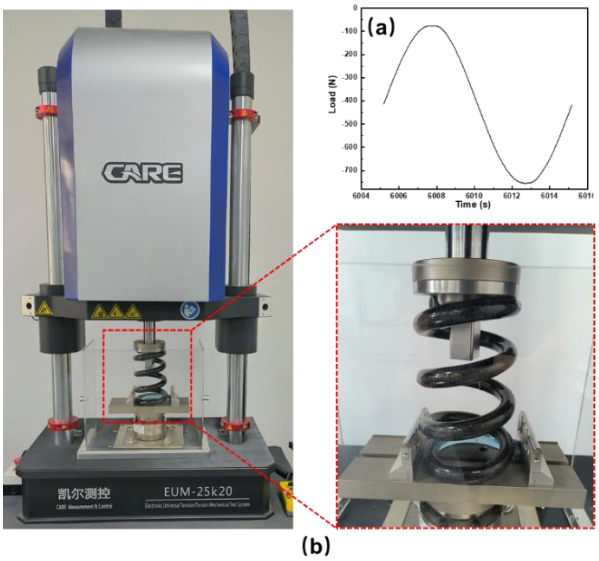

Fig. 7.1 Fatigue test of TBCHSs

7.1.3 Fatigue degradation

The failure of TBCHSs under cyclical loading is very complex, mainly including resin cracking, interfacial debonding and fiber fracture. In the actual loading process, the fatigue damage is not caused by a single cause, but by the joint action of the three forms.

And the main cause of damage and failure will also change with the increase of loading times. Regardless of the cause, the damage will lead to the gradual decline of the overall fatigue resistance of the TBCHSs, which is called the fatigue degradation process of the spring performance. The damage is seen as a cumulative process in the process of performance degradation. Spring stiffness will decrease with the increase of the number of loaded coils. Because TBCHSs will not break suddenly, it is necessary to define the failure criteria of TBCHSs first. When loaded to a certain number of turns n, the spring stiffness is called E (n) and the damage stiffness is called D (n). The relationship between the two is shown in the formula:

$$D(n) = 1 - \frac{E(n)}{E(0)} \qquad (7.1)$$

D(n) is damage stiffness, E(n) is stiffness at n cycles, $E_{(0)}$ is initial stiffness

This macroscopic expression of fatigue damage is called a residual stiffness method. The slope at a certain number of turns is the residual stiffness E (n) of the spring according to the load-displacement curve. The decrease of slope with the increase of the number of cyclic loadings indicates that the residual stiffness E (n) decreases and the damage stiffness D (n) increases. Finally, the fatigue life of the TBCHSs can be showed by the change of curve slope. In the project, when the damage stiffness is greater than 10%, the spring failure is confirmed.

7.1.4 Analysis of fatigue test results

The damage stiffness of 10% is defined as fatigue failure in the test under three stress levels of 100%, 90% and 70%. The load-displacement curves of the spring under different stress levels are extracted respectively after the spring fatigue test is completed. To clearly see the change trend of the load-displacement curve, the load-displacement curves at 25%, 50%, 75% and 100% of the total cycle of fatigue test is shown in Fig. 7.2. The fatigue life of TBCHSs increases with the decrease of stress level by comparing the experimental results. In addition, displacement-load curves are also named hysteresis loop. The tightness of the hysteresis loops under three stress level increases with the increase of the fatigue cycle, which indicates that the change rate of the spring stiffness is reduced gradually.

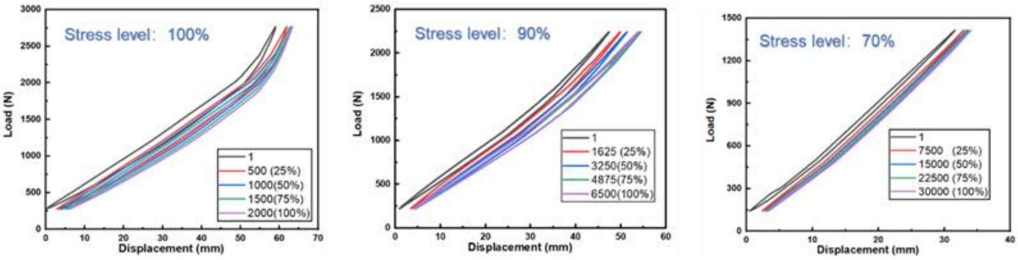

Fig. 7.2 The load-displacement curves at 25%, 50%, 75% and 100% of the total cycle of TBCHSs.

The area enclosed by the hysteresis loop represents the plastic strain energy consumed by TBCHSs during fatigue loading. The plastic strain energy increases with the increase of stress level, as shown in Fig. 7.3 (a), which indicates that the plastic strain energy consumed is higher at high stress level. Fig. 7.3 (b) shows that the stiffness degradation of TBCHSs can be divided into two stages: rapid decline stage and slow decline stage. The failure stiffness of the spring is 38.7kgf/mm according to the residual stiffness method, therefore the life of TBCHSs under 100% and 90% stress levels is 2000 and 6500 respectively. And when the stress level drops to 70%, the stiffness decreases only 1.3% after 30000 cycles, which shows that the TBCHSs can be used for long time under the stress level of less than 70%. The stiffness of the TBCHSs changes significantly in the first stage at 70% stress level, and then enters the second stage of stable change, which accounts for a large proportion of the whole life. The characteristics of the two stages in the fatigue loading process are also the manifestation of the material damage accumulation process. In the first stage, the defects in the TBCHSs will cause stress concentration and thus initial damage. This process is a resin and interface crack initiation stage, so there will be a significant change of stiffness in the first stage. When the damage and crack propagation are stable, it will enter the second stage. The resin crack will gradually expand from the outside to the inside, and the crack between the resin and the yarn interface will expand along the yarn direction. The second stage is gentle and durable. Finally, when the material damage accumulates to a certain extent, the TBCHSs failure. Fig. 7.3 (c) shows the change mode of the deflection, The displacement increases sharply at first and then slowly with the increase of the number of cycles, which illustrate the performance of TBCHSs is stable and will not fail suddenly.

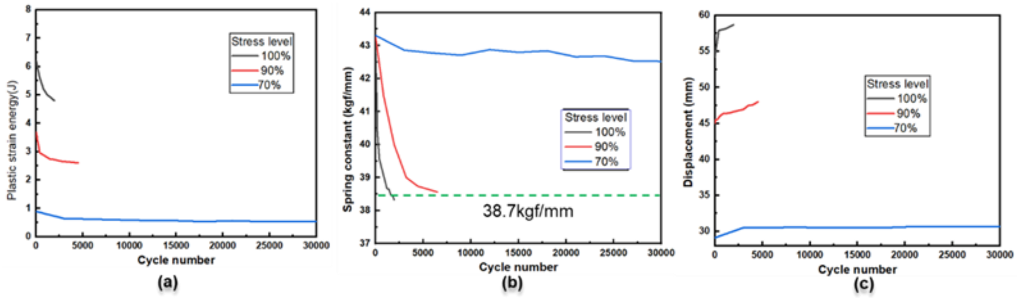

Fig. 7.3 (a) The plastic strain energy of TBCHSs under stress levels of 100%, 90% and 70%, (b) the spring stiffness of TBCHSs under stress level of 100%, 90% and 70%, (c) the displacement of TBCHSs under stress level of 100%, 90% and 70%,

7.2 Fatigue damage analysis

The fatigue life of the spring can be measured, and the failure form of the spring surface can be seen intuitively by using the experimental method to study the fatigue performance of the TBCHSs. However, it is difficult to grasp the generation of spring failure and the transmission of damage by experimental method, and it is difficult to observe the microcracks generated during the spring failure process. These problems hinder the application and development of TBCHSs to a certain extent. Therefore, this project uses finite element analysis software to simulate the spring fatigue process to have a deeper understanding of the spring structure effect, material internal damage, damage transmission and stress distribution.

7.2.1 Fundamental assumption

The TBCHSs is composed of carbon fiber fabric and resin matrix, the carbon fiber fabric is composed of multiple carbon fibers. The fiber bundles are soaked and bonded by the resin matrix after the composite molding process, so the resin matrix exists between the carbon fiber bundles. To study the effect of spring material properties and damage, the basic assumptions are as follows:

1. The resin completely infiltrates the fiber bundle and distributes evenly in the fiber bundle.
2. The monofilament in the fiber bundle is continuous and parallel to each other.
3. The mechanical properties of the fiber and matrix as well as the structure of the preform have not changed before and after the TBCHSs molding.
4. The yarn is the composite structure of resin and fiber bundles, and its mechanical properties are homogenization mechanical parameters.
5. The bond between the resin and the fiber bundle is intact without debonding.
6. The influence of defects, cracks and porosity in raw materials and manufacturing process of TBCHSs are ignored.

7.2.2 Setting of boundary condition

To accurately simulate the spring fatigue process, the boundary conditions of spring fatigue simulation should be determined to be consistent with the experimental conditions. The relatively stable cyclic displacement in the experiment is selected as the displacement applied in the finite element calculation. The bottom end of the TBCHSs is fixed, and the upper end applies sinusoidal displacement. The displacement parameters are determined by the sine wave formula as shown in the formula.

$$\begin{cases} \mathrm{a}=\mathrm{A}_0+\sum_{1}^{N}\left[A_\mathrm{n}\cos\mathrm{n}\omega(\mathrm{t}-\mathrm{t}_0)\ +B_\mathrm{n}\sin\mathrm{n}\omega(\mathrm{t}-\mathrm{t}_0)\right],\mathrm{t}\geq\mathrm{t}_0 \\ \mathrm{a}=A_0,\mathrm{t}<\mathrm{t}_0 \end{cases} \tag{7.2}$$

where **a**, Amplitude; **A$_0$**, initial amplitude; **N**, Fourier series term; **A$_n$**, cos term coefficient (n=1,2, 3,….N); **B$_n$** ,sin term coefficient (n=1,2,3,….N); **ω**, Displacement velocity; **t$_0$**, initial time.

7.2.3 Failure criterion of fatigue

Hashin criterion is one of the famous failure criteria, which is used to predict the damage evolution process in composite materials and is widely used in academic and engineering fields. The 3Dhashin criterion is used as the fatigue failure criterion to simulate the damage evolution process of TBCHSs. The following are four different failure modes included in the Hashin criterion:

$$F_{ft}=\left(\frac{\sigma_{11}}{X_T}\right)^2+\alpha\left(\frac{\sigma_{12}}{S_{12}}\right)^2+\alpha\left(\frac{\sigma_{13}}{S_{13}}\right)^2\geq 1 \tag{6.3}$$

Fiber compression failure（$\sigma_{11}\leq 0$）

$$F_{fc} = \left(\frac{\sigma_{11}}{X_C}\right)^2 \geq 1 \tag{6.4}$$

Matrix tensile failure（$\sigma_{22} + \sigma_{33} \geq 0$）

$$F_{mt} = \left(\frac{\sigma_{22}+\sigma_{33}}{Y_T}\right)^2 + \frac{1}{S_{23}^2}(\sigma_{23}^2 - \sigma_{22}\sigma_{33}) \left(\frac{\sigma_{12}}{S_{12}}\right)^2 + \left(\frac{\sigma_{13}}{S_{13}}\right)^2 \geq 1 \tag{6.5}$$

Matrix compression failure（$\sigma_{22} + \sigma_{33} \leq 0$）

$$(f_{mc})^2 = \left[\left(\frac{X_C}{2S_{23}}\right)^2 - 1\right]\frac{(\sigma_{22}+\sigma_{33})}{Y_C} + \frac{(\sigma_{22}+\sigma_{33})^2}{4S_{12}^2} + \frac{\sigma_{23}^2-\sigma_{22}\sigma_{33}}{S_{23}^2} + \frac{\sigma_{12}^2+\sigma_{13}^2}{\sigma_{12}^2} \geq 1 \tag{6.6}$$

where σ_{ij}(ij=1,2,3) is the effective stress component; X_T and X_C are axial tensile and

compressive failure strengths; Y_T and Y_C are longitudinal tensile and compressive failure strengths; and S12, S13 and S23 are shear failure strengths; α is Shear failure coefficient.

7.2.4 Damage morphology analysis

There will be damage in the fatigue test of TBCHSs, therefore the damage morphology of TBCHSs during the fatigue process is further explored through FEM. Periodic amplitude and analysis step are the key points in fatigue simulation. The setting of periodic amplitude requires the combination of displacement, displacement amplitude, initial amplitude, velocity. and two analysis steps should be set in fatigue simulation to ensure the correct range of sine curve, as shown in Fig. 7.4.

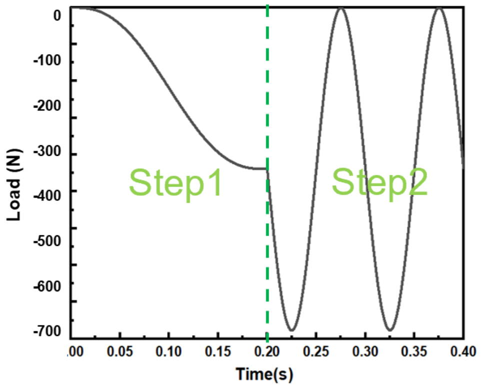

Fig. 7.4 Setting of two analysis steps of TBCHSs during fatigue simulation

The damage evolution of three stages under 100% stress level is extracted. Fig. 7.5 shows that the resin in the inner diameter area first cracks and propagates during the fatigue process. However, fiber only shows fiber bundle cracking and buckling and do not break, which indicate that the carbon fiber has a great contribution to the spring performance.

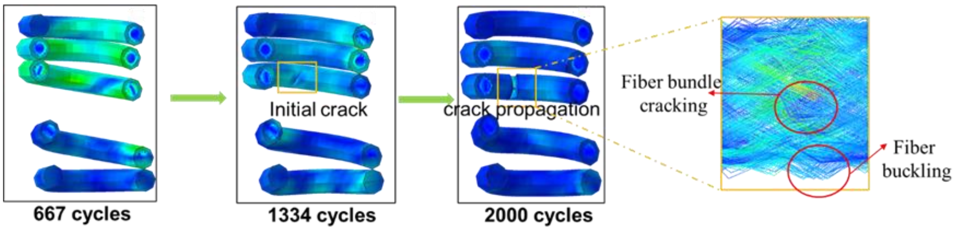

Fig. 7.5 The damage evolution of TBCHS under 100% stress level

7.3 Summary

The fatigue life and failure process of the TBCHSs under cyclic load have been researched by experiment and simulation respectively. It is obvious that TBCHS has the best static and impact performance according to the above performance analysis, therefore TBCHS is selected for fatigue performance research. The displacement and load curves from fatigue experiment shown that the fatigue life of TBCHSs increases with the decrease of stress level. In addition, the tightness of the hysteresis loops under three stress level increases with the increase of the fatigue cycle, which indicates that the spring performance is stable gradually with increasing cycle numbers. The life of TBCHSs under 100% and 90% stress levels is 2000 and 6500 respectively. And when the stress level drops to 70%, the stiffness decreases only 1.3% after 30000 cycles, which shows that the TBCHSs can be used for long time under the stress level of less than 70%. The simulation result of damage propagation of TBCHSs under 100% stress level shown that the resin in the inner diameter area first cracks and propagates during the fatigue process. However, fiber only shows fiber bundle cracking and buckling and do not break, which indicate that the carbon fiber reinforcement has a great contribution to the fatigue performance.

8. APPLICATION OF TBCHSs

With details on design, process manufacturing, structure selection and performance optimization of CHS, this chapter will report the feasibility of installing TBCHSs in the vehicle for evaluation. The installation experiment has been implemented on Jeep TJ 2004 in Kraft Motorsports Pty Ltd., in Perth, Australia. Due to the limitation of installation environment, the large professional instruments cannot be used to evaluate the indicator of installation. Therefore, small and portable strain testers have been used to evaluate the installation effect by strain analysis.

8.1 Application vehicle - Jeep TJ2004

The installation environment of front and rear suspension springs of Jeep TJ 2004 is different due to the different suspension configurations. Both upper and downer holders of front suspension spring is horizontal, which means the front spring is subjected to the pure vertical load. However, the upper holder of rear suspension spring is with 15° angle and the downer holder is horizonal, which means the rear suspension is subjected to vertical and lateral loads. The reasons for the upper and downer holder of front suspension spring are horizonal are as follows.

1. Steering system requirements

The front suspension spring must work with the steering system. A vertical upper holder helps ensure that the wheels can maintain a stable angle and position during steering. A tilted design may affect the precision and response of the steering.

2. Front axle design

Jeep TJ 2004 uses a solid front axle design for the front suspension. A vertical upper holder is more compatible with the solid front axle design, helping to provide consistent suspension geometry and better handling performance.

3. Structural and space constraints

The front of the vehicle usually needs to accommodate the engine, steering mechanism, and other components. The vertical upper holder design can better adapt to these space constraints and ensure that the suspension system works efficiently in a limited space.

4. Simplified design and manufacturing

The vertical design can simplify the design and manufacturing process of the suspension system. The vertical upper holder design is more common and is easier to manufacture and maintain.

The rear suspension upper holder of the 2004 Jeep TJ is not vertical, but is angled, based on several design considerations to optimize vehicle performance and handling. Here are some key reasons:

1. Lateral movement reduction

The angled upper holder reduces suspension movement in the lateral direction. This helps improve vehicle stability, especially when driving off-road, where the suspension system needs to deal with various lateral forces.

2. Improved handling

The angled upper holder design optimizes suspension geometry, allowing the wheels to maintain better alignment as they move up and down. This has a positive impact on vehicle handling and steering response.

3. Improved suspension geometry

The angled upper holder helps optimize suspension geometry, reducing wheel angle changes (such as camber and toe angle changes) caused by suspension movement. This improves tire contact and grip on different terrains and driving conditions.

4. Increased suspension travel

The tilted upper holder design provides greater suspension travel, allowing the suspension system to better cope with extreme terrain changes in off-road conditions. The increased suspension travel helps keep the wheels grounded, improving the vehicle's off-road capabilities and stability.

5. Structural design constraints

In some cases, the structural design of the body and chassis may limit the installation position and angle of the suspension holder. The tilted design can better accommodate these structural limitations while maintaining the functionality of the suspension system.

The rear suspension system of the Jeep TJ 2004 can provide excellent off-road performance while maintaining good on-road driving experience with these design considerations. This design allows the vehicle to perform well in a variety of driving conditions, making it one of the classic off-road vehicles.

In short, the design of the upper holder of the front suspension is vertical while the rear suspension has a certain angle, which is based on their different functional requirements and structural considerations. The vertical design can better meet the requirements of the front suspension in terms of steering, space utilization and load handling, while the angle design of the rear suspension focuses on optimizing stability and suspension travel. This design difference ensures the best performance of Jeep TJ 2004 in various driving conditions.

8.2 Test

8.2.1 Test preparation and precautions

The strain tester in the experiment is DMYB1808 Dynamic and static resistance strain gauges and the strain model is 120-3AA. The process of strain tests is complex, and every preparation is important. If there is one step that is not correct, the test cannot be carried out successfully or cannot get the accurate data. Therefore, it is important to focus on the preparation steps. The steps to connect the DMYB1808 dynamic and static resistance strain gauge and the 120-3AA strain gauge are as follows.

Required equipment and materials: DMYB1808 dynamic and static resistance strain gauge, 120-3AA strain gauge, connection wire, soldering tool or terminal, adhesive, cleaning tool (such as alcohol, cotton cloth).

Connection steps：

1. Preparation: check the strain tester and strain gauge to make sure they are intact and prepare the connection wire, which is usually a thin wire, and make sure both ends of the wire are peeled for easy connection.
2. Strain gauge pasting: clean the surface of the TBCHSs with alcohol and cotton cloth to ensure that there is no oil and dust. Use a special adhesive (such as instant glue or special glue for strain gauges) to paste the strain gauge on the cleaned surface of the TBCHSs for making sure the strain gauge is pasted flat to avoid bubbles and wrinkles.
3. Connect the strain gauge leads: solder one end of the connecting wire to the welding point of the strain gauge. The 120-3AA strain gauge has two welding points, and two wires need to be soldered to these two welding points respectively. Make sure the welding points are firm and there are no cold solder joints.
4. Protect the contacts: use some insulating tape or heat shrink tubbing at the welding points or terminal blocks to protect the contacts from external force damage or short circuit.
5. Connect to the strain gauge: connect the other end of the connecting wire to the input port of the DMYB1808 dynamic and static resistance strain gauge. The connection is based on the quarter bridge connection method, because the strain gauge we used is quarter bridge.
6. Check the connection: check whether all connections are firm and make sure that the wires are not exposed to the outside to avoid short circuits or interference and ensure that the strain gauge is well pasted, and the connecting wire is not pulled or compressed.
7. Set up the strain gauge: turn on the power of the DMYB1808 dynamic and static resistance strain gauge and select the bridge type of the strain gauge according to the

type of strain gauge we used. Perform zero-point calibration and full-scale calibration to ensure accurate measurement.

8. Set parameters: set the corresponding parameters of the strain gauge according to the sensitivity coefficient and other parameters of the strain gauge. The collection frequency of data is 100 Hz that is the maximum frequency of the device.

Finally, the DMYB1808 dynamic and static resistance strain gauge and 120-3AA strain gauge can be correctly connected and tested to ensure the accuracy and reliability of the measurement data through the above steps.

8.2.2 Strain test method

8.2.2.1 Strain test of TBCHSs installed on Jeep TJ 2004

To understand the strain situation of different positions and direction of TBCHSs, the strain gauges was sticked on the surface of wire of TBCHSs along with different positions and directions. Due to the different of installation environment of front and rear suspension TBCHSs, the key point of strain test of front and rear suspension TBCHSs is different. Therefore, the position and direction of collected strain should be considered respectively based on the load characteristics. To clearly descript the strain of the TBCHSs corresponding different positions after installing on the vehicle, anterior, and posterior regions refer to the direction of vehicle body are first defined, as depicted in Fig. 8.1 (a). Anterior and posterior regions are nearby headstock and tailstock region, respectively.

The strain law of the front TBCHSs under the installation environment is tested. The upper and downer holders are both horizontal planes, indicating that the front TBCHSs is subjected to a vertical compression load. The strain response of the front TBCHSs is relatively complex under loading. The strain in the anterior and posterior regions, the inner and outer diameter areas, the axial, radial and tangential directions, and the upper, middle and downer coils are not same. Therefore, to reveal the strain law in detail, it is necessary to conduct a comprehensive analysis of the strain from these four levels. The portable DMYB1808 dynamic and static resistance strain gauges used to collect strain data has only 8 channels, it is impossible to test the strain in all positions and directions at the same time. So, the strain test is divided into two steps. The first step is to simultaneously test the axial, radial and tangential strains in the inner and outer diameter areas of the anterior region of the middle coil and the axial strain in the inner and outer diameter areas of the posterior region to determine which position and direction of the same coil has the largest strain, the strain pasting method is shown in Fig. 8.1 (b). The axial, tangential and radial strains in the outer diameter area are expressed as Outer A, Outer T and Outer R, respectively, and the axial, tangential and radial strains in the inner diameter area are expressed as Inner A, Inner T and inner R, respectively.

As far as the installation environment of the rear suspension TBCHSs is concerned, the downer holder is horizontal and the upper holder is 15° to the horizontal plane, indicating that the load direction is not completely vertical. In addition to the axial force, the TBCHSs in the loading mode will also be subjected to lateral load, which will cause asymmetry in the force and deformation of the TBCHSs. Similarly, the strain test is divided into two steps from the four levels of strain in the anterior and posterior region, the inner and outer diameter areas, the axial, radial and tangential directions, and the upper, middle and downer coils. In addition, the posterior region of rear TBCHSs will be subjected to tensile and the anterior region will be subjected to compression under the action of lateral force, resulting in a more obvious strain difference between the anterior and posterior region. Therefore, the focus of stress analysis is mainly on the comparison between the anterior and posterior region. The first step is to simultaneously test the axial, radial and tangential strains at the outer diameter area of the anterior and posterior region of the middle coil and the axial strain at the inner diameter of the anterior and posterior region to determine which position and direction of the strain in the same coil is the largest. The strain pasting method is shown in Fig. 8.1 (c).

Then, JEEP TJ 2004 had been lifted and the TBCHSs had been installed on the suspension system to replace metal spring, as shown in Fig. 8.1 (d). The connection wire of strain had been connected to DMYB1808 dynamic and static resistance strain gauges that were connected to data collection equipment, as depicted in Fig. 8.1 (e). Subsequentially, the equipment of collecting data commences to record the data during the vehicle had been fallen slowly until totally contact ground.

The strain direction and position of front and rear TBCHSs in second step should be ensured according to the result of strain analysis of the first step. Therefore, the specific strain collection in the second step will be described after the strain analysis of first step.

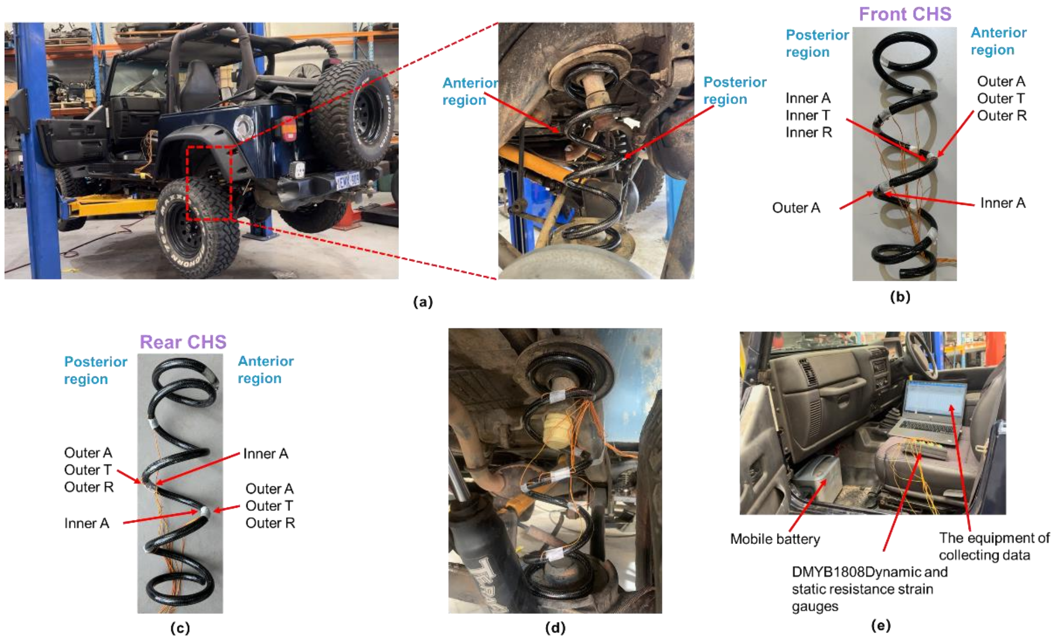

Fig. 8.1 (a) The distinguishing of anterior and posterior region of TBCHSs, (b) paste method of front TBCHS for testing strain data in different directions, (b) paste method of rear TBCHS for testing strain data in different directions, (d) installment of TBCHSs and (e) strain test during the vehicle had been fallen slowly until totally contact ground

8.2.2.2 The tensile and bend of resin

Resin optimization was conducted by tensile and bend test, test process is shown in Fig. 8.2. Test standard of tensile is according to GB/T528-2009. The test sample shape of tensile is dumbbell, all length of sample is 155 mm, gauge length is 25 mm, measure width is 6 mm and thickness is 3 mm. In the tensile test, the two ends of the sample are bonded with reinforced aluminum sheets, which can avoid the damage of the two ends of the sample due to the excessive force of the clamp during the tensile test and prevent the sliding of the contact surface between the clamp and the sample to affect the accuracy of the test data during the test. The test sample size of bend is 80 mm×10 mm×4 mm. The bend test is carried out based on GB/T2567-2008. The test span of bend is 64 mm. Both tensile and bend properties of resin are tested by Instron 5969 strength machine at the speed of 1 mm/min. Every type includes three samples for obtaining accurate data.

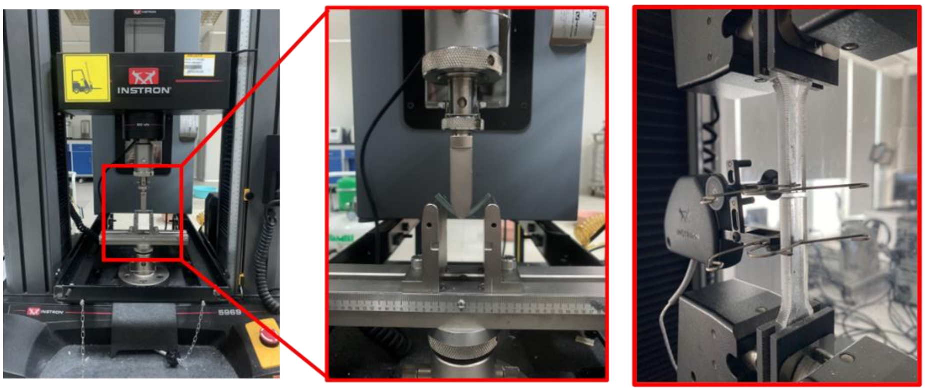

Instron 5969 **Bend** **Tensile**

Fig. 8.2 Tension and bending test of resin

Due to the displacement and load information are collected during the two types of tests, the conversation from displacement and load data to strain and stress data is necessary. The conversation method is different between tensile and bend, and the strain and stress conversation method of tensile and bend are below.

In terms of tensile, the displacement load data can convert to strain stress data respectively, the conversation process is following. The tensile stress can be calculated by the following equation.

$$\sigma = \frac{F}{A_0} \qquad (8.1)$$

σ is tensile stress, F is load, A_0 is the cross section of the sample

The tensile strain can be obtained by the following equation.

$$\varepsilon = \frac{\Delta L}{L_0} \qquad (8.2)$$

ε is the tensile strain, ΔL is the the elongation of sample, L_0 is the initial scale of the sample.

In terms of bend, the displacement load data can convert to strain stress data respectively, the conversation process is following. The stress in bend test is usually considered to be the bend stress, which can be calculated by the following formula:

$$\sigma = \frac{3PL}{2\mathrm{bd}^2} \qquad (8.3)$$

σ is bend stress, P is applied load，L is the bend span (the distance between support points), b is the width of sample and d is the thickness of sample.

The bend strain can be calculated by the following equation:

$$\varepsilon = \frac{6D\mathrm{d}}{L^2} \qquad (8.4)$$

ε is bend strain，D is the displacement of the sample at the load point, d is the thickness of sample, L is the bend span (the distance between support points).

8.3 Result and discussion

8.3.1 Damage morphology analysis

The mesoscopic compression damage mechanisms of composite materials mainly include fiber breakage, fiber bundle splitting, fiber buckling, matrix cracking, interlaminar debonding, etc. The macroscopic compression damage mode of composite materials is mainly composed of a variety of mesoscopic damages. In the compression composite structure, the macroscopic failure mode is mainly divided into steady-state failure mode, unsteady-state failure mode and mixed compression process. The steady-state compression form means that the sample is steady and gradually damaged from one end to the other during the compression process. In this form, the sample has better buffering energy absorption; the unsteady-state compression form means that the sample suffers from sudden damage such as overall buckling instability or brittle fracture in the middle part during the compression process. In this process, the sample absorbs less energy; the mixed compression form is a combination of the above two compression failure characteristics. This form is mainly manifested in that the sample presents a steady-state compression process in the early stage of compression. During this process, the sample produces unpredictable damage and fracture mechanism, resulting in an unsteady-state process in the subsequent stage.

Fig. 8.3 shows the damage morphology of front and rear suspension TBCHSs during vehicle slowly drop until total on the ground. There is no damage happening in the front TBCHSs until the vehicle is totally on the ground, as shown in Fig. 8.3(a). However, the upper support post totally attaches with lower support post, meaning the weight of vehicle is acted on support post but TBCHSs. This is because the stiffness of the TBCHSs is not enough, so that the deformation of TBCHSs is large. In addition, the damage morphology of rear TBCHSs is shown in Fig. 8.3 (b). It is obvious that the damage of rear TBCHSs gradually occur just on resin part with the dropping of vehicle. And the damage just happens at the middle coil of TBCHSs, meaning the damage of TBCHSs is unsteady damage. The unsteady-state process is mainly divided into two forms: overall buckling instability and unsteady-state brittle fracture; overall buckling instability indicates that the specimen undergoes a large buckling deformation during the compression process and cannot continue to withstand higher loads; unsteady-state brittle damage is a sudden brittle fracture of the specimen during the compression process, resulting in sudden instability of the specimen. It is clearly shown that there exist two damage models that are crack and debonding in posterior region of rear TBCHSs. Therefore, the damage model of rear TBCHSs is unsteady-state brittle damage. The crack 1, crack 2 and debonding occur in turn under different positions with descend of vehicle. The crack damage and debonding always appears on the posterior region and there is no damage on anterior region. This is because the holder in rear suspension is not vertical but with 15° angle, which will cause different position of rear TBCHSs is not subjected to same compression. The reason there is no damage on anterior region is that anterior is mainly subjected to compression. The crack with certain angles always occur on the posterior region as posterior region is subjected to shear. And the serious debonding appears on the posterior region as posterior is also subjected to tensile. Moreover, in terms of compression spring, it has little ability to resist tensile, so that serious damage happens. In general, the damage just occurs on the posterior region of rear TBCHSs, which is caused by shear. There is no damage overall front TBCHSs and the anterior region of rear TBCHSs.

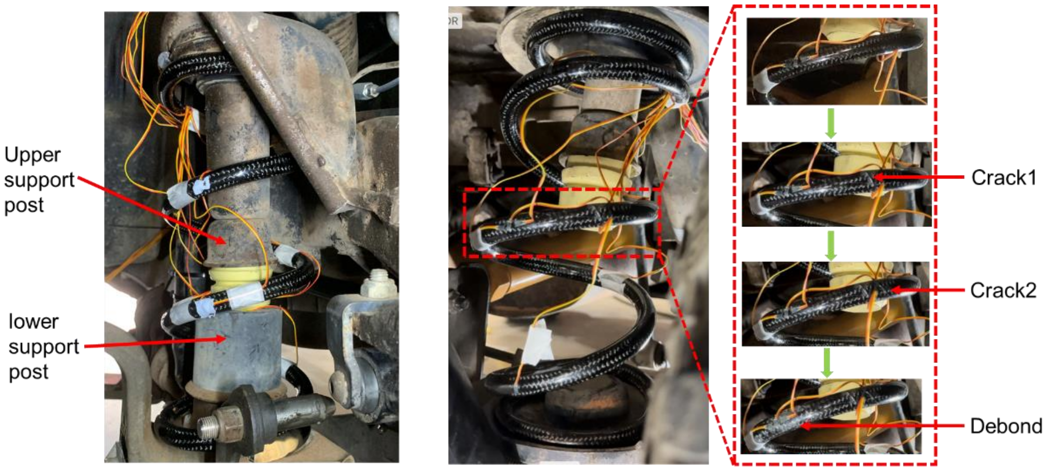

(a) Front CHSs

(b) Rear CHSs

Fig. 8.3 (a) damage morphology of front TBCHSs and (b) damage morphology of rear TBCHSs.

8.3.2 Strain analysis of TBCHSs during installation

8.3.2.1 Strain analysis of front TBCHSs during installation

The main failure modes of the TBCHSs are resin cracking and resin debonding based on the morphology of TBCHSs, so the key point of optimizing the TBCHSs is to optimize the resin composition. To further understand the reasons for resin failure, a detailed analysis was conducted from the perspective of strain. Fig. 8.4 (a) shows the strain information of the first step of the front TBCHSs from suspension to completely landing. It can be seen from Fig. 8.4 (a) that the strain changes linearly during the compression of the front TBCHSs, and the strain remains unchanged after the vehicle is completely landed. The axial strain of the outer diameter area of the posterior region is similar to the axial strain of the outer diameter area of the anterior region, and the axial strain of the inner diameter area of the posterior region is similar to the axial strain of the inner diameter area of the anterior region, indicating that the strain difference at the corresponding positions and directions of the anterior and posterior region is not large. This is because the front TBCHSs is subjected to a vertical compression load, which makes the force more uniform. Therefore, it is sufficient to analyze the strains of the inner and outer diameters area of the anterior region in different directions in the future. It is obvious that the strains in the three directions of the inner diameter area of the anterior region are all negative while the strains in the three directions of the outer diameter area of the anterior region are all positive, which means that the inner diameter area of the anterior region is mainly compressive strain, and the outer diameter area of the anterior region is mainly tensile strain. When the front TBCHSs is subjected to a vertical compression load, the overall length of the TBCHSs will be shortened, which means that the TBCHSs has undergone compression deformation from the perspective of macroscopic overall deformation. But from the perspective of microscopic local deformation, the spring wire of TBCHSs is subjected to complex stress. Although the front TBCHSs is compressed and deformed macroscopically under the action of vertical compressive load, the spring wire of front TBCHSs in the outer diameter area will be elongated along the helical direction, which will generate tensile strain from a microscopic perspective. This is because the spring wire of front TBCHSs is subjected to the bending moment during compression, which causes tensile stress on the outer diameter area of the spring wire. The inner diameter area of the spring wire is subjected to compressive force under the action of the bending moment. So compressive strain will be generated locally, and the inner diameter area of the spring wire will tend to shorten. The tensile strain in the outer diameter area decreases in the axial, tangential and radial directions, respectively, to 0.3548, 0.2750, and 0.0840. The compressive strain in the inner diameter area also decreases in the axial, tangential and radial directions, respectively, to 0.4346, 0.1638 and 0.0432. Axial stress is usually the dominant stress because it is the main load direction of the TBCHSs. Sorting the strains at these six locations shows that the axial compressive strain in the inner diameter area is the largest. This is because the inner diameter area is closer to the center of force than the outer diameter area, so it is subjected to greater local stress during the force transmission process. In addition, the bending and torsion of the TBCHSs will cause stress concentration in the inner diameter area. The second one is the axial tensile strain in the outer diameter area. For tangential strain, the outer diameter area is far away from the center of the spring axis and is more affected by the bending moment, so the tangential tensile strain of the outer diameter area is greater than the tangential compressive strain of the inner diameter area. For radial strain, the outer diameter area will expand slightly when compressed to generate positive tensile radial strain. And the inner diameter area will shrink slightly radially due to compression, so its strain is the smallest.

For carbon fiber reinforced composites, the tensile strength is much greater than the compressive strength, indicating it is easier to be damaged at the compressive strain position. Combining the above analysis, the axial and tangential compression strain are larger in inner diameter area, so we chose the axial and tangential compression strains in inner diameter area for the second step of analysis. The second step is for testing the strain date among different coils of front TBCHSs. The aim of this type of comparison is to reveal the strain rule of from up to down of front TBCHSs. The test results are shown in Fig. 8.4 (b), number 1, 2 and 3 represent the upper middle and downer coils of the TBCHSs, respectively. The axial and tangential strains of the inner diameter area of the upper coil are expressed as inner A1 and inner T1, the axial and tangential strains of the inner diameter area of the middle coil are expressed as inner A2 and inner T2, and the axial and tangential strains of the inner diameter area of the downer coil are expressed as inner A3 and inner T3. The inner A1, inner A2, inner A3, inner T1, inner T2, inner T3 are 0.4047, 0.4346, 0.3754, 0.1310, 0.1638, 0.1017 respectively. The axial and tangential compression strains of the middle coil are the largest, followed by the upper coil and finally the downer coil. This is because each coil of the front TBCHSs participates in the load bearing as the compression load is applied. However, since the front TBCHSs is subjected to the vertical compression loads generated by the sprung mass and the unsprung mass at the same time during the process of the vehicle's suspension to land, causing the spring will have a cumulative effect during the deformation process, so the middle coil close to the compression center are more deformed. In addition, since the sprung mass is greater than the unsprung mass, the strain of the upper coil is greater than the strain of the downer coil. In general, the strains that are most likely to cause damage in the front TBCHSs are the axial and tangential compression strains of the inner diameter area of the middle coil. However, the front TBCHSs did not suffer any damage during the entire test process by combining with the morphological analysis, indicating that the compression damage strain of the front TBCHSs is greater than the range currently tested.

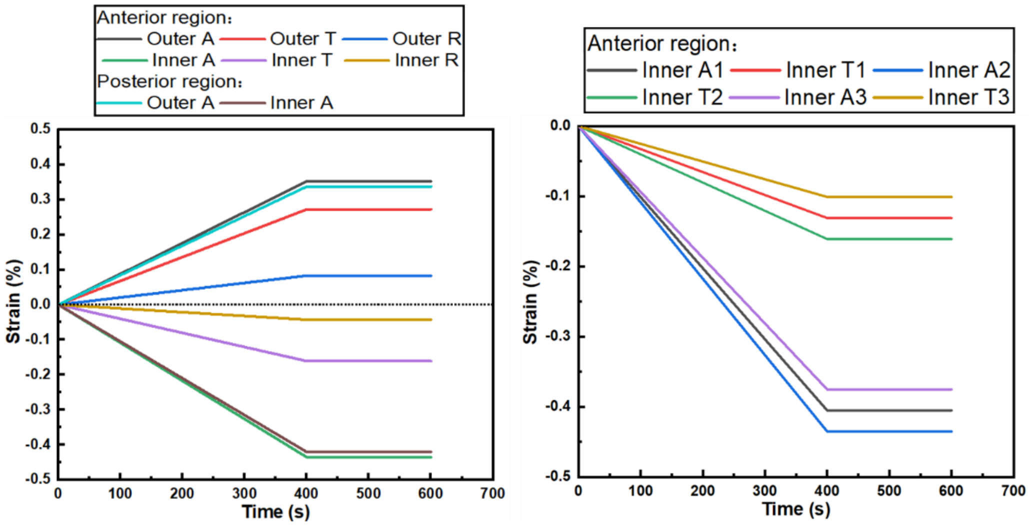

(a) (b)

Fig. 8. 4 (a) The strain of axial, radial and tangential directions of inner and outer diameter region of anterior and posterior region of front TBCHSs in middle coil and (b) the strain of axial and tangential directions of inner diameter region of anterior region of front TBCHSs in different coils.

8.3.2.2 Strain analysis of rear TBCHSs during installation

The strain of the first step of rear TBCHSs is shown in Fig. 8.5 (a). The strain of the anterior region is negative due to compression, and the strain of the posterior region is positive due to tension under the action of lateral force. The axial strain of the inner diameter area of the anterior and posterior region is always smaller than the axial strain of the outer diameter area, indicating that the outer diameter area can generally bear greater stress under the action of lateral force, whether it is tension or compression. Therefore, the strains of the outer diameter areas of the anterior and posterior region in different directions are mainly analyzed in the following. The compressive strain of the outer diameter area of the anterior region decreases in the axial, tangential and radial directions, respectively, to 0.6432, 0.3967, and 0.0657. And the tensile strain of the outer diameter area of the posterior region also decreases in the axial, tangential and radial directions, respectively, to 0.7971, 0.6529, and 0.1084. From the comparison of strain data, the tensile strain of the posterior region is always greater than the compressive strain of the anterior region in any direction. This is because the rear TBCHSs will bend laterally under the asymmetric loading effect, and the spring wire on the posterior region is farther away from the loading point, resulting in a stronger bending moment effect. In terms of the posterior region, the axial tensile strain of the outer diameter area of the posterior region is the largest. This is because the posterior region is subjected to macroscopic tensile force along the axial direction under the lateral force load, the spring wire in the outer diameter area of the posterior region is subjected to microscopic tensile force, and the outer diameter area is far from the center axis. These factors together lead to the largest axial tensile strain in the outer diameter area of the posterior region. For tangential strain of the posterior region, the tension in the posterior region of the rear TBCHSs has not only axial components but also horizontal components, which will cause shear force on the spring wire in the tangential direction. Therefore, the outer diameter area of the posterior region will be stretched in the tangential direction. For radial strain of the posterior region, the outer diameter area of the posterior region is slightly enlarged along the radial direction due to lateral tension, resulting in a certain radial tensile force. The strain mechanics of the anterior region of rear TBCHSs is similar with the posterior region. On the compression side of the anterior region, the axial compressive strain of the outer diameter area of the anterior region is larger. This is because the anterior region is subjected to macroscopic compression along axial direction under the lateral force load, the spring wire in the outer diameter area of the anterior region is subjected to microscopic compression deformation, and the outer diameter area is far from the center axis, resulting in a large axial compressive strain in the outer diameter area of anterior region. For the tangential strain in the anterior region, the compression in the anterior region of the rear TBCHSs has not only an axial component but also a horizontal component, which will cause the spring wire to generate shear force in the tangential direction, so the outer diameter area of the anterior region will be compressed in the tangential direction. For radial strain, the outer diameter area of the anterior region is slightly reduced due to lateral compression, resulting in a certain radial compression force.

Above analysis illustrates that the rear TBCHSs is more likely to be damaged at the part subjected to tensile strain in the posterior region under the loading condition of lateral force. Therefore, we selected the axial and tangential strains with larger tensile in the posterior region for the second step of analysis. The second step is to simultaneously test the axial and tangential strains of the outer diameter area of the upper, middle and downer coils in the posterior region to determine which coil has the largest strain. The test results are shown in Fig. 8.5(b), the axial and tangential strains of the outer diameter area of the upper coil in the posterior region are represented as outer A1 and outer T1, respectively; the axial and tangential strains of the outer diameter area of the middle coil in the posterior region are represented as outer A2 and outer T2, respectively; and the axial and tangential strains of the outer diameter area of the downer coil in the posterior region are represented as outer A3 and outer T3. The outer A1, outer A2, outer A3, outer T1, outer T2, outer T3 are 0.6249, 0.7971, 0.5551, 0.4815, 0.6529, 0.4120 respectively. No matter axial or tangential, the strains of the middle, upper and downer coils decrease successively. The reason is like that of the front TBCHSs. Due to the cumulative effect of deformation, the middle coil near the center is more deformed. And the sprung mass is greater than the unsprung mass, so the strain of the upper coil is greater than the strain of the downer coil.

In general, the strains that are most likely to cause damage in the rear TBCHSs are the axial and tangential strains of the outer diameter area of the middle coil in the posterior region. The rear TBCHSs produced resin cracks at an angle of 50° to the horizontal direction and resin debonding in the outer diameter area of the middle coil in the posterior region during the entire test process by combining with the morphological analysis. From the perspective of strain, the strain in this area is greater than the damage strain of the rear TBCHSs. The fundamental reason for the 50° crack in the resin is that the applied load is converted into axial, tangential and radial strain components in the middle coil. The axial and tangential strains are much greater than the radial strain based on the analysis of Fig. 8.5 (a) and the combined strain of the axial and tangential strains may form a shear combined strain in the 50° direction. This shear combined strain causes cracks in the spring wire along 50° direction. The way to avoid resin crack damage is to increase resin strength. In addition, the debonding phenomenon between the fiber and the resin indicates that the strain difference at the interface between the fiber and the resin is more serious. The interface between the fiber and the resin is an important area for deformation transmission. If the strain difference at the interface is too large, which will cause debonding. Since the fiber modulus is large, the fiber strain is smaller than resin under the same load. The way to improve the debonding phenomenon is to increase the modulus of the resin to reduce the strain difference between the fiber and the resin. These situations reflect the weakness of the rear TBCHSs under the specific load. The analysis illustrates the key to solving damage problem of the rear TBCHSs is to improve the performance of the resin matrix.

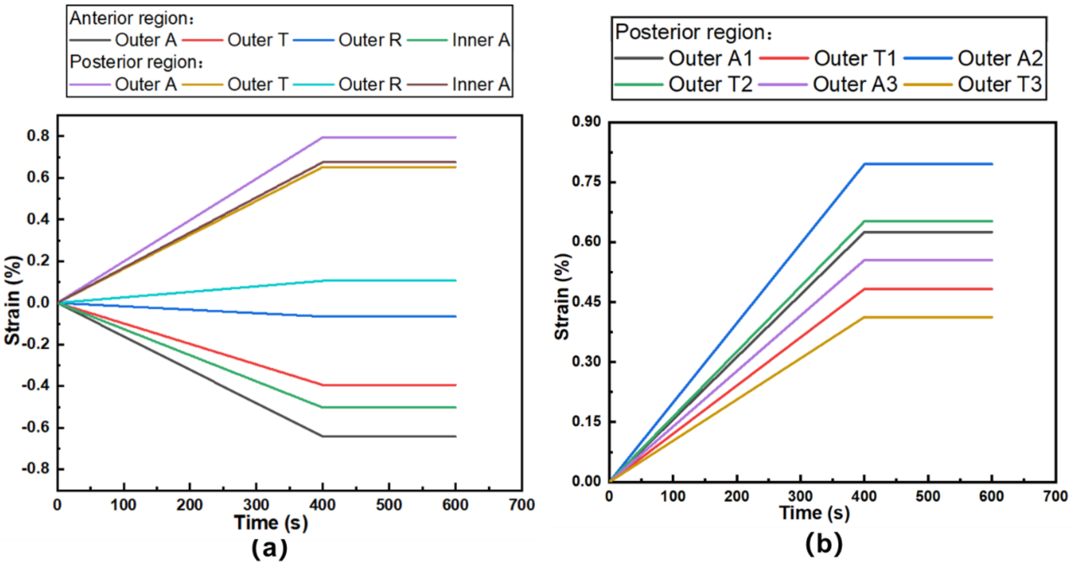

Fig. 8.5 (a) The strain of axial, radial and tangential directions of inner and outer diameter region of anterior and posterior region of rear TBCHSs in middle coil and (b) the strain of axial and tangential directions of outer diameter region of posterior region of rear TBCHSs in different coils.

8.3.3 Optimization of resin and geometry of TBCHSs

8.3.3.1 Optimization of resin of TBCHSs

Due to the damage that just happened in the resin part of the TBCHS, the optimization of resin is the key point to improve the TBCHS to avoid damage. originally, to save the cost of experiment the low-cost room temperature resin GCC135/GCC137 have been chosen to firstly optimize the reinforcement in our previous work(Chen, Chong, et al., 2024; Chen, Xing, et al., 2024). After that, the medium temperature resin R118/H103 have been selected by comparing the performance under different curing temperature to further optimize the performance of resin. However, the above results show that the performance of medium temperature curing resin is still not enough. Therefore, the high temperature curing resin TDE86/70 acid anhydride has been chosen for further optimization. Based on the above analysis we can know the reason for resin damage of TBCHSs is the combination effects of large axial strain caused by tensile and tangential strain caused by bend. Therefore, the tensile and bend performance of three types of resins under different curing temperature have been compared for ensuring the optimization degree of resin.

Fig. 8.6 showed the tensile strain-stress curves of GCC135/GCC137, R118/H103, TDE86/70 acid anhydride under different curing temperature. It is obvious that the curves of GCC135/GCC137, R118/H103 are non-linear while the curves of TDE86/70 acid anhydride are linear. Because the GCC135/GCC137 is room temperature curing resin, there is just one curve in fig. 8.6 (a). And in terms of R118/H103 (Fig. 8.6 (b)), the resin curing at 120℃/2H has the largest strain and stress. When the curing time increase to 8H at same 120℃, strain and stress. And when the curing temperature decline by 60℃ and curing time rise to 16H, the stress and strain decline significantly. To clearly compare the performance of resins, the special value of several indicators including tensile fracture strain, tensile strength, tensile modulus and tensile toughness of resin have been listed in Table 8.1. Tensile fracture strain is the maximum strain, tensile strength is the maximum stress, tensile modulus is stress divided by strain, and tensile toughness is the area under strain-stress curve.

The tensile fracture strain, tensile strength, tensile modulus and tensile toughness of R118/H103 curing at 120℃/2H are large 12.46%, 24.32%, 19.81% and 43.8% than that of R118/H103 curing at 120℃/8h respectively. Although the tensile modulus of R118/H103 curing at 60℃/16h is large 31% than that of R118/H103 curing at 120℃/2h, the tensile fracture strain, tensile strength, and tensile toughness are small 56.23%, 23.37, and 71.65% respectively. Therefore, the optimal curing temperature of R118/H103 is 120℃/2H.

As for TDE86, the curing temperature difference is mainly in the third stages, that is the post curing stage, because the first two curing stages have little effect on performance based on the same product. The post curing stage mainly impacts the toughness and modulus. The tensile fracture strain, tensile strength, tensile modulus and tensile toughness decrease with the increasing post curing time, as shown in Fig. 8.6 (c). Therefore, the optimal curing temperature of TDE86 is 90℃/2h+130℃/2h+180℃/2h. The tensile fracture strain, tensile strength, tensile modulus and tensile toughness of TDE86 curing at 90℃/2h+130℃/2h+180℃/2h can be 42.45%, 140.8%, 65.05% and 291.19% larger than that of TDE86 curing at 85℃/3.5h+130℃/1h+160℃/6h respectively. The performance of both R118/H103 and TDE86/70 acid anhydride decline with increasing curing time, this is because the long curing time cause aging of resin so that the mechanical performance decreases.

Fig. 8.6 (d) is the comparison of optimal performance of three types of resin. It is obvious that the TDE86 has the largest tensile strength and modulus. Although the tensile fracture strain of TDE86 is small lightly than other two, the tensile strength, tensile modulus and tensile toughness of TDE86 are 55.54%, 37.09% and 23.49% larger than R118/H103 and 170.70%, 25.92% and 69.89% larger than GCC135 respectively. Therefore, TDE86 will be used to manufacture the TBCHSs under curing temperature 90℃/2h+130℃/2h+180℃/2h.

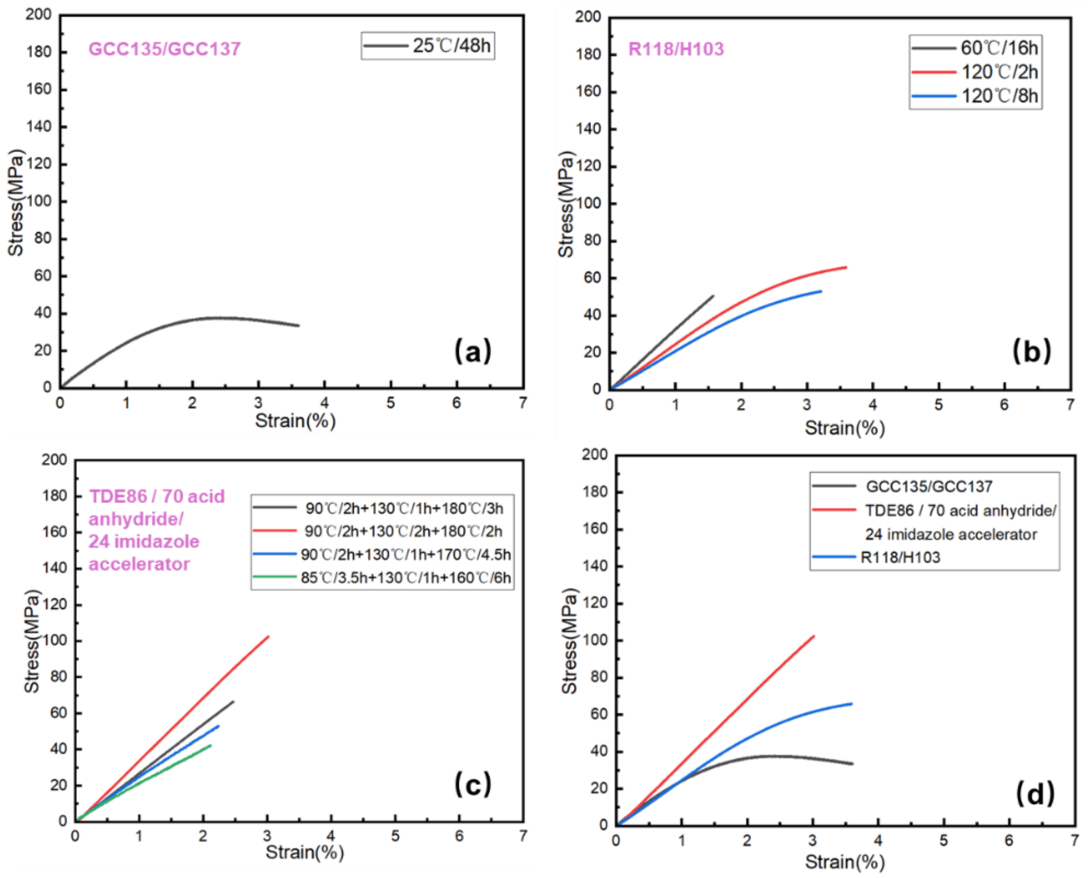

Fig. 8.6 (a) the tensile strain-stress curves of GCC135/GCC137, (b) the tensile strain-stress curves of R118/H103, (c) the tensile strain-stress curves of TDE86/70 acid anhydride/24 imidazole accelerator and (d) the optimal tensile strain-stress curves of GCC135/GCC137, R118/H103, TDE86/70 acid anhydride/24 imidazole accelerator

Table 8.1：the tensile fracture strain, tensile strength, tensile modulus and toughness of three types of resin under different curing temperatures.

Resin	**Curing temperature**	**Tensile fracture strain （%）**	**Tensile strength (MPa)**	**Tensile modulus (GPa)**	**Tensile toughness (MJ/m^3)**
GCC135/GCC137	25℃/48h	3.62	37.81	2.70	102.49
R118/H103	60℃/16h	1.58	50.42	3.27	39.96
	120℃/2h	3.61	65.80	2.48	140.99
	120℃/8h	3.21	52.93	2.07	98.04
TDE86 / 70 acid anhydride/	90℃/2h+130℃/1h+180℃/3h	2.47	66.36	2.69	78.06

24 imidazole accelerator	90 ℃ /2h+130 ℃ /2h+180℃/2h	3.02	102.35	3.40	174.12
	90 ℃ /2h+130 ℃ /1h+170℃/4.5h	2.24	52.91	2.44	59.48
	85 ℃ /3.5h+130 ℃ /1h+160℃/6h	2.12	42.50	2.06	44.51

Fig. 8.7 showed the bend strain-stress curves of GCC135/GCC137, R118/H103, TDE86/70 acid anhydride under different curing temperatures. The bend curves characterize and the performance trend of the three types of resin (Fig. 8.7 (a-c)) are similar with tensile performance. The unstable of initial stage is caused by the jig of test instrument, but there is no effect on the performance of resin. The result shown that the optimal curing temperature of R118/H103 and TDE86 is 120℃/2h and 90℃ /2h+130℃/2h+180℃/2h.

Fig. 8.7 (d) is the comparison of optimal performance of three types of resin. It is obvious that the TDE86 has the largest bend strength and modulus. The flexural fracture strain of TDE86 is smaller than others, but according to Table 8.2, the flexural strength, flexural modulus and flexural toughness of TDE86 are 55.52%, 68.25% and 6.29% larger than R118/H103 and 141.07%, 96.87% and 6.17% larger than GCC135 respectively.

The result of bend performance is consistent with tensile performance, which can prove the accuracy of the two experiments. Finally, TDE86 resin under curing temperature 90 ℃ /2h+130 ℃ /2h+180 ℃ /2h is selected to further optimize the performance of TBCHSs.

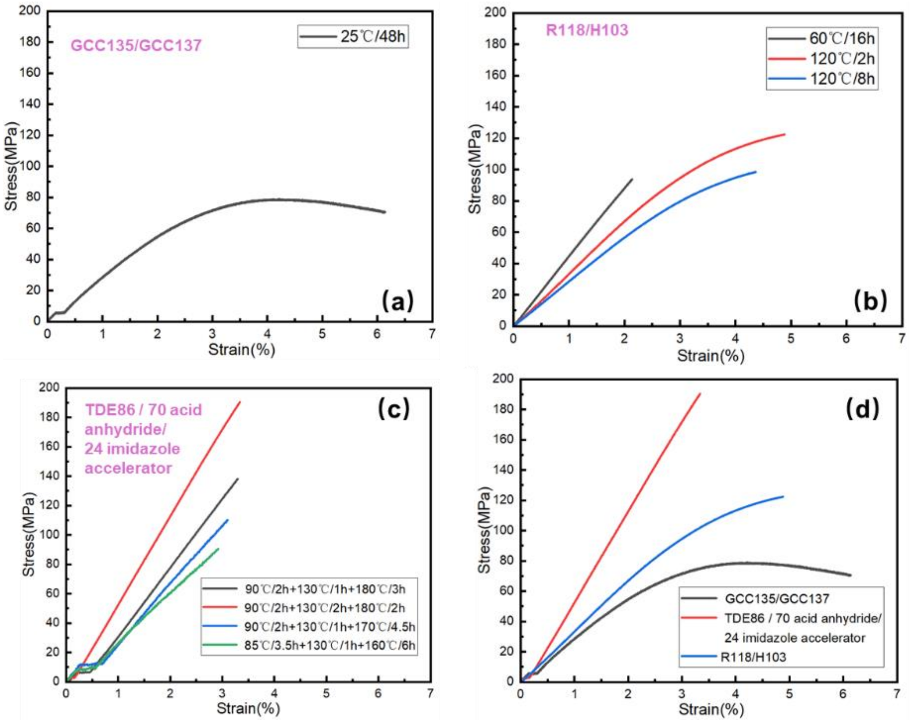

Fig. 8.7 (a) the flexural strain-stress curves of GCC135/GCC137, (b) the flexural strain-stress curves of R118/H103, (c) the flexural strain-stress curves of TDE86/70 acid anhydride/24 imidazole accelerator and (d) the optimal flexural strain-stress curves of GCC135/GCC137, R118/H103, TDE86/70 acid anhydride/24 imidazole accelerator

Table 8.2：the flexural fracture strain, flexural strength, flexural modulus and flexural toughness of three types of resin under different curing temperatures.

Resin	**Curing temperature**	**Flexural fracture strain （%）**	**Flexural strength (MPa)**	**Flexural modulus (GPa)**	**Flexural toughness (MJ/m^3)**
GCC135/GCC137	25℃/48h	6.15	78.96	2.88	357.08
R118/H103	60℃/16h	2.14	93.78	4.44	101.08
	120℃/2h	4.88	122.39	3.37	356.65
	120℃/8h	4.36	98.46	2.89	248.01
TDE86 / 70 acid anhydride/	90℃/2h+130℃/1h+180℃/3h	3.30	138.08	4.18	206.24

24 imidazole accelerator	90℃/2h+130℃/2h+180℃/2h	3.35	190.35	5.67	379.11
	90℃/2h+130℃/1h+170℃/4.5h	3.10	110.12	3.55	156.63
	85℃/3.5h+130℃/1h+160℃/6h	2.92	90.52	3.10	125.15

8.3.3.2 Optimization of geometry of TBCHSs

To meet the installation environment requirements, the contour size and the diameter of spring wire of TBCHSs is same as the steel spring on JEEP TJ2004. However, we find the geometry of spring is not totally limited through observing and measuring the installation environment, which means the geometry of TBCHSs can be adjusted to some extent for improving the performance. It is well known that the diameter of spring wire has a huge impact on the stiffness of spring, because the stiffness of spring is proportional to the fourth power of the diameter of spring wire. Therefore, apart from changing the resin, the diameter of spring wire of TBCHSs also is changed from 15 mm to 25 mm for maximum optimization of TBCHSs. 25mm is the maximum limitation of spring wire, which is determined based on the installation environment. After ensuring the optimization schedule, the optimal TBCHSs have been manufactured through the same manufacturing method, but the PVC mold and related joints have been enlarged to match the geometry of optimal TBCHSs.

8.3.4 Strain analysis of optimal TBCHSs during installation

The optimal TBCHSs have been installation on JEEP TJ2004 again, as depicted in Fig. 8.8. We can observe from Fig. 8.8 that there is no damage happening on the optimal front TBCHSs and the upper support post does not attach with lower support post, meaning the weight of vehicle is acted on optimal TBCHSs but support post. The optimal front TBCHSs have the ability to become the front suspension spring of the vehicle. Moreover, there is no damage happening on optimal rear TBCHSs under the whole installation process that is from the suspension to totally on the ground, indicating the optimal TBCHSs have ability to subject the lateral force caused by the installation environment of rear spring.

Fig. 8.8 The installation experiment of optimal front and rear TBCHSs.

In addition, the strain information of optimal TBCHSs have been collected under simulation installation on Intron5969 for clearly detecting the spring situation. The strain collecting positions and directions of optimal front and rear TBCHSs is same as previous front and rear TBCHSs. The strain of optimal front and rear TBCHSs is shown in Fig. 8.9. The curve shape and strain trend of optimal front and rear TBCHSs is same with the previous front and rear TBCHSs respectively, because they are under the same installation environment. However, it is obvious that the strain range of optimal front and rear TBCHSs is significantly less than the previous front and rear TBCHSs. This proves that the optimal front and rear TBCHSs has little deformation than previous front and rear TBCHSs under that same installation environment, meaning that the possibility of resin damage is negligible.

As for the optimal front TBCHSs, the strain of corresponding position and directions of anterior and posterior region is also similar. And the strain range is from -0.2458~0.1972 and the relatively large strain is still the axial and tangential directions in the inner diameter region by comparing the strain of axial, radial and tangential directions of inner and outer diameter region of anterior and posterior region of optimal front TBCHSs in middle coil (Fig. 8.9 (a)). Therefore, the strain of axial and tangential directions of inner diameter region of anterior region of optimal front TBCHSs in different coils is tested and shown in Fig. 8.9 (b). The strain in middle coil is largest, the axial and tangential strain of optimal front spring are -0.2458 and -0.0901 that is 43.54% and 41.96% smaller than -0.4313 and -0.1527 of previous front TBCHSs.

As for the optimal rear TBCHSs, the strain of posterior region is large than anterior region. And the strain range is from -0.3626~0.4451 and the relatively large strain is the axial and tangential directions in the outer diameter region of posterior region by comparing the strain of axial, radial and tangential directions of inner and outer diameter region of anterior and posterior region of optimal front TBCHSs in middle coil

(Fig. 8.9 (c)). Therefore, the strain of axial and tangential directions of outer diameter region of posterior region of optimal rear TBCHSs in different coils is tested and shown in Fig. 8.9 (d). The strain in middle coil is largest, the axial and tangential strain of optimal rear spring are 0.4456 and 0.3659 that is 43.90% and 42.28% smaller than 0.7943 and 0.6339 of previous rear TBCHSs.

From above analysis we can know that the strain of optimal TBCHSs less by about 42% than that of previous TBCHSs under the same installation environment. The decrease of strain of optimal TBCHSs is related to the increasing of tensile and bend modulus of TDE86 by combining the tensile and bend performance analysis of TDE86 and R118. In addition to the advantage of modulus, the strength and toughness of tensile and bend of TDE86 also are much larger than R118, which means that the optimal TBCHSs has higher strength and can absorb and release more energy during deformation. Therefore, the optimal TBCHSs have high safety to successfully replace steel spring.

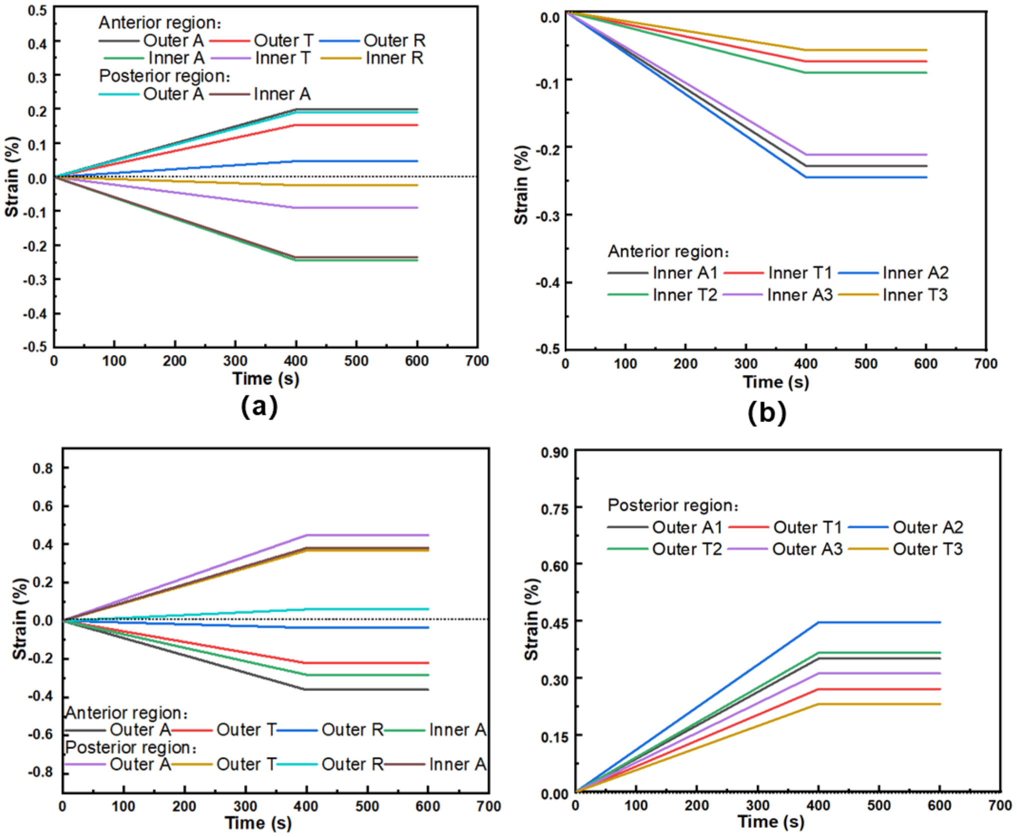

(a) (b)

(c) (d)

Fig. 8.9 (a) The strain of axial, radial and tangential directions of inner and outer diameter region of anterior and posterior region of optimal front TBCHSs in middle coil, (b) the strain of axial and tangential directions of inner diameter region of anterior region of optimal front TBCHSs in different coils, (c) The strain of axial, radial and tangential directions of inner and outer diameter region of anterior and posterior region of optimal rear TBCHSs in middle coil and (d) the strain of axial and tangential directions of outer diameter region of posterior region of optimal rear TBCHSs in different coils.

8.4 Summary

The feasibility of applicating TBCHSs has been evaluated through analyzing strain information and damage morphology of TBCHSs after installing them in field on the front and rear suspension system of Jeep TJ 2004. The experiment result showed that there is no damage to the front TBCHSs. The damage just occurs on the resin component of the posterior region of rear TBCHSs. Moreover, the strain analysis of TBCHSs during installation process illustrates the keys to solving damage problem of the rear TBCHSs are to improve the performance of the resin matrix. Therefore, the resin optimization has been carried out through comparing tensile and bend performance of three types of resin under different curing conditions. The result shown that the TDE86 curing at 90℃/2h+130℃/2h+180℃/2h has the best performance. Hence, the optimal TBCHSs have been manufactured by using TDE86 resin. The optimal TBCHSs have been installed on the vehicle again. There is no damage in the optimal front and rear TBCHSs during installation. The strain of optimal TBCHSs during installation is less than that of original TBCHSs, which illustrate the optimal TBCHSs have higher strength and stiffness. Therefore, the optimization of TBCHSs improve the possibility of potential application.

9. CONCLUSION

Helical spring plays a very important role in transportation, aerospace and industry field. The past few years have witnessed a potentially increase of CHSs deployment due to their light weight, high chemical resistance, excellent mechanical properties, making them promising metal alternatives. They can not only save fuels and thus expand overall cruising ranges but also reduce greatly carbon dioxide emissions. However, the insufficient of design method and the lack of comprehensive performance evaluation methods limit the application and development of CHSs. To solve this problem, the reinforcement structure of CHSs first is designed by combining the force analysis and textile structure. And static and dynamic performance have been optimized based on braided angle and braided layer number. The installation experiment also has been carried out in field to prove the feasibility of CHSs application. The detailed information of design, optimization and application is following.

Spring force analysis illustrates that when the spring is forced, the spring wire section is mainly subject to torque, which mean that increasing the performance of the outer surface of the spring wire is the most effective way for increasing CHS performance. Therefore, combined with textile structure, several CHSs that can change the outer structure are designed, including UCHS, MCHS, WCHS and BCHS. The four types of CHSs have been manufactured by injection-winding technology that is invented in the research. The characteristics of the injection-winding technology are low cost, easy assemble and portable. There are two types of molds, that are PVC injection mold and winding mold, need to be used. PVC injection mold can control the resin flow and the diameter of the spring wire of CHSs, and winding mold is used to fix the size of the CHSs. After manufacturing, the result shown that BCHS have optimal stiffness among them according to the initial compression comparison, the BCHS have been selected for studying further static and dynamic performance. The static performance has been optimized based on SBCHS with different braided angle of 0°, 15° and 30° (UCHS, SBCHS15° and SBCHS30°) The compression experimental results show that the spring constant of SBCHS15◦ and SBCHS30◦ can reach 105.4% and 171.4% higher than that of UCHS respectively. The internal mechanism of significantly improving compression performance of SBCHS is revealed by using a meso model. Numerical result shows that the mises stress of SBCHS15◦ and SBCHS30◦ can be 2.43 and 3.14 times higher than that of UCHS respectively, which means SBCHS30◦ have ability to bear more load. In addition, because the CHSs will be compression for a long time based on the application condition, the resilience (the ratio of the final height after unloading for 96 h to the initial height of the springs) have been researched. The resilience of UCHS, SBCHS15°, SBCHS30° and steel spring are 99.7%, 98.7%, 98.2% and 96.1% respectively, which proves SBCHSs have a better resilience than that of steel spring. Most of the research about optimization of helical springs is mainly focusing on spring constant and mass. Therefore, the research proposes meaningful indicator that is the specific spring stiffness (spring constant divided by mass). The results show that the specific spring stiffness of SBCHSs increases with an increasing braid angle. In addition, it is worth mentioning that the specific spring stiffness of SBCHS30° is higher than that of the steel spring with same geometry size. The result means that SBCHS30° can have a lighter mass than steel spring with the same spring constant, indicating SBCHS30° have more advantage than steel springs in reducing carbon emissions industry field. Therefore, the 30° braided angle have been selected to further optimized the dynamic performance based on the braided layer number.

Then, the dynamic impact performance first was explored by comparing MBLs-CHS including SBCHS, DBCHS and TBCHS. The impact response of MBLs-CHS is investigated using drop-weight impact tests. Experimental results elucidate a sequential improvement in the impact performance of SBCHS, DBCHS, and TBCHS. Specifically, TBCHS demonstrates enhancements of up to 5.1%, 78.3%, and 34.1% in deformation resistance, Fmax, and Ee, respectively, compared to SCHS. Subsequently, the internal mechanism behind this improvement have been elucidated by finite element model. Although solid model can represent accurately the 3D geometry and braided rules of MBLs-CHS. The stiffness characteristic of solid model is not consistent with the flexible characteristic of MBLs made of fibre yarns, which illustrates the extremely complex fibre interaction in MBLs caused by the shifting and nesting between the layers during braiding. In fact, the cross section of solid MBLs model of SBCHS, DBCHS and TBCHS can display that there are extensive gaps among fibre yarns and between adjacent braided layers, highlighting the presence of defects in the solid model. Therefore, the virtual fiber model (VFM) is introduced as an effective solution to address the limitations of the direct numerical solid model. The simulation result shown that the force-bearing contribution of the corresponding braided layers in SBCHS, DBCHS, and TBCHS is similar, emphasizing that the impact response difference is primarily attributed to the additional braided layer. Additionally, stress and motion responses of VFM revealed non-linear characteristics in stress, displacement, and velocity waves transitioning of MBLs-CHS. Finally, the impact mitigation ability of MBLs-CHS can be calculated based on velocity responses of VFM, highlighting that of TBCHS improves by 111.6% and 42.0% compared to SBCHS and DBCHS, respectively. Although the impact performance of SBCHS, DBCHS, and TBCHS have been compared and analyzed by combining experiment and simulation, the stiffness degradation is difficult to evaluate. And understanding stiffness degradation and developing suitable damage detection method for MBLs-CHS are important for their application and further development. Therefore, a coupled plasticity damage model for capturing stiffness degradation of MBLs-CHS is developed. Experimental results show that there is minor damage that only happens in the resin component of MBLs-CHS during impact. The element removal fraction in the simulation result is used to evaluate the damage severity, which is suggested to increase with impact energy (E_i) and decrease sequentially for SBCHS, DBCHS, and TBCHS. Specifcally, damage severity of TBCHS decreases by 51.3 % under 60 J impaction compared to that of SBCHS.

Although simulation results can predict damage severity and locations, damage evolution is challenging to detect physically in real time. So, time domain analysis is introduced to explore the in real time relationship between impact force and damage.

The amplitude intensity from time domain information is used to express the damage severity. The amplitude intensity increases with increasing Ei in each MBLs-CHS and decreases sequentially for SBCHS, DBCHS and TBCHS at the same Ei, which means the damage severity follows the same trend. The characterised damage trend using time domain analysis is consistent with simulation results, verifying the feasibility of the damage evaluation method of time domain. Moreover, to ensure the safety under impact, the prediction of potential stiffness degradation of MBLs-CHS under impact is implemented. The stiffness degradation under various amplitude intensity of MBLs-CHS have been fitted to predict the global stiffness degradation of MBLs-CHS in real time. The fitting formulas are univariate quadratic equations. The stiffness degradation firstly grows gradually with increasing amplitude intensity, but the growth rate declines gradually with increasing amplitude intensity. In addition, the difference of stiffness degradation of SBCHS, DBCHS and TBCHS is small at the initial stage and then increases gradually with increasing amplitude intensity. This illustrates that the advantage of reinforcement of SBCHS, DBCHS and TBCHS is not obvious at the initial stage and then the advantage increases with increasing amplitude intensity, indicating that stiffness degradation is expected to be eliminated by increasing the number of braided layers.

Based on above dynamic impact analysis, the TBCHS not only have best impact performance but also have minimum damage than SBCHS and DBCHS. Because MBLs-CHS will become the engineering parts to bear cyclic load during use, the fatigue performance research is important for ensuring the safety. Therefore, TBCHS is used to further explore the fatigue performance. The test and analysis of fatigue performance of TBCHS based on three stress levels of 100%, 90%, and 70%, the fatigue performance of TBCHS at three stress levels is obtained. The displacement and load curves from fatigue experiment shown that the fatigue life of TBCHSs increases with the decrease of stress level. In addition, the tightness of the hysteresis loop under three stress level increases with the increase of the fatigue cycle, which indicates that the fatigue performance of TBCHS is stable gradually with increasing cycle numbers. The area enclosed by the hysteresis loop represents the plastic strain energy consumed by TBCHSs during fatigue loading. The plastic strain energy increases with the increase of stress level, which indicates that the plastic strain energy consumed is higher at high stress level. The failure stiffness of TBCHSs is 38.7kgf/mm according to the residual stiffness method. The life of TBCHSs under 100% and 90% stress levels is only 2000 and 6500 respectively based on the failure stiffness of 38.7kgf/mm. But when the stress level drops to 70%, the stiffness decreases only 1.3% after 30000 cycles, which shows that the TBCHSs can be used for long time under the stress level of less than 70%. The displacement during fatigue test increases sharply at first and then slowly with the increase of the number of cycles, which illustrate the performance of TBCHSs is stable and will not fail suddenly. Then the fatigue model of TBCHS is established by finite element method, the evolution mechanism of spring fatigue damage is analyzed. The simulation result of damage propagation of TBCHSs under 100% stress level shown that the resin in the inner diameter area first cracks and propagates during the fatigue process. However, fiber only shows fiber bundles cracking and buckling and do not break, which indicate that the carbon fiber reinforcement has a great contribution to the fatigue performance to highlight the effectivity of structure optimization of reinforcement.

Apart from the optimization of static and dynamic performance, the feasibility of replace metal spring using TBCHS have been further investigated through installing TBCHSs in the vehicle. The installation experiment has been implemented on Jeep TJ 2004 in Kraft Motorsports Pty Ltd., in Perth, Australia. The feasibility of applicating TBCHSs has been evaluated through analyzing strain information and damage morphology of TBCHSs after installing them in field on the front and rear suspension system of Jeep TJ 2004. The experiment result showed that there is no damage to the front TBCHSs. The damage just occurs on the resin component of the posterior region of rear TBCHSs. Moreover, the strain analysis of TBCHSs during installation process illustrates the keys to solving damage problem of the rear TBCHSs are to improve the performance of the resin matrix. Therefore, the resin optimization has been carried out through comparing tensile and bend performance of three types of resin under different curing conditions. The result shown that the TDE86 curing at 90℃/2h+130℃/2h+180℃/2h has the best performance. Hence, the optimal TBCHSs have been manufactured by using TDE86 resin. The optimal TBCHSs have been installed on the vehicle again. There is no damage in the optimal front and rear TBCHSs during installation. The strain of optimal TBCHSs during installation is less than that of original TBCHSs, which illustrate the optimal TBCHSs have higher strength and stiffness. Therefore, the resin optimization of TBCHSs improve the possibility of potential application. This research establishes a robust foundation for performance studies and offers valuable guidelines for the engineering application of CHSs.

10. FUTURE WORK AND PROSPECTION

10.1 Future work

10.1.1 Strain analysis of original metal springs and optimal TBCHSs during driving

The optimal TBCHS already have been successfully installed on the vehicle in chapter 8. But it is unknown whether they can be successfully used while driving. The driving performance needs to be further explored for ensuring the feasibility of replace steel spring using optimal TBCHSs. The strain of TBCHS in driving period should be monitored and compared with the original metal spring to clearly understand the application feasibility and advantage of TBCHS.

Currently, the strain of original metal spring under different driving speeds of 20 km/h, 40 km/h and 60km/h including the process of speed up and slow down have been collected. The strain test during driving period have been implemented at long, straight and unbusy road for ensuring safety. The strain of three stages of speed up, constant speed and slow down have been distinguished by using black dotted line, as shown in Fig. 10.1. The strain fluctuation of front metal spring is larger than the rear metal spring, this is because the front of the car is heavier than the rear. The front of the car has not only lots of parts including engine and transmission etc. but also includes the weight of the driver. Therefore, there is a large weight that causes large strain. In terms of front metal spring, the fluctuation phenomenon is gradually becoming more obvious with increasing travel speed. The maximum strain fluctuation occurs during speed up, because the vehicle is unsteady during speed. When the speed is constant the strain almost is unchanged apart from slight vibration, because the vehicle is in a steady situation. When the speed decreases the slightly fluctuation of strain happens. The strain range of front metal spring is 0.0305. In terms of rear metal spring, although the fluctuation phenomenon is not obvious, the strain fluctuation of speed up and slowdown is still clearly larger than constant. The reason is the same as the front one. The strain range of rear metal spring is 0.0103. The result showed that the fluctuation degree of the strain at all positions and directions of front and rear metal springs under the three types of speed is small. Therefore, we can judge that if the optimal TBCHSs can be successfully installed on the vehicle, there exist large possible they can be successfully used during driving period.

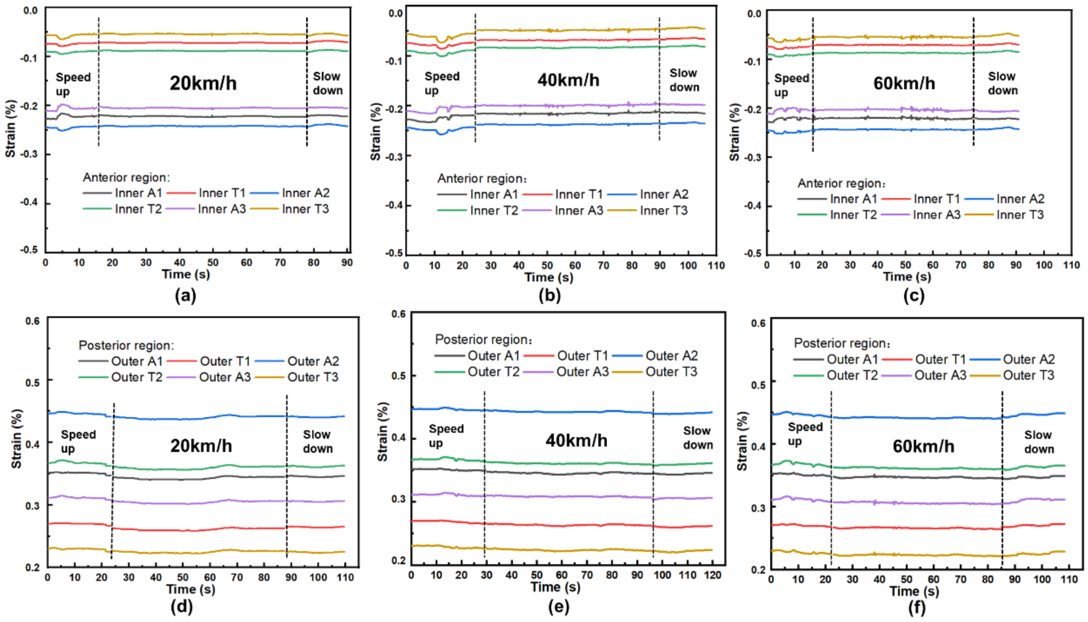

Fig. 10.1 (a) the strain of front metal spring during process of acceleration, constant speed of 20 km/h and deceleration, (b) the strain of front metal spring during process of acceleration, constant speed of 40 km/h and deceleration, (c) the strain of front metal spring during process of acceleration, constant speed of 60 km/h and deceleration, (d) the strain of rear metal spring during process of acceleration, constant speed of 20 km/h and deceleration, (e) the strain of rear metal spring during process of acceleration, constant speed of 40 km/h and deceleration and (f) the strain of rear metal spring during process of acceleration, constant speed of 60 km/h and deceleration.

It is well known that apart from the speed up, constant speed and slow down, turning, going uphill and downhill are also common operations in car driving. Therefore, the strain of turning, going uphill and downhill also have been collected in the unbusy and eligible two road sections. The road of uphill and downhill is same, because the vehicle makes a u turn to through the same path. The speed of turning is 20 km/h and the speed of going uphill and downhill is 60 km/h. The turning refers to the left turn, because the strain gauges are pasted on the front and rear spring that are installed on right of vehicle. When the vehicle turn left the front and rear metal springs will be subjected to large load. The strain of front and rear metal springs during turning, uphill and downhill have been plotted in Fig. 10.2. The result shows that the time of turning is 1.92 s and the time of uphill and downhill is 3.61 and 3.06 s respectively. The time of downhill is less than that of uphill, the vehicle's inertia causes the vehicle to accelerate downhill. When the vehicle turns left the strain of front and rear metal springs increase significantly. Because when the vehicle turns left the weight of the whole vehicle body is acted on the right of vehicle, causing both metal springs is subjected to larger load. The axial and tangential strain of front metal spring increases 21.33% and 33.52% respectively while the axial and tangential strain of rear metal spring increases 15.67% and 26.85% respectively. The strain increment of front metal spring is larger than that of rear metal spring. This is because the front of the vehicle is heavier that will have more weight suddenly act on the front metal spring. Moreover, the increment of tangential direction of front and rear metal springs is bigger than that of axial direction. This is because when the vehicle turns left, the subjected additional load of the front and rear metal spring includes not only vertical but also lateral load, and the effect of lateral load is larger than the vertical load. When the vehicle goes uphill, the strain of front metal spring declines while that of rear metal spring increases. Because the weight of vehicle body is concentrated on the rear of the vehicle while going uphill, the rear metal spring is subjected to more weight than the front one. Both strain increment of axial and tangential of front metal spring during uphill is same 15.29% and that of axial and tangential of rear metal spring during uphill is same 18.54% because the additional lateral load can be ignored during uphill. When the vehicle goes downhill, the strain of front metal spring increases while that of rear metal spring declines. Because the weight of vehicle body is concentrated on the front of the vehicle while going downhill, the front metal spring is subjected to more weight than the rear one. Both strain increment of axial and tangential of front metal spring during downhill is same 16.27% and that of axial and tangential of rear metal spring during downhill is same 13.66%. The reason is similar with the uphill that is the additional lateral load can be ignored during downhill.

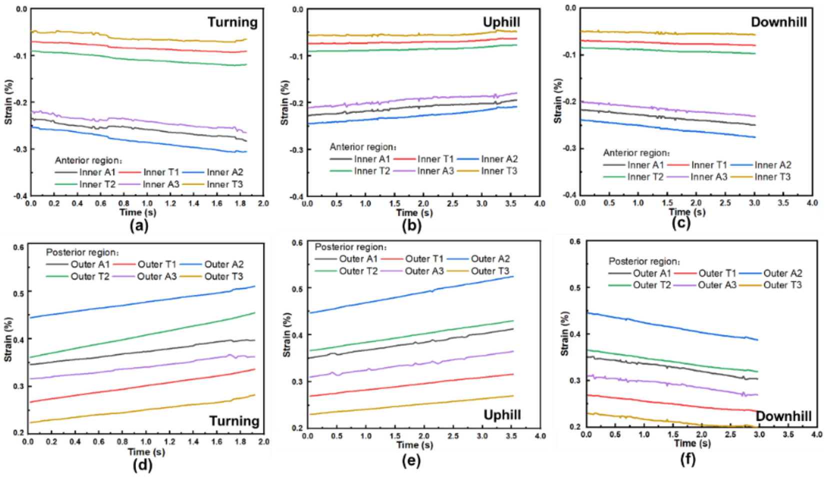

Fig. 10.2 (a) the strain of front metal spring during process of turning, (b) the strain of front metal spring during process of uphill, (c) the strain of front metal spring during process of downhill, (d) the strain of rear metal spring during process of turning, (e) the strain of rear metal spring during process of uphill and (f) the strain of rear metal spring during process of downhill.

The strain law of front and rear metal springs has been analyzed in detail. However, due to the lack of strain gauge and human resources, the strain of optimal front and rear TBCHSs during driving have not been collected. Therefore, the strain of optimal front and rear TBCHSs need to be collected and analyzed in the future work. So that the advantage and disadvantage of TBCHSs and metal springs can be understood clearly.

10.1.2 Stiffness degradation under aging test

If the optimal TBCHSs can be used to replace the metal spring, meaning optimal TBCHSs will be used on the vehicle long-term. This will involve two keys performances that are fatigue and aging. In the research, the fatigue performance has already been studied. Therefore, the aging performance should be researched in the future. Exposures to ultraviolet radiation, temperature cycles and moisture are known to degrade the polymeric matrix. Optimal TBCHS will be subjected to accelerated aging in an aging chamber with controlled conditions of temperature, humidity and UV-radiation. Then the relationship between stiffness degradation and aging conditions will be revealed to clearly understand the aging performance.

10.2 Prospections

3D printing technology has been able to prepare parallel structure CHSs, which shows that 3D printing has the potential to solve the manufacturing and batch production problems of CHSs with various structures and lays a foundation for the popularization of CHSs. Metal materials can be added to CHSs to improve its mechanical properties and functionalize CHSs, such as flame retardant and shielding electromagnetic interference. The dynamic damage of CHSs can be monitored in real time combined with intelligent sensing technology to ensure its safety performance in the process of use.

10.2.1 New manufacturing technology of CHSs

3D printing, also known as additive manufacturing, is a manual manufacturing method. It can create complex geometry without cost and time penalty (Zhuo et al., 2021). Therefore, it is usually used to produce prototype parts. 3D printing technology has been used to realize the manufacturing of helical structure (Bayaniahangar et al., 2021). Chapiro (Chapiro, 2016) pointed out that 3D printing technology can well develop the anisotropic mechanical properties of composites, which provides a promising way to give full play to the potential of composites. Material extrusion process is one of the

3D printing techniques capable of achieving continuous fibre composite printing. In recent years, many researchers have made various improvements to the continuous printing technology of fiber composites (Azarov et al., 2019). Yuan *et al.* (Yuan et al., 2021) used 3D printing technology to realize the manufacture of parallel structure CHSs, as shown in Fig. 10.3. In addition, Ekoi *et al.* (Ekoi et al., 2021) manufactured woven carbon fiber composites using 3D printing technology. The test and analysis results show that it has excellent fatigue strength and reveals its potential in high cycle load applications. These show that 3D printing has the potential to solve the problems of manufacturing and batch production of CHSs with various structures. In addition, 3D printing allows the customization of part strength by aligning fibres in designated directions and controlling fibre volume fraction throughout the part, which means that CHSs with equal and variable stiffness can be prepared according to the demand. Moreover, Mohammadizadeh *et al.* (Mohammadizadeh et al., 2019) have comprehensively summarized the analysis methods of mechanical properties of 3D printed continuous fiber composites, which lays a foundation for replacing traditional polymer composites. When the 3D printing technology and corresponding analysis method of CHSs are matured, it will be of great significance to the application of CHSs in the aerospace field. For example, it can quickly manufacture emergency helical structure parts of space station to ensure the safe and long-term running of space station on orbit in the future.

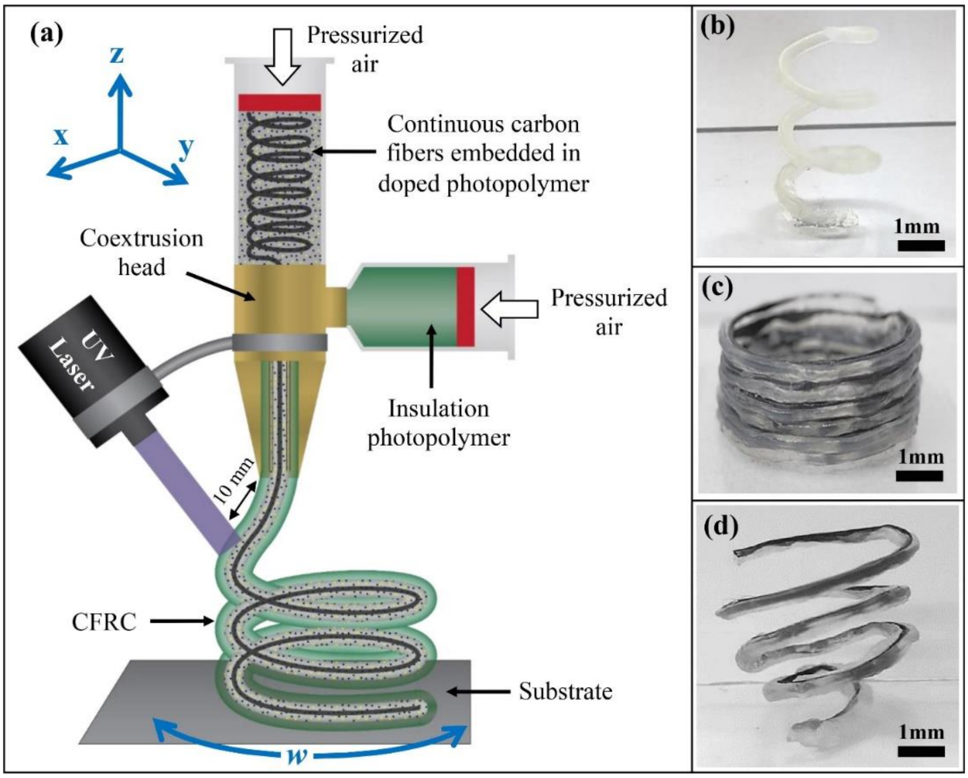

Fig. 10.3 (a) Shows the schematics of the UV-assisted coextrusion deposition of 3D continuous carbon fiber multifunctional composites; (b) a printed free standing CHSs; (c) a hollow cylinder structure CHSs and (d) a free-standing tapered CHSs (*Yuan et al., 2021*).

10.2.2 CHSs mixed with metal

CHSs are subjected to shear during compression, and the shear modulus of reinforcement fiber is poor (Reiner et al., 2021). To improve the sheer performance of CHSs, metal should be added to CHSs. Since the main stress area is the periphery of the spring wire, the copper wire braided tube can be used to wrap the reinforcement to maximize the shear performance of CHSs. In addition to improving the mechanical properties of CHSs, the addition of metal materials can also make the matrix in CHSs have excellent flame retardant properties due to the nonflammability and high specific heat capacity of the metal (Hou et al., 2021). Researchers added metal flame retardants to organic flame retardants mixed into the matrix, which overcomes the product performance defects caused by poor compatibility of metal flame retardants (Ma et al., 2020). In addition, Duan *et al.* (Duan et al., 2021) prepared ultra-efficient electromagnetic interference shielding composites by constructing a perfect 3D carbon metal hybrid network in the matrix, which widened the application potential of CHSs in military industry, for example, weapons with helical structure can avoid enemy detection during operation. It can be seen from the above research that the addition of metal materials leads to the development of multifunctional CHSs.

10.2.3 Intelligent sensing monitoring system for CHSs

To ensure the safety performance of CHSs, it is necessary to detect its damage. Although non-destructive testing (NDT) technology has been widely used in some industrial applications, expensive equipment and off-line execution mode limit the further development of NDT technology (Pegorin et al., 2018). These limitations led researchers to find a self-sensing embedded system embedded with electrically conductive fillers such as carbon-based materials without affecting the integrity of the structure. The excellent electrical, thermal and mechanical properties of carbon nanotubes (CNTs) inspired researchers to mix them into polymer matrix composites as damage sensors (Thostenson et al., 2001). Carbon nanotubes form a conductive network which makes composite material exhibit good electrical signal response during mechanical loading, to evaluate the damage state of the composite material by monitoring the electrical response change under mechanical loading. The sensor has good application potential in composites. At present, damage sensing under static loading condition has been done extensively (Vadlamani et al., 2012). However, the application environment of CHSs is cyclic loading, to avoid catastrophic failure, timely detection of structural damage under dynamic load is an extremely important task for CHSs. Heeder *et al.* (Heeder et al., 2012) reported high strain rate electro-compressive response of CNTs embedded epoxy composites. Lim *et al.* (Lim et al., 2011) also investigated the electrical response of CNTs embedded woven fabric/epoxy composites under dynamic compression loading by using split Hopkinson pressure bar. However, the test system of these methods is more complex, which is not conducive to the real-time detection of the CHSs in the service environment. The multimeter detection method not only makes the detection process simpler but also has lower cost and high efficiency. If the resistance of the multimeter rises sharply during use, it means that there is serious damage inside CHSs, and the CHSs should be replaced in time to avoid safety accidents.

PUBLICATIONS AND AWARDS

Papers

1. L Chen, J Chong, Y Ouyang, L Wu, et al. Understanding stiffness degradation of composite helical springs with multi-braided layers under impact[J]. Composites Part A: Applied Science and Manufacturing, 2024:108327.
2. Chen L, Chong J, Jiang Q, et al. Understanding the static performance of composite helical springs with braided nested structures[J]. Composites Part A: Applied Science and Manufacturing, 2023: 107822.
3. Chen L, Xing W, Wu L, et al. Understanding multiple parameters affecting static and dynamic performances of composite helical springs[J]. Journal of Materials Research and Technology, 2022;20:532–50.
4. Chen L, Wu L, Fu H, et al. Design and Performance Evaluation of Polymer Matrix Composite Helical Springs[J]. Polymers, 2022, 14(18): 3900.
5. Chen L, Xing W, Chong J, et al. Analysing Impact Characteristics of Composite Helical Springs with Multi-braided Layers Based on Virtual Fiber Model[J]. Composites Communications, 2025: 102255.

International conference

- 10th Australasian Congress on Applied Mechanics (Adelaide, Australia)
- 11th Australasian Congress on Applied Mechanics (Brisbane, Australia)

Awards

- 2024 Chris Marlin Postgraduate Student Publication Prize of Flinders university, Australia
- 2023 College of Science and Engineering Higher Degree by Research International Conference Support Grant

ACKNOWLEDGEMENT

My doctoral study is coming to an end. I would like to thank Flinders University for providing me with a platform and opportunity to learn knowledge and for providing me with a scholarship. I appreciate the funding support from ARC Training Centre for Green Chemistry in Manufacturing on providing me a PhD scholarship on this study.

There are many people who helped me during my doctoral study. First, I would like to thank my supervisor, Professor Youhong Tang, for providing me with the opportunity to study for a doctorate, which gives me hope when I was confused in my life. He has provided me with a lot of help since I applied for my doctorate. He has devoted a lot of effort to every stage of my project. With his rich knowledge reserves, rigorous scientific research style and strong sense of responsibility, he has carefully guided me from every detail of the experiment to the logic, analysis and wording of the paper. He not only helped me master professional knowledge and skills in the doctoral stage but also focused on training my ability to independently design experiments and write papers. During this period, I understand that doing scientific research requires not only rigor, carefulness and patience, but also active thinking. Only by reading the literature carefully, doing every step of the experiment steadily, and mastering the research direction and cutting-edge dynamics of my own project can I gain achievements. He is also a mentor who considers the scientific research career of students. He has always encouraged me to attend international conferences and communicate with people in the same scientific research field to broaden my horizons. He will also lead me to cooperate with more schools to expand my scientific research field. He always tries his best to fight for and coordinate scientific research resources for me, assist me in removing obstacles on the road of scientific research. In addition to academic studies, he also gave me a lot of guidance in dealing with people, teaching me to be friendly with others, which also promoted the smooth progress of my experimental tests from the side.

I would like to thank the School of Textile Science and Engineering of Tiangong University for providing me with a scientific research platform during my remote learning. The excellent scientific research conditions and environment of the school meet my scientific research needs. I would also like to thank the School of International Exchange of Tiangong University for providing me with accommodation and ensuring my scientific research life. I would like to thank Professors Liwei Wu and Qian Jiang of Tiangong University for providing me with rich scientific research resources and a strong scientific research atmosphere during my doctoral studies. The preparation of the sample reinforcement in this study is from the scientific research platform of these two teachers. To ensure that I could complete my studies successfully, the two teachers allowed me to join their research group, spent a lot of time carefully guiding my research, revising my thesis, helping me find test methods and instruments, and ensuring that my research could proceed smoothly. Thanks to Professor Xiaoyuan Pei of Tiangong University, who always tried her best to help me every time I needed an experimental platform and arranged students to assist me in doing experiments. At the same time, she also carefully explained the experimental safety rules to me to ensure that I could pay attention to my own safety and avoid accidents during the experiment. The sample curing steps in this study were all carried out in the laboratory arranged by Professor Xiaoyuan Pei.

Thanks to Mr Joel Chong, an industrial partner, for providing me with scientific research opportunities. And using his own resources to help me do the testing. The application of TBCHSs in Chapter 8 of this thesis was completed in his car repair shop (Kraft Motorsports) in Perth. He not only provided me with a test vehicle (JEEP TJ 2004) but also provided me with a lot of human resources. He actively arranged staff to assist me in the TBCHSs installation test. Thanks to Mr. Tony Penstone and other staff for taking time out of their busy schedule to help me with my installation test. Thanks to the CSE engineering services team at Flinders University, who patiently provided training and assisted in the test when I needed. Mr. Tim Hodge trained me in how to use the hexapod vibration platform, Instron and fatigue rotating machines, and always made reasonable time arrangements for my tests. And the student Mr. Miller McRae spent his time to provide me with TBCHSs installation services on the simulator for the FSAE which belongs to FMT and assisted me in the design and customization of the holder that matches the size of the TBCHSs.

In addition, many classmates also gave me great help. First, I would like to thank Mr. Yunzhong Wang for his help in my life from enrollment to graduation, which made me feel warm in an unfamiliar environment. Secondly, I would like to thank Mr. Qi Hu for always being willing to spend time discussing and solve problems with me when I encounter problems in my work. I would like to thank Dr. Wenjin Xing for answering my questions seriously when I encounter professional problems. I would like to thank my family for silently supporting every decision I make and giving me a stronger belief in learning. Finally, I would like to thank all the teachers who served as reviewers for their precious time to comment on and guide my thesis.

REFERENCE

Al-Qureshi, H. J. J. o. m. p. t. (2001). Automobile leaf springs from composite materials. *118*(1-3), 58-61.

Arularasan, R., & Sabapathy, Y. (2014). Fabrication And Testing Of FRP Open Coil Springs. *Applied Mechanics and Materials*, *592*, 1065-1069.

Ashok, N. A., Kumar, R., Singh, M., Singh, J., Gulati, P., & Singh, J. (2021, June). Development Method, Manufacturing Process of Fibre Reinforced Polymer Composite Type Helical Springs: A Review *Recent Trends in Engineering Design*, Singapore.

Ayadi, S, & Taïeb, E. H. (2017). Natural Frequencies of Composite Cylindrical Helical Springs. *Springer International Publishing Switzerland* 2017.

Azarov, A. V, Antonov, F. K., Golubev, M., Khaziev, A. R., & Ushanov, S. A. (2019). Composite 3D printing for the small size unmanned aerial vehicle structure. *Composites Part B: Engineering*, *169*, 157-163.

Azzam, B. (2010). An optimum design for composite helical springs. *Proceedings of the Institution of Mechanical Engineers, Part D: Journal of Automobile Engineering*, *224*(3), 347-354.

Bai, J., Liu, T., Wang, Z., Lin, Q., Cong, Q, Wang, Y.,…Bu, G. (2021). Determining the best practice–Optimal designs of composite helical structures using Genetic Algorithms. *Composite Structures*, *268*, 113982.

Bai, J., Liu, T., Wang, Z., Lin, Q., Cong, Q., Wang, Y.,…Bu, G. (2021). Determining the best practice–optimal designs of composite helical structures using genetic algorithms. *Composite Structures*, *268*, 113982.

Bakhshesh, M., & Bakhshesh, M. (2012). Optimization of steel helical spring by composite spring. *International journal of multidisciplinary science and engineering*, *3*(6), 47-51.

Bayaniahangar, R., Ahangar, S. B., Zhang, Z., Lee, B. P., & Pearce, J. M. (2021). 3-D printed soft magnetic helical coil actuators of iron oxide embedded polydimethylsiloxane. *Sensors and Actuators B: Chemical*, *326*, 128781.

Bhatia, S. S., & Bergaley, A. (2014). Analysis of the design of helical compression spring to study the behavior of steel and composite used as spring materials. *International Journal of Engineering Sciences & Research Technology (IJESRT)*, 576-584.

Bhudolia, S. K., Gohel, G., Vasudevan, D., Leong, K. F., & Gerard, P. (2022). On the mode II fracture toughness, failure, and toughening mechanisms of wholly thermoplastic composites with ultra-lightweight thermoplastic fabrics and innovative Elium® resin. *Composites Part A: Applied Science and Manufacturing*, *161*, 107115.

Boonniteewanich, J., Pitivut, S., Tongjoy, S., Lapnonkawow, S., & Suttiruengwong, S. (2014). Evaluation of carbon footprint of bioplastic straw compared to petroleum based straw products. *Energy Procedia*, *56*, 518-524.

Zhan, B., Sun, L., Huang, B., Zhao, G., & Wang, Q. (2018). Design and optimization of automotive composite helical spring. *Journal of Beijing University of Aeronautics and Astronautics*, *44*(7), 1520-1527.

Çalım, F. F. (2009). Dynamic analysis of composite coil springs of arbitrary shape. *Composites Part B: Engineering*, *40*(8), 741-757.

Chakladar, N. D., Mandal, P., & Potluri, P. (2014). Effects of inter-tow angle and tow size on carbon fibre friction. *Composites Part A: Applied Science and Manufacturing 65*, 115-124.

Chapiro, M. (2016). Current achievements and future outlook for composites in 3D printing. *Reinforced Plastics*, *60*(6), 372-375.

Charles, L., & Srikanth, P. (2014). Development of a lightweight CFRP coil spring. *SAE Technical Paper*.

Chawla, K. K. (2012). Composite materials: science and engineering. *Springer Science & Business Media*.

Chen, B, & Chou, T. (2000). Compaction of woven-fabric preforms: nesting and multi-layer deformation. *Composites Science and Technology*, *60*(12-13), 2223-2231.

Chen, F., Hiltner, A., & Baer, E. (1992). Damage and failure mechanisms of continuous glass fiber reinforced polyphenylene sulfide. *Journal of composite materials*, *26*(15), 2289-2306.

Chen, L, Chong, J., Jiang, Q, Wu, L, & Tang, Y. (2024). Understanding the static performance of composite helical springs with braided nested structures. *Composites Part A: Applied Science and Manufacturing*, *176*, 107822.

Chen, L., Wu, L., Chong, J., & Tang, Y. (2021). Composite helical springs with cladding structures-design, manufacturing, and mechanism studies. *ACAM10: 10th Australasian Congress on Applied Mechanics: 10th Australasian Congress on Applied Mechanics*,

Chen, L., Wu, L., Fu, H., & Tang, Y. (2022). Design and Performance Evaluation of Polymer Matrix Composite Helical Springs. *Polymers*, *14*(18), 3900.

Chen, L., Xing, W., Chong, J., Jiang, Q., Ouyang, Y., Wu, L., & Tang, Y. (2024). Understanding stiffness degradation of composite helical springs with multi-braided layers under impact. *Composites Part A: Applied Science and Manufacturing*, 108327.

Chen, L., Xing, W., Wu, L., Chong, J., Lei, T., Jiang, Q., & Tang, Y. (2022). Understanding multiple parameters affecting static and dynamic performances of composite helical springs. *Journal of Material Research Technology*, *20*, 532-550.

Chen, P., Lu, C., Yu, Q., Gao, Y., Li, J., & Li, X. (2006). Influence of fiber wettability on the interfacial adhesion of continuous fiber - reinforced PPESK composite. *Journal of Applied Polymer Science*, *102*(3), 2544-2551.

Chen, S. a., Zhang, Y., Zhang, C., Xiong, X., Li, G., & Hu, H. (2014). A simple way to prepare C/SiC spring. *International Journal of Applied Ceramic Technology*, *11*(1), 186-192.

Cheng, Y., Chen, L., & Chen, X. (2015). A beam scanning method based on the helical antenna for space-based AIS. *The Journal of Navigation*, *68*(1), 52-70.

Chiu, C., Hwan, C., Tsai, H., & Lee, W. (2007). An experimental investigation into the mechanical behaviors of helical composite springs. *Composite Structures*, *77*(3), 331-340.

Chiu, C., Tsai, K., Lee, Y., & Hwan, C. (2009). The effects of hybrid laminate structures on the compression and fatigue properties of helical composite springs. *Journal of advanced materials*, *41*(3), 57-69.

Chiu, C., Hwan, C., Tsai, H., & Lee, W. (2007). An experimental investigation into the mechanical behaviors of helical composite springs. *Composite Structures*, *77*(3), 331-340.

Choi, B., & Choi, B. (2015). Numerical method for optimizing design variables of carbon-fiber-reinforced epoxy composite coil springs. *Composites Part B: Engineering*, *82*, 42-49.

Choi, B., & Choi, B. (2015). Numerical method for optimizing design variables of carbon-fiber-reinforced epoxy composite coil springs. *Composites Part B: Engineering*, *82*, 42-49.

Clauberg, J., Huber, B., & Ulbrich, H. (2012). Simulation and Validation of Valve Springs in Valve Train Simulations. *Proceedings of the Eighth International Conference on Engineering Computational Technology*.

Clauberg, J., & Huber, R. (2013). Using non-smooth mechanics and parallelization techniques for the efficient simulation of different types of valve springs (0148-7191).

Daelemans, L., Cohades, A., Meireman, T., Beckx, J., Spronk, S., Kersemans, M.,…Van Paepegem, W. (2018). Electrospun nanofibrous interleaves for improved low velocity impact resistance of glass fibre reinforced composite laminates. *Materials & Design*, *141*, 170-184.

Opukuro, D., Amafabia, D., Haritos, G., & Montalvao, D. (2017). A review of structural health monitoring techniques as applied to composite structures. *Structural Durability & Health Monitoring*.

Xu, D., & Yin, Z. (2003). High strengthening spring steels and effect of alloying elements. *Metal heat treatment*, *28*(12), 30-36.

Xu, D., & Yin, Z. (2004). The tendency to high strength of spring steels and the effect of alloying elements. *Iron and steel*, *39*(1), 67-71.

Djomseu, P., Sardou, M. A., & Berg, T. R. (2008). Composite Coil Spring Development and Testing. *ASME/IEEE Joint Rail Conference*.

Dong, K. J., Wang, B., & Yu, A. (2013). Modeling of particle flow and sieving behavior on a vibrating screen: from discrete particle simulation to process performance prediction. *Industrial & Engineering Chemistry Research*, *52*(33), 11333-11343.

Drach, A., Drach, B., & Tsukrov, I. (2014). Processing of fiber architecture data for finite element modeling of 3D woven composites. *Advances in Engineering Software*, *72*, 18-27.

Duan, H., He, P., Zhu, H., Yang, Y., Zhao, G., & Liu, Y. (2021). Constructing 3D carbon-metal hybrid conductive network in polymer for ultra-efficient electromagnetic interference shielding. *Composites Part B: Engineering*, *212*, 108690.

Durville, D., Baydoun, I., Moustacas, H., Périé, G., & Wielhorski, Y. (2018). Determining the initial configuration and characterizing the mechanical properties of 3D angle-interlock fabrics using finite element simulation. *International Journal of Solids and Structures*, *154*, 97-103.

Ekanthappa, J., Basavarajappa, S., & Shankar, G. S. (2017). Fabrication & experimentation of the glass-epoxy helical spring reinforced with graphite powder. *Materials Today: Proceedings*, *4*(10), 11034-11038.

Ekanthappa, J., Basavarajappa, S., & Sogalad, I. (2013). Investigation on design and fabrication of continuous fiber reinforced composite helical spring for automobile suspension. *National Conference on Challenges in Research & Technology in the Coming Decades*.

Ekanthappa, J., Shankar, G. S., Amith, B., & Gagan, M. (2016, September). Fabrication and experimentation of FRP helical spring. *IOP Conference Series: Materials Science and Engineering,* Bristol.

Ekanthappa, J., Shankar, G. S. S., Amith, B. M., & Gagan, M. (2016). Fabrication and experimentation of FRP helical spring. *IOP Conference Series: Materials Science and Engineering*, *149*.

Ekoi, E. J., Dickson, A. N., & Dowling, D. P. (2021). Investigating the fatigue and mechanical behaviour of 3D printed woven and nonwoven continuous carbon fibre reinforced polymer (CFRP) composites. *Composites Part B: Engineering*, *212*, 108704.

El Said, B., Green, S., & Hallett, S. R. (2014). Kinematic modelling of 3D woven fabric deformation for structural scale features. *Composites Part A: Applied Science and Manufacturing*, *57*, 95-107.

Frank, J. (2020). Analysis and optimization of composite helical springs. *California State University, Sacramento*.

Frank, J. K. (2020). Analysis and optimization of composite helical springs [D, *California State University*. Sacramento:.

Gao, Y., Mai, Y., & Cotterell, B. (1988). Fracture of fiber-reinforced materials. *Zeitschrift für angewandte Mathematik und Physik*, *39*(4), 550-572.

Garcea, S., Wang, Y., & Withers, P. (2018). X-ray computed tomography of polymer composites. *Composites Science and Technology*, *156*, 305-319.

Ghassemieh, E. (2011). Materials in automotive application, state of the art and prospects. *New trends and developments in automotive industry*, *20*, 364-394.

Gobbi, M., & Mastinu, G. (2001). On the optimal design of composite material tubular helical springs. *Meccanica*, *36*(5), 525-553.

Goyal, D., & Pabla, B. (2016). The vibration monitoring methods and signal processing techniques for structural health monitoring: a review. *Archives of Computational Methods in Engineering*, *23*, 585-594.

Green, S., Long, A., El Said, B., & Hallett, S. (2014). Numerical modelling of 3D woven preform deformations. *Composite Structures*, *108*, 747-756.

Hamed, H. A. R., Ismail, M. R., & Najam, A. R. (2020). Design, Analysis and Manufacturing Polymer Fiber Reinforced Composite Helical Spring. *Al-Nahrain Journal for Engineering Sciences*, *23*(4), 338-344.

Heeder, N., Shukla, A., Chalivendra, V., & Yang, S. (2012). Sensitivity and dynamic electrical response of CNT-reinforced nanocomposites. *Journal of Materials Science*, *47*(8), 3808-3816.

Hou, Y., Xu, Z., Chu, F., Gui, Z., Song, L., Hu, Y., & Hu, W. (2021). A review on metal-organic hybrids as flame retardants for enhancing fire safety of polymer composites. *Composites Part B: Engineering*, 109014.

Houlu, H., & Chunan, D. (2008). Application status and development trend of automobile air spring. *Heavy truck*(3), 26-28.

Hu, J., Yu, T., Yin, S., & Xu, J. (2019). Low-speed impact mitigation of recoverable DNA-inspired double helical metamaterials. *International Journal of Mechanical Sciences*, *161*, 105050.

Huber, R., Clauberg, J., & Ulbrich, H. (2010). An efficient spring model based on a curved beam with non-smooth contact mechanics for valve train simulations. *SAE International Journal of Engines*, *3*(1).

Hwan, C., Chiu, C., Lee, W., & Lee, W. (2010). The effects of rubber core diameter and the number of braided outer layers on the compression and fatigue properties of helical composite springs. *Journal of advanced materials*, *42*(1), 65-77.

Isart, N., El Said, B., Ivanov, D., Hallett, S., Mayugo, J., & Blanco, N. (2015). Internal geometric modelling of 3D woven composites: A comparison between different approaches. *Composite Structures*, *132*, 1219-1230.

Isart, N., Mayugo, J. A., Blanco, N., Ripoll, L., Solà, A., & Soler, M. (2015). Geometric model for 3D through-thickness orthogonal interlock composites. *Composite Structures*, *119*, 787-798.

Jadhav, G. B., Gawande, V., & Ambi, T. (2015). Review on development and analysis of helical spring with combination of conventional and composite materials. *International Journal of Engineering Research and General Science*, *3*(2), 1180-1184.

Jancirani, J., & Assarudeen, H. (2015). A review on structural analysis and experimental investigation of fiber reinforced composite leaf spring. *Journal of Reinforced Plastics and Composites*, *34*(2), 95-100.

Jang, D., & Jang, S. (2014). Development of a lightweight CFRP coil spring. *SAE 2014 World Congress and exhibition.*

Jiang, Q., Qiao, Y., Zhao, F., Pan, Z., Wu, X., Wu, L., & Fu, H. (2021). Composite helical spring with skin - core structure: Structural design and compression property evaluation. *Polymer Composites*, *42*(3), 1292-1304.

Zhong, J. (2017). Research on the Forward Design and Properties of Automobile Suspension Spring fabricated by Fabric Reinforced Composites. *[D, Jilin University].* Changchun.

Jin, D., Xiong, Z., & Yang, Y. (2013). Stiffness and Strength Analysis of Composite Cylindrical Helical Springs. *Automotive Engineering*, *35*(8), 755-758722.

Jones, R. M. (2018). Mechanics of composite materials. *CRC press*.

Kacar, I., & Yildirim, V. (2011). Natural frequencies of composite cylindrical helical springs under compression. In *Vibration Problems ICOVP 2011* (pp. 119-124). Springer.

Kacar, I., & Yildirim, V. (2016). Free vibration/buckling analyses of noncylindrical initially compressed helical composite springs. *Mechanics Based Design of Structures and Machines*, *44*(4), 340-353.

Kaoua, S. A., Taibi, K., Benghanem, N., Azouaoui, K., & Azzaz, M. (2011). Numerical modelling of twin helical spring under tensile loading. *Applied Mathematical Modelling*, *35*(3), 1378-1387.

Kara, Y. (2017). A review: Fiber reinforced polymer composite helical springs. *Journal of Materials Science & Nanotechnology*, *5*(1), 101-106.

Kazemi, M. E., Shanmugam, L., Dadashi, A., Shakouri, M., Lu, D., Du, Z.,…Yang, L. (2021). Investigating the roles of fiber, resin, and stacking sequence on the low-velocity impact response of novel hybrid thermoplastic composites. *Composites Part B: Engineering*, *207*, 108554.

Ke, J., Wu, Z., Liu, Y., Xiang, Z., & Hu, X. (2020). Design method, performance investigation and manufacturing process of composite helical springs: A review. *Composite Structures*, *252*, 112747.

Kim, D., & David, J. W. (1990). A combined model for high speed valve train dynamics (partly linear and partly nonlinear) (0148-7191).

Kim, S. J., Shin, J., Kim, J. G., Park, K. H., & Jang, K. S. (2021). Circular braided glass fiber/epoxy composites with helical architecture (coil spring) fabricated by p laster ‐ sacrificial compression molding for structural automotive applications. *Journal of Applied Polymer Science*, *138*(19), 50405.

Krishnamoorthy, A., & Karthik, R. (2015). Study of composite helical spring using glass fibre with araldite LY556 and XY54. *Applied Mechanics and Materials*, *766*, 523-527.

Krot, P., & Zimroz, R. (2019). Methods of springs failures diagnostics in ore processing vibrating screens. *IOP Conference Series: Earth and Environmental Science*.

Kumar, M. S., & Vijayarangan, S. (2007). Static analysis and fatigue life prediction of steel and composite leaf spring for light passenger vehicles. *Journal of Scientific & Industrial Research*, *66*(2), 128-134.

Kun, F., Sizhu, W., & Mingtu, M. (2011). Lightweight of automobile. *Modern parts*(12), 42-47.

Lee, K. (2004). Dynamic contact analysis for the valvetrain dynamics of an internal combustion engine by finite element techniques. *Proceedings of the Institution* *of Mechanical Engineers, Part D: Journal of Automobile Engineering*, *218*(3), 353-358.

Li, D., Lu, Z., Chen, L., & Li, J. (2009). Microstructure and mechanical properties of three-dimensional five-directional braided composites. *International Journal of Solids and Structures*, *46*(18-19), 3422-3432.

Li, Y., Sun, B., & Gu, B. (2017). Impact shear damage characterizations of 3D braided composite with X-ray micro-computed tomography and numerical methodologies. *Composite Structures*, *176*, 43-54.

Lim, A. S., An, Q., Chou, T., & Thostenson, E. T. (2011). Mechanical and electrical response of carbon nanotube-based fabric composites to Hopkinson bar loading. *Composites science and technology*, *71*(5), 616-621.

Ling, C. (2020). Preparation and properties of carbon fiber composite helical spring. *[D, Tiangong University]*. Tianjin.

Liu, C., Xie, J., Sun, Y., & Chen, L. (2019). Micro-scale modeling of textile composites based on the virtual fiber embedded models. *Composite Structures*, *230*, 111552.

Liu, S., Qin, S., Jiang, Y., Song, P., & Wang, H. (2021). Lightweight high-performance carbon-polymer nanocomposites for electromagnetic interference shielding. *Composites Part A: Applied Science and Manufacturing*, *145*, 106376.

Liu, T., Bai, J., Lin, Q., & Cong, Q. (2021). An analytical model for predicting compressive behaviour of composite helical Structures: Considering geometric nonlinearity effect. *Composite Structures*, *255*, 112908.

Liu, T., Bai, J., Lin, Q., & Cong, Q. (2021). An analytical model for predicting compressive behaviour of composite helical structures: Considering geometric nonlinearity effect. *Composite Structures*, *255*, 112908.

Lomov, S. V., Verpoest, I., Peeters, T., Roose, D., & Zako, M. (2003). Nesting in textile laminates: geometrical modelling of the laminate. *Composites Science and Technology*, *63*(7), 993-1007.

Londhe, A. B. (2013). FEA and analytical analysis of natural fibers composite leaf spring. *International Journal of Mechanical Engineering and Research*, *3*(4), 355-360.

Luger, M., Traxl, R., Hofer, U., Hirzinger, B., & Lackner, R. (2018). RUC-based multi-scale model for braid-reinforced polymers: Application to coil springs. *Composites Part B: Engineering*, *155*, 431-443.

Ma, S., Hou, Y., Xiao, Y., Chu, F., Cai, T., Hu, W., & Hu, Y. (2020). Metal-organic framework@ polyaniline nanoarchitecture for improved fire safety and mechanical performance of epoxy resin. *Materials Chemistry and Physics*, *247*, 122875.

Mahadik, Y., & Hallett, S. (2010). Finite element modelling of tow geometry in 3D woven fabrics. *Composites Part A: Applied Science and Manufacturing*, *41*(9), 1192-1200.

Makinde, O., Ramatsetse, B. I., & Mpofu, K. (2015). Review of vibrating screen development trends: Linking the past and the future in mining machinery industries. *International Journal of Mineral Processing*, *145*, 17-22.

Manjunatha, T., & Budan, D. A. (2012). Manufacturing and experimentation of composite helical springs for automotive suspension. *International Journal of Mechanical Engineering and Robotics Research*, *1*(2), 229-241.

Miyagawa, H., Mase, T., Sato, C., Drown, E., Drzal, L. T., & Ikegami, K. (2006). Comparison of experimental and theoretical transverse elastic modulus of carbon fibers. *Carbon*, *44*(10), 2002-2008.

Miyagawa, H., Sato, C., Mase, T., Drown, E., Drzal, L. T., & Ikegami, K. (2005). Transverse elastic modulus of carbon fibers measured by Raman spectroscopy. *Materials Science and Engineering a-Structural Materials Properties Microstructure and Processing*, *412*(1-2), 88-92.

Mohammadizadeh, M., Imeri, A., Fidan, I., & Elkelany, M. (2019). 3D printed fiber reinforced polymer composites-Structural analysis. *Composites Part B: Engineering*, *175*, 107112.

Na, X., & Chun, Z. (2019). Fatigue Life Simulation Analysis of Bogie Steel Spring for High Speed Emu. *Modern manufacturing technology and equipment*, *269*(04), 195-199.

Nagao, H., Nakagawa, T., & Hirai, H. (1998). Manufacture of carbon fiber reinforced carbon composite coil spring by preformed-yarn, method. *Kobunshi ronbunshu (Tokyo)*, *55*(2), 96-102.

Ning, F., & Yu, W. (2016). Computer-aided modeling of braided structures overbraiding non-cylindrical prisms based on surface transformation. *Advanced Engineering Software*, *98*, 69-78.

Oh, S., & Choi, B. (2013). A Determination of Design Parameters for Application of Composite Coil Spring in a Passenger Vehicle. *Journal of the Korean Society of Manufacturing Process Engineers*, *12*(1), 77-83.

Oh, S. H., & Choi, B. L. (2014). Analytical and Experimental Study for Development of Composite Coil Springs. *Transactions of the Korean Society of Mechanical Engineers A*, *38*(1), 31-36.

Pan, Z., Gu, B., & Sun, B. (2016). Thermo-mechanical behaviors of 3-D braided composite material subject to high strain rate compressions under different temperatures. *Mechanics of Advanced Materials and Structures*, *23*(4), 385-401.

Pastorcic, D., Vukelic, G., & Bozic, Z. (2019). Coil spring failure and fatigue analysis. *Engineering Failure Analysis*, *99*, 310-318.

Pawar, H., & Desale, D. (2018). Optimization of three wheeler front suspension coil spring. *Procedia manufacturing*, *20*, 428-433.

Pegorin, F., Pingkarawat, K., & Mouritz, A. (2018). Electrical-based delamination crack monitoring in composites using z-pins. *Composites Part A: Applied Science and Manufacturing*, *104*, 120-128.

Peng, L., Liu, C., & Wang, H. (2016). Health identification for damping springs of large vibrating screen based on stiffness identification. *Journal of China Coal Society*, *41*, 1568-1574.

Pourdeyhimi, B., Maze, B., Farukh, F., & Silberschmidt, V. (2019). Structure and mechanics of textile fibre assemblies. *In: Elsevier Amsterdam*, The Netherlands:.

Ramaswamy, K., Modi, V., Rao, P. S., Martin, P. P., McCarthy, C. T., & O'Higgins, R. M. (2023). An investigation of the influence of matrix properties and fibre–matrix interface behaviour on the mechanical performance of carbon fibre-reinforced PEKK and PEEK composites. *Composites Part A: Applied Science and Manufacturing*, *165*, 107359.

Ratle, F., Lecarpentier, B., Labib, R., & Trochu, F. (2004, September). Multi-objective Optimization of a Composite Material Spring Design Using an Evolutionary Algorithm. *Parallel Problem Solving from Nature - PPSN VIII*, Berlin.

Reiner, J., Feser, T., Waimer, M., Poursartip, A., Voggenreiter, H., & Vaziri, R. (2021). Axial crush simulation of composites using continuum damage mechanics: FE software and material model independent considerations. *Composites Part B: Engineering*, *225*, 109284.

Renugadevi, K., Devan, P., & Thomas, T. (2019). Fabrication of Calotropis Gigantea fibre reinforced compression spring for light weight applications. *Composites Part B: Engineering*, *172*, 281-289.

Rodriguez, C. G., Moncada, M. A., Dufeu, E. E., & Razeto, M. I. (2016). Nonlinear model of vibrating screen to determine permissible spring deterioration for proper separation. *Shock and Vibration*, *2016*.

Sancaktar, E., & Gowrishankar, S. (2009, August). Natural Frequencies of Composite Cylindrical Helical Springs Manufactured Using Filament Winding. *International Design Engineering Technical Conferences and Computers and Information in Engineering Conference,* San Diego.

Sardou, M. A., Damotte, E. E., Zunino, C., & Djomseu, P. (2005). Light weight, low cost, composite coil springs are a reality (0148-7191).

Sarh, B., & Kad, B. (2010). Quasi-Static Spring Rate Evaluation of Carbon Fiber Composite Coil Springs. *Journal of advanced materials*, *42*(1), 5-12.

Schell, J., Renggli, M., van Lenthe, G. H., Müller, R., & Ermanni, P. (2006). Micro-computed tomography determination of glass fibre reinforced polymer meso-structure. *Composites Science and Technology*, *66*(13), 2016-2022.

Sequeira, A. A., Singh, R. K., & Shetti, G. K. (2016). Comparative analysis of helical steel springs with composite springs using finite element method. *Journal of Mechanical Engineering and Automation*, *6*(5A), 63-70.

Sevenois, R., Garoz, D., Gilabert, F., Spronk, S., Fonteyn, S., Heyndrickx, M.,…Van Paepegem, W. (2016). Avoiding interpenetrations and the importance of nesting in analytic geometry construction for Representative Unit Cells of woven composite laminates. *Composites Science and Technology*, *136*, 119-132.

Shende, M. A. M., Gandhare, S. N., & Untawale, S. (2016). Failure analysis of helical coil spring in automobile system using finite element method. *International Journal of Research in Science & Engineering*, *2*(5), 1-17.

Shinde, R. M., Godase, S. P., & Sawant, S. M. (2018, April). Comparison of weights of steel and composite coil spring for two wheeler suspension systems. *Proceedings of 4th RIT Post Graduates Conference*.

Shokrieh, M. M., & Rezaei, D. (2003). Analysis and optimization of a composite leaf spring. *Composite Structures*, *60*(3), 317-325.

Sommer, D. E., Thomson, D., Falcó, O., Quino, G., Cui, H., & Petrinic, N. (2022). Damage modelling of carbon fibre composite crush tubes: Numerical simulation and experimental validation of drop weight impact. *Composites Part A: Applied Science and Manufacturing*, *160*, 107033.

Sproewitz, T., Block, J., Bäger, A., Hauer, L., & Schuetze, M. (2011, March). Deployment verification of large CFRP helical high-gain antenna for AIS signals. *2011 Aerospace Conference*.

Stephen, C., Selvam, R., & Suranjan, S. (2019, March). A Comparative Study of Steel and Composite Helical Springs Using Finite Element Analysis. *2019 Advances in Science and Engineering Technology International Conferences (ASET),* Dubai.

Stephen, C., Selvam, R., & Suranjan, S. (2019). A comparative study of steel and composite helical springs using finite element analysis. *Advances in Science and Engineering Technology International Conferences (ASET)*.

Subramanian, C., & Senthilvelan, S. (2010). Effect of reinforced fiber length on the joint performance of thermoplastic leaf spring. *Materials & Design*, *31*(8), 3733-3741.

Sui, G., Fan, Y., Zhong, W., Zhang, Z., Sun, Z., & Chen, R. (2001). Manufacture and experiment study of composite cylindroid spiral spring. *Fuhe Cailiao Xuebao(Acta Materiae Compositae Sinica)(China)*, *18*(1), 46-49.

Suresh, G., Vignesh, R., Aravinth, B., Padmanabhan, K., & Thiagararajan, A. (2014). Fabrication and analysis of nano composite cylindrical helical spring. *International Journal of Innovative Research in Science, Engineering and Technology*, *3*(2), 1208-1213.

Tabatabaei, S., & Lomov, S. V. (2015). Eliminating the volume redundancy of embedded elements and yarn interpenetrations in meso-finite element modelling of textile composites. *Computers & Structures*, *152*, 142-154.

Tao, Z. (2016). The study about forming process of cabon fiber reinforced composite spring. *Shanghai University of engineering and technology.*

Thostenson, E. T., Ren, Z., & Chou, T.-W. (2001). Advances in the science and technology of carbon nanotubes and their composites: a review. *Composites science and technology*, *61*(13), 1899-1912.

Vadlamani, V. K., Chalivendra, V. B., Shukla, A., & Yang, S. (2012). Sensing of damage in carbon nanotubes and carbon black‐embedded epoxy under tensile loading. *Polymer Composites*, *33*(10), 1809-1815.

Wang, Y., & Sun, X. (2001). Digital-element simulation of textile processes. *Composites Science and Technology*, *61*(2), 311-319.

Wooster, W. (1964). Theory of elasticity of an anisotropic elastic body by SG Lekhnitskii. *Acta Crystallographica*, *17*(6), 793-793.

Wu, C., Yang, K., Gu, Y., Xu, J., Ritchie, R. O., & Guan, J. (2019). Mechanical properties and impact performance of silk-epoxy resin composites modulated by flax fibres. *Composites Part A: Applied Science and Manufacturing*, *117*, 357-368.

Wu, L., Chen, L., Fu, H., Jiang, Q., Wu, X., & Tang, Y. (2020). Carbon fiber composite multistrand helical springs with adjustable spring constant: design and mechanism studies. *Journal of Materials Research and Technology*, *9*(3), 5067-5076.

Wu, L., Zhao, F., Li, Y., Sun, X., Liu, S., & Jiang, Q. (2023). Progressive damage analysis of three-dimensional hybrid braided composite under short beam shear loading. *Composite Structures*, *313*, 116960.

Wu, L., Zhao, F., Xie, J., Wu, X., Jiang, Q., & Lin, J.-H. (2020). The deformation behaviors and mechanism of weft knitted fabric based on micro-scale virtual fiber model. *International Journal of Mechanical Sciences*, *187*, 105929.

Xie, J., Chen, X., Zhang, Y., Fang, G., & Chen, L. (2018). Experimental and numerical investigation of the needling process for quartz fibers. *Composites Science and Technology*, *165*, 115-123.

Xie, Y., & Koslowski, M. (2017). Numerical simulations of inter-laminar fracture in particle-toughened carbon fiber reinforced composites. *Composites Part A: Applied Science and Manufacturing*, *92*, 62-69.

Xiong, Z., Song, R., Wu, R., Kang, Z., Zhang, H., & Liu, Q. (2017). Study on Rigidity and Strength of a New Type of Helical Composite Spring. In T. CW (Ed.), *Mechanics and Materials Science* (pp. 163-174). World Scientific.

Xiong, Z., Song, R., & Kang, Z. (2015). Analysis on rigidity of composite helical spring and its influence factors. *Engineering Mechanics*, *32*(9), 216-221.

Xu, J., Li, Y. B., Chen, X., Ge, D., Liu, B., Zhu, M., & Park, T.-H. (2011). Automotive windshield—pedestrian head impact: energy absorption capability of interlayer material. *International Journal of Automotive Technology*, *12*, 687-695.

Xun, L., Wu, Y., Huang, S., Sun, B., Gu, B., & Hu, M. (2022). Degradation of torsional behaviors of 3-D braided thin-walled tubes after atmospheric thermal ageing. *Thin-Walled Structures*, *170*, 108555.

Yanbiao, S. (2020). Numerical simulation and experimental study of a unidirectional basalt fiber helical composite spring. *[D, Jilin University]*. Changchun.

Yang, Y., Jin, D., & Gao, X. (2013). Static stifiness prediction theory and simulation of CFRP cylindrical coil spring. *Autometical Engineering*(7), 21-25.

Yildirim, V. (2001). Free vibration characteristics of composite barrel and hyperboloidal coil springs. *Mechanics of Composite Materials and Structures*, *8*(3), 205-217.

Yildirim, V. (2001). Free vibration of uniaxial composite cylindrical helical springs with circular section. *Journal of sound and vibration*, *239*(2), 321-333.

Ying, H., & Aimin, Y. (2012). Free Vibration of Unidirectional Composite Cylindrical Helical Springs with Rectangular Cross section. *Journal of Tongji University*, *40*(12), 1870-1875.

Ying, H., & Aimin, Y. (2013). Free vibration of laminated composite non-cylindrical helical springs with rectangular cross-section. *Journal of Vibration Engineering*, *26*(3), 335-342.

Ying, M. (2014). Preparation and properties of composite compression helical spring based on VARI. *[D, Tiangong University].* Tianjin.

Yokota, T., Taguchi, T., & Gen, M. (1997). A solution method for optimal weight design problem of herical spring using genetic algorithms. *Computers & industrial engineering*, *33*(1-2), 71-76.

Yong, S., Bin, S., Jing, W., & Wufeng, T. (2009). Technology development and production process situation of spring steel. *Metal Products*, *35*(3), 22-25.

Yang, Y., Jin, D., & Gao, X. (2013). Static Stiffness Prediction Theory and Simulation of CFRP Cylindrical Coil Spring. *Automobile Technology*(07), 21-25.

Yu, A., & Hao, Y. (2013). Warping effect in free vibration analysis of unidirectional composite non-cylindrical helical springs. *Meccanica*, *48*(10), 2453-2465.

Yu, A., & Hao, Y. (2013). Effect of warping on natural frequencies of symmetrical cross-ply laminated composite non-cylindrical helical springs. *International Journal of Mechanical Sciences*, *74*, 65-72.

Yuan, S, Hao, H., Zong, Z., & Li, J. (2017). A study of RC bridge columns under contact explosion. *International Journal of Impact Engineering*, *109*, 378-390.

Yuan, S, Li, S., Zhu, J., & Tang, Y. (2021). Additive manufacturing of polymeric composites from material processing to structural design. *Composites Part B: Engineering*, 108903.

Zebdi, O., Boukhili, R., & Trochu, F. (2009). Optimum design of a composite helical spring by multi-criteria optimization. *Journal of Reinforced Plastics and Composites*, *28*(14), 1713-1732.

Zhan, B., Sun, L., Huang, B., Zhao, G., & Wang, Q. (2018). Design and optimization of automotive composite helical spring. *J Beijing Uni Aer and Ast*, *44*(7), 1520.

Zhang, N., Yang, F., Shen, C. Y., Castro, J., & Lee, L. J. (2013). Particle erosion on carbon nanofiber paper coated carbon fiber/epoxy composites. *Composites Part B-Engineering*, *54*, 209-214.

Zhang, X., & Zhang, Y. (2006). Research of Number Control Machine for Processing High Accuracy Spiral Spring of Many Radices. *Machine Tool Hydraulics*, *12*, 44-48.

Zhong, J. (2017). Research on the forward design and properties of automobile suspension spring fabricated by fabric reinforced composites. *Jilin University.*

Zhou, G., Sun, X., & Wang, Y. (2004). Multi-chain digital element analysis in textile mechanics. *Composites Science and Technology*, *64*(2), 239-244.

Zhou, H., Zhang, W., Liu, T., Gu, B., & Sun, B. (2015). Finite element analyses on transverse impact behaviors of 3-D circular braided composite tubes with different braiding angles. *Composites Part A: Applied Science and Manufacturing*, *79*, 52-62.

Zhuo, P., Li, S., Ashcroft, I. A., & Jones, A. I. (2021). Material extrusion additive manufacturing of continuous fibre reinforced polymer matrix composites: A review and outlook. *Composites Part B: Engineering*, *224*, 109143.